

The Three Ss of Gravitational Wave Astronomy: Sources, Signals, Searches

Thesis by
Ilya Mandel

In Partial Fulfillment of the Requirements
for the Degree of
Doctor of Philosophy



California Institute of Technology
Pasadena, California

2008
(Submitted March 11, 2008)

© 2008

Ilya Mandel

All Rights Reserved

Acknowledgements

Any credit for this thesis is shared with my colleagues and collaborators. All shortcomings are entirely my own.

Kip Thorne has been a generous mentor, encouraging of my successes, patient with my failures, and unwavering in his dedication to the pursuit and teaching of science. Although some of my recent chapter drafts were as full of his trademark red and blue ink as my first paper written under his supervision, I hope that I have learned something from his wisdom and experience about how to do research and how to write about it.

Jon Gair is both a senior colleague and one of my closest friends. While fondly recalling discussing bumpy black holes along the way to the top of Mount Kilimanjaro or serenading bears in Yosemite, I look forward to our future joint adventures both in and out of physics.

I am lucky to have met Cole Miller several years ago, to become infected with his passion for astrophysics, and to have the opportunity of learning from him.

Alexander Silbergleit, Michael Heifetz, Francis Everitt, and the rest of the Gravity Probe B team got me interested in gravitational physics while I was an undergraduate, and continued to care for me long after I left Stanford.

Of course, I am grateful to all of my co-authors whose work is included in this thesis: Pau Amaro-Seoane, Stanislav Babak, Jeandrew Brink, Duncan A. Brown, Jeff Crowder, Curt J. Cutler, Hua Fang, Marc Freitag, Jonathan R. Gair, Chao Li, Geoffrey Lovelace, M. Coleman Miller, Kip S. Thorne, and Michele Vallisneri.

A number of people have given useful advice on various aspects of the research presented here. These include Ronald J. Adler, Luc Bouten, Yanbei Chen, Teviet

Creighton, Steve Drasco, Clovis Hopman, Yuri Levin, Lee Lindblom, Robert Owen, Yi Pan, E. Sterl Phinney, Frans Pretorius, Richard Price, Mark A. Scheel, and Alexander S. Silbergleit.

I thank Curt Cutler, Sterl Phinney, Kip Thorne, and Alan Weinstein for serving on my candidacy and thesis committees and for their advice and encouragement.

I am grateful for the support I received over the years from the Caltech Physics, Mathematics, and Astronomy division in the form of a Teaching Assistant Stipend and reading grants, and from the following sources: NSF Grant PHY-0099568, NASA Grant NAG5-12834, and the Brinson Foundation.

Last, but not least, a big thank you to Alejandro, Craig, Cynthia, Dennis, Donal, JoAnn, Lenya, Paul, Pavlin, Prasun, Tanya, and all of the other flatmates and friends whose company I have enjoyed. BB, you are the best!

Mom, thank you for everything.

Abstract

As gravitational wave astronomy prepares for the first detections of gravitational waves from compact-object binary inspirals, theoretical work is required on the study of (i) gravitational-wave sources, (ii) the signals emitted by those sources, and (iii) the searches for those signals in detector data. This thesis describes work on all three fronts. (i) We discuss intermediate-mass-ratio inspirals (IMRIs) of black holes or neutron stars into intermediate-mass black holes (IMBHs) that could be detected with Advanced LIGO. We analyze different mechanisms of IMRI formation and compute IMRI event rates of up to tens of events per year for Advanced LIGO. We study the spin evolution of IMBHs that grow through a series of minor mergers. We explore how a deviation of an IMRI's central body from a Kerr black hole influences geodesics, including the possibility of chaotic orbital dynamics. We also address the scientific consequences of extreme-mass-ratio inspiral (EMRI) detections by LISA for astrophysics and general relativity, and the difficulties associated with detecting and analyzing EMRI signals. (ii) We study the periodic standing-wave approximation (PSWA), which can potentially provide accurate waveforms in the last inspiral cycles of a comparable-mass black-hole binary. Using a simple model, we find that the solution to Einstein's equations for inspiraling black holes can be recovered to a high accuracy by the addition a perturbative radiation-reaction field to the standing-wave, noninspiraling solution. (iii) We demonstrate the utility of searching for and analyzing tracks in time-frequency spectrograms of a gravitational-wave signal as a means of estimating the parameters of a massive black-hole binary inspiral, as observed by LISA.

Contents

Acknowledgements	iii
Abstract	v
1 Introduction	1
1.1 Sources: Extreme- and Intermediate- Mass-Ratio Inspirals	2
1.1.1 Intermediate-Mass-Ratio Inspirals	2
1.1.1.1 IMRI Overview—Chapter 2	2
1.1.1.2 IMRI Rates—Chapter 3	4
1.1.1.3 IMRIs and IMBH Spin—Chapter 4	5
1.1.2 Geodesics in Bumpy Spacetimes—Chapter 5	6
1.1.3 LISA EMRIs—Chapter 6	7
1.2 Signals: the Periodic Standing-Wave Approximation—Chapter 7	8
1.3 Searches: Mock LISA Data Challenge—Chapter 8	9
2 Prospects for Detection of Gravitational Waves from Intermediate-Mass-Ratio Inspirals	14
3 Rates and Characteristics of Intermediate-Mass-Ratio Inspirals Detectable by Advanced LIGO	26
3.1 Introduction	27
3.2 Astrophysical Setting, Capture Mechanisms, and Typical Eccentricities	29
3.2.1 Hardening of a CO–IMBH Binary via Three-Body Interactions	31
3.2.2 Kozai Resonance	35

3.2.3	Direct Captures	38
3.2.4	Tidal Capture of a Main-Sequence Star	40
3.2.5	Tidal Effects	41
3.2.5.1	Tidal Disruption	41
3.2.5.2	Tidal Capture	44
3.3	Event Rates	50
3.3.1	Advanced LIGO IMRI Sensitivity	50
3.3.2	Number Density of Globulars with a Suitable IMBH	54
3.3.3	IMRI Rate per Globular Cluster and Event Rate	56
3.4	Effect of Eccentricity on Matched Filter Searches	58
3.5	Summary	61
3.6	Appendix A. Waveforms and Signal-to-Noise Ratio Calculation	64
3.7	Appendix B. Ringdowns	69
4	Spin Distribution Following Minor Mergers and the Effect of Spin on the Detection Range for Low-Mass-Ratio Inspirals	79
4.1	Introduction	80
4.2	Spin Evolution	82
4.3	Fokker-Planck Equation for Spin Evolution	84
4.4	Spin Evolution via Monte Carlo Simulations	88
4.5	Effect of Black-Hole Spin on Detection Ranges for Low-Mass-Ratio Inspirals	92
4.6	Appendix A. Fokker-Planck equation	98
5	Observable Properties of Orbits in Exact Bumpy Spacetimes	102
5.1	Introduction	103
5.2	Bumpy Black Hole Spacetimes	108
5.2.1	Spacetime Properties	110
5.2.2	Geodesic Motion	111
5.3	Isolating Integrals	117
5.3.0.1	Poincaré Maps for the Manko-Novikov spacetimes	119

5.3.0.2	Frequency Component Analysis	121
5.3.0.3	Comparison to Other Results	121
5.3.0.4	Accessibility of the Ergodic Domain	123
5.4	Last Stable Orbit	127
5.4.1	Circular Equatorial Orbits	127
5.4.2	Innermost Stable Circular Orbit	128
5.5	Periapsis and Orbital-Plane Precessions	130
5.5.1	Epicyclic Frequencies	132
5.5.2	Precessions	132
5.5.3	Effect of Eccentricity	136
5.6	Summary	140
5.7	Appendix A. Chaotic Motion in Newtonian Gravity	143
5.8	Appendix B. Weak Field Precessions	144
5.8.1	Relativistic Precession	144
5.8.2	Precession due to a Quadrupole Moment	145
6	Detection and Science Applications of Intermediate- and Extreme	
	Mass-Ratio Inspirals into Massive Black Holes	162
6.1	Background	163
6.2	EMRI detection	166
6.2.1	Data analysis algorithms	166
6.2.1.1	Current status	167
6.2.1.2	Outstanding challenges	171
6.2.2	Source modelling	174
6.2.2.1	Current status	174
6.2.2.2	Outstanding challenges	179
6.3	Testing relativity theory	185
6.3.1	Current status	186
6.3.1.1	Comparisons of rival theories	186
6.3.1.2	Tests of consistency within General Relativity	187

6.3.2	Outstanding challenges	192
6.4	EMRI science	196
6.4.1	What can we learn from the characterisations of EMRI/IMRI dynamics, i.e., the observed eccentricities etc. of the orbits?	200
6.4.2	What can we learn about the inspiralling compact objects from EMRIs/IMRIs?	203
6.4.3	What can we learn about the MBHs from EMRIs/IMRIs?	203
6.4.4	What can we learn about cosmology and early structure formation from EMRIs/IMRIs?	204
6.4.5	How can EMRIs/IMRIs be used to test GR, or (assuming GR is correct) that the central massive object is a Kerr BH?	205
6.5	Conclusions	206
7	The Geometry of a Naked Singularity Created by Standing Waves Near a Schwarzschild Horizon, and its Application to the Binary Black Hole Problem	217
7.1	Introduction and Summary	218
7.2	The Mapping Between the BBH Problem and our Model Scalar-Field Problem	221
7.3	Standing-Wave Scalar Field	224
7.3.1	Perturbative standing-wave solution	224
7.3.1.1	Perturbative formalism for the standing-wave spacetime	224
7.3.1.2	First-order metric perturbations due to the standing-wave scalar field	227
7.3.2	Time-averaged fully nonlinear standing-wave solution	231
7.3.2.1	Formalism for nonlinear solution with back reaction	232
7.3.2.2	Singular standing-wave spacetime	233
7.3.2.3	Comparison of standing-wave and Schwarzschild spacetimes	238
7.4	Downgoing Scalar Field	240

7.5	Reconstruction of Downgoing Scalar Field from Standing-Wave Scalar Field	242
-----	--	-----

8 A Three-Stage Search for Supermassive Black Hole Binaries in LISA

	Data	248
8.1	Introduction	249
8.2	Stage 1: Search for Tracks in the Time–Frequency Plane	252
8.3	Stage 2: Grid-Based Search	257
8.4	Stage 3: Markov Chain Monte Carlo	258
8.5	Results for MLDC Challenge	260
8.6	Future Directions	263

List of Figures

- 3.1 The eccentricity at $f_{\text{GW}} = 10$ Hz is plotted as a function of the periapsis at capture. for a CO inspiraling into an IMBH of mass $M = 100 M_{\odot}$. The eccentricity at capture is set to 1, and the eccentricity at $r_p \approx 16 GM/c^2$, where $f_{\text{GW}} = 10$ Hz, follows from Eq. (3.9). 39
- 3.2 Tidal-dissipation-driven inspiral in phase space for an inspiraling star with initial eccentricity of $e = 1$ and initial periapsis $r_p = 1000 r_c$. The plot shows eccentricity on the horizontal axis and the ratio r_p/r_c on the vertical axis. The radius r_c characterizes the frequency of normal modes in the star as defined by Eq. (3.25). 49
- 3.3 Range of a network of three Advanced LIGO detectors for the circular-equatorial-orbit inspiral of a $1.4 M_{\odot}$ object into an IMBH, as a function of IMBH mass M . The three curves show IMRI spins of $\chi = 0.2$ (dashed), 0 (solid), and -0.2 (dot-dashed). Positive χ means prograde orbit; negative χ means retrograde. The quadratic fit given in Eq. (3.28) is a fit to the $\chi = 0$ curve. 53
- 3.4 The overlaps \mathcal{O} between a circular template $h(t)$ and signals $s(t)$ with varying eccentricities, e . For both signal and template, the intrinsic parameters $\vec{\theta} = (M = 100 M_{\odot}, m = 1.4 M_{\odot}, \chi, e)$ are kept constant, with maximization performed only over time of arrival and phase. The overlaps for two values of χ are shown. 62
- 3.5 Fraction of the total energy radiated into each harmonic of the orbital frequency as the particle inspirals in a circular equatorial orbit from $10 r_{\text{isco}}$ to r_{isco} . This energy fraction is shown as a function of BH spin. 68

- 3.6 SNR contributed by the lowest four harmonics of the orbital frequency, as a function of the central BH mass, for circular equatorial orbits. The harmonics are indicated by different line styles — $k = 1$ (dashed), $k = 2$ (solid), $k = 3$ (dotted) and $k = 4$ (dot-dash). Curves are shown for three different BH spins, $\chi = 0$, $\chi = 0.5$ and $\chi = -0.5$ (i.e., retrograde inspirals into a $\chi = 0.5$ BH), indicated by different symbols - crosses, circles and pluses respectively. 70
- 3.7 Range of a network of three Advanced LIGO detectors for the ringdown of an IMBH following a merger with a CO. The luminosity-distance range in Mpc is plotted as a function of IMBH mass M ; cosmological redshift is included. Dashed lines denote $m = 1.4 M_{\odot}$ inspiraling NSs, with pluses corresponding to IMBH spin $\chi = 0.3$ and crosses to $\chi = 1$. Solid lines denote $m = 10 M_{\odot}$ inspiraling BHs, with circles, squares, and triangles corresponding to spins $\chi = 0$, $\chi = 0.3$, and $\chi = 1$, respectively. Dotted line with stars denotes $m = 20 M_{\odot}$ BHs spiraling into an IMBH with spin $\chi = 0.3$ 72
- 4.1 Monte-Carlo predictions for the black-hole spin distribution following black-hole growth via minor mergers from $t = M/m = 5$ to $t = M/m = 10$. The histogram shows the spin distribution at $t = 10$ for a black hole with initial spin $\chi = 0.9$, and the solid curve is a Gaussian fit to that distribution. The dashed curve is a Gaussian fit to the spin distribution at $t = 10$ for a black hole that has initial spin $\chi = 0.1$ at $t = 5$ 89
- 4.2 Monte-Carlo black-hole spin distribution following black hole growth via minor mergers from $t = M/m = 50$ to $t = M/m = 100$. The spin distribution for a black hole with initial spin $\chi = 0.9$ is shown with a solid curve, and one for initial spin $\chi = 0.1$ is shown with a dashed curve. 91

4.3	The ratio between the inclination-averaged Advanced-LIGO detection range for intermediate-mass-ratio inspirals into Kerr black holes of a given spin and the detection range for IMRIs into non-spinning black holes. The solid curve represents black holes with mass $M = 100 M_{\odot}$; the dashed curve, mass $M = 200 M_{\odot}$	94
4.4	The ratio between LISA detection ranges (at SNR= 30) for extreme-mass-ratio inspirals of $m = 10 M_{\odot}$ compact objects into Kerr black holes of mass $M = 10^6 M_{\odot}$ and a given spin vs. non-spinning black holes.	96
4.5	The ratio between LISA detection ranges (at SNR= 30) for extreme-mass-ratio inspirals of $m = 10 M_{\odot}$ compact objects into Kerr black holes of mass $M = 10^7 M_{\odot}$ and a given spin vs. non-spinning black holes.	97
5.1	Spacetime structure for $\chi = 0.9$. The upper row shows zeros of g_{tt} for $q = -1$ (left column), $q = 0$ (middle column) and $q = 1$ (right column). This defines the boundary of the ergoregion of the spacetime. The region with $g_{tt} > 0$ is shaded. The bottom row shows points where $g_{\phi\phi}$ changes sign for the same values of q , and the region where $g_{\phi\phi} < 0$ is shaded. This defines the region where closed timelike curves exist. The middle bottom panel is empty since there is no such region in the Kerr spacetime. The shape of the two boundaries is qualitatively the same for other values of q with the same sign, although both regions grow as $ q $ is increased.	112
5.2	The fractional errors in energy E (solid line), angular momentum L_z (dashed line), and the quantity $g_{\alpha\beta}\dot{x}^{\alpha}\dot{x}^{\beta}$ (dotted line) accumulated over 1700 orbits of a geodesic with $E = 0.92$ and $L_z = 2.5M$ in a spacetime with spin $\chi = 0.9$ and anomalous quadrupole moment $q = 0.95$	114

- 5.3 Effective potential for geodesic motion around a Kerr black hole, with $E = 0.95$, $L_z = 3M$ and $\chi = 0.9$. The curves indicate zeros of the effective potential. Allowed orbits are found in the small region around $\rho = 0$, $z = 0$ (rising and plunging orbits) or in the region containing $\rho = 10$, $z = 0$ (bound orbits). 148
- 5.4 Effective potential for geodesic motion around a bumpy black hole with $\chi = 0.9$, $q = 0.95$, $E = 0.95$, and $L_z = 3M$. The thick dotted curves indicate zeros of the effective potential. The trajectory of a typical geodesic in the outer region is shown by a thin curve. The regular pattern of self-intersections of the geodesic projection onto the $\rho - z$ plane indicates (nearly) regular dynamics. 149
- 5.5 Poincaré map showing $d\rho/d\tau$ vs ρ for crossings of the $z = 0$ plane for a sequence of orbits in the outer allowed region of the Kerr spacetime with $E = 0.95$, $L_z = 3M$ and $\chi = 0.9$. The closed curves indicates the presence of a fourth isolating integral, which we know to be the Carter constant. 150
- 5.6 Poincare map for a geodesic in the outer region of Fig. 5.4. 150
- 5.7 Poincare map for a geodesic in the inner region of Fig. 5.4. 151
- 5.8 Absolute values of the Fourier transforms of $\rho(t)$ (solid line), $z(t)$ (dashed line), and the gravitational wave component $h_+(t)$ (dotted line) in the frequency domain for an orbit in the outer region of Fig. 5.4. The frequency is displayed in units of $1/M$; the amplitude scaling is arbitrary. 151
- 5.9 Absolute values of the Fourier transforms of $\rho(t)$ (solid line), $z(t)$ (dashed line), and the gravitational wave component $h_+(t)$ (dotted line) in the frequency domain for an orbit in the inner region of Fig. 5.4. The frequency is displayed in units of $1/M$; the amplitude scaling is arbitrary. 152
- 5.10 The evolution of the separation $\Delta\rho$ between the inner and outer bounded regions in the equatorial plane along an inspiral in a Manko-Novikov spacetime with $\chi = 0.9$ and $q = 0.95$. $\Delta\rho = 0$ means that the two regions have merged and there is a single bounded region. 152

5.11 Properties of the equatorial ISCO in spacetimes with $\chi = 0$, as a function of q . We show the ρ coordinate of the ISCO (left panel) and the dimensionless frequency of the orbit at the ISCO (right panel). As described in the text, the ISCO radius has three branches, depending on whether it is determined by one of the two branches of radial instability or the branch of vertical instability. These branches are indicated separately in the diagram. For values of q where all three branches are present, the dashed line denotes the “OSCO” and the dotted line denotes $\tilde{\rho}_{\text{ISCO}}$ as discussed in the text. Allowed orbits lie above the curve in the left panel, and below the curve in the right panel. 153

5.12 As Figure 5.11, but now for a spin of $\chi = 0.9$. There are now two ISCO curves, one for prograde orbits and one for retrograde orbits. The allowed range of orbital frequencies is given by the region in between the two curves in the right hand panel. 153

5.13 Periapsis precession p_ρ versus azimuthal frequency Ω_ϕ for $\chi = 0$ and various values of q 154

5.14 Periapsis precession p_ρ versus azimuthal frequency Ω_ϕ for $\chi = 0.9$ and various values of q 154

5.15 Orbital-plane precession p_z versus azimuthal frequency Ω_ϕ for $\chi = 0$ and various values of q . We do not show the case $q = 0$ here, since there is no orbital-plane precession in Schwarzschild. 155

5.16 Orbital-plane precession p_z versus azimuthal frequency Ω_ϕ for $\chi = 0.9$ and various values of q 155

5.17 Difference between periapsis precessions in a bumpy spacetime with $\chi = 0$ and the Schwarzschild spacetime, $\Delta p_\rho(\Omega_\phi, q) = p_\rho(\Omega_\phi, q) - p_\rho(\Omega_\phi, q = 0)$. 156

5.18 Difference between periapsis precessions in a bumpy spacetime with $\chi = 0.9$ and the Kerr spacetime with $\chi = 0.9$, $\Delta p_\rho(\Omega_\phi, q) = p_\rho(\Omega_\phi, q) - p_\rho(\Omega_\phi, q = 0)$ 156

5.19	Difference between orbital-plane precessions in a bumpy spacetime with $\chi = 0.9$ and the Kerr spacetime with $\chi = 0.9$, $\Delta p_z(\Omega_\phi, q) = p_z(\Omega_\phi, q) - p_z(\Omega_\phi, q = 0)$	157
5.20	Example of onset of chaos in the Newtonian quadrupole-octupole potential (5.25). All plots are for orbits which start with $\dot{\rho} = 0 = \dot{z}$, $\rho/M = 3$ and have specific angular momentum $L_z = 1.7M$. The left hand panels are for energy $E = 0.82$, while the right hand panels have energy $E = 0.81$. The top two plots show zeros of the effective potential, $V_{\text{eff}} = 0$, as defined by equation (5.26), and the paths followed by the orbits in the (ρ, z) plane. The bottom two plots are Poincaré maps for crossings of the $z = 0$ plane in each case.	158
6.1	Power spectral density of one of the unequal arm Michelson TDI channel. It contains 1 MBH inspirals at luminosity distances of 3.3 Gpc and 1 EMRI at luminosity distances of 2.3 Gpc. The duration of the EMRI was taken to be one and a half years. The galactic binary realisation used here was drawn from the distribution described in [80].	168
6.2	Spectrogram of the signal from an EMRI on an inclined and eccentric orbit. One can see several harmonics modulated by orbital precession and LISA's orbital motion.	170
6.3	The two polarisations of an NK EMRI waveform with a mass ratio of 10^{-7} . The GW amplitude is measured in units of the mass of the compact object over distance (μ/D) and time is measured in units of MBH mass M . The eccentricity is ~ 0.3 , the semi-latus rectum $p \sim 12M$, the inclination of the plane to the MBH spin axis is 140 degrees and the detector (observer) is 30 degrees above the azimuthal plane.	180
6.4	Contours of constant “detectable lifetime” (as defined in the text) for the circular-equatorial inspiral of a $10M_\odot$ black hole into an MBH with spin $a = 0.99$, as a function of MBH mass M and redshift z	201

6.5	As for Figure 6.4, this figure shows contours of constant “detectable lifetime”, τ , for the circular-equatorial inspiral of a $10M_{\odot}$ black hole into an MBH. Here we show $\tau = 1$ year contours for several different spins of the central black hole, as labelled in the key. Negative spins indicate retrograde circular-equatorial inspirals into black holes of the same spin magnitude.	202
7.1	The standing-wave scalar field in a Schwarzschild background (solid curve) and the effective potential (dashed curve) for angular frequency $\omega = 0.049$	226
7.2	Metric perturbations for a standing-wave scalar field in a Schwarzschild background with angular frequency $\omega = 0.19$ and amplitude $\Psi_0 = 0.015$ far from the black hole, corresponding to a binary separation $a \approx 6M$, [Eq. (7.12a)].	230
7.3	Embedding diagram for the spacetime with time-averaged standing-wave scalar field of angular frequency $\omega = 0.19$ and amplitude $\Psi_0 = 0.015$ at large radii [corresponding to the binary black hole separation $a \approx 6M$; Eq. (7.12a)]. The solid line represents embedding in Euclidean space; the dashed line, embedding in Minkowski space. Regions I, II and III are labeled on plot.	238
7.4	(a) Redshift $z = \delta\lambda/\lambda$ of light emitted from radius r and received by an observer at $r = 10$. (b) Redshift for an observer at $r = 0.0001$. A distant observer would see light emitted from $r = 0.0001$ redshifted by $\ln(z + 1) \approx 10^5$. These curves are drawn for the spacetime with time-averaged standing-wave scalar field that has angular frequency $\omega = 0.19$ and amplitude $\Psi_0 = 0.015$ at large radii [corresponding to the binary black hole separation $a \approx 6M$; Eq. (7.12a)].	239

- 7.5 (a) Fractional differences of the metric components $g_{tt} = -g_{r^*r^*}$ (solid curve) and $g_{\theta\theta}$ (dashed curve) between Schwarzschild spacetime D and standing-wave scalar field spacetime S with scalar-wave amplitude and frequency chosen to model BBH separation $a \approx 6M$ [Eq. (7.12a)]. (b) Same quantities plotted for scalar field parameters chosen to model BBH separation $a \approx 15M$ [Eq. (7.12b)]. 240
- 7.6 (a) The fractional difference in the amplitudes of the reconstructed scalar field and downgoing scalar field $\delta d/d \equiv (d^{SW+RR} - d^{down})/d^{down}$ (solid curve) and the phase difference between the two fields $\delta\phi_d = \phi_d^{SW+RR} - \phi_d^{down}$ (dashed curve), plotted vs. r^* . Scalar-wave amplitude and frequency chosen to model BBH separation $a \approx 6M$. (b) Same quantities plotted for scalar-field parameters chosen to model BBH separation $a \approx 15M$ 244
- 8.1 Time–frequency plot of the brightest pixel in each time bin, as computed for the X channel of Challenge 1 training set 1.2.1. The bottom plot is a blown-up version of the top plot showing the presumed track found on the first pass through the data. 255
- 8.2 The stars represent individual points on the TF map obtained during the second pass through the data in the $X(t)$ channel of where Training Set 1.2.1. The curve is the result of fitting these points to the model (8.1). 256
- 8.3 Comparison of our best-fit $X(t)$ to the true $X(t)$ for a) a short stretch of time near t_c and b) a short stretch near the beginning of the dataset. Clearly, our fit is excellent near t_c , where most of the SNR accumulates, but much poorer at early times. 262

List of Tables

6.1	This table shows the signal-to-noise ratio (SNR) at a distance of 1Gpc for systems with a variety of observed masses M and m . Also shown is the maximum redshift at which such a source could be detected, z_{max} , and the intrinsic masses of the system, $M_i = M/(1 + z_{max})$ and $m_i = m/(1 + z_{max})$, that a source at redshift z_{max} would need to have in order to have apparent red-shifted masses M and m . The SNRs were computed assuming the optimal TDI combination of LISA data streams could be constructed for five years of observation. All sources have MBH spin of $S/M^2 = 0.8$, inclination of 45° and eccentricity at plunge of 0.25. The waveforms were computed using the numerical kludge model [40, 6] and the LISA response was included using the Synthetic LISA simulator [106]. These results were used for computing event rate estimates using the semi-coherent search [43].	198
8.1	Parameters extracted via TF searches from the X , Y and Z channels of blind Challenge dataset 1.2.1. N is the number of data points obtained during the second pass through the data and Σ is the sum of the squares of the residuals, as defined in (8.2).	255
8.2	True values and estimates from three steps for the challenge parameters. In stages 1 and 2 estimates were made only for parameters M_c and η (and therefore m_1 and m_2) and t_c	262

Chapter 1

Introduction

The gravitational-wave community is poised on the threshold of exciting discoveries. First-generation ground-based interferometers, such as LIGO [1] and VIRGO [2], are actively searching for gravitational waves, with peak sensitivities at a few hundred hertz. Advanced LIGO [3], a future upgrade, will have both a greater range for detections and an increased sensitive band. A planned space-based mission, LISA [4], will operate at peak sensitivities around a millihertz. Of particular interest for LIGO and LISA are the gravitational waves emitted during the inspirals of compact-object binaries [5]. These include, for LIGO, stellar-mass binaries composed of black holes (BHs) or neutron stars (NSs); and for LISA, massive black hole (MBH) binaries with components in the $10^5 M_\odot - 10^7 M_\odot$ range, extreme-mass-ratio inspirals (EMRIs) of stellar-mass compact objects into MBHs, and galactic white dwarf (WD) binaries. These inspirals might also include intermediate-mass-ratio inspirals (IMRIs) of either stellar-mass compact objects into intermediate mass black holes (IMBHs) detectable with Advanced LIGO, or IMRIs of IMBHs into MBHs detectable with LISA.

Astrophysical estimates of the abundances of various source classes suggest that the first gravitational-wave detections are likely to be made within the next decade [6, 7, 8]. Once detected, gravitational waves will provide a unique way to explore the universe — to observe in detail a variety of astrophysical and relativistic phenomena. However, the detection and analysis of gravitational waves pose a number of theoretical challenges. These can be broadly divided into three categories: (i) sources: the exploration of the possible astrophysical sources of gravitational waves and of the

scientific consequences of gravitational-wave detection — the investigation of general relativity in the strong field regime and applications to astrophysics; (ii) signals: the accurate modeling of signals from various sources (an essential foundation for gravitational-wave data analysis); and (iii) searches: gravitational-wave data analysis — the perfection of methods for signal detection and parameter extraction. In this thesis, we describe some advances in all three areas of Gravitational Wave Astronomy: Sources, Signals, and Searches.

1.1 Sources: Extreme- and Intermediate- Mass-Ratio Inspirals

Observations of extreme- or intermediate- mass-ratio inspirals of compact objects into intermediate-mass or massive black holes will offer an exceptional opportunity to explore strong-field general relativity, and to glean important information about the astrophysical history of the universe. Observed EMRI or IMRI waves should contain a complete map of the spacetime of the central black hole or, equivalently, the values of all the hole’s multipole moments [9] and should also contain details of tidal coupling between the central hole and the inspiraling object [10, 11]. An EMRI or IMRI signal can reveal whether the central body is indeed a black hole or is something else, e.g., an exotic massive object such as a boson star [12, 13]. This can be determined by extracting from the signal the central body’s lowest few multipole moments; if they have a specific pattern dictated by the measured mass and spin, the body is a Kerr hole; otherwise, it must be something else [9, 14].

1.1.1 Intermediate-Mass-Ratio Inspirals

1.1.1.1 IMRI Overview—Chapter 2

Advanced LIGO may be able to detect intermediate-mass-ratio inspirals of stellar-mass black holes or neutron stars into ~ 50 to ~ 300 solar-mass IMBHs. A single detection would be significant in itself, since it could provide the first unambiguous

proof of the existence of IMBHs, for which only indirect evidence exists so far [15]. Advanced LIGO IMRIs will allow us to probe the strong-field regime with modest accuracy well before LISA flies. In particular, it will be possible to measure the quadrupole moment Q of the central body to an accuracy $\Delta Q/M^3 \lesssim 1$, which would be enough to distinguish whether the IMBH is a Kerr black hole or a boson star [16].

Chapter 2 of this thesis is a paper by Duncan A. Brown, Jeandrew Brink, Hua Fang, Jonathan R. Gair, Chao Li, Geoffrey Lovelace, *Ilya Mandel*, and Kip S. Thorne [16] on the prospects for the detection of gravitational waves from IMRIs with Advanced LIGO, and related issues. This paper provides an overview of recent results on IMRIs obtained by members of Kip Thorne’s group at Caltech and their collaborators.

If there is an IMBH in each globular cluster that grows from ~ 50 to ~ 350 solar masses via mergers with compact objects in the age of the universe [17], Advanced LIGO could achieve tens of IMRI detections per year. (A more detailed rates estimate is discussed in the next paragraph and in Chapter 3). IMRI waveforms fall between the ranges of validity of post-Newtonian waveforms (inapplicable because of the large number of cycles that IMRIs spend at small radii) and EMRI waveforms based on solutions of the Teukolsky equation (suspect because the IMRI mass ratio is not sufficiently extreme). We estimate that Teukolsky waveforms may be sufficient for detection, perhaps leading to a loss of $\lesssim 10\%$ in signal-to-noise ratio (SNR), but better waveforms will be necessary for parameter extraction. Chapter 2 also introduces orbital motion in a non-Kerr spacetime and discusses the possibility of the loss of the full set of integrals of motion (in Kerr, these are energy, angular momentum, and the Carter constant) in a stationary, axisymmetric, reflection symmetric and asymptotically flat (SARSAF) spacetime with an anomalous non-Kerr value of the mass quadrupole moment; more details are presented in Sec. 1.1.2 and Chapter 5.

I contributed to this paper a calculation of event rates for IMRIs, an independent computation of the accuracy of Teukolsky waveforms, and some of the analysis of geodesic motion in non-Kerr spacetimes. I was responsible for writing the “Event Rates for IMRIs” section and contributed some prose to other sections.

1.1.1.2 IMRI Rates—Chapter 3

A more careful computation of the IMRI event rates detectable by Advanced LIGO requires the analysis of specific IMRI formation mechanisms. We present this analysis in Chapter 3, which is identical to the text of a paper by *Ilya Mandel*, Duncan A. Brown, Jonathan R. Gair, and M. Coleman Miller [18].

In Chapter 3, we consider four mechanisms of IMRI formation: (i) The hardening of a NS-IMBH binary or BH-IMBH binary can proceed through three-body interactions with other stars in the cluster, followed by an inspiral driven by gravitational radiation reaction; we believe this to be the most important IMRI formation mechanism for IMBHs in the Advanced-LIGO mass range. (ii) Hardening via the Kozai resonance can drive up the eccentricity of the inner binary in a hierarchical triple system and can be important if binary–binary encounters are common. (iii) A direct capture of a BH or NS by an IMBH is unlikely to be important because the direct capture cross-section grows as $M^{12/7}$ and is relatively small for the light IMBHs that can be detected by Advanced LIGO. (The detectable IMBH mass is limited from above by the requirement that the gravitational wave frequency exceed the Advanced-LIGO low-frequency cutoff of ~ 10 Hz.) (iv) The inspiral of a compact remnant from a tidally captured main sequence star will not be a significant source for Advanced LIGO.

We estimate that Advanced LIGO may detect one neutron star IMRI every three years or ten black hole IMRIs per year, and more if the interferometer is optimized for detections at low frequencies. These rates are extremely uncertain, however, due to our lack of knowledge about the distribution and mass function of IMBHs (or, in fact, whether they exist at all). We also consider the circularization of inspirals due to the emission of gravitational waves. We find that, although the degree of circularization varies depending on the IMRI formation mechanism, even direct-capture inspirals (which are the most likely to display significant eccentricities) in $\sim 90\%$ of all cases will have eccentricity $\lesssim 0.1$ when the gravitational wave frequency reaches 10 Hz. This implies that circular templates can be used while searching for IMRI signals in

Advanced-LIGO data.

For this paper, I computed the eccentricities resulting from various capture scenarios (except for tidal effects), the expected Advanced-LIGO detection rates for inspirals, and the expected rates for ringdowns. I was the primary author of Sections 3.1, 3.2.1–3.2.3, 3.3, 3.5, and 3.7, and coordinated the research and writing for the whole paper.

1.1.1.3 IMRIs and IMBH Spin—Chapter 4

Minor mergers with compact objects that follow intermediate-mass-ratio inspirals will contribute both mass and angular momentum to the IMBH, leading to the evolution of the IMBH spin [19, 20]. In Chapter 4, which is based fully on my own work (in preparation for publication), we compute the probability distribution for the spin of an IMBH following a series of minor mergers with isotropically-distributed inspiraling compact objects. This computation is carried out by a combination of two approaches: (i) analytical fits to the Fokker-Planck equation governing the stochastic process of spin evolution, and (ii) numerical Monte-Carlo simulations of spin evolution in situations when the Fokker-Planck analysis is not applicable. We find, for example, that an IMBH that grows from $70 M_{\odot}$ to $140 M_{\odot}$ through the capture of $1.4 M_{\odot}$ neutron stars will have dimensionless spin parameter $\chi \equiv S_1/M^2 \sim 0.2 \pm 0.08$.

Prograde inspirals into rapidly spinning black holes have lower last-stable-orbit (LSO) radii and higher LSO frequencies than inspirals into non-spinning black holes, and will therefore typically radiate into a frequency band where Advanced LIGO is more sensitive. After averaging over all orbital inclinations, we find that Advanced LIGO will be able to detect IMRIs in a larger volume of space if all IMBHs were to have the same non-zero spin χ than if all IMBHs were non-spinning. For plausible values of IMBH mass and spin, the ratio of the two volumes may reach ~ 1.4 . We carry out a similar analysis for LISA EMRIs, and find that LISA will detect EMRIs into $\sim 10^7 M_{\odot}$ MBHs to an inclination-averaged range that is ~ 8 times greater if the MBHs are maximally spinning than if they are non-spinning. This creates a bias in favor of detecting EMRIs into rapidly spinning MBHs. This bias will be significant

for the extraction of the MBH spin distribution from LISA EMRI statistics.

I am responsible for all of the research and prose in this chapter.

1.1.2 Geodesics in Bumpy Spacetimes—Chapter 5

As noted above, it should be possible, in principle, to extract the multipole structure of a massive body from its imprint on the gravitational waves emitted in the course of an EMRI or IMRI [9, 21]. If the massive body is a Kerr black hole, the “no-hair” theorem predicts that all of its multipole moments are determined by its mass and spin. Therefore, measuring the multipole structure will make it possible to explore whether the body is a Kerr black hole or something else, such as a boson star or a naked singularity [9, 14]. This exploration will require constructing waveforms from inspirals in non-Kerr, “bumpy” spacetimes [22] and using them in the data analysis, in order to determine, from the observed waves, the source’s multipole moments and (if they are near the Kerr values) to constrain their deviations from Kerr.

In Chapter 5 we consider the first step toward the generation and analysis of inspiral waveforms in bumpy spacetimes by considering the effect of an anomalous mass quadrupole moment Q on test-particle orbital dynamics. In that chapter, which is based on the joint work of Jonathan R. Gair and *Ilya Mandel* (in preparation for a future publication), we use the Manko-Novikov metric as a model of a “bumpy” (non-Kerr) spacetime. We find strong evidence that, while geodesic motion in Kerr has the full set of isolating integrals, one of these integrals, the Carter constant, disappears in prolate Manko-Novikov spacetimes. This leads to chaotic motion in some regions of these spacetimes, as exhibited by space-filling Poincaré maps. We give evidence, however, that these chaotic regions are not accessible in the course of an astrophysical inspiral, however, and that geodesic motion in the accessible regions is tri-periodic to a high precision. We compute the precession of the periapsis and of the orbital plane due to the presence of an anomalous Q . The shifts in precession frequencies from their Kerr values are significant in the strong-field regime, which may aid in the detection of the central body’s bumpiness.

The results in this chapter were obtained either jointly or independently by Jonathan Gair and myself. I wrote most of the prose in Sections 5.1, 5.2, 5.3, and 5.6, but Jonathan Gair also contributed to those sections while I contributed to the prose in Section 5.5, for which he was the primary author.

1.1.3 LISA EMRIs—Chapter 6

There is a great deal of astrophysical information that could be gained from the detection of EMRIs in addition to the probes of general relativity described above. LISA EMRIs data can be analyzed to answer some of the following astrophysical questions: What is the mass function of massive black holes? What are their mechanisms of formation? (High spin suggests growth by accretion, while low spin is indicative of growth through random mergers.) What is the distribution of various types of compact objects in the vicinity of massive black holes? Which capture mechanism is suggested by an observed EMRI eccentricity distribution? Are compact objects formed externally or in the disk (as indicated by EMRI inclinations)?

In Chapter 6, we consider these possible benefits of EMRI detections, as well as the use of EMRIs as tests of general relativity. The status of EMRI waveform modeling and EMRI data analysis are also reviewed. We particularly focus on outstanding issues in the field of EMRI science. This chapter is based on a review article by Pau Amaro-Seoane, Jonathan R. Gair, Marc Freitag, M. Coleman Miller, *Ilya Mandel*, Curt J. Cutler, and Stanislav Babak [23]. A review of the astrophysics of EMRI sources is omitted since I did not make significant contributions to that section.

My primary contributions to this chapter were to the discussion of IMRI waveform accuracy and the review of testing general relativity with EMRIs and IMRIs.

1.2 Signals: the Periodic Standing-Wave Approximation— Chapter 7

For comparable-mass binary black holes, accurately computing gravitational waves from the last stages of inspiral, where the signal is strongest, is crucial to successful data analysis. However, such computations are extremely challenging, as post-Newtonian approximations fail for the last ~ 25 cycles of the inspiral waves [24]. Full $3 + 1$ numerical relativity has recently made great progress in computing the gravitational waves from the last ~ 30 cycles of the inspiral; however, numerical relativity codes may be too slow to be useful for placing templates. An alternative approach is the periodic standing wave approximation (PSWA), suggested by Detweiler [25] and actively pursued by Price and collaborators [26, 27]. In the PSWA, the energy and angular momentum of the binary are conserved by the imposition of standing gravitational waves, so the spacetime exhibits a “helical” symmetry that greatly simplifies numerical simulations. In the absence of tidal locking, the standing waves of the PSWA destroy black-hole horizons, leaving naked singularities in place of Kerr black holes [28]. To confirm the validity of the PSWA, it is necessary to determine the accuracy with which the physical spacetime with true black holes can be reconstructed from the standing-wave spacetime with naked singularities by adding a perturbative radiation-reaction field, as suggested by Thorne [29].

In Chapter 7, which is identical to the text of a paper by *Ilya Mandel* [28], we consider a simple model problem consisting of a single spherically symmetric black hole that is converted into a naked singularity by spherical standing waves of a scalar field. The spacetime remains nearly Schwarzschild outside the Schwarzschild horizon but deviates strongly from Schwarzschild at $r \sim 2M$ and below. We show that by adding a perturbative radiation-reaction field to the standing-wave solution, a physical (downgoing) solution to the scalar-wave equation can be recovered with sufficient accuracy to offer optimism that PSWA will give accurate gravitational waveforms for the final stages of binary-black-hole inspiral.

The research and prose in this paper are my work, with considerable advice from

Kip Thorne.

1.3 Searches: Mock LISA Data Challenge—Chapter 8

Among other potential discoveries, LISA will make the first observations of gravitational waves from the coalescences of massive-black-hole (MBH) binaries. Astrophysical estimates suggest that LISA may detect several such coalescences per year [7], with a signal-to-noise ratio reaching as high as several thousand [30]. The detection of MBH inspirals is one of the priorities of the Mock LISA Data Challenges [31].

In Chapter 8, we demonstrate that massive-black-hole-binary-inspiral waveforms can be accurately extracted from LISA data in the presence of noise. The text of Chapter 8 is identical to a paper by Duncan A. Brown, Jeff Crowder, Curt Cutler, *Ilya Mandel* and Michele Vallisneri, which reports on the success of our three-stage approach consisting of (i) a time-frequency spectrogram analysis, (ii) a grid-based matched-filtering search, and (iii) a Markov Chain Monte Carlo search, in determining the parameters of a MBH binary present in the signal from the first round of the Mock LISA Data Challenge [32].

My contribution to this research is in the analysis of time-frequency maps. Gravitational-wave signals from MBH binary inspirals will be easily visible as tracks on time-frequency plots due to their high SNR. We find that the chirp mass of non-spinning MBHs on a circular orbit can be estimated to better than one percent from a time-frequency search at an SNR of a few hundred. This estimate allows a significant reduction in the number of templates necessary in the second-stage matched-filtering search, by restricting the region of parameter space which must be covered with templates. (Matched filtering followed by Markov Chain Monte Carlo is probably the best method for accurate parameter determination.) I am involved in ongoing efforts to make parameter estimation from time-frequency plots robust in low SNR conditions, to detect multiple MBH inspiral tracks simultaneously, and to detect MBH inspiral tracks in the presence of other signals, including a confusion noise background.

I carried out the research reflected in Section 8.2 and wrote most of the prose in

that section.

Bibliography

- [1] Barish, B. C. & Weiss, R. 1999. *Physics Today*, **10**, 44
- [2] Acernese, F., *et al.* 2006. *Class. Quant. Grav.*, **23**, S635
- [3] Fritschel, P. 2003. gr-qc/0308090
- [4] Danzmann, K., *et al.*, *LISA – Laser Interferometer Space Antenna, Pre-Phase A Report*, Max-Planck-Institute für Quantenoptic, Report MPQ 233 (1998)
- [5] Thorne, K. S. 1987. In *300 Years of Gravitation*, edited by S. Hawking and W. Israel (Cambridge University Press)
- [6] Kalogera, V., Belczynski, K., Kim, C., O’Shaughnessy, R., and Willems, B. 2007. *Physics Reports, Hans Bethe Centennial Volume*, **442**, 75, astro-ph/0612144
- [7] Vecchio, A. 2004. *Phys. Rev. D***70**, 042001, arXiv:astro-ph/0304051
- [8] Barack, L., Creighton, T., Cutler, C., Gair, J., Larson, S., Phinney, E. S., Thorne, K. S., and Vallisneri, M. 2003. available on-line at <http://www.tapir.caltech.edu/listwg1/EMRI/LISTEMRIreport.pdf>
- [9] Ryan, F. D. 1995 *Phys. Rev. D* **52** 5707
- [10] Thorne, K. S. 2003. Chapter 5 of *The future of Theoretical Physics and Cosmology*, eds. G. Gibbons, E. Shellard, and S. Rankin (Cambridge University Press)
- [11] Fang, H. & Lovelace, G. 2005. *Phys. Rev. D***72**, 124016
- [12] Ryan F. D. 1997. *Phys. Rev. D***55** 6081

- [13] Kesden, M., Gair J. R., and Kamionkowski. M. 2005. Phys. Rev. D**71** 044015
- [14] Hughes, S. A. 2006. In *Laser Interferometer Space Antenna: 6th International LISA Symposium*, vol. 873 of *American Institute of Physics Conference Series*, pp. 233-240, arXiv:gr-qc/0608140
- [15] Miller, M. C., & Colbert, E. J. M. 2004. IJMPD, 13, 1
- [16] Brown, D. A., Brink, J., Fang, H., Gair, J. R., Li, C., Lovelace, G., Mandel, I., & Thorne, K. S. 2007. Phys. Rev. Lett, accepted, arXiv:gr-qc/0612060
- [17] Phinney, E. S. 2005, private communication
- [18] Mandel, I., Brown, D. A., Gair, J. R., Miller, M. C. 2007, submitted to ApJ, arXiv:0705.0285
- [19] S. A. Hughes & R. D. Blandford. 2004, ApJ, 585, L101
- [20] Miller, M. C. 2002, ApJ, 581, 438
- [21] Li, C. 2007. In preparation
- [22] Collins, N. A. & Hughes, S. A. 2004. Phys. Rev. D**69**, 124022, arXiv:gr-qc/0402063
- [23] Amaro-Seoane, P., Gair, J. R., Freitag, M., Miller, M. C., Mandel, I., Cutler, C. J., Babak, S. 2007, submitted to Class. Quant. Grav.arXiv:astro-ph/0703495
- [24] Brady, P. R., Creighton, J. D. E., and Thorne, K. S. 1998. Phys. Rev. D**58**, 61501
- [25] Detweiler, S. 1994. Phys. Rev. D**50**, 4929
- [26] Price, R. 2004. Class. Quant. Grav., **21**, S281
- [27] Andrade, Z. *et al.* 2004. Phys. Rev. D**70**, 064001
- [28] Mandel, I. 2005. Phys. Rev. D**72**, 084025

- [29] Thorne, K. S. 2002. Unpublished notes
- [30] Flanagan, E. E. & Hughes, S. A. 1998. *Phys. Rev. D***57**, 4535
- [31] Arnaud K A *et al.* (Mock LISA Data Challenge Task Force) 2006. In *Laser Interferometer Space Antenna, Sixth International LISA Symposium* AIP Conf. Proc. 873, ed. Merkowitz S M and Livas J C p 619
- [32] Brown, D. A., Crowder, J., Cutler, C., Mandel, I., Vallisneri, M. 2007. Submitted to *Class. Quant. Grav.*, arXiv:0704.2447

Chapter 2

Prospects for Detection of Gravitational Waves from Intermediate-Mass-Ratio Inspirals

We explore the prospects for Advanced LIGO to detect gravitational waves from neutron stars and stellar mass black holes spiraling into intermediate-mass black holes ($M \sim 50M_{\odot}$ to $350M_{\odot}$). We estimate an event rate for such *intermediate-mass-ratio inspirals* of up to $\sim 10\text{--}30 \text{ yr}^{-1}$. Our numerical simulations show that if the central body is not a black hole but its metric is stationary, axisymmetric, reflection symmetric and asymptotically flat then the waves will likely be tri-periodic, as for a black hole. We report generalizations of a theorem due to Ryan (1995) which suggest that the evolutions of the waves' three fundamental frequencies and of the complex amplitudes of their spectral components encode (in principle) a full map of the central body's metric, full details of the energy and angular momentum exchange between the central body and the orbit, and the time-evolving orbital elements. We estimate that Advanced LIGO can measure or constrain deviations of the central body from a Kerr black hole with modest but interesting accuracy.

Accepted for publication in Physical Review Letters: Duncan A. Brown, Jeandrew Brink, Hua Fang, Jonathan R. Gair, Chao Li, Geoffrey Lovelace,

Ilya Mandel, Kip S. Thorne (2007). A preprint is available online at <http://arxiv.org/abs/gr-qc/0612060>.

First-generation interferometric gravitational-wave (GW) detectors, such as LIGO [1] and VIRGO [2], are now searching for GWs at or near their design sensitivities. In the next decade, Advanced LIGO (AdvLIGO) [3] and its international partners will increase the volume of the universe searched a thousand-fold or more. The most promising sources of GWs for this network are the inspiral and coalescence of black hole (BH) and/or neutron star (NS) binaries. Current inspiral searches target sources with total mass $M \lesssim 40M_{\odot}$: NS binaries with masses $1\text{--}3M_{\odot}$, BH binaries with masses $3\text{--}40M_{\odot}$, and NS-BH binaries with components in these mass ranges [4, 5].

Ultra-luminous X-ray observations and simulations of globular cluster dynamics suggest the existence of intermediate mass black holes (IMBHs) with masses $M \sim 10^2\text{--}10^4M_{\odot}$ [6]. The GWs from the inspiral of a NS or stellar-mass BH into an IMBH with mass $M \sim 50\text{--}350M_{\odot}$ will lie in the frequency band of AdvLIGO. These *intermediate-mass-ratio inspirals* (IMRIs) are analogous to the extreme-mass-ratio inspirals (EMRIs) of stellar-mass objects spiraling into $\sim 10^6M_{\odot}$ BHs, targeted by the planned space-based LISA observatory [7]. We consider NSs and BHs, as less compact objects (e.g. white dwarfs) are tidally disrupted at frequencies too low to be detectable in AdvLIGO.

If we consider the possibility that the central body of an IMRI (or EMRI) is not a black hole, but some other general relativistic object (e.g. a boson star or a naked singularity [8]), then we can quantify the accuracy with which it has the properties predicted for a black hole: (i) that it obeys the black-hole no-hair theorem (its spacetime geometry is the Kerr metric, fully determined by its mass and spin), and (ii) that its *tidal coupling* (tide-induced transfer of energy and angular momentum between orbit and body) agrees with black-hole predictions. Searching for other types of objects may yield an unexpected discovery.

This letter reports on our initial explorations of the prospects for AdvLIGO to detect the GWs from IMRIs and to probe the properties of the IMRIs' central bodies.

We report on: (i) IMRI event rate estimates in AdvLIGO, (ii) estimates of the efficacy of GW template families for IMRI searches, (iii) explorations of the character of the IMRI (EMRI) waves if the central body is not a black hole, (iv) generalizations of Ryan’s theorem concerning the information about the central body carried by IMRI and EMRI waves, and (v) estimates of the accuracies with which information can be extracted by AdvLIGO from IMRIs.

Event Rates for IMRIs with an IMBH central body. We (Mandel, Brown, Gair & Miller [12]) estimate that for low IMBH spins $\chi = \text{spin angular momentum}/M^2 \lesssim 0.3$, the distance (*range*) R in Mpc to which a network of three 4 km AdvLIGO detectors could see IMRIs at a network signal-to-noise ratio (SNR) of 8 is

$$R \approx [1 + (\chi^2/2)(M/100M_\odot)^{1.5}] \sqrt{m/M_\odot} \times [800 - 540(M/100M_\odot) + 107(M/100M_\odot)^2].$$

(For IMBHs grown by mergers, typical spins will be $\chi \sim \sqrt{m/M} \sim 0.2$, with few if any above ~ 0.4 .)

Core-collapsed globular clusters are the most likely locations for IMRIs; they may contain an IMBH and a high density of stellar mass BHs and NSs [6]. Simulations show that it is possible to grow IMBHs with masses up to $M_{\text{max}} \sim 350 M_\odot$ through a series of mergers in the core of a cluster [9]. Phinney [10] suggests estimating an upper limit on the IMRI rate in globular clusters as follows: assume each cluster has a black hole that grows from $\sim 50M_\odot$ to $\sim 350M_\odot$ by capturing objects of mass m in 10^{10} years. Core-collapsed clusters have a space density of 0.7 Mpc^{-3} , which gives an estimated IMRI rate of $\sim 0.7 \times (300M_\odot/m) \times 10^{-10} \text{ Mpc}^{-3}\text{yr}^{-1}$. This leads to a limit of ~ 10 IMRI detections per year in AdvLIGO.

A kick velocity $V_{\text{kick}} > 50 \text{ km/s}$ will eject the merged black hole from the cluster, placing an upper limit on m of $m/M \lesssim 0.08$ (V_{kick} depends on the symmetric mass ratio $\eta = mM/(m+M)^2$ as $V_{\text{kick}} \approx 12000\eta^2\sqrt{1-4\eta}(1-0.93\eta) \text{ km/s}$ [11]). Black holes with masses $m \gtrsim 10M_\odot$ will likely merge with the IMBH or be ejected from the core in under 10^{10} years. An estimate based on the dynamics of binary hardening

via 3-body interactions yields a rate of one detection per three years for NS–IMBH inspirals or ten detections per year for BH–IMBH inspirals [12]. Optimizing the AdvLIGO sensitivity at low frequencies could improve these rates by a factor of ~ 3 . For Initial LIGO [1], however, rates are much lower due to lower sensitivity across the noise curve and a lack of sensitivity below 40 Hz, reducing M_{\max} to $\lesssim 100M_{\odot}$. We estimate an IMRI rate in current detectors of $< 1/1000 \text{ yr}^{-1}$.

Search Templates for IMRI Waves with an IMBH central body. Matched filter searches for IMRIs require templates of sufficient accuracy that the mismatch between template and signal does not cause a large loss in event rate. The most accurate IMRI templates currently available come from black-hole perturbation theory via numerical solution of the Teukolsky equation [13]. Post-Newtonian (PN) templates [14, 15] and PN approximations to Teukolsky waveforms [16] are inadequate because IMRIs enter the detector frequency band when the binary separation is $r \lesssim 15M$ and the PN expansion is poor.

Inspiral waveforms from black-hole perturbation theory are known only to first order in η plus $O(\eta^2)$ in radiation reaction. It is important to determine the effect of conservative finite-mass-ratio corrections $O(\eta^2)$, but tools to study these are not yet in hand. We (Brown [17]) estimate these effects by computing the mismatch (for AdvLIGO) between restricted PN stationary-phase templates containing all known η terms, and the same templates linearized in η plus $O(\eta^2)$ radiation reaction (cut off at the IMRI’s innermost stable circular orbit); this is the fractional SNR loss due to using templates linearized in η . Mismatches are computed at each PN order between 1.0 and 3.5 inclusive. For a $1.4 M_{\odot}$ NS– $100 M_{\odot}$ IMBH IMRI, the mismatch is $\lesssim 30\%$ for $\chi < 0.8$, and $\lesssim 15\%$ for $\chi < 0.3$. For IMRIs with a larger IMBH mass, the mismatch decreases, as expected. By allowing the linearized PN waveforms to have mass parameters different from those of the nonlinear PN waveforms, and minimizing the mismatch over these parameters, mismatch falls to less than 10% in all except the most rapidly spinning cases [17]. Therefore, it is reasonable to expect that the Teukolsky waveforms will lose no more than 10% of the SNR due to linearization in η (hence no more than a 30% loss of event rate). For detection, it will be worthwhile, but

not essential, to improve Teukolsky waveforms by incorporating nonlinear corrections, but accurate parameter measurement will require improvements.

IMRI and EMRI Orbits and Waves; Tri-periodic vs. Ergodic. Here we entertain the possibility that the central body is not a black hole. We assume its external spacetime geometry is stationary, axially and reflection symmetric and asymptotically flat (SARSAF) with metric in the form $ds^2 = -\alpha^2 dt^2 + \varpi^2 (d\phi - \omega dt)^2 + g_{\theta\theta} d\theta^2 + g_{rr} dr^2$ and all coefficients independent of the Killing time t and axial angle ϕ . If the spacetime initially is not axisymmetric, rotation will make it non-stationary; then presumably GW emission drives it to stationarity and axisymmetry on astrophysically small time-scales. Almost all stationary, axially symmetric, self-gravitating objects studied observationally or theoretically are reflection symmetric.

A SARSAF solution to the vacuum Einstein equations is determined uniquely by two families of scalar multipole moments: *mass moments* $M_0 \equiv M$, M_2 (mass quadrupole moment), M_4, \dots ; and *current moments* S_1 (spin angular momentum), S_3, S_5, \dots [18]. For the Kerr metric (describing astrophysical black holes), the moments are fully determined by the mass M and dimensionless angular momentum $\chi \equiv S_1/M^2$ via $M_\ell + iS_\ell = M^{l+1}(i\chi)^\ell$; this is the no-hair theorem. We hope to use LISA to measure as many moments as possible, via EMRI waves, and determine the accuracy with which each moment satisfies this Kerr formula; AdvLIGO can do the same for IMRIs.

For EMRIs and IMRIs, the orbiting object moves along an orbit that is nearly a geodesic of the background metric; gravitational radiation reaction drives it slowly from one geodesic to another. If the central body is a Kerr black hole, then: (i) each geodesic has three isolating integrals of the motion: energy E , axial angular momentum L_z , and Carter constant Q (and a fourth, “trivial” integral, the length of the orbit’s tangent vector); (ii) the emitted gravitational waves are tri-periodic with $h^{\mu\nu} = \Re \sum_{Pkmn} h_{Pkmn}^{\mu\nu} e^{i(k\Omega_\theta + m\Omega_\phi + n\Omega_r)t}$ (for integer values of k, m, n) [19]. Here $P = +, \times$ is the polarization, and the three *principal frequencies* $\Omega_\theta, \Omega_\phi, \Omega_r$, in a precise but subtle sense, are associated with the orbital motion in the polar (θ), azimuthal (ϕ) and radial (r) directions. The fundamental frequencies and complex

amplitudes evolve with time as radiation reaction drives the orbit through a sequence of geodesics.

If the third integral (the Carter constant) is lost in SARSAF spacetimes, motion may be ergodic rather than tri-periodic, which would make detection of the gravitational waves difficult. Guéron and Letelier [20] have used Poincaré maps to search for ergodic geodesics in the static ($S_\ell = 0$) Erez-Rosen metric and we (Gair, Li, Lovelace, Mandel & Fang [21]) have carried out similar studies for a variant of the stationary ($S_\ell \neq 0$) Manko-Novikov metric [22]. Both of these metrics have arbitrary mass quadrupole moment M_2 , and higher order moments fixed by M_2 , S_1 and M . The Poincaré maps in these spacetimes reveal no sign of ergodic geodesics when $M_2 < 0$ (oblate spacetimes). In some prolate spacetimes ($M_2 > 0$) both with spin (Manko-Novikov) and without (Erez-Rosen), there are geodesics at very small radii $r \sim \text{few } M$ that appear ergodic, but none at large radii. Gravitational radiation reaction drives the evolution of energy and angular momentum in a way which makes it unlikely that the apparently ergodic geodesics could be encountered in the course of an inspiral [21]. For the apparently non-ergodic (integrable) geodesics, the spatial coordinates are multi-periodic functions of Killing time t to a numerical accuracy of 10^{-7} , and a general argument [23] based on the structure of the gravitational propagator shows that their gravitational waves will have the same kind of tri-periodic form as for Kerr black holes.

There are three possible explanations for the presence of large-radius orbits that appear integrable and small-radius orbits that appear ergodic in the same spacetime: (i) The orbits are actually integrable and actually ergodic, respectively. (ii) All the orbits are ergodic, but at large radii they appear integrable to numerical accuracy because of the KAM theorem [24]. (iii) All the orbits are integrable, but at small radii they are made to appear chaotic by some ill-understood numerical instability. For the theory of dynamical systems, it is important to learn which is the case, but for EMRI and IMRI wave observations, apparent integrability (or ergodicity) has the same observational implications as actual integrability (or ergodicity).

Information Carried by IMRI and EMRI Waves; Generalizing Ryan's

Theorem. What information about the central body is encoded in the waveforms? We shall assume the waveforms to be tri-periodic. In principle, a large amount of information can be encoded in the time evolution of the waves' three fundamental frequencies $\Omega_\theta(t)$, $\Omega_\phi(t)$, $\Omega_r(t)$ and their complex amplitudes $h_{Pkmn}(t)$. It has been speculated that these encode, fully and separably, the values of all the central body's multipole moments $\{M_\ell, S_\ell\}$ and hence its metric [25], the rates at which the orbiting object's tidal pull deposits energy and angular momentum into the central body, \dot{E}_{body} and \dot{L}_{body} (*tidal coupling*) [26], and the orbit's semi-latus rectum $p(t)$, eccentricity $e(t)$ and inclination angle $\iota(t)$ (which carry the same information as the isolating integrals) [27]. That this might be so is suggested by a special case that Ryan [25] has studied. A trivial extension of Ryan's theorem [27] leads to the following algorithm for extracting information from the waves. Observe the time-evolving modulation frequencies as functions of the time-evolving fundamental frequency $f = \Omega_\phi/\pi$. From these, deduce the functions $\Omega_A(\Omega_\phi)$ and thence $\Omega_A(v)$ for $A = \theta, r$; expand in powers of $v \equiv (M\Omega_\phi)^{1/3} \simeq$ (orbital velocity); and read out the moments (redundantly) from the two expansions. Then, knowing the moments and thence the metric, use the geodesic equation to deduce $p(t)$ from $\Omega_\phi(t)$ and use wave-generation theory to deduce $e(t)$ and $\iota(t)$ from particular modulation amplitudes, $h_{Pkmn}(t)$.

We have generalized Ryan's theorem to strongly elliptical but nearly equatorial orbits (Li [23]), to include tidal coupling (Li and Lovelace [27]), and are working on further generalizations. For *strongly elliptical but nearly equatorial orbits* the three fundamental frequencies are independent of ι at first order. We expand these frequencies $\Omega_A(M_\ell, S_\ell, e, p)$ (with $A = \theta, \phi, r$) in powers of $1/p$, with coefficients that depend on e and the moments. Suppose we observe a series of $2N + 1$ values of $(\Omega_\theta, \Omega_\phi, \Omega_r)$ (for any integer N) during the course of an inspiral. This gives us $6N + 3$ numbers, from which we can read off (via an algorithm based on our expansions of the fundamental frequencies [23]): (i) the time evolution of $e(t)$ and $p(t)$ ($2N + 1$ values of each), (ii) the lowest $N + 1$ mass moments, and (iii) the lowest N current moments. By observing the evolving amplitudes of the orbital-precession-induced modulations encoded in h_{Pkmn} , we can recover the time evolution of ι . Hence, in principle, we

have a full description of the spacetime. In practice the methods of extracting the information are likely to be quite different from these algorithms. Development of practical methods is a topic of our current research.

In the absence of tidal coupling Ryan demonstrated that, for a nearly circular, nearly equatorial orbit, the central body’s moments are encoded not only in the waves’ modulations, but also in the phase evolution of the waves’ dominant harmonic $f = \Omega_\phi/\pi$. We have extended this analysis to deduce the power being deposited in the central body by tidal coupling, \dot{E}_{body} [27]. We assume the moments and metric have been deduced from the precessional modulations and then use deviations from the Ryan-theorem phase evolution to deduce \dot{E}_{body} . Following Ryan, we quantify the waves’ phase evolution by $\Delta N(t) \equiv f^2/\dot{f} = d(\text{number of wave cycles})/d \ln f$. From this definition of ΔN , we infer the rate of change of orbital energy: $\dot{E}_{\text{orb}} = (dE_{\text{orb}}/d\Omega_\phi)(\Omega_\phi^2/\pi\Delta N)$. All (time-evolving) quantities on the right side can be deduced from observation plus the geodesic equation (for $dE_{\text{orb}}/d\Omega_\phi$). From the deduced metric and the frequency $f(t)$ we can compute the power radiated to infinity \dot{E}_∞ ; and thence by energy conservation we can deduce the power being deposited in the central body $\dot{E}_{\text{body}} = -\dot{E}_{\text{orb}} - \dot{E}_\infty$ [27]. We can also infer the angular momentum transferred tidally to the central body, \dot{L}_{body} , via $\dot{L}_{\text{body}} = \dot{E}_{\text{body}}/\Omega_\phi$ (valid for nearly circular, nearly equatorial orbits).

The above argument assumes that we can compute \dot{E}_∞ without knowing the boundary conditions of the inspiral-induced metric perturbation at the central body, since we do not know the nature of the central body *a priori*. For highly compact central bodies (those deep inside the perturbing field’s “effective potential”) this is true to high but not complete accuracy. The effect of boundary conditions at the central body on the inspiral phase evolution is communicated outward to infinity mainly at low frequencies (the orbital frequency and its low-order harmonics), and these perturbations have great difficulty penetrating through the effective potential. If the spacetime metric is Kerr, we have shown that the influence of the inner boundary condition on the energy radiated to infinity is $\delta\dot{E}_\infty \sim v^{10}\dot{E}_\infty$ [27]—five orders smaller in the linear velocity v than the tidal coupling $\dot{E}_{\text{body}} \sim v^5\dot{E}_\infty$ [28]. Thus, to high

accuracy we can deduce \dot{E}_∞ and thence \dot{E}_{body} from observations, without knowing the body's precise nature.

Measurement Accuracies for AdvLIGO. We have estimated how accurately AdvLIGO, via IMRI waves, can constrain deviations of the central body's quadrupole moment M_2 (Brown [17]) and tidal coupling \dot{E}_{body} (Fang [29]) from those of a Kerr black hole. In the absence of accurate waveforms, we used PN waveforms as both signals and templates. This may introduce systematic error, but we believe our results are indicative of the accuracies AdvLIGO can achieve. Our source is the circular inspiral of a neutron star into a $100M_\odot$ IMBH (under the assumption that radiation reaction has circularized the orbit [12]). The orbit is inclined to the hole's equatorial plane, to produce a modulation that is crucial for breaking degeneracy between the IMBH spin χ and M_2 and \dot{E}_{body} .

To investigate M_2 , we began with templates accurate to 3.5PN order in phase evolution [15] and 1.5PN in spin-orbit coupling [14], added the effects of quadrupole-monopole interaction [30] to both the phase and the precessional modulation and numerically mapped the ambiguity function of these waveforms. For a NS-IMBH IMRI ($M_2 = -\chi^2 M^3$) with spin $\chi = 0.8$ and SNR ~ 10 , we found AdvLIGO measurement errors $\Delta \ln M \sim 0.006$, $\Delta \ln \chi \sim 0.02$, and $\Delta \ln M_2 \sim 0.6$. If the IMBH spin is $\chi = 0.3$, the error increases to $\Delta \ln M \sim 0.01$, $\Delta \ln \chi \sim 0.3$, and $\Delta \ln M_2 \sim 2$. The accuracy of measurement depends strongly on binary orientation; larger precessional modulation reduces the errors [17].

We can model tidal coupling as $\dot{E}_{\text{body}} \equiv \epsilon \dot{E}_{\text{BH}}$, where \dot{E}_{BH} is the energy flow into a Kerr black hole [28] and seek to measure deviations parameterized by ϵ . We constructed precessing waveforms [31], with orbital inspiral phase given by the 3.5 PN approximation of the Teukolsky waveforms [16], and modulation linearized in inclination angle [32]. We restricted inclination angles to $\iota < \pi/4$, fixed the direction to the source and the central body's spin orientation, and used the Fisher matrix to estimate parameter measurement accuracies. For a black-hole central body with spin $\chi = 0.8$ and SNR = 10, we could measure ϵ to $\Delta \ln \epsilon \sim 1$ to 2, increasing to $\Delta \ln \epsilon \sim 30$ at $\chi = 0.3$.

While these errors are larger than hoped, (i) the quadrupole moment $|M_2|$ of a boson star with $\chi = 0.3$ is expected to be in the range 15 to 100 $\chi^2 M^3$ [8], so AdvLIGO could readily identify such a central body, (ii) for small spins $\dot{E}_{\text{BH}} \simeq -\frac{1}{4}\chi v^5 \dot{E}_\infty$, and hence for $\chi = 0.3$, the accuracy of measuring tidal coupling is $\Delta \dot{E}_{\text{body}} \sim 30 \times 0.001 \dot{E}_\infty$, i.e. 3% of the power radiated to infinity, an interesting accuracy for central bodies with anomalously large \dot{E}_{body} , and (iii) observing an IMRI in each of the three AdvLIGO detectors increases the accuracy of parameter estimation quoted by a factor of $\sqrt{3}$; including additional detectors, e.g. Advanced VIRGO, could improve this further. In practice, parameter estimation will be pursued using Markov Chain Monte Carlo techniques [33, 17].

Our results suggest that AdvLIGO will be able to verify with interesting accuracy that an IMRI's central body is a black hole, and perform interesting searches for non-Kerr central bodies. AdvLIGO's accuracies for probing the central body are far worse than LISA's (as expected, due to the thousand-fold fewer wave cycles), but AdvLIGO is likely to be operational some years before LISA. Its studies of central bodies will be a valuable precursor to LISA's EMRI science, and might possibly yield a big surprise.

Bibliography

- [1] B. C. Barish and R. Weiss, *Phys. Today* **10**, 44 (1999).
- [2] F. Acernese et al., *Class. Quant. Grav.* **23**, S635 (2006).
- [3] P. Fritschel (2003), [gr-qc/0308090](#).
- [4] B. Abbott et al., *Phys. Rev. D* **72**, 082001 (2005).
- [5] B. Abbott et al., *Phys. Rev. D* **73** 062001 (2006).
- [6] M. C. Miller and E. J. M. Colbert, *Int. J. Mod. Phys. D* **13**, 1 (2004).
- [7] J. R. Gair et al. *Class. Quant. Grav.* **21**, S1595 (2004).
- [8] F. D. Ryan, *Phys. Rev. D* **55**, 6081 (1997).
- [9] R. M. O’Leary et al., *Ap. J.* **637**, 937 (2005).
- [10] E. S. Phinney (2005), private communication.
- [11] J. A. González et al. (2006), [gr-qc/0610154](#).
- [12] I. Mandel, D. A. Brown, J. R. Gair, and M. C. Miller, Submitted to *Ap. J.*, [astro-ph/0705.0285](#).
- [13] S. A. Hughes, *Phys. Rev. D* **64**, 064004 (2001).
- [14] L. E. Kidder et al., *Phys. Rev. D* **47**, R4183 (1993).
- [15] L. Blanchet et al., *Phys. Rev. D* **65**, 061501(R) (2002).
- [16] H. Tagoshi et al., *Phys. Rev. D* **54**, 1439 (1996).
- [17] D. A. Brown, in preparation.
- [18] R. Hansen, *J. Math. Phys.* **15**, 24 (1974).
- [19] S. Drasco and S. A. Hughes, *Phys. Rev. D* **69**, 044015 (2004).

- [20] E. Guéron and P. S. Letelier, Phys. Rev. E **66**, 046611 (2002).
- [21] J. R. Gair, C. Li, and I. Mandel, Phys. Rev. D **77**, 024035 (2008).
- [22] V. S. Manko and I. D. Novikov, Class. Quant. Grav. **9**, 2477 (1992).
- [23] C. Li, in preparation.
- [24] M. Tabor, *Chaos and Integrability in nonlinear Dynamics* (John Wiley & Sons Inc., 1989).
- [25] F. D. Ryan, Phys. Rev. D **52**, 5707 (1995).
- [26] H. Fang and G. Lovelace, Phys. Rev. D **72**, 124016 (2005).
- [27] C. Li, and G. Lovelace, Submitted to Phys. Rev. D, [gr-qc/0702146](#).
- [28] H. Tagoshi et al., Prog. Theor. Phys. **98**, 829 (1997).
- [29] H. Fang, Ph.D. thesis, Caltech, Pasadena, CA.
- [30] E. Poisson, Phys. Rev. D **57**, 5287 (1998).
- [31] T. A. Apostolatos et al., Phys. Rev. D **49**, 6274 (1994).
- [32] M. Shibata et al., Phys. Rev. D **51**, 1646 (1995).
- [33] C. Rover et al., Class. Quant. Grav. **23**, 4895 (2006).

Chapter 3

Rates and Characteristics of Intermediate-Mass-Ratio Inspirals Detectable by Advanced LIGO

Gravitational waves (GWs) from the inspiral of a neutron star (NS) or stellar-mass black hole (BH) into an intermediate-mass black hole (IMBH) with mass $M \sim 50M_{\odot}$ to $350M_{\odot}$ may be detectable by the planned advanced generation of ground-based gravitational-wave interferometers. Such *intermediate-mass-ratio inspirals* (IMRIs) are most likely to be found in globular clusters. We analyze four possible IMRI formation mechanisms: (i) hardening of a NS–IMBH or BH–IMBH binary via three body interactions, (ii) hardening via Kozai resonance in a hierarchical triple system, (iii) direct capture, and (iv) inspiral of a CO from a tidally captured main-sequence star; we also discuss tidal effects when the inspiraling object is a NS. For each mechanism we predict the typical eccentricities of the resulting IMRIs. We find that IMRIs will have largely circularized by the time they enter the sensitivity band of ground-based detectors. Hardening of a binary via three-body interactions, which is likely to be the dominant mechanism for IMRI formation, yields eccentricities under 10^{-4} when the GW frequency reaches 10 Hz. Even among IMRIs formed via direct captures, which can have the highest eccentricities, around 90% will circularize to eccentricities under 0.1 before the GW frequency reaches

10 Hz. We estimate the rate of IMRI coalescences in globular clusters and the sensitivity of a network of three Advanced LIGO detectors to the resulting GWs. We show that this detector network may see up to tens of IMRIs per year, though rates of one—few per year may be more plausible. We also estimate the loss in signal-to-noise ratio that will result from using circular IMRI templates for data analysis and find that, for the eccentricities we expect, this loss is negligible.

Submitted to the *Astrophysical Journal* by Ilya Mandel, Duncan A. Brown, Jonathan R. Gair and M. Coleman Miller (2007). Preprint available online at <http://arxiv.org/abs/0705.0285> .

3.1 Introduction

Observational evidence from cluster dynamics and from ultra-luminous X-ray sources suggests that there may exist a population of intermediate-mass black holes (IMBHs) with masses in the $M \sim 10^{2-4} M_{\odot}$ range [61, 88]. Numerical simulations of globular clusters suggest that IMBHs could merge with numerous lower-mass compact objects (COs) during the lifetime of the cluster [86, 62, 63, 64, 65, 39, 40, 67, 66], through a combination of emission of gravitational radiation, binary exchange processes, and secular evolution of hierarchical triple systems. Gravitational waves (GWs) will be generated during the intermediate-mass-ratio inspiral (IMRI) of a stellar-mass object (black hole (BH) or neutron star (NS), since a white dwarf or a main-sequence star would be tidally disrupted) into an IMBH. For IMBH mass $\lesssim 350 M_{\odot}$, these waves are potentially detectable with the planned advanced generation of ground-based GW interferometers: Advanced LIGO and its international partners [10, 34].

IMRIs will be important as probes of strong gravity and cluster dynamics due to their mass range and dynamical histories. For example, from Advanced LIGO IMRI data it may be possible to measure the quadrupole moment, Q , of an IMBH to an accuracy of $\Delta Q \sim Q_{\text{Kerr}}$, where Q_{Kerr} is the quadrupole moment of a Kerr BH [14].

This is sufficient to distinguish a BH from a Boson Star, for which the quadrupole moment can be many times the Kerr value. In addition, since the formation of IMBHs in clusters seems to require short mass segregation timescales (see § 3.2), detection of IMBH mergers and their associated masses will yield information about young dense clusters and their evolution.

In this paper we discuss the astrophysical and data analysis aspects of IMRIs. In § 3.2, we provide the astrophysical setting for IMRIs and describe the formation mechanisms. We estimate the typical eccentricities resulting from different capture mechanisms and find that inspirals will largely circularize by the time the GW frequency reaches the Advanced LIGO band ($f_{\text{GW}} \gtrsim 10$ Hz). We show, in particular, that three-body hardening, which is likely to be the dominant IMRI formation mechanism, will result in binary eccentricities $e < 10^{-4}$ in the Advanced LIGO band. Even direct capture, which is the most likely mechanism to yield high eccentricities, leads to $\sim 90\%$ of IMRIs with $e < 0.1$ in the Advanced LIGO band. In § 3.3, we estimate an upper limit on the rate of IMRIs detectable by Advanced LIGO of up to ten events per year. A more sophisticated, but model-dependent, rate estimate ranges from one event per three years for NS IMRIs to ten events per year for ten-solar-mass BH IMRIs. The event rate can be enhanced by a factor of ~ 3.5 by optimizing Advanced LIGO for detections at low frequencies.¹ Searches for IMRIs in Advanced LIGO data will likely use matched filtering techniques, for which accurate waveform templates are required. In § 3.4, we estimate that there will be a negligible loss in signal-to-noise ratio if circular templates are used to search for IMRIs with the expected eccentricities in Advanced LIGO data.

¹We used the Advanced LIGO Bench code to perform this optimization: <http://www.ligo.mit.edu/bench/bench.html>

3.2 Astrophysical Setting, Capture Mechanisms, and Typical Eccentricities

An IMBH cannot result from the evolution of a solitary star in the current universe, because even a star of initial mass $\sim 10^2 M_\odot$ will be reduced well below this mass by winds and pulsational instabilities driven by metal-line opacities (cf. [35], Fig. 7 and associated discussion). Some IMBHs might be formed from the first, metal-free, stars [57], but these IMBHs are unlikely to participate in multiple mergers with COs. Instead, we focus on the proposal that IMBHs can be produced in the current universe via runaway stellar collisions in dense young stellar clusters. If the most massive stars segregate to the center in less than their $\sim 2 \times 10^6$ yr lifetimes [19, 75, 73, 42, 41, 32, 31, 29], then stellar mergers can overcome mass losses and the collision product can reach hundreds to thousands of solar masses, presumably evolving into an IMBH.

When supernovae start to occur, the resulting mass loss leads to an expansion of the cluster, which thus transitions into a more collisionless stage of existence. From this point on, COs can be captured by the IMBH and generate observable GWs as they inspiral under radiation reaction and eventually merge with the IMBH.

Early in the history of the globular cluster the inspiraling objects in IMRIs are likely to be $m \sim 10 M_\odot$ BHs, which may form a dense subcluster composed purely of BHs around the IMBH [67, 66]. Late in the cluster’s history, once the BH central subcluster has largely evaporated, NSs will likely replace the larger BHs as the inspiraling objects.

There are several ways in which stellar-mass COs can be captured by an IMBH. Most mechanisms of capture involve binaries, because the cross section of a binary is orders of magnitude larger than that of a single CO.

Extensive numerical studies of binary-single interactions demonstrate that hard binaries (defined, e.g., so that the total energy of the binary-single system is negative) tend to be tightened by three-body interactions [43]. These studies also show that massive objects such as stellar-mass BHs and IMBHs tend to swap into binaries. The most likely capture mechanism involves the formation of a CO–IMBH binary, which

is subsequently hardened by repeated three-body interactions until radiation reaction becomes significant and the binary coalesces.

Hardening can also occur via binary-binary interactions; unlike binary-single interactions, these can result in a stable hierarchical triple. Some fraction of these end up in orientations favorable for the secular Kozai resonance [55], in which the inner binary (which contains the IMBH) periodically increases and decreases its eccentricity while keeping its semimajor axis constant. The periapsis distance can therefore be quite low in parts of the cycle, and can lead to coalescence without Newtonian recoil [63, 93], although recoil from gravitational radiation will still occur (see § 3.3.2). The importance of the Kozai resonance depends on the frequency of binary-binary interactions, which is unknown at present.

In addition to these mechanisms, which usually require multiple interactions to lead to merger, a hyperbolic encounter at a close enough periapsis can produce direct capture via emission of gravitational radiation. Assuming the IMBH does not have a significant radius of influence, the effective cross section for radiative capture of the CO by an IMBH is proportional to $M^{12/7}$, where M is the mass of the IMBH [79]. For two-body encounters this process is likely to be important only for masses high enough ($\gtrsim 10^3 M_\odot$) that the frequency of the GWs throughout the subsequent inspiral will be below the sensitivity range of ground-based detectors. However, direct capture during a three-body interaction could be significant [40].

Finally, an IMBH could tidally capture a main-sequence star. If the captured star evolves to a CO while in orbit around the IMBH, the remnant could remain bound to the IMBH and ultimately spiral in via GW emission. This scenario has been suggested as a possible explanation for the observed population of ultraluminous X-ray sources [50, 49].

Additionally, orbital energy may couple to vibrational normal modes of the inspiraling object in the case when the inspiraling object is a NS. In principle, the energy loss to tidal heating of a NS could change the inspiral trajectory, or even disrupt the NS.

The IMRI enters the Advanced LIGO band when

$$f_{\text{GW}} = \frac{\omega_{\text{orb}}(r_p)}{\pi} = \frac{1}{\pi} \sqrt{\frac{M}{r_p^3}} \gtrsim 10 \text{ Hz}, \quad (3.1)$$

i.e., when the periapsis is $r_p \approx 16GM/c^2 = 1600GM_\odot/c^2$ for $M = 100M_\odot$. The frequency of the dominant quadrupolar ($k = 2$) harmonic in the GWs emitted at the innermost stable circular orbit is

$$f_{\text{GW, ISCO}} \approx 44.0 \frac{M}{100 M_\odot} \text{ Hz} \quad (3.2)$$

for inspirals into non-spinning BHs.

Below, we discuss the eccentricity of an IMRI at the time its GW frequency enters the Advanced LIGO band for each of the mechanisms mentioned above: (i) formation of a CO–IMBH binary and subsequent hardening via three-body interactions; (ii) Kozai resonance of a hierarchical triple system; (iii) direct capture when a solitary CO passes close to the IMBH; (iv) tidal capture of a main-sequence star which subsequently evolves to leave a CO. We also consider the impact of (v) tidal interactions with an inspiraling NS.

3.2.1 Hardening of a CO–IMBH Binary via Three-Body Interactions

This mechanism proceeds as follows. The IMBH rapidly swaps into a binary because it is far more massive than any other object in the globular cluster. Advanced LIGO can detect IMRIs at redshifts $z \lesssim 0.2$ (§ 3.3.1), so it will predominantly observe globular clusters late in their history. On a timescale that is short relative to the merger time, a NS or a BH will encounter the binary containing the IMBH and will exchange for the companion in this binary, since stellar remnants are the most massive objects in the late cluster other than the IMBH itself. From that point on, stars of all types (although biased towards the heavy ones that segregate towards the center) engage in three-body interactions. Numerical simulations show that interactions tend

to tighten a binary if it is hard. This can be understood heuristically for three equal-mass objects by noting that ejection will tend to occur at roughly the binary orbital speed, hence if this is greater than the initial encounter speed at infinity the binary loses energy. Binary tightening proceeds until the binary can merge through radiation reaction from the emission of GWs.

For the unequal mass binaries we consider here, simulations by Quinlan [78] show that a single interaction of a field star of mass m_* with a binary of total mass M will on average change the binary energy by a fractional amount $\Delta E/E = \mathcal{O}(m_*/M)$, roughly independent of the component masses of the binary. More precisely, approximately $(2\pi/22)M/m_*$ interactions are required to reduce the semimajor axis of a hard binary by one e -folding [78].

The rate at which objects interact with the IMBH binary is

$$\dot{N} = n\zeta v, \quad (3.3)$$

where n is the number density, v is the relative speed, and ζ is the gravitationally focused cross section $\zeta = \pi a(2GM/v^2)$ for an interloper to approach within the binary's semimajor axis a of the binary. Since this rate is proportional to a , the total time for the binary to harden until the semimajor axis equals a is dominated by the last e -folding time:

$$T_{\text{harden}} \approx \frac{2\pi}{22} \frac{M}{m_*} \frac{1}{\dot{N}} \approx 2 \times 10^8 \left(\frac{10^{13} \text{ cm}}{a} \right) \text{ yr}, \quad (3.4)$$

where we set $m_* = 0.5 M_\odot$, $v = 10^6 \text{ cm s}^{-1}$, and $n = 10^{5.5} \text{ pc}^{-3}$ (the number density of all stars in a core-collapsed globular cluster; Pryor & Meylan 77).

For a sufficiently massive BH, a cusp is formed and the interactions are no longer described by individual binary-single encounters. We can estimate roughly the mass above which this occurs. Consider a core of number density n_{core} and velocity dispersion σ . For an IMBH of mass M , the radius of influence (inside of which the IMBH dominates the potential) is $r_{\text{infl}} = GM/\sigma^2$. For a true cusp, [6] showed that

the number density would go as $n(r) = n_{\text{core}}(r/r_{\text{infl}})^{-7/4}$. The total number of objects inside r_{infl} is then

$$N(r < r_{\text{infl}}) = \int_0^{r_{\text{infl}}} 4\pi r^2 n_{\text{core}} (r/r_{\text{infl}})^{-7/4} dr = (16\pi/5)r_{\text{infl}}^3 n_{\text{core}}. \quad (3.5)$$

Scaling to canonical values, this gives

$$N(r < r_{\text{infl}}) \approx 0.3(M/100 M_{\odot})^3 (\sigma/10 \text{ km s}^{-1})^{-6} (n_{\text{core}}/10^{5.5} \text{ pc}^{-3}) \quad (3.6)$$

Therefore, in the mass range most relevant to Advanced LIGO, it is unlikely that there will be a significant cusp, hence our treatment of isolated binary-single interactions is reasonable. For more massive BHs a cusp might form, although we note that for $M < 1000 M_{\odot}$ the typical distance wandered by the IMBH in the core is larger than the radius of influence, hence cusp formation could be made more difficult. This is, however, worth further study.

The gravitational radiation merger timescale for an intermediate-mass-ratio binary of semimajor axis a , eccentricity e , reduced mass $\mu \approx m$, and total mass approximately equal to the IMBH mass M , is [69]

$$T_{\text{merge}} \approx 10^{17} \frac{M_{\odot}^3}{M^2 m} \left(\frac{a}{10^{13} \text{ cm}} \right)^4 (1 - e^2)^{7/2} \text{ yr}. \quad (3.7)$$

Simulations and phase space arguments show that three-body interactions cause the eccentricity of the binary to sample a thermal distribution $P(e)de = 2ede$ [43], in the Newtonian realm where gravitational radiation is not significant. If an interaction leaves the binary with a high eccentricity, however, it is more likely to merge. Gültekin, Miller, & Hamilton [40] examined the eccentricity of the binary after its final three-body encounter, and found a typical value of $e \approx 0.98$ due to this bias. Taking this as the typical value for eccentricity, we find

$$T_{\text{merge}} \approx 10^8 \left(\frac{M_{\odot}}{m} \right) \left(\frac{100 M_{\odot}}{M} \right)^2 \left(\frac{a}{10^{13} \text{ cm}} \right)^4 \text{ yr}. \quad (3.8)$$

In fact, there is a distribution of eccentricities after the last encounter, rather than a single eccentricity value of 0.98. However, Monte Carlo simulations, which are described below, confirm the typical merger times and final eccentricities computed here analytically by assuming the final-encounter eccentricity of 0.98. Moreover, simulations indicate that the fraction of direct plunges from highly radial orbits must be extremely small, because they would require improbably small periapsis separations.

The IMRI rate will be maximized when the total merger time, $T = T_{\text{harden}} + T_{\text{merge}}$, is minimized. Minimizing T with respect to a , we find that the total merger time is $T \approx 3 \times 10^8$ yr for the inspiral of a $m = 1.4 M_{\odot}$ NS into a $M = 100 M_{\odot}$ IMBH, yielding an IMRI rate per globular cluster of $\sim 3 \times 10^{-9}$ yr $^{-1}$. If the inspiraling object is a $m = 10 M_{\odot}$ BH, and the IMBH mass is again $M = 100 M_{\odot}$, then the total merger time is $T \approx 2 \times 10^8$ yr, and the IMRI rate per globular cluster is $\sim 5 \times 10^{-9}$ yr $^{-1}$.

These numbers are close to the answers obtained with Monte Carlo simulations using the same procedure as in Gültekin, Miller, & Hamilton (2006). We find from these simulations that the total time to merger averages 5×10^8 yr for $1.4 M_{\odot}$ NSs, and 3×10^8 yr for $10 M_{\odot}$ BHs, interacting with field stars of mass $0.5 M_{\odot}$ and an IMBH of mass $100 M_{\odot}$. We also find that, as we assumed, once a CO is in a binary with an IMBH it stays there; only a fraction $\approx 6 \times 10^{-4}$ of encounters swapped out a NS, and only 1 of the 5×10^4 encounters swapped out a BH. Therefore, as we indicated, the object that eventually merges with the IMBH is highly likely to be a CO.

This mechanism requires the cluster to be in a core-collapsed state, and for this state to persist for a time $\gg 2 \times 10^8$ yr. Core collapse is expected to persist in the absence of significant heating, as will be the case for clusters with IMBHs in the mass range of interest, so 2×10^8 yr should be easily achievable. About 20% of clusters currently are in a state of core collapse, so this state can indeed be sustained for times of order a Hubble time, or much longer than 2×10^8 yr. We consider only these core-collapsed systems as likely hosts of IMRIs when computing event rates below.

Radiation reaction from GW emission dominates the evolution once the GW merger timescale T_{merge} [Eq. (3.8)] is shorter than the average time between three-

body encounters, $1/\dot{N}$, defined by Eq. 3.3. For the NS–IMBH system ($m = 1.4 M_\odot$, $M = 100 M_\odot$), this occurs when the semimajor axis takes the value $a \approx 5 \times 10^{12}$ cm. As discussed earlier, the eccentricity at this time is $e \approx 0.98$, and hence the periapsis is $r_p \approx 10^{11}$ cm $\approx 7000 GM/c^2$. For the BH–IMBH system ($m = 10 M_\odot$, $M = 100 M_\odot$), radiation reaction dominates for $a \lesssim 8 \times 10^{12}$ cm, corresponding to a periapsis of $r_p \approx 1.6 \times 10^{11}$ cm $\approx 10000 GM/c^2$.

Keplerian orbits evolving under radiation reaction satisfy [cf. Eq. (5.11) of [69]]

$$r_p e^{-12/19} (1 + e) [1 + (121/304)e^2]^{-870/2299} = \text{constant}, \quad (3.9)$$

from which we can obtain the eccentricity at a particular frequency, given the initial values of periapsis and eccentricity. We find that for this capture mechanism, the eccentricity when the source enters the Advanced LIGO band ($f_{\text{GW}} = 10$ Hz) is very small: $e \lesssim 3 \times 10^{-5}$ for the NS–IMBH system and $e \lesssim 2 \times 10^{-5}$ for the BH–IMBH system. The orbit will thus have circularized by the time the IMRI is in the Advanced LIGO band. This is consistent with the results of [40], who also found that IMRI binaries formed through this channel would circularize before they entered the Advanced LIGO band.

3.2.2 Kozai Resonance

A stable hierarchical triple system could experience Kozai resonance that would drive the eccentricity of the inner binary to a value close to unity [55], leading to a small periapsis separation and binary tightening and eventual merger through gravitational radiation reaction [63, 93]. Some simulations (e.g., those of O’Leary et al. [67]) suggest that the four-body (binary-binary) interactions that are required to place the binary on the Kozai merger track constitute only a small fraction of the total number of merger events in the cluster. If so, four-body interactions play a minor role in IMRI formation. These simulations may not consider all possibilities, however. In particular, in the [67] model, binaries are only destroyed (through mergers, or by being kicked out of the subcluster). Therefore, the binary fraction decreases with

time, meaning that binary-binary interactions are uncommon late in the cluster's history. There may be a way to replenish the number of BHs in binaries, however. Approximately 5-20% of normal stars in globulars are in binaries [83, 12] (this fraction is closer to 50-70% in the field, but in globulars the wide binaries are disrupted). If such a binary goes through the BH subcluster, a BH could swap in, so that even if no BHs were originally in binaries, the binary fraction could increase.

Although computing the relative contribution of Kozai resonance mergers to the total number of IMRIs requires more detailed modeling of the cluster dynamics, it is possible to estimate the largest eccentricity that could result from this mechanism (see [93] for a more detailed discussion in the context of stellar-mass BHs). For this calculation, we will assume that the Kozai resonance drives the binary to a sufficiently high eccentricity to allow merger via radiation reaction within one Kozai cycle. In reality, the semimajor axis and eccentricity would evolve gradually over multiple Kozai cycles, leading to larger typical periapses and smaller eccentricities, so our assumption will overestimate the typical eccentricities of IMRIs in the Advanced LIGO band.

We assume that the eccentricity is near its maximum for a fraction 0.01 of the total Kozai cycle (based on Fig. 1 of [53]), and compare this time with the radiation reaction timescale. If the radiation reaction merger time is much longer than the time near maximum eccentricity, we assume that gravitational radiation is insignificant. If instead the timescale for Kozai resonance to drive the eccentricity to some value $e \approx 1$ is much larger than the timescale for radiation reaction to circularize the orbit down from e , then the eccentricity will never reach e in practice, even though e may be less than the maximum possible eccentricity for the given configuration (see below). Therefore, the maximum eccentricity reachable when including gravitational radiation is given approximately by the condition that the radiation reaction timescale is equal to the time near that high eccentricity.

The time scale for the Kozai cycle is given by, e.g., Eq. (4) of [63]:

$$\tau_{\text{Kozai}} \approx \text{few} \times \left(\frac{M_1 b_2^3}{m_2 a_1^3} \right)^{1/2} \left(\frac{b_2^3}{G m_2} \right)^{1/2} \approx 3 \times \left(\frac{M_1}{100 M_\odot} \right)^{1/2} \left(\frac{M_\odot}{m_2} \right) \left(\frac{b_2}{a_1} \right)^3 \left(\frac{a_1}{10^{13} \text{ cm}} \right)^{3/2} \text{ yr}, \quad (3.10)$$

where, in the notation of [63], M_1 is the total mass (approximately equal to the mass of the IMBH), m_1 is the mass of the inner companion, m_2 is the mass of the outer companion, a_1 is the semimajor axis of the inner binary and b_2 is the semiminor axis of the outer binary. Setting the time scale for merger by gravitational radiation, given in Eq. (3.7), equal to $\tau_{\text{GR}} = 0.01 \tau_{\text{Kozai}}$, yields

$$\left(\frac{a_1}{10^{13} \text{ cm}}\right)^{5/2} \epsilon^{7/2} \approx 3 \times 10^{-15} \left(\frac{M_1}{100 M_\odot}\right)^{5/2} \left(\frac{m_1}{m_2}\right) \left(\frac{b_2}{a_1}\right)^3 \quad (3.11)$$

where $\epsilon \equiv 1 - e^2$.

Relativistic precession constrains the maximal eccentricity, or minimal ϵ , that can be achieved in a Kozai cycle. That minimal ϵ is given by Eqs. (6) and (8) of [63] as:

$$\epsilon \approx \frac{1}{9} \left(8 \frac{b_2^3 G M_1^2}{m_2 a_1^4 c^2}\right)^2 \approx 1.6 \times 10^{-7} \left(\frac{m_2}{M_\odot}\right)^{-2} \left(\frac{M_1}{100 M_\odot}\right)^4 \left(\frac{a_1}{10^{13} \text{ cm}}\right)^{-2} \left(\frac{b_2}{a_1}\right)^6. \quad (3.12)$$

In order to compute the maximal plausible eccentricity at $f_{\text{GW}} = 10$ Hz, we need to estimate the minimal periapsis radius at the peak of the Kozai cycle, when radiation reaction becomes dominant, since eccentricity will be close to unity there [cf. Eq. (3.9)]. That is, we must minimize $r_p = a_1(1 - e) \approx a_1\epsilon/2$. This minimum value is found by solving Eqs. (3.11) and (3.12). We find

$$\frac{a_1\epsilon}{10^{13} \text{ cm}} \gtrsim 1.8 \times 10^{-5} \left(\frac{m_2}{M_\odot}\right)^{-4/9} \left(\frac{M_1}{100 M_\odot}\right)^{13/9} \left(\frac{b_2}{a_1}\right)^2 \left(\frac{m_1}{m_2}\right)^{2/9}. \quad (3.13)$$

Stability requires that the semiminor axis of the outer binary is at least a few times greater than the semimajor axis of the inner binary, so we set $b_2/a_1 = 5$. We again assume $M_1 = 100 M_\odot$, $m_1 = 1.4 M_\odot$, and $m_2 = M_\odot$ (although this choice violates the restricted three-body assumption under which Eq. (8) of [63] was derived). These parameter values predict a minimal $r_p \gtrsim 170GM/c^2$ at the time when radiation reaction takes over; hence, according to Eq. (3.9), the maximal eccentricity of IMRIs formed via the Kozai resonance mechanism in the Advanced LIGO band is $e \approx 0.01$.

3.2.3 Direct Captures

If we assume that the IMBH is wandering in the stellar cluster, the effective cross section for direct captures via two-body relaxation (GW emission) is proportional to the $(12/7)$ power of the total mass [79], so an IMBH has a relatively small capture cross section, making this capture mechanism relatively unlikely. If we instead assume that the $M - \sigma$ relation holds for globular clusters, which is equivalent to saying that the IMBH dominates the dynamics in the center of the cluster, the capture rate would increase towards smaller IMBH masses, like $M^{-1/4}$ [48], and this channel would contribute significantly to the total rate. However, as discussed in Section 3.2.1, the IMBHs of interest for Advanced LIGO, with $M \sim 100M_\odot$, have a very small radius of influence and so they will not have a significant influence on the dynamics in the cluster center. The direct capture mechanism, in any case, can yield higher eccentricities than scenarios involving binaries.

The critical periapsis separation r_p for the direct capture of a CO of mass m , moving at infinity with velocity v , by an IMBH of mass $M \gg m$ is [cf. Eq. (11) of [80]]:

$$\frac{r_p^{\max} c^2}{GM} \approx 950 \left(\frac{m}{M}\right)^{2/7} \left(\frac{v}{10^6 \text{ cm s}^{-1}}\right)^{-4/7}. \quad (3.14)$$

If $M = 100 M_\odot$, $m = 1.4 M_\odot$, and $v = 10^6 \text{ cm s}^{-1}$, direct capture is possible at a maximum periapsis of $r_p^{\max} c^2 / (GM) \approx 280$; if $m = 10 M_\odot$ and M and v are the same as above, the maximum periapsis is $r_p^{\max} c^2 / (GM) \approx 500$. For such small periapses, gravitational focusing implies $r_p \propto b^2$, where b is the impact parameter. Hence, the probability distribution $P(b) \propto b$ in impact parameter corresponds to a uniform distribution in periapsis at capture, $P(r_p) = \text{constant}$.

In Figure 3.1, we plot the eccentricity of an IMRI at the frequency at which it enters the Advanced LIGO band as a function of the initial periapsis at capture, following Eq. (3.9). The initial eccentricity at capture can be computed from the energy lost during the first pass; however, the exact value does not significantly affect the eccentricity at $f_{\text{GW}} = 10 \text{ Hz}$, so we set the eccentricity at capture to be $e = 1$. The initial periapsis is uniformly distributed between $r_p^{\min} = 4GM/c^2$ (orbits with

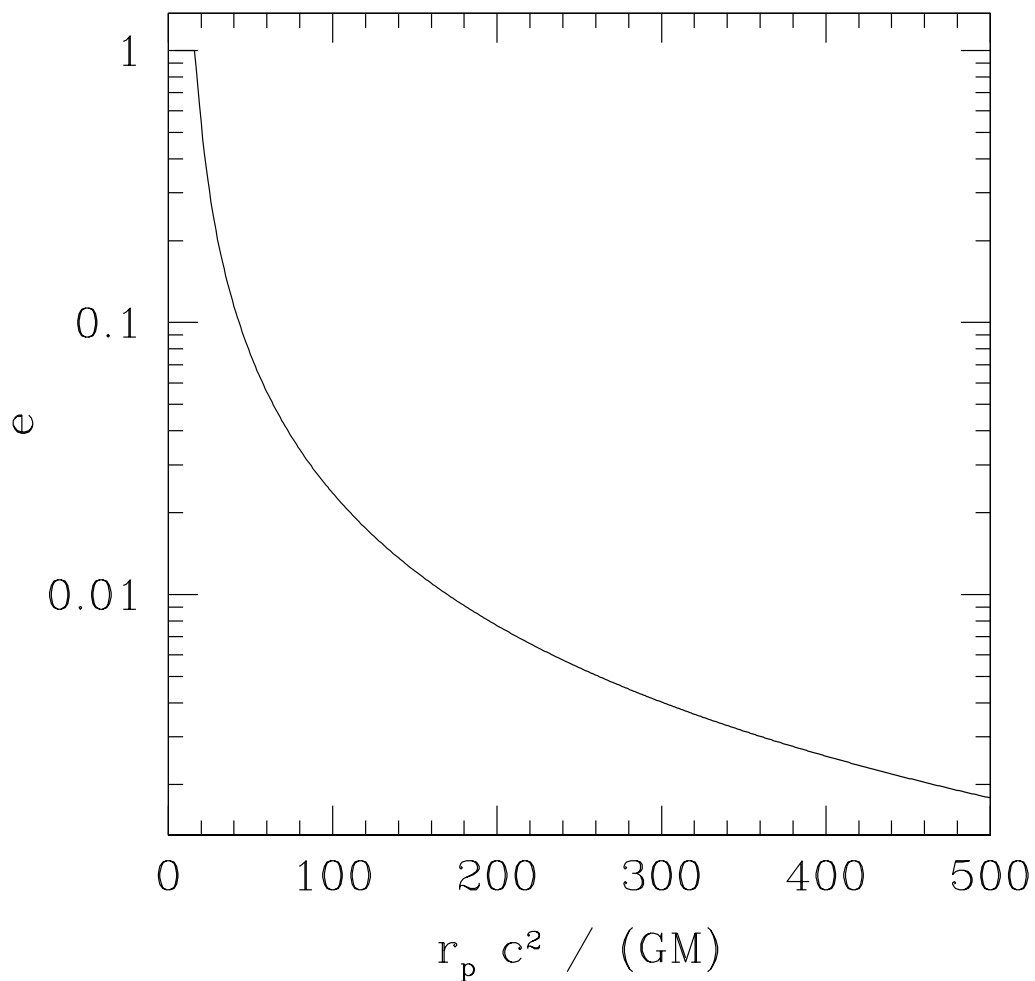


Figure 3.1: The eccentricity at $f_{\text{GW}} = 10$ Hz is plotted as a function of the periapsis at capture, for a CO inspiraling into an IMBH of mass $M = 100 M_{\odot}$. The eccentricity at capture is set to 1, and the eccentricity at $r_p \approx 16 GM/c^2$, where $f_{\text{GW}} = 10$ Hz, follows from Eq. (3.9).

periapsis under $4GM/c^2$ will plunge rather than inspiral) and r_p^{\max} . Therefore, to determine the total fraction of directly captured IMRIs that circularize to a given level $e \leq e_{\text{cutoff}}$ by the time they are in the detector band, it is sufficient to find the fraction of the interval $[r_p^{\min}, r_p^{\max}]$ for which the curve in Fig. 3.1 stays below e_{cutoff} .

Thus, for the chosen IMBH mass of $M = 100 M_\odot$, if the CO is a $m = 1.4 M_\odot$ NS, 86% of all directly captured IMRIs will be circularized to $e \leq 0.1$ by the time they are in the Advanced LIGO band. If the CO is a $m = 10 M_\odot$ BH, 92% of all directly captured IMRIs will be circularized to $e \leq 0.1$ and 67% will be circularized to $e \leq 0.01$ by the time they are in the detector band.

3.2.4 Tidal Capture of a Main-Sequence Star

It has been suggested that Ultraluminous X-ray (ULX) sources are systems in which a main-sequence star that has been tidally captured is transferring mass to an IMBH via Roche lobe overflow [50]. In such a system, after the star reaches the end of its main-sequence lifetime and undergoes a supernova, it may leave a CO on an orbit about the IMBH [49] and this object may then spiral into the IMBH via GW emission. Although work on this problem has focused on sources that might be detected by LISA, results have also been presented for the $\sim 100M_\odot$ IMBHs that we consider here. For $M \sim 100M_\odot$, only 1–2% of systems leave a CO that inspirals into the IMBH within a Hubble time, and these remnants are always NSs [49]. Following [49] we can estimate the rate of these events by assuming that there is ~ 1 ULX in each galaxy. The ULX phase lasts approximately the main-sequence lifetime of the captured star, which is $\sim 10^7$ years, so we estimate that the capture rate is 10^{-7} per year. Multiplying by the fraction of events that successfully inspiral, we estimate a rate of $1\text{--}2 \times 10^{-9}$ IMRIs per galaxy per year. There are typically ~ 100 globular clusters per galaxy, so the rate per globular cluster is $\sim 10^{-11}$ per year, which is considerably smaller than the binary hardening rate. Thus, while this channel could lead to some IMRIs detectable by Advanced LIGO, the rate is likely to be significantly lower than the binary hardening channel.

A NS captured via this mechanism would begin to inspiral into the IMBH with eccentricity $e \lesssim 0.9$ [49] and periapsis approximately equal to the tidal radius, $(M/M_*)^{1/3}R_*$, where $M_* \gtrsim 10M_\odot$ and R_* are respectively the mass and radius of the main sequence star. Assuming, conservatively, $R_* \gtrsim 10^5\text{km}$, this capture periapsis is typically $\gtrsim 500(GM/c^2)$. For an $M = 100M_\odot$ IMBH, equation (3.9) predicts $e \approx 0.002$ when the source enters the Advanced LIGO band. In practice, the eccentricity is likely to be even smaller. It is thus quite clear that this capture mechanism also produces sources that are essentially circular when they enter the Advanced LIGO band.

3.2.5 Tidal Effects

If the inspiraling object is a NS, tides may be significantly excited as it passes the central IMBH. If sufficient energy goes into tidal heating, the NS could be disrupted. Prior to disruption the orbital inspiral will be modified as orbital energy and angular momentum are lost into tidal heating. Tidal interactions are not important for the IMRI events we are considering, however, as we demonstrate below.

3.2.5.1 Tidal Disruption

A star will be tidally disrupted by a BH when the gravitational tidal force acting over the star due to the BH exceeds the self gravity of the star. Assuming a Newtonian potential, this leads to the usual tidal disruption radius

$$R_{\text{td}} = R_* \left(\frac{M}{m} \right)^{\frac{1}{3}} = 41.5\text{km} \left(\frac{R_*}{10\text{km}} \right) \left(\frac{M/100M_\odot}{m/1.4M_\odot} \right)^{\frac{1}{3}}, \quad (3.15)$$

in which R_{td} is the radius at which tidal disruption occurs, m and R_* are the mass and radius of the star, and M is the mass of the BH. The gravitational field outside a Kerr BH is not Newtonian, but (3.15) still provides a reasonable estimate of the tidal disruption radius. Comparing this to the Schwarzschild radius of a $100M_\odot$ BH, $R_S = 2GM/c^2 = 300\text{km}$, suggests that, even when relativistic effects and BH spin are

included, tidal disruption could only occur very close to the central BH. Earlier in this section we showed that the orbits of IMRI objects are effectively circular by the time the CO gets close to the IMBH. The tidal effects for stars on circular orbits are most extreme for prograde equatorial orbits, since these come closest to the central body. Thus, we shall use results for prograde, equatorial circular orbits for a more accurate calculation of tidal disruption.

Vallisneri [91] analyzed NS disruption using the correct tidal field for objects in prograde, circular, equatorial orbits around a Kerr BH, and found that the GW frequency at which tidal disruption occurred, f_{td} , satisfied the relationship

$$R_* = \begin{cases} 3.25\text{km} (m/1.4M_\odot)^{\frac{1}{3}} (M/50M_\odot)^{\frac{2}{3}} (GMf_{td}/c^3)^{-0.71} & GMf_{td}/c^3 \leq 0.045 \\ 1.55\text{km} (m/1.4M_\odot)^{\frac{1}{3}} (M/50M_\odot)^{\frac{2}{3}} (GMf_{td}/c^3)^{-0.95} & GMf_{td}/c^3 \geq 0.045 \end{cases} \quad (3.16)$$

An inspiraling object plunges into the BH when it reaches the innermost stable prograde circular orbit (ISCO). This has radius [9]:

$$\frac{c^2 R_{\text{isco}}}{GM} = 3 + \sqrt{3\chi^2 + Z^2} - \sqrt{(3-Z)(3+Z+2\sqrt{3\chi^2+Z^2})},$$

$$\text{where } Z = 1 + \left[(1+\chi)^{\frac{1}{3}} + (1-\chi)^{\frac{1}{3}} \right] (1-\chi^2)^{\frac{1}{3}}, \quad (3.17)$$

where $\chi = S_1/M^2$ is the dimensionless spin parameter of the BH.

The condition that the star is not disrupted before plunge sets a maximum radius for the NS. If we require the tidal disruption frequency to be greater than the frequency of a prograde circular orbit at the ISCO, $GMf_{\text{isco}}/c^3 = \{\pi[\chi + (c^2 R_{\text{isco}}/GM)^{3/2}]\}^{-1}$ [9], then Eqs. (3.16)–(3.17) imply that the NS escapes disruption provided

$$R_* < \begin{cases} 7.33\text{km} (m/1.4M_\odot)^{\frac{1}{3}} (M/50M_\odot)^{\frac{2}{3}} \left\{ \chi + [c^2 R_{\text{isco}}/(GM)]^{\frac{3}{2}} \right\}^{0.71} & \chi \leq 0.6894 \\ 4.59\text{km} (m/1.4M_\odot)^{\frac{1}{3}} (M/50M_\odot)^{\frac{2}{3}} \left\{ \chi + [c^2 R_{\text{isco}}/(GM)]^{\frac{3}{2}} \right\}^{0.95} & \chi \geq 0.6894 \end{cases} \quad (3.18)$$

Reasonable NS models have a maximum radius of ~ 16 km or less, so this criterion will be satisfied for a $50M_\odot$ IMBH if the spin $\chi < 0.95$. For a $100M_\odot$ IMBH, the condition is satisfied for all spins up to 0.998. As discussed later, we expect IMBHs that grow

through minor mergers to have only moderate spin $\chi \lesssim 0.3$, so tidal disruption should not occur for such IMBHs.

Although the NS cannot be directly tidally disrupted, tidal oscillations will be excited every time the star passes through periapsis. If sufficient energy is deposited into such tides, the star could eventually be disrupted through this tidal heating [30]. To assess whether this effect could be important, we consider the orbital energy lost to leave the star on an orbit with periapsis r_p and eccentricity e divided by the binding energy of the star, $E_{\text{orb}}/E_{\text{bind}}$. If the inspiral was entirely driven by tidal dissipation, and the tidal energy was not efficiently radiated, this would be the ratio of the energy in tidal oscillations to the stellar binding energy. Under these assumptions, if this ratio was of the order of 1 or more, then tidal heating could disrupt the star. In practice, however, most of the orbital energy is lost to gravitational radiation, since, as we shall see below, tidal oscillations can only be excited during the late stages of inspiral. Thus most of the energy does not go into tidal heating and therefore this ratio would have to be significantly greater than 1 for tidal disruption to occur.

Assuming a Keplerian orbit, this ratio is equal to [30]

$$\frac{E_{\text{orb}}}{E_{\text{bind}}} = 4.8(1 - e) \frac{GM}{c^2 r_p} \left(\frac{R_*}{10\text{km}} \right) \left(\frac{m}{1.4M_\odot} \right)^{-1}, \quad (3.19)$$

where we have assumed the star has zero kinetic energy at infinity. (Assuming that the stellar velocity is 10 km s^{-1} at infinity changes this result by only 2.3×10^{-9} for a $1.4M_\odot$ NS of radius 10km.) For an inspiral into a Schwarzschild BH, plunge occurs when $c^2 r_p(1 + e) = 2(3 + e)GM$; therefore for any eccentricity we have $(1 - e)GM/(c^2 r_p) < 1/6$ at plunge. This means that the energy ratio defined in (3.19) can only be greater than one for $R_* > 12.5 \text{ km}$. Tidal disruption due to heating is very unlikely to occur. This conclusion also applies to BHs of moderate spin. For an orbit that is circular at plunge into a BH with spin $\chi = 0.35$, the ratio $E_{\text{orb}}/E_{\text{bind}}$ is approximately equal to one at ISCO for $R_* = 10\text{km}$.

If systems existed in which a NS was on a prograde inspiral orbit into a rapidly spinning BH, the periapsis at plunge would be much closer to the central body and

the energy ratio would exceed unity at plunge. However, the energy ratio would still be small. The radius of the innermost stable circular orbit for a BH of spin $\chi = 0.9$ is at $c^2 r_p = 2.32GM$, at which radius $E_{\text{orb}}/E_{\text{bind}} \sim 2$ for $R_* = 10\text{km}$. The disruption criterion that $E_{\text{orb}}/E_{\text{bind}} \sim 1$ assumes that the orbital energy is dissipated entirely by tidal interactions. In practice, the inspiral will mainly be driven by GW emission, since most of the orbital energy is lost in the regime where GW emissions are quite significant. Tidal dissipation would have to occur on a very short timescale to dominate over gravitational radiation reaction effects, and this will not happen in practice. We can thus conclude that disruption of the NS due to tidal heating will not occur. This is in contrast to main sequence stars which, being less compact, will be disrupted before reaching the ISCO [30]. We note that this conclusion does not change when the relativistic orbital energy is used in place of the Keplerian expression.

3.2.5.2 Tidal Capture

Although tidal interactions should not shorten the inspiral by causing disruption of the NS, if orbital energy and angular momentum of the binary are lost into normal modes of the star, the inspiral trajectory will be modified. In principle, this could modify the capture rate and the typical eccentricities expected at plunge. Significant oscillations are only likely to be excited by tidal interactions if the orbital frequency is comparable to the frequency of normal modes in the NS. We can estimate the latter from the frequency associated with the free fall time in the NS:

$$\omega_{\text{osc}} \approx \frac{\sqrt{2}}{\pi} \sqrt{\frac{Gm}{R_*^3}} = 5.9\text{kHz} \left(\frac{m}{1.4M_\odot} \right)^{\frac{1}{2}} \left(\frac{R_*}{10\text{km}} \right)^{-\frac{3}{2}}. \quad (3.20)$$

This is just an approximation, but it gives the correct order of magnitude for the normal mode frequency. Press & Teukolsky [76] computed normal modes using a polytropic stellar model with index $n = 3$. They found an f -mode frequency that agrees with Eq. (3.20), but with a prefactor of 6.2 kHz instead of 5.9 kHz.

Other stellar modes, in particular g -modes, can have significantly lower frequency, and thus will be excited earlier in the inspiral. Press and Teukolsky tabulate frequen-

cies for g -modes up to g_{14} , which has a frequency a factor of 0.15 smaller than the f -mode. An $n = 3$ polytrope is not a good model for a NS, but it still provides a reasonable estimate of the frequency range for thermal g -modes. NSs also support crustal g -modes that arise from chemical stratification, and core g -modes that arise from stratification in the number densities of charged particles. Finn [22] computed frequencies of crustal g -modes in zero-temperature NSs, using a range of stellar models. He found that the longest period modes had periods of ~ 20 ms. Reisenegger & Goldreich [82] computed the frequencies of core g -modes, and found that these have similar frequencies to the crustal modes. Taking ~ 50 ms as a reasonable maximum for the g -mode period gives a frequency of 20Hz.

Inertial (r -)modes in rotating NSs typically have frequencies of the order of the spin frequency of the NS ($f \sim 10 - 100$ Hz). [47] examined the excitement of r -modes by Newtonian tidal driving and found that this was fairly weak. However, [28] computed the effect of post-Newtonian gravitomagnetic driving and found that this was significantly greater. For rapidly rotating NSs, the inertial-frame frequency can be much smaller than the corotating-frame frequency, which allows f and p modes to be excited [47]. This requires very rapid NS rotation, $f_{\text{rot}} \sim 500$ Hz. [47] examined such modes in the context of comparable mass binaries, but concluded that such NS spins were unlikely to be found in binary systems. In the IMRI case, where a free NS is captured, the NS spin could be much higher in principle, making these modes potentially interesting. [47] and [28] considered only modes in the LIGO frequency range, $10\text{Hz} < f < 1000\text{Hz}$, but the mode spectrum extends to lower frequencies. However, the frequency at which each resonance occurs is a single-valued function of the spin of the NS.

We compare these frequencies to the orbital frequency of a prograde circular orbit at radius r

$$\omega_{orb} = 0.65\text{kHz} \left[\left(\frac{c^2 r}{GM} \right)^{\frac{3}{2}} + \chi \right]^{-1} \left(\frac{M}{50M_{\odot}} \right)^{-1} \quad (3.21)$$

Any NS that comes within a distance $\approx 280GM/c^2$ from an $M = 100 M_{\odot}$ IMBH will be directly captured as a result of GW emission. The additional energy lost

in tidal interactions could increase this capture cross section. However, for $r = 300GM/c^2$ (cf. Sec. 3.2.3), $\omega_{\text{orb}} = 0.13\text{Hz}$ which is much less than the frequency of oscillations of the star. The g -mode frequency is two orders of magnitude higher than the orbital frequency at that radius and so it is unlikely to be significantly excited. The g -mode frequencies become comparable to the orbital frequency for a Schwarzschild BH when $c^2r \lesssim 10GM$. Thus, g -modes are likely to be excited in the late stages of inspiral, but not earlier. As mentioned above, the spectrum of NS r -modes and the f and p mode resonances of rapidly rotating NSs extend to low frequencies [47, 28]. However, the resonant frequencies are determined by the NS spin, so it would require extreme fine tuning for a given NS to be captured at precisely the periapsis that allows excitement of those modes. The capture rate is unlikely to be increased by this mechanism either, although these modes could also be excited later in the inspiral.

Press & Teukolsky [76] provide an expression for the energy dissipated in tides in an object of mass m and radius R_* that passes a point mass of mass M on a Keplerian orbit with periapsis R_{min} :

$$\Delta E_{\text{tidal}} = \left(\frac{Gm^2}{R_*}\right) \left(\frac{M}{m}\right)^2 \left(\frac{R_*}{R_{\text{min}}}\right)^6 T_2 \left(\sqrt{\frac{m}{M}} \left[\frac{R_{\text{min}}}{R_*}\right]^{\frac{3}{2}}\right) \quad (3.22)$$

This expression is integrated over all thermal normal modes, including g -modes up to g_{14} . Once again, this result is based on an $n = 3$ polytropic stellar model, which is not a good model of a NS. However, it should provide an order of magnitude estimate for the energy lost in thermal modes. In Eq. (3.22) we include only the $l = 2$ modes, since other modes are suppressed by $(R_*/R_{\text{min}})^2 \ll 1$ relative to these modes. We also take the extreme mass ratio limit $M \gg m$. The function $T_2(\eta)$ behaves as $T_2(\eta) \sim 0.65\eta^{-2.34}$ at large η (we have derived this “by eye” from Figure 1 in [76]). We can thus compute the ratio of the energy dissipated in tides to the energy dissipated in GW emission, $\Delta E_{\text{GW}} = [85\pi m^2/(12\sqrt{2}Mc^5)](GM/R_{\text{min}})^{7/2}$, for an object on a

parabolic Keplerian orbit with periapsis R_{\min}

$$\frac{\Delta E_{\text{tidal}}}{\Delta E_{\text{GW}}} \approx 0.05 \left(\frac{GM}{c^2 R_{\min}} \right)^{6.01} \left(\frac{R_*}{20\text{km}} \right)^{8.51} \left(\frac{M}{50M_\odot} \right)^{-5.34} \left(\frac{m}{1.4M_\odot} \right)^{-3.17} \quad (3.23)$$

It is clear that, under these model assumptions, the tidal perturbation to the orbit at capture is always much weaker than the perturbation induced by GW emission. For comparison, since $\Delta E_{\text{GW}} \propto r_p^{-7/2}$, a 10% increase in the energy lost in a single pass by the central BH increases the minimum periapsis required for direct capture by only a factor of $1.1^{2/7} \approx 1.03$ or $\sim 3\%$.

The above arguments indicate that the excitement of NS modes will not increase the capture rate nor lead to NS disruption during an IMRI. However, orbital energy lost into oscillations could modify the inspiral trajectory by either causing a cumulative phase shift in the emitted GWs or by changing the eccentricity of the orbit in the LIGO band. [28] calculated the phase difference in the GWs that arises from the excitement of r -modes, finding $\Delta\Phi \sim 3.4R_{10}^4 f_{s100}^{2/3} M_{1.4}^{-1} m_{1.4}^{-2} (M_{1.4} + m_{1.4})^{-1/3}$, where R_{10} is the NS radius in units of 10km, $M_{1.4}/m_{1.4}$ are the masses of the primary/secondary in units of $1.4M_\odot$ and f_{s100} is the spin frequency (or r -mode frequency) in units of 100Hz. For an IMRI with $M = 50M_\odot$, this gives $\Delta\Phi \sim 0.003$ if we set $R_{10} = f_{s100} = m_{1.4} = 1$. Typically we require a phase shift of $\Delta\Phi \sim 1$ for an effect to be observable, so the excitement of r -modes will not leave an imprint on the inspiral. The phase shift induced by the resonant excitement of f and p modes in rapidly rotating NSs can be significantly higher. [47] quote $\Delta\Phi \sim 234m_{1.4}^{-4.5} R_{10}^{3.5} m_{1.4}^2 / (M_{1.4}(m_{1.4} + M_{1.4})) f_{gw100}^{-1}$ for the most extreme case of the $(22, 2)$ f -mode resonance (with the same notation as before but now denoting the GW frequency in units of 100Hz by f_{gw100}). For an $M = 50M_\odot$ IMRI, this gives $\Delta\Phi \sim 0.2f_{gw100}^{-1}$. This could be a measurable shift if the resonance is excited near 10Hz. However, the phase shift is only this large for IMBHs at the low mass end of the IMRI range, and provided the NS spin is tuned to ensure that the resonance is excited near 10Hz. More work will be needed to quantify how large a phase shift would be measurable with Advanced LIGO, accounting for correlations between the waveform parameters.

We can estimate qualitatively what effect tidal dissipation would have on the orbital eccentricity and periapsis. The phase space trajectory that an inspiral follows is determined entirely by the ratio dE/dL_z . Assuming a Keplerian orbit, we have

$$\frac{dr_p}{de} = \frac{r_p \left(2 \sqrt{(1+e)GM} - r_p^{\frac{3}{2}} dE/dL_z \right)}{(1+e) r_p^{\frac{3}{2}} dE/dL_z - 2(1-e) \sqrt{(1+e)GM}}. \quad (3.24)$$

We now suppose that the inspiral was driven entirely by tidal dissipation. Typically the dominant excited mode would be an $m = 2$ mode, for which $\Delta L_z = 2\Delta E/\omega_{00}$, where ω_{00} is the frequency of the mode (this assumes that the stellar oscillations can be modeled as a linear Lagrangian system; Friedman & Schutz 33). We write

$$\omega_{00} = \sqrt{\frac{GM}{r_c^3}}, \quad (3.25)$$

where r_c is the radius of the circular (Keplerian) orbit that would have the same frequency as the $m = 2$ mode. With this substitution, equation (3.24) defines the evolution of r_p/r_c over the inspiral. Equations (3.20) and (3.21) indicate that the capture periapsis, r_p^0 , will typically be much greater than r_c . Solutions with $r_p^0 > 2^{5/3}r_c$ are all qualitatively the same, and we show a typical example in Figure 3.2, for capture periapsis of $1000 r_c$ and a capture eccentricity of 1. For a $100M_\odot$ IMBH, taking $\omega_{00} = 6$ kHz yields $c^2 r_c \approx 0.5GM$, so this figure represents a capture at $r_p \approx 500 GM/c^2$, the upper end of the allowed direct capture range for a $m = 10 M_\odot$ BH. The figure shows the inspiral in eccentricity-periapsis space. Under this simple model of tidal interactions, the periapsis increases while the eccentricity decreases. In practice, the inspiral will be driven by a combination of GW emission and any tidal dissipation that occurs. These results suggest that tidal effects would tend to make the eccentricities at plunge smaller than they would be for inspirals driven by radiation reaction alone.

Equations (3.20)–(3.23) indicate that normal modes are unlikely to be excited during an inspiral into an IMBH, although high order g -modes, r -modes and f -modes in rapidly rotating NSs might be excited during the very late stages of inspiral. Thus,

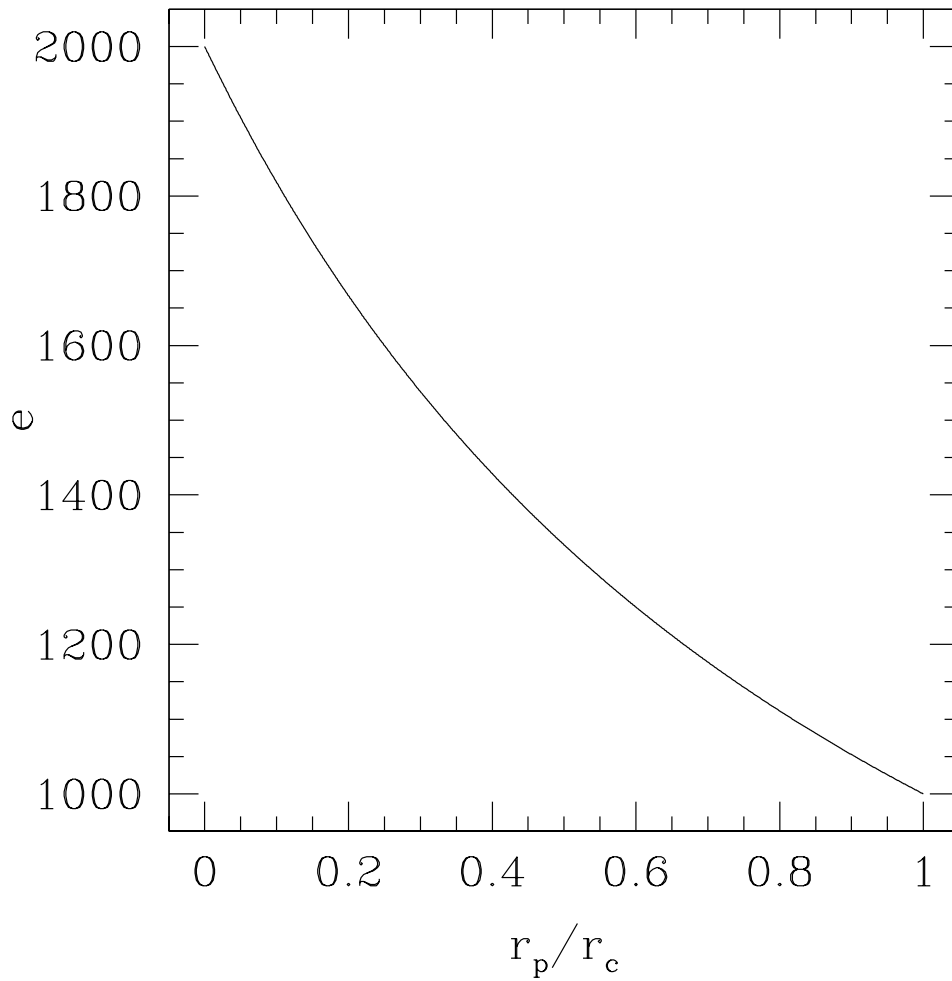


Figure 3.2: Tidal-dissipation-driven inspiral in phase space for an inspiraling star with initial eccentricity of $e = 1$ and initial periapsis $r_p = 1000 r_c$. The plot shows eccentricity on the horizontal axis and the ratio r_p/r_c on the vertical axis. The radius r_c characterizes the frequency of normal modes in the star as defined by Eq. (3.25).

we can safely ignore the effect of tides on the capture rates. Tidal effects could modify the inspiral, although the above calculation indicates that this should not modify our conclusions about the typical eccentricities at plunge. The excitement of f -modes might leave a measurable imprint on the GW signal. However, the induced phase shift is only marginally detectable and this mechanism requires the NS to be rapidly rotating.

3.3 Event Rates

In this section, we estimate the rate of IMRIs in globular clusters detectable by Advanced LIGO. To do this, we must consider three elements: (i) the distance sensitivity of the detectors to GWs from IMRIs (and hence the volume of the universe the detectors can see), (ii) the number density of globular clusters, and (iii) the rate of IMRIs per globular cluster.

3.3.1 Advanced LIGO IMRI Sensitivity

For GW sources with known waveforms (or at least waveforms well approximated by analytic or numerical techniques), matched filtering is used to search for signals in GW detector data [92, 2]. The signal-to-noise ratio (SNR) ρ of a template $h(t)$ in data $s(t)$ collected by a detector which has one-sided noise power spectral density $S_n(|f|)$ is given by

$$\rho = \frac{4}{\sigma} \int_0^\infty \frac{|\tilde{s}(f)\tilde{h}^*(f)|}{S_n(|f|)} df, \quad (3.26)$$

where $\tilde{s}(f)$ is the Fourier transform of the signal $s(t)$, $\tilde{h}(f)$ is the Fourier transform of the inspiral template $h(t)$, $*$ denotes complex conjugation, and σ is defined by

$$\sigma^2 = 4 \int_0^\infty \frac{|\tilde{h}(f)|^2}{S_n(|f|)} df. \quad (3.27)$$

This definition of SNR follows the normalization of [17] and [2]. We place the template $h(t)$ at a canonical source distance of 1 Mpc and choose the optimal orientation of

the detector to maximize the SNR, and so the maximum distance to which a single detector matched filter search is sensitive at a given SNR ρ is given by $D = \sigma/\rho$ Mpc. (This is the same quantity as the “inspiral horizon distance” used by the LIGO and Virgo Collaborations [1].)

To compute the sensitivity of a single Advanced LIGO detector to IMRIs, we need to compute the quantity σ^2 defined in Eq. (3.27) using a particular waveform model. We have done this with waveforms based on BH perturbation theory [24], which are valid in the limit $m/M \ll 1$. The waveforms, which include non-quadrupolar harmonics of the orbital frequency in addition to the dominant quadrupolar harmonic, are described in Appendix 3.6, where we also discuss the relative SNR contributed by the four lowest harmonics. The noise power spectral density $S_n(|f|)$ was taken from [34]. GW detectors have an orientation-dependent response. The relation between the *range* R (defined as the radius of a sphere whose volume is equal to the volume of the universe in which inspiral sources could be detected with an SNR threshold of ρ) and maximum distance D at a fixed SNR is given by $R = D/2.26$ [23].

We assume a value of $\rho = 8$ for the threshold SNR required for a detection, since this is the value typically used to compute Initial LIGO detection ranges for comparable-mass black hole binaries [1]. This is a reasonable approximation, as a binary black hole inspiral with a total mass of $6 M_\odot$ has approximately 500 gravitational-wave cycles between the 40 Hz low-frequency cutoff of Initial LIGO and coalescence — roughly the same number of gravitational-wave cycles that an IMRI signal in Advanced LIGO will have between the Advanced LIGO low-frequency cutoff of 10 Hz and coalescence. The threshold will be computed more accurately when an IMRI search is implemented and the amount of non-stationarity of the Advanced LIGO data is known. If the $\rho = 8$ threshold cannot be achieved in practice (or if it can be improved), then the detection rates derived below can be scaled appropriately.

Advanced LIGO will consist of a network of three 4-km detectors. Demanding that GWs are found coincident in all three detectors increases the network range by a factor of $\sqrt{3}$ relative to the range of a single detector at a given SNR (due to the lower false alarm rate of the network). Fig. 3.3 shows the range R of a network of three

Advanced LIGO detectors for circular-equatorial-orbit IMRIs of $m = 1.4M_\odot$ objects into a Kerr IMBH of mass M , assuming that the network SNR required for a confident detection was $\rho = 8$. This is equivalent to the range of a single detector with SNR of $\rho = 8/\sqrt{3}$. The $\chi = 0$ (non-spinning IMBH) curve in Fig. 3.3 is well-approximated by a quadratic fit:

$$R \approx \sqrt{m/M_\odot} \times \left[800 - 540 \left(\frac{M}{100 M_\odot} \right) + 107 \left(\frac{M}{100 M_\odot} \right)^2 \right] \text{Mpc}. \quad (3.28)$$

The scaling of the range in Eq. (3.28) as \sqrt{m} does not follow from the fit, but rather from the following reasoning. The amplitude of GWs from IMRIs will scale linearly with the mass of the smaller object m , but the number of cycles in the LIGO band will also drop by roughly a factor of m . Hence, the total signal-to-noise ratio (SNR) will grow as \sqrt{m} , so inspirals of more massive COs will be seen a factor of \sqrt{m} further away.

The combination of the spin of the central object and the inclination of the orbital plane of the inspiraling particle will have a significant effect on the signal from an IMRI. The frequency of the ISCO is much higher for prograde inspirals into rapidly spinning BHs than for inspirals into non-spinning holes; the SNR can be strongly enhanced for such orbits. Conversely, retrograde inspirals will have lower SNR. Averaging over random inclination angles, Mandel [58] computed the ratio between (i) the detection range for Advanced LIGO in a universe uniformly populated by IMBHs of a given mass and spin and (ii) the detection range in a universe with an equal density of Schwarzschild IMBHs with the same mass. He found that the detection range can be enhanced by a factor of 1.7 (3.8) for maximally spinning Kerr BHs with $M = 100M_\odot$ ($M = 200M_\odot$); the increase in the volume of observable space and, hence, the event rates, is the cube of these numbers.

If IMBHs grow mainly by random mergers, they will not be rapidly spinning as the contributions of subsequent mergers to the hole's spin largely cancel out. The angular momentum imparted to the IMBH by a CO is $L_{\text{obj}} \propto mM$, since the radius at ISCO is $r_{\text{ISCO}} \propto M$. This causes the dimensionless spin parameter of the hole

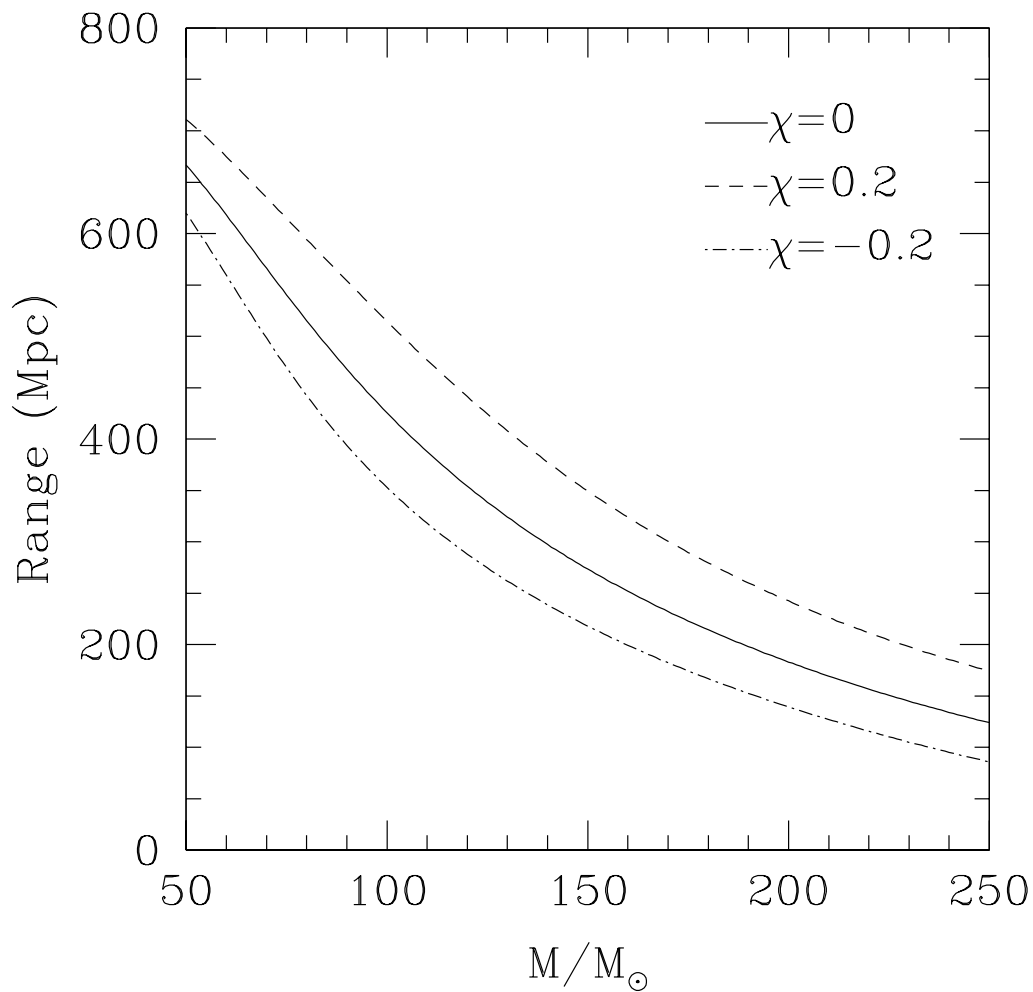


Figure 3.3: Range of a network of three Advanced LIGO detectors for the circular-equatorial-orbit inspiral of a $1.4 M_{\odot}$ object into an IMBH, as a function of IMBH mass M . The three curves show IMRI spins of $\chi = 0.2$ (dashed), 0 (solid), and -0.2 (dot-dashed). Positive χ means prograde orbit; negative χ means retrograde. The quadratic fit given in Eq. (3.28) is a fit to the $\chi = 0$ curve.

$\chi = S_1/M^2$ to change by $\sim L_{\text{obj}}/M^2 \propto m/M$. After $\sim M/m$ such mergers, necessary for the hole to grow to mass M , the typical spin of the hole will be $\chi \sim \sqrt{m/M}$. More precise calculations [51, 60, 58] show that the spin of IMBHs involved in LIGO IMRIs will rarely exceed $\chi = 0.3$ for IMBHs that gained a significant fraction of their mass via minor mergers. For small values of χ , Eq. (24) of [58] yields a correction to the range presented in Eq. (3.28) due to the inclusion of the IMBH spin; the detection range in Mpc as a function of M , m , and χ is

$$\frac{R}{\text{Mpc}} \approx \left[1 + 0.6 \chi^2 \left(\frac{M}{100 M_\odot} \right) \right] \sqrt{\frac{m}{M_\odot}} \left[800 - 540 \left(\frac{M}{100 M_\odot} \right) + 107 \left(\frac{M}{100 M_\odot} \right)^2 \right]. \quad (3.29)$$

This range estimate does not include the cosmological redshift. The redshift due to the expansion of the universe decreases the frequency of the GWs. For $M \sim 100 M_\odot$ IMRIs, the redshifted GWs will lie in a less sensitive part of the LIGO noise curve, thereby reducing the range. For IMRIs detectable with Advanced LIGO, redshifts are typically $\lesssim 0.2$; for example, the inspiral of a $1.4M_\odot$ NS into a non-spinning $100M_\odot$ IMBH is visible to a redshift of 0.09. We estimate that for typical sources, properly including the redshift reduces the Advanced LIGO event rate by $\sim 10\%$.

Advanced LIGO will have several parameters which may be tuned during the operation of the detector to optimize the noise power spectral density (PSD) in order to search for specific sources. These tunable parameters include the laser power and the detuning phase of the signal recycling mirror. If a noise PSD optimized for detections of CO-IMBH binaries is used instead of the default PSD assumed in Fig. 3.3, the range for such sources is increased by a factor of ~ 1.5 , corresponding to an event rate increase by a factor of ~ 3.5 .

3.3.2 Number Density of Globulars with a Suitable IMBH

The second element in the rate calculation is the number density of globular clusters that have an IMBH in the relevant mass range. This is highly uncertain. To contribute significantly, a cluster must have had a sufficiently small initial relaxation

time to allow the formation of an IMBH through some mild runaway process when the cluster was young, yet not have formed an IMBH with $M > 350 M_{\odot}$ (since this would put IMRIs beyond the Advanced LIGO frequency range). Recent theoretical arguments by Trenti and colleagues [44, 89, 90, 88] suggest that dynamically old globulars with large core to half-mass radius ratios have been heated by a $\sim 1000 M_{\odot}$ IMBH, so these clusters would not contribute to the Advanced LIGO IMRI rate. Note, though, that [52] has shown that current observations of the core to half-light ratios in globulars do not require $1000 M_{\odot}$ BHs in most clusters. Core-collapsed globular clusters, which constitute $\sim 20\%$ of all globular clusters [71], may contain IMBHs of the right mass. We will parametrize the unknown fraction of relevant globular clusters by some fraction f . Globular clusters have a space density of $8.4 h^3 \text{ Mpc}^{-3}$ [74], which for $h = 0.7$ yields 2.9 Mpc^{-3} . Therefore, we will use the number density $\sim 0.3 (f/0.1) \text{ Mpc}^{-3}$. This factor f depends on both the number of clusters with an IMRI in the right mass range, and the number of clusters that have been in a state of core-collapse long enough for the binary hardening mechanism to occur. These factors are degenerate, however, since clusters with heavier IMBHs will not be in a state of core collapse, as described above. The fraction f also depends on what proportion of the objects merging with the IMBH are COs as opposed to main-sequence stars. Our Monte Carlo simulations, which were discussed earlier, indicate that this proportion is close to 1.

The fraction f of globular clusters containing IMBHs may be further lowered by ejections of IMBHs from their clusters by recoil kicks imparted to the IMBHs by dynamical processes and by gravitational radiation emission. If the kick exceeds $\approx 50 \text{ km s}^{-1}$, which is the escape velocity from a massive globular cluster, the IMBH will escape from the cluster, thereby becoming unavailable for future events. Kicks can arise from the process of hardening via three-body encounters [56, 84, 39, 40]. Gültekin, Miller and Hamilton (2006) show (cf. their Fig. 12) that when the seed mass is $100 M_{\odot}$, only about 50% of all BHs grow to $300 M_{\odot}$ without being ejected, and this fraction drops to 10% for a seed mass of $50 M_{\odot}$.

Kicks also arise from GW emission. During the last stages of the merger of

unequal mass BHs, a net flux of angular momentum will be carried away by the GWs, imparting a kick to the resulting BH [68, 11, 25, 26, 81, 94, 21, 13, 18, 45, 8, 37, 85]. The most recent results on merger velocity kicks, based on numerical relativity, show that the kick velocity for a non-spinning central object depends on the symmetric mass ratio $\eta = mM/(m + M)^2$ as $V_{\text{kick}} \approx 12000\eta^2\sqrt{1-4\eta}(1 - 0.93\eta)$ km s⁻¹ [37]. The requirement $V_{\text{kick}} < 50$ km s⁻¹ places an upper limit on m of $q = m/M \lesssim 0.08$.

If the IMBH is rapidly spinning, recent numerical relativity results suggest the kick can be a lot higher [7, 15, 16, 38, 46, 54]. [7] and [15] provide a fit to numerical relativity results that gives the kick as a function of the various orbital parameters. This formula indicates that if the IMBH has moderate spin $\chi \lesssim 0.5$ and the secondary is non-spinning, then we require $q \lesssim 0.05$ to ensure the IMBH has a high probability of remaining in the globular cluster today after undergoing multiple mergers. This constraint can be relaxed to $q \lesssim 0.067$ if $\chi \lesssim 0.3$. If the objects merging with the IMBH are BHs with a mass of $10M_{\odot}$, this constrains the initial IMBH mass to be $M \gtrsim 150M_{\odot}$. If the merging objects are $1.4M_{\odot}$ NSs, even IMBHs with a seed mass of $50M_{\odot}$ are safe from ejection.

As argued earlier, mergers with BHs are likely to be important early in the IMBH evolution, when its mass is smaller, with NS mergers becoming dominant later. This could mean that a significant number of IMBHs were ejected from globular clusters early in their evolution. However, without firm knowledge of the initial seed masses of IMBHs nor the relative number of mergers with BHs and NSs that each IMBH undergoes, it is impossible to draw definitive conclusions. We normalize f to 10% in the rates calculations that follow, but emphasize that this quantity is highly uncertain at present.

3.3.3 IMRI Rate per Globular Cluster and Event Rate

The final contribution to the rate estimate is the merger rate per globular cluster. Existing numerical simulations of globular clusters suggest that mergers in the sub-cluster of $\sim 10M_{\odot}$ BHs at the center of the globular cluster can lead to the creation

of IMBHs with masses up to $\sim 350M_\odot$ in $\sim 10^{10}$ years [67]. However, the results of such simulations are very sensitive to the choice of cluster models and to assumptions about kick velocities, the interaction between the BH subcluster and the rest of the cluster, etc. Therefore, we present two methods for computing the rate per globular: (i) an upper limit independent of cluster model; and (ii) an estimate based on a more realistic model for cluster dynamics.

We estimate a theoretical upper limit on the IMRI event rate in a globular cluster using the following method, originally suggested by Phinney [72]. We assume that each globular cluster has a BH that grows from $M \sim 50M_\odot$ to $M \sim 350M_\odot$ by capturing a sequence of COs of identical mass m over the age of the cluster. Then $300M_\odot/m$ captures will happen in each globular cluster in $\sim 10^{10}$ years. This leads to a rate of $(300 M_\odot)/m \times (10^{10} \text{ yr})^{-1}$ per cluster.

Although this rate is plausible, it may be a significant over-estimate for several reasons. Firstly, it assumes that all the mass that the IMBH acquires in growing from $M \sim 50M_\odot$ to $M \sim 350M_\odot$ comes from mergers with COs. In practice, the IMBH will also acquire mass via gas accretion, and by captures of main-sequence stars and white dwarfs, which will be tidally disrupted before becoming significant GW sources but will still add mass to the IMBH. Secondly, this estimate does not include the likelihood that the merger product will be kicked out of the cluster through recoil, as discussed in the previous section. Thirdly, this estimate assumes that the rate at which the IMBH grows via IMRIs from $50 M_\odot$ to $350 M_\odot$ is constant in time. However, Advanced LIGO can only detect mergers that occurred at distances $\lesssim 1$ Gpc, i.e., relatively recently, so the relevant rate is the rate late in the history of the globular cluster, which is likely to be much lower. For example, [67] found in their numerical simulations that the rate dropped from $\sim 10^{-7}/\text{yr}$ to $\sim 3 \times 10^{-10}/\text{yr}$ after 10^{10} years for some plausible cluster models.

For the theoretical upper limit, the total rate is given by $\alpha \overline{V(M, m, \chi)}$, where $\alpha \sim 0.3 (f/0.1) \text{ Mpc}^{-3} (300 M_\odot)/m (10^{10} \text{ yr})^{-1}$ is the IMRI rate in the universe, $V(M, m, \chi) = (4/3)\pi R^3$ is the volume in which Advanced LIGO can see an event, and on overbar, \overline{V} , denotes the average over mass M in the range between $50M_\odot$ and

$350M_{\odot}$. If we take $f = 0.1$, $\chi = 0.2$ as the typical IMBH spin and all inspiraling objects are $1.4M_{\odot}$ NSs, the rate is ≈ 3 events per year; if $f = 0.1$, $\chi = 0.2$ and inspiraling objects are $10M_{\odot}$ BHs, the event rate is ≈ 10 per year. These values are based on the range fit in Eq. (3.29), so they assume that orbital frequency harmonics through $m = 4$ are included in the data analysis, but cosmological redshift and Advanced LIGO optimization are not included. When all of these considerations are taken into account, an theoretical upper-limit estimate suggests that Advanced LIGO may detect up to thirty IMRIs per year. A similar estimate for Initial LIGO shows that because of lower overall sensitivity and a higher low-frequency cutoff (40 Hz for Initial vs. 10 Hz for Advanced LIGO), the upper limit on the Initial LIGO IMRI rate is only about 1/1000 events per year.

A more realistic estimate is based on the assumption that the hardening of a CO–IMBH binary via three-body interactions represents the primary capture mechanism leading to IMRIs. The rate for IMRIs created by this scenario is $\approx 3 \times 10^{-9} \text{ yr}^{-1}$ per globular cluster for NS–IMBH IMRIs and $\approx 5 \times 10^{-9} \text{ yr}^{-1}$ for BH–IMBH IMRIs [see § 3.2.1]. Hence, the NS–IMBH IMRI rate in the local universe is $\alpha \approx 10^{-9} (f/0.1) \text{ Mpc}^{-3} \text{ yr}^{-1}$, while the BH–IMBH IMRI rate is $\alpha \approx 1.5 \times 10^{-9} (f/0.1) \text{ Mpc}^{-3} \text{ yr}^{-1}$. If we assume that all IMBHs have a mass $\sim 100M_{\odot}$ and $f = 0.1$, this yields an Advanced LIGO rate of one IMRI per three years if the typical CO is a NS or ten IMRIs per year if the typical CO is a $m = 10 M_{\odot}$ BH. If the interferometer is optimized for the detection of IMRIs, the NS–IMBH and BH–IMBH rates are increased to one event per year and thirty events per year, respectively.

In addition to detections of inspirals, Advanced LIGO could also detect the ring-down of an IMBH following a merger. This possibility is discussed in Appendix 3.7.

3.4 Effect of Eccentricity on Matched Filter Searches

As discussed in § 3.3.1, matched filtering is used to search for GWs with known waveforms in detector noise. In order to be an optimal search technique, the matched filter requires accurate templates that correctly model the signals being sought [92].

Since source parameters (e.g., the masses and the IMBH spin) can vary, the matched filter is constructed for a “bank” of templates: a set of waveform models which depend on the parameters that characterize the source. The accuracy of a template bank is characterized by the fitting factor (FF) [4], which measures the overlap between the GW signal and the nearest template. A fitting factor close to unity indicates that the templates are accurate for detection of the desired signals. A fitting factor less than unity will mean that we are unable to detect a fraction $(1 - \text{FF}^3)$ of the theoretically detectable events. (The quantity $1 - \text{FF}$ is often referred to as the mismatch.) To search for signals, template banks are constructed so that the mismatch between any desired signal and the nearest template does not cause an unacceptable loss in SNR (typically $\text{FF} \approx 0.97$ for LIGO).

In this section, we examine the effect of eccentricity on searching for IMRI signals in Advanced LIGO detectors. The effect of eccentricity on the fitting factor was previously examined by [59] and it was found that the fitting factor between a circular and eccentric waveform template was high provided $e \lesssim 0.2$. However, their results do not apply directly to IMRIs since they computed fitting factors only for binaries with mass ratios close to one, and used the first generation LIGO noise curve.

We consider a matched-filter search for IMRIs and determine the loss in SNR (and hence range) if eccentricity is not included in the template bank, i.e., circular templates are used to search for potentially eccentric waveforms. We compute the fitting factor as follows. The template $h(t)$ appearing in the expression for the matched filter SNR ρ [Eq. (3.26)] depends on a number of parameters characterizing the source, such as the masses of the binary and the time of arrival of the signal. We denote these parameters $\vec{\lambda}$ and define the ambiguity function $\mathcal{A}(\vec{\lambda})$ by

$$\mathcal{A}(\vec{\lambda}) = \frac{\langle s|h(\vec{\lambda}) \rangle}{\sqrt{\langle s|s \rangle \langle h(\vec{\lambda})|h(\vec{\lambda}) \rangle}}, \quad (3.30)$$

where $\langle a|b\rangle$ is the matched filter inner product given by

$$\langle a|b\rangle = 4 \int_0^\infty \frac{\tilde{a}(f)\tilde{b}^*(f)}{S_n(|f|)} df. \quad (3.31)$$

We separate the parameters $\vec{\lambda}$ into $\vec{\lambda} = (t_0, \phi_0, \vec{\theta})$, where t_0 and ϕ_0 the time of arrival and phase of the binary, respectively. In the case of circular equatorial binaries, it is trivial to maximize over the parameters t_0 and ϕ_0 analytically (the phase by projecting the signal onto two orthogonal basis vectors and the time by a Fourier transform) and so these are called *extrinsic parameters*. The remaining template parameters $\vec{\theta}$, which include the binary masses, eccentricity and IMBH spin, determine the shape of the waveform and are known as *intrinsic parameters*. For circular inspiral templates, the ambiguity function \mathcal{A} reduces to the overlap \mathcal{O} , given by

$$\mathcal{O}(\vec{\theta}) = \max_{t_0, \phi_0} \frac{\langle s|h(\vec{\theta})\rangle}{\sqrt{\langle s|s\rangle\langle h(\vec{\theta})|h(\vec{\theta})\rangle}}, \quad (3.32)$$

The fitting factor is given by the maximum of the overlap function over the remaining parameters

$$\text{FF} = \max_{\vec{\theta}} \mathcal{O}(\vec{\theta}). \quad (3.33)$$

For the signal $s(t)$ and template $h(t)$ we use numerical kludge waveforms. This is a family of waveforms that were constructed as models for extreme mass ratio inspiral systems, in which $m/M \ll 1$. The waveform family is constructed by first computing an accurate phase-space trajectory by integrating prescriptions for the evolution of the orbital elements (the orbital energy, angular momentum and Carter constant or equivalently the orbital radius, eccentricity and inclination) [36]. The orbit of the small body is then calculated by integration of the Kerr geodesic equations along the sequence of geodesics defined by the phase space trajectory. Finally, a kludge waveform is generated from the orbit by applying weak-field emission formulae [5]. This waveform family predicts the inspiral rates for nearly-circular orbits very well [36] and has been shown to be extremely faithful (overlaps in excess of $\sim 95\%$ over much of the parameter space) to more accurate perturbative waveforms [5]. Although the

mass ratio of an IMRI system is probably too high to make these waveforms accurate as search templates, they should provide reliable predictions of the fitting factor.

For these calculations we used $M = 100 M_{\odot}$ for the IMBH mass, $m = 1.4 M_{\odot}$ for the companion mass and considered two spin values $\chi = 0$ and $\chi = 0.2$. We used the Advanced LIGO power spectral density $S_n(|f|)$ given by [34]. As discussed above, to compute the fitting factor one must maximize over the parameters $\vec{\theta}$ of the template. However, we find that even without maximizing over the intrinsic parameters, the overlap (and hence the fitting factor) between circular and eccentric templates is greater than 0.99 for eccentricities $e < 0.01$, i.e., for more than two thirds of IMRIs formed by direct capture (the mechanism likely to give the largest eccentricities). Since we expect that most of the IMRI systems will have eccentricities significantly less than $e = 0.01$ by the time they have entered the Advanced LIGO band, eccentricity will be negligible for data analysis and circular templates may be used to search for these systems.

Fig. 3.4 shows the overlap between eccentric signals and circular templates for prograde equatorial inspirals and eccentricities greater than 0.01. Analysis of inclined inspirals demonstrates that the overlaps between eccentric signals and circular templates remain greater than 0.99 for eccentricities $e < 0.01$, and greater than 0.93 for eccentricities $e < 0.05$. Although the overlap decreases for eccentricities greater than 0.01, we anticipate higher values of the fitting factor when we maximize over the other intrinsic parameters. An interesting question will be to determine whether eccentricities greater than 0.01 can be measured (and thus be used to investigate the relative prevalence of the various capture mechanisms) or if eccentricity is degenerate with masses and the other intrinsic parameters.

3.5 Summary

In this paper, we have discussed a potential source of GWs for ground based interferometers — the *intermediate-mass-ratio inspiral* of a stellar mass CO (a NS or BH) into an IMBH in the center of a globular cluster. For IMBHs with masses in the

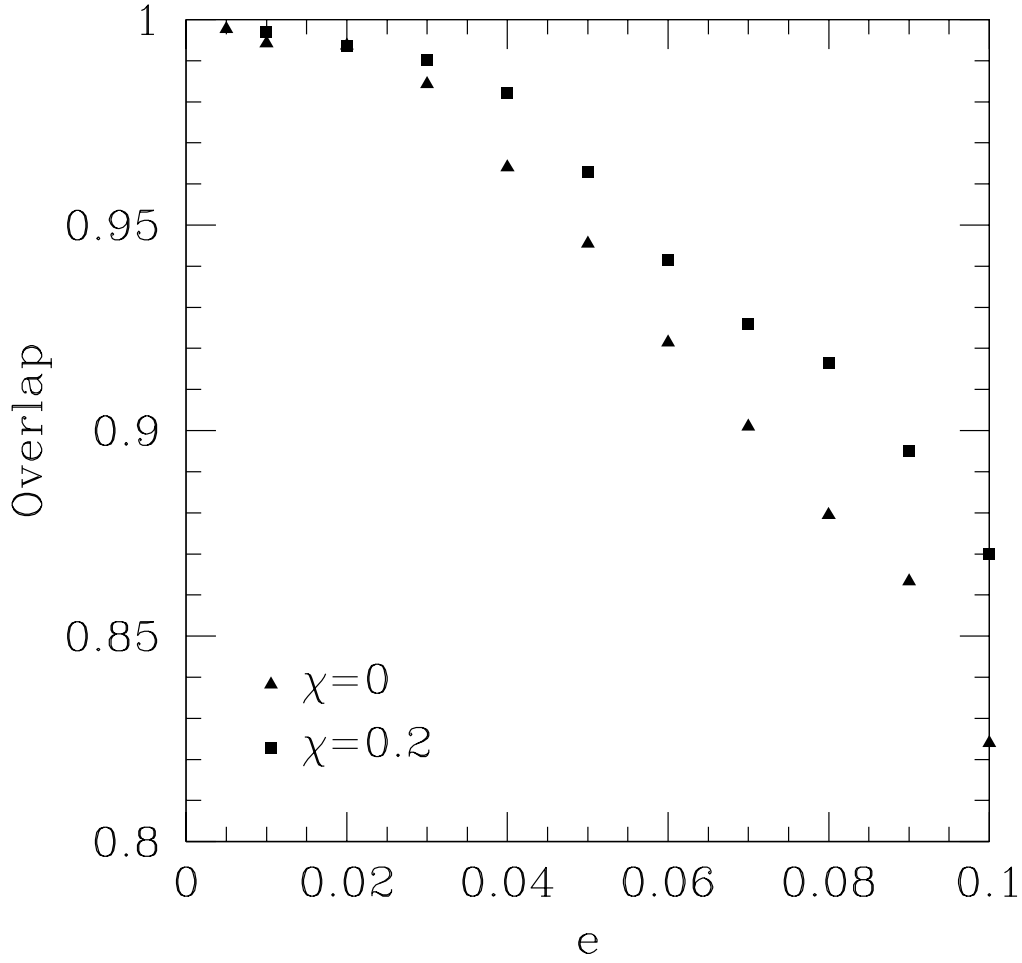


Figure 3.4: The overlaps \mathcal{O} between a circular template $h(t)$ and signals $s(t)$ with varying eccentricities, e . For both signal and template, the intrinsic parameters $\vec{\theta} = (M = 100 M_{\odot}, m = 1.4 M_{\odot}, \chi, e)$ are kept constant, with maximization performed only over time of arrival and phase. The overlaps for two values of χ are shown.

range $50 - 350M_{\odot}$, the GWs emitted will be at frequencies in the Advanced LIGO band. We have shown that Advanced LIGO should be able to detect the inspiral of a $1.4M_{\odot}$ NS into an IMBH at distances up to 700 Mpc, depending on the mass and spin of the IMBH. Assuming all IMBHs were grown by CO–IMBH mergers gives an upper limit on the Advanced LIGO event rate of ~ 10 per year. We have shown that if the inspiraling CO is a NS, a more likely estimate of the rate is one event per three years, while the rate for BH–IMBH IMRIs could reach the upper limit. If Advanced LIGO is optimized for detections at low frequencies, the event rate estimates would increase by a factor of ~ 3.5 .

We have also discussed four mechanisms by which such IMRI systems could form: i) binary hardening via 3-body interactions; ii) hardening via Kozai resonance; iii) direct capture; and iv) tidal capture of a main-sequence star. In all four cases, we find that the residual eccentricity when the inspiral enters the LIGO sensitivity band will be small. Finally, we have estimated the sensitivity of Advanced LIGO to the eccentricity of IMRI systems. We have found that the eccentricities we expect are negligible for data analysis, and therefore circular-orbit templates may be used to search for IMRI binaries in Advanced LIGO.

IMRIs are a somewhat speculative source of GWs, since evidence for the existence of IMBHs is not yet conclusive. The body of evidence is steadily growing, however. Since little is known about the abundance of IMBHs in the universe, the event rates presented here are naturally somewhat uncertain. However, our results are sufficiently promising to make IMRIs a source worth searching for in Advanced LIGO data. If IMRI events are detected with Advanced LIGO, these will provide irrefutable evidence for the existence of BHs with intermediate mass, and will provide information on the mass and spin of IMBHs, plus the eccentricities of the inspiraling objects. This information will be very useful for constraining models of IMBH formation and growth, and for exploring stellar dynamics in the centers of globular clusters.

3.6 Appendix A. Waveforms and Signal-to-Noise Ratio Calculation

To compute the range to which a source can be seen, as presented in § 3.3.1, we must evaluate the SNRs of typical sources. To do this requires a model of the waveform. In the weak field, waveforms may be well approximated by post-Newtonian results. The leading order post-Newtonian result takes the system to be a Keplerian binary and estimates the gravitational radiation from the leading-order quadrupole formula [70, 69]. This predicts $\tilde{h}(f) \propto f^{-7/6}\Theta(f - f_{\text{ISCO}})$, where the step function Θ is included to ensure the radiation cuts off at f_{ISCO} , the GW frequency at the innermost stable circular orbit of the binary. The post-Newtonian results are a weak field expansion and are only valid where velocities are much less than the speed of light. As a consequence, the leading order post-Newtonian waveforms over-predict the SNR of an IMRI source, since they effectively spend too many cycles at each frequency as the ISCO is approached.

An alternative GW model can be obtained from perturbation theory, by expanding in terms of the mass ratio, m/M , assumed to be small. The IMRI systems considered in this paper lie somewhere between these two extremes — the mass ratio is not quite small enough to use perturbative techniques, but the source spends a long time in the regime where post-Newtonian results are not valid. Waveform models have not yet been developed specifically for IMRI systems. However, by the time Advanced LIGO comes online, it is likely that models will have been constructed by combining post-Newtonian and perturbative techniques. This is discussed in more detail by [3]. If accurate waveforms are not available, we will require sources to have higher SNRs to be detected, thus reducing the ranges from the values that we quote. However, the loss in SNR from using an inaccurate template is likely to be only a few tens of percent [3], which is considerably smaller than the uncertainties in the astrophysical mechanisms that govern the event rates we are computing.

Out of the set of currently available waveform families, we believe the most accurate SNRs will come from the perturbative waveforms. Although the perturbative

waveform will not be a precise model of the true waveform, the total energy content of the GWs will be roughly correct since the perturbative methods use a reliable model of the spacetime close to the central BH. To generate the range estimates quoted in this paper, we therefore computed the SNR via a perturbative model, as described below.

Finn & Thorne [24] used perturbation theory to compute the SNR contributed by the lowest four harmonics of the orbital frequency for circular, equatorial inspirals into Kerr BHs. Their calculation is accurate in the sense that it is based on perturbation theory, but it relies on three assumptions: i) the orbit is in the extreme mass ratio limit, i.e., $m/M \ll 1$; ii) the orbit of the small body is circular; and iii) the orbit of the small body is equatorial. Assumption (ii) is valid for our case and assumption (i) is probably sufficiently accurate (the mass ratio here is intermediate while not extreme). Assumption (iii) is not necessarily valid, but we can derive results for both prograde and retrograde equatorial orbits from the Finn & Thorne [24] waveforms and then average over possible orbital inclinations of the inspiraling object by assuming the effect of averaging is the same as it is for the leading-order post-Newtonian model [58].

It is conventional to use m to denote harmonic number when discussing harmonics of the azimuthal frequency. However, in this paper we will use k to avoid confusion with the mass of the CO. The SNR contributed by the k th harmonic of the orbital frequency, $f_k = k\omega_{orb}/(2\pi)$, is given by [24]:

$$\rho_k^2 = \int \frac{[h_{c,k}(f_k)]^2}{f_k S_n(f_k)} d \ln f_k, \quad (3.34)$$

where $S_n(f)$ is the one-sided power spectral density of the detector noise, and $h_{c,k}(f_k)$ is the characteristic amplitude of the k th harmonic when it passes through frequency f_k . This reduces to the earlier expression (3.27) via the substitution $2\tilde{h}(f) = \sum_k h_{c,k}(f)/f$. The characteristic amplitude is related to the energy radiated to infin-

ity in each harmonic and is given by

$$h_{c,1} = \frac{5}{\sqrt{672\pi}} \frac{\sqrt{mM}}{r_o} \tilde{\Omega}^{1/6} \mathcal{H}_{c,1}, \quad (3.35)$$

$$h_{c,k} = \sqrt{\frac{5(k+1)(k+2)(2k+1)!k^{2k}}{12\pi(k-1)[2^k k!(2k+1)!!]^2}} \times \frac{\sqrt{mM}}{r_o} \tilde{\Omega}^{(2m-5)/6} \mathcal{H}_{c,m} \quad \text{for } m \geq 2 \quad (3.36)$$

Here $\tilde{\Omega} = GM\omega_{orb}/c^3$ is the dimensionless orbital angular frequency and r_o is the distance to the source. The relativistic correction, $\mathcal{H}_{c,k}$, can be written as

$$\mathcal{H}_{c,k} = \sqrt{\mathcal{N} \dot{\mathcal{E}}_{\infty k}}. \quad (3.37)$$

In this expression, \mathcal{N} is the relativistic correction to the number of cycles spent near a particular frequency, and $\dot{\mathcal{E}}_{\infty k}$ is the relativistic correction to the rate of energy lost to infinity in harmonic m . These corrections can be computed via integration of the Teukolsky-Sasaki-Nakamura equations and are tabulated in [24]. We note that the various corrections are defined relative to their Newtonian values.

Using the results of Finn & Thorne [24], we can compute the total SNR ρ_{tot} contributed by the lowest 4 harmonics of the orbital frequency from the time the source enters the detector band (when $f_4 = 10\text{Hz}$) until plunge, for various spins and masses of the central BH:

$$\rho_{\text{tot}} = \sqrt{\sum_{k=1}^4 \rho_k^2}. \quad (3.38)$$

This SNR was used to derive the range formulae presented in § 3.3.1. We can also compute the leading-order post-Newtonian SNR by including only the quadrupolar $k = 2$ mode, and setting the correction $\mathcal{H}_{c,2} = 1$. We find that for $\chi \lesssim 0.5$ and $50M_{\odot} < M < 250M_{\odot}$, the post-Newtonian SNR is typically an overestimate by a factor of ~ 1.4 . We note that the data in [24] does not extend to the full range of radii needed for these calculations. Where necessary, we extrapolated their results to larger radius using appropriate power laws. We have verified that the results are insensitive to the exact form of this extrapolation.

The simplest template to use to detect a circular inspiral would include only the

dominant, quadrupolar, component of the orbital frequency. It is useful to estimate how much SNR we would lose by ignoring higher harmonics. For circular inspirals in the equatorial plane of a Kerr BH, the fraction of the total energy radiated during an inspiral from infinity that is radiated between a certain Boyer-Lindquist radius r_i and plunge, effectively depends only on the ratio of the initial radius r_i to the radius of the innermost stable circular orbit, $r_i/r_{\text{isco}}(\chi)$ and is otherwise independent of χ . Here χ is the central BH spin as usual, and r_{isco} is the radius of the innermost stable circular orbit, as given in Eq. (3.17). The energy radiated in higher harmonics of the orbital frequency is suppressed relative to that in the dominant $k = 2$ harmonic by powers of M/r . As the BH spin increases $r_{\text{isco}}/M \rightarrow 1$ for prograde orbits, and so a larger fraction of the energy is radiated in the regime where $r \sim M$. We would therefore expect higher harmonics to contribute most significantly to the total energy flux for prograde inspirals into BHs with large spins. We computed the fraction of the total energy radiated into each harmonic as a function of the BH spin, while the particle inspirals from $r = 10 r_{\text{isco}}$ to $r = r_{\text{isco}}$. This is the range of radii for which Finn & Thorne [24] tabulate data and in this range $\sim 85\%$ of the total energy is radiated in any circular equatorial inspiral. The energy fractions are shown in Figure 3.5. We see that for $|\chi| \lesssim 0.3$, which is the expected IMBH spin range if the IMBH grows via minor mergers, $\sim 8\%$ of the energy is radiated into harmonics other than the dominant $k = 2$ harmonic, and most of this energy goes into the $k = 3$ harmonic.

The contribution of a harmonic to the signal-to-noise ratio of a source depends not only on the energy that goes into that harmonic, but also on the shape of the noise curve — higher harmonics enter the detector band earlier, contribute their signal at frequencies where the noise power spectral density is lower, and therefore have an enhanced contribution to the SNR. Figure 3.6 shows the relative SNR contributed by each harmonic, defined as ρ_k/ρ_{tot} , as a function of IMBH mass, for various IMBH spins. Note that this result does not depend on the mass of the inspiraling CO, since we are working in the extreme mass ratio limit. We see that for prograde inspirals, we can lose $\sim 10 - 25\%$ of the SNR by using templates containing the $k = 2$ mode only, but this is mostly recovered by including the $k = 3$ mode in the search templates. (We

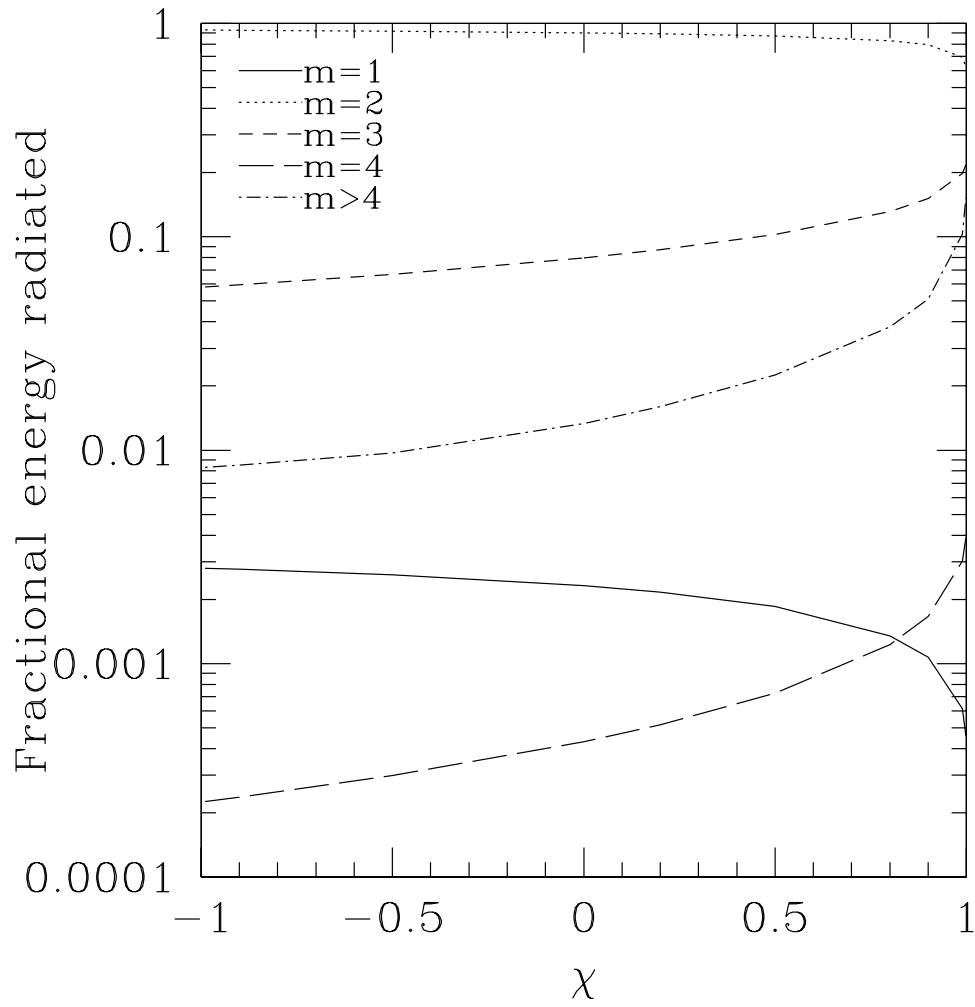


Figure 3.5: Fraction of the total energy radiated into each harmonic of the orbital frequency as the particle inspirals in a circular equatorial orbit from $10r_{\text{isco}}$ to r_{isco} . This energy fraction is shown as a function of BH spin.

can lose up to $\sim 50\%$ of the SNR by using simple templates for retrograde inspirals into high mass IMBHs, but the SNRs for such events are very small, making their detection unlikely.)

The SNRs computed from these perturbative waveforms are not totally accurate for the reasons given earlier. Corrections will include finite-mass effects, contributions from the spin of the small BH and the effect of $k > 4$ harmonics of the orbital frequency. It is clear from Figure 3.5 that for larger spins, a significant amount of energy goes into harmonics with $k > 4$. These harmonics spend even longer in band and so their inclusion would increase the SNR. However, we cannot compute their contribution to the SNR since [24] do not tabulate these contributions separately. Overall, the SNRs computed here should be accurate to $\sim 10\%$ and will be more accurate than those computed from the leading order post-Newtonian waveforms.

3.7 Appendix B. Ringdowns

Following the coalescence of an IMBH with a CO, the BH enters the ringdown phase, characterized by oscillations of its quasinormal modes, particularly the dominant $l = m = 2$ mode. For IMRIs, the total energy emitted in GWs during the ringdown is $\sim 0.5m^2/M$ [27], which is a factor of $O(m/M)$ smaller than the total energy emitted over the inspiral. However, the ringdown GW frequency [20],

$$f \approx \frac{1}{2\pi M} [1 - 0.63(1 - \chi)^{0.3}], \quad (3.39)$$

is higher than the ISCO frequency, and is therefore closer to the minimum of the Advanced LIGO noise power spectral density for the typical masses under consideration. For this reason, ringdowns may be detectable by Advanced LIGO despite their lower energy content. This is particularly true if $m \gtrsim 10 M_\odot$ BHs, rather than NSs, are common as inspiraling companions, since the range for ringdowns scales as m^2 at low redshifts. Moreover, ringdowns will be the only way to detect CO coalescences with slowly-spinning IMBHs with masses above $350 M_\odot$, since inspirals into such massive

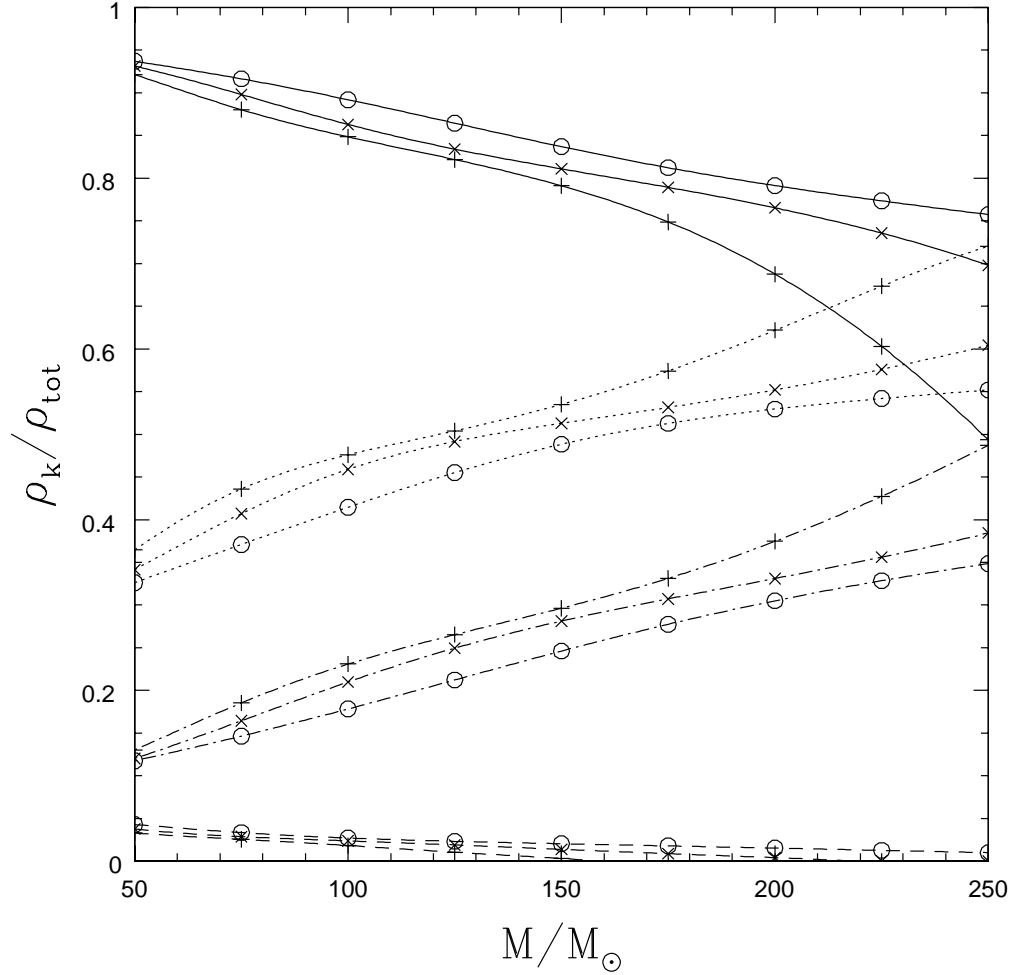


Figure 3.6: SNR contributed by the lowest four harmonics of the orbital frequency, as a function of the central BH mass, for circular equatorial orbits. The harmonics are indicated by different line styles — $k = 1$ (dashed), $k = 2$ (solid), $k = 3$ (dotted) and $k = 4$ (dot-dash). Curves are shown for three different BH spins, $\chi = 0$, $\chi = 0.5$ and $\chi = -0.5$ (i.e., retrograde inspirals into a $\chi = 0.5$ BH), indicated by different symbols - crosses, circles and pluses respectively.

IMBHs will produce GWs at frequencies below the detector low-frequency limit.

The typical Advanced LIGO ringdown-wave ranges (in terms of luminosity distance) as a function of IMBH mass are plotted in Fig. 3.7 for several choices of inspiraling object mass and IMBH spin. Because some ranges reach out to significant redshifts (up to $z \sim 0.5$), the effect of redshifting is already included in these ranges, unlike in Fig. 3.3. Redshifting also explains why the range does not scale strictly as m^2 , as high redshifts bring the GW frequency at the detector down into the region where the interferometer is less sensitive.

The astrophysical rate of ringdowns per cluster is greater than or equal to the rate of IMRIs, since every IMRI culminates in a merger and ringdown (but ringdowns could follow coalescences without observable inspirals, i.e., those with direct plunges). The distance sensitivity to ringdowns following inspirals of $1.4 M_\odot$ NSs is probably too low to make them detectable by Advanced LIGO: the total detectable event rate for NS–IMBH ringdowns is ~ 20 times lower than the event rate for NS–IMBH inspirals if the IMBH mass is $M = 100 M_\odot$ and spin is $\chi = 0.3$. However, Advanced LIGO will be considerably more sensitive to ringdowns than to inspirals in other mass ranges. For example, ringdowns from $10 M_\odot + 300 M_\odot$ coalescences could be detected in a volume ~ 200 times greater than the detection volume for inspirals from these coalescences; if all IMBHs had mass $M = 300 M_\odot$, and all COs were $m = 10 M_\odot$ BHs with coalescence rate equal to $\approx 5 \times 10^{-9}$ per year per cluster as in § 3.2.1, then the total detectable IMRI ringdown event rate would reach ~ 50 per year. Thus, if our expectations about the likely masses involved in IMRIs are incorrect, and coalescences of COs with higher masses with more massive IMBHs are common, searches for ringdown waves can provide a useful back-up to IMRI searches.

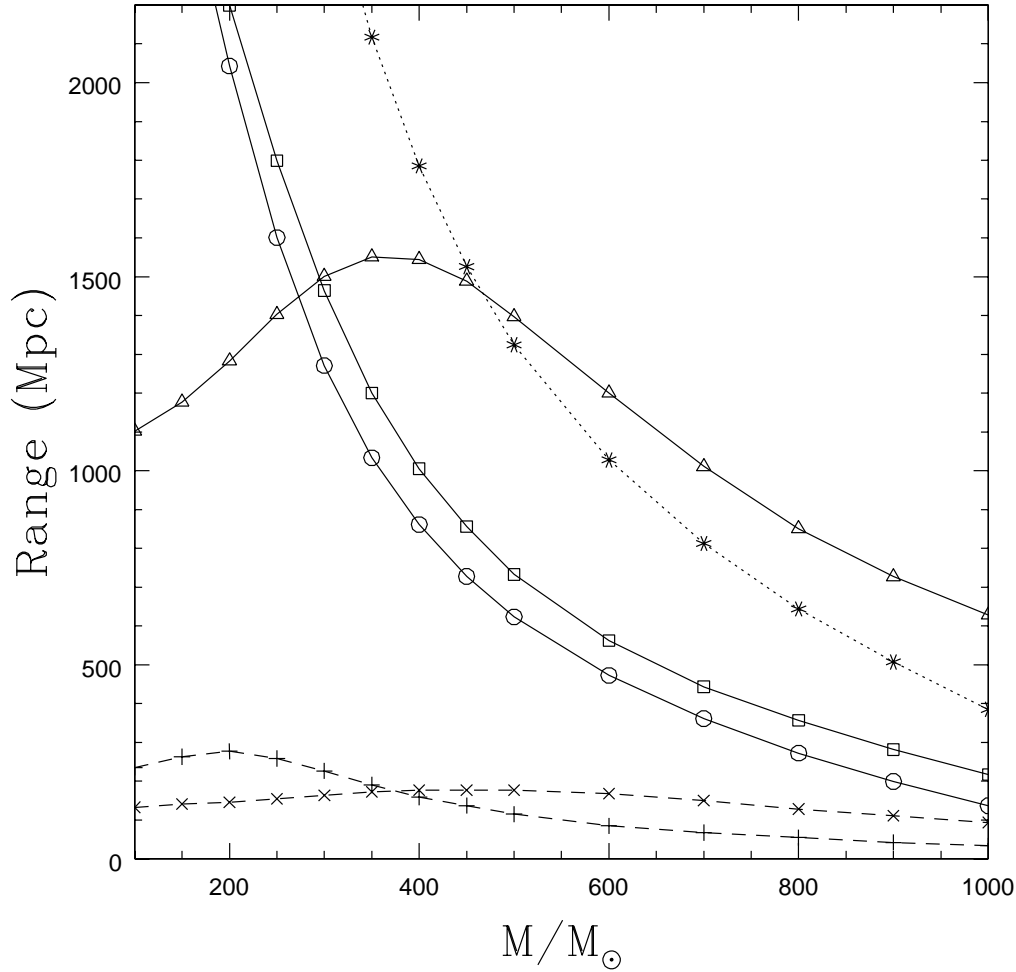


Figure 3.7: Range of a network of three Advanced LIGO detectors for the ringdown of an IMBH following a merger with a CO. The luminosity-distance range in Mpc is plotted as a function of IMBH mass M ; cosmological redshift is included. Dashed lines denote $m = 1.4 M_{\odot}$ inspiraling NSs, with pluses corresponding to IMBH spin $\chi = 0.3$ and crosses to $\chi = 1$. Solid lines denote $m = 10 M_{\odot}$ inspiraling BHs, with circles, squares, and triangles corresponding to spins $\chi = 0$, $\chi = 0.3$, and $\chi = 1$, respectively. Dotted line with stars denotes $m = 20 M_{\odot}$ BHs spiraling into an IMBH with spin $\chi = 0.3$.

Bibliography

- [1] Abbott, B., et al. (LIGO Scientific Collaboration). 2005, arXiv:0704.3368
- [2] Allen, B., Anderson, W. G., Brady, P. R., Brown, D. A., & Creighton, J. D. E. 2005, arXiv:gr-qc/0509116
- [3] Amaro-Seoane, P., Gair, J. R., Freitag, M., Miller, M. C., Mandel, I., Cutler, C. J. & Babak, S. 2007, *Class. Quant. Grav.*, 24, R113
- [4] Apostolatos, T. A. 1996, *Phys. Rev. D*, 52, 605
- [5] Babak, S. V., Fang, H., Gair, J. R., Glampedakis, K., & Hughes, S. A. 2007, *Phys. Rev. D*, 75, 024005
- [6] Bahcall, J. N., & Wolf, R. A. 1976, *ApJ*, 209, 214
- [7] Baker, J. G., Boggs, W. D., Centrella, J., Kelly, B. J., McWilliams, S. T., Miller, M. C., & van Meter, J. 2007, *ApJ*, submitted (arXiv:astro-ph/0702390)
- [8] Baker, J. G., Centrella, J., Choi, D.-I., Koppitz, M., van Meter, J. R., & Miller, M. C. 2006, *ApJ*, 653, L93
- [9] Bardeen, J. M., Press, W. H., & Teukolsky, S. A. 1972, *ApJ*, 178, 347
- [10] Barish, B. C., & Weiss, R. 1999, *Phys. Today*, 52, 44
- [11] Bekenstein, J. D. 1973, *ApJ*, 183, 657
- [12] Bellazzini, M., Fusi Pecii, F., Montegriffo, P., Messineo, M., Monaco, L. & Rood, R. T. 2002, *Astron. J.*, 123, 1509

- [13] Blanchet, L., Qusailah, M. S. S., & Will, C. M. 2005, *ApJ*, 635, 508
- [14] Brown, D. A., Brink, J., Fang, H., Gair, J. R., Li, C., Lovelace, G., Mandel, I., & Thorne, K. S. 2007, *Phys. Rev. Lett*, 99, 201102
- [15] Campanelli, M., Lousto, C. O., Zlochower, Y., & Merritt, D. 2007a, *ApJ*, 659, L5
- [16] Campanelli, M., Lousto, C. O., Zlochower, Y., & Merritt, D. 2007b, *Phys. Rev. Lett*, 98, 231102
- [17] Cutler, C., & Flanagan, E. E. 1994, *Phys. Rev. D*, 49, 2658
- [18] Damour, T., & Gopakumar, A. 2006, *Phys. Rev. D*, 73, 124006
- [19] Ebisuzaki, T., et al. 2001, *ApJ*, 562, L19
- [20] Echeverria, F. 1988, *Phys. Rev. D*, 40, 3194
- [21] Favata, M., Hughes, S. A., & Holz, D. E. 2004, *ApJ*, 607, L5
- [22] Finn, L. S. 1987, *MNRAS*, 227, 265
- [23] Finn, L. S., & Chernoff, D. F. 1993, *Phys. Rev. D*, 47, 2198
- [24] Finn, L. S., & Thorne, K. S. 2000, *Phys. Rev. D*, 62, 124021
- [25] Fitchett, M. J. 1983, *MNRAS*, 203, 1049
- [26] Fitchett, M. J., & Detweiler, S. 1984, *MNRAS*, 211, 933
- [27] Flanagan, E. E., & Hughes, S. A. 1998, *Phys. Rev. D*, 57, 4535
- [28] Flanagan, E. E., & Racine, E. 2007, *Phys. Rev. D*, 75, 044001
- [29] Fregeau, J. M., Larson, S. L., Miller, M. C., O'Shaughnessy, R., & Rasio, F. A. 2006, *ApJ*, 646, L135
- [30] Freitag, M., 2003, *ApJ*, 583, L21

- [31] Freitag, M., Gürkan, M. A., & Rasio, F. A. 2006, MNRAS, 368, 141
- [32] Freitag, M., Rasio, F. A., & Baumgardt, H. 2006, MNRAS, 368, 121
- [33] Friedman, J. L., & Schutz, B. F. 1978, ApJ, 221, 937
- [34] Fritschel, P. 2003, arXiv:gr-qc/0308090
- [35] Fryer, C. L., & Kalogera, V. 2001, ApJ, 554, 548
- [36] Gair, J. R., & Glampedakis, K. 2006, Phys. Rev. D, 73, 064037
- [37] Gonzalez, J. A., Sperhake, U., Bruegmann, B., Hannam, M., & Husa, S. 2007a, Phys. Rev. Lett, 98, 091101
- [38] Gonzalez, J. A., Hannam, M. D., Sperhake, U., Brüggmann, B., & Husa, S. 2007b, Phys. Rev. Lett, 98, 231101
- [39] Gültekin, K., Miller, M. C., & Hamilton, D. P. 2004, ApJ, 616, 221
- [40] Gültekin, K., Miller, M. C., & Hamilton, D. P. 2006, ApJ, 640, 156
- [41] Gürkan, M. A., Fregeau, J. M., & Rasio, F. A. 2006, ApJ, 640, L39
- [42] Gürkan, M. A., Freitag, M., & Rasio, F. A. 2004, ApJ, 604, 632
- [43] Hoggie, D. C. 1975, MNRAS, 173, 729
- [44] Hoggie, D. C., Trenti, M., & Hut, P. 2006, MNRAS, 368, 677
- [45] Herrmann, F., Hinder, I., Shoemaker, D., & Laguna, P. 2007a, Class. Quant. Grav., 24, 33
- [46] Herrmann, F., Hinder, I., Shoemaker, D., Laguna, P., & Matzner, R. A. 2007b, ApJ, 661, 430
- [47] Ho, W. C. G. & Lai, D. 1999, MNRAS, 308, 153
- [48] Hopman, C., & Alexander, T. 2005, ApJ, 629, 362

- [49] Hopman, C., & Portegies Zwart, S. F. 2005, MNRAS Lett., 363, L56
- [50] Hopman, C., Portegies Zwart, S. F., & Alexander, T. 2004, ApJ, 604, L101
- [51] Hughes, S. A., & Blandford, R. D. 2003, ApJ, 585, L101
- [52] Hurley, J. R. 2007, MNRAS, 379, 93
- [53] Innanen, K. A., Zheng, J. Q., Mikkola, S., & Valtonen, M. J. 1997. AJ, 113 (5), 1915
- [54] Koppitz, M., Pollney, D., Reisswig, C., Rezzolla, L., Thornburg, J., Diener, P., & Schnetter, E. 2007, arXiv:gr-qc/0701163
- [55] Kozai, Y. 1962, AJ, 67, 591
- [56] Kulkarni, S. R., Hut, P., & McMillan, S. L. W. 1993, Nature, 364, 421
- [57] Madau, P., & Rees, M. J. 2001, ApJ, 551, L27
- [58] Mandel, I. 2007, ApJ, submitted, arXiv:0707.0711
- [59] Martel, K., & Poisson, E. 1999, Phys. Rev. D, 60, 124008
- [60] Miller, M. C. 2002, ApJ, 581, 438
- [61] Miller, M. C., & Colbert, E. J. M. 2004, IJMPD, 13, 1
- [62] Miller, M. C., & Hamilton, D. P. 2002a, MNRAS, 330, 232
- [63] Miller, M. C., & Hamilton, D. P. 2002b, ApJ, 576, 894
- [64] Mouri, H., & Taniguchi, Y. 2002a, ApJ, 566, L17
- [65] Mouri, H., & Taniguchi, Y. 2002b, ApJ, 580, 844
- [66] O'Leary, R., O'Shaughnessy, R., & Rasio, F. A. 2007, PRL, submitted (arXiv:astro-ph/0701887)

- [67] O’Leary, R. M., Rasio, F. A., Fregeau, J. M., Ivanova, N., & O’Shaughnessy, R. 2006, *ApJ*, 637, 937
- [68] Peres, A. 1962, *Phys. Rev.*, 128, 2471
- [69] Peters, P. C. 1964, *Phys. Rev. B*, 136, 1224
- [70] Peters, P. C., & Mathews, J. 1963, *Phys. Rev.*, 131, 435
- [71] Phinney, E. S. 1991, *ApJ*, 380, L17
- [72] Phinney, E. S. 2005, private communication
- [73] Portegies Zwart, S., Baumgardt, H., Hut, P., Makino, J., & McMillan, S. L. W. 2004, *Nature*, 428, 724
- [74] Portegies Zwart, S., & McMillan, S. L. W. 2000, *ApJ*, 528, L17
- [75] Portegies Zwart, S., & McMillan, S. L. W. 2002, *ApJ*, 576, 899
- [76] Press, W. H., & Teukolsky, S. A. 1977, *ApJ*, 213, 183
- [77] Pryor, C., & Meylan, G. 1993, in *Structure and Dynamics of Globular Clusters.*, eds. Djorgovski S. G., Meylan G. (San Francisco: ASP), vol. 50, p. 357
- [78] Quinlan, G. D. 1996, *New Astronomy* 1, 35
- [79] Quinlan, G. D., & Shapiro, S. L. 1987, *ApJ*, 321, 199
- [80] Quinlan, G. D., & Shapiro, S. L. 1989, *ApJ*, 343, 725
- [81] Redmount, I. H., & Rees, M. J. 1989, *Commun. Astrophys.*, 14, 165
- [82] Reisenegger, A., & Goldreich, P. 1992, *ApJ*, 395, 240
- [83] Rubenstein, E. P., & Bailyn, C. D. 1997, *ApJ*, 474, 701
- [84] Sigurdsson, S., & Hernquist L. 1993, *Nature*, 364, 423
- [85] Sopena, C. F., Yunes, N., & Laguna, P. 2007, *ApJ*, 656, L9

- [86] Taniguchi, Y., Shioya, Y., Tsuru, T. G., & Ikeuchi, S. 2000, PASJ, 52, 533
- [87] Thorne, K. S., in *Three hundred years of gravitation*, edited by S. W. Hawking and W. Israel (Cambridge University Press, Cambridge, 1987), chap. 9, pp. 330–458
- [88] Trenti, M. 2006, arXiv:astro-ph/0612040
- [89] Trenti, M., Ardi, E., Mineshige, S., & Hut, P. 2007, MNRAS, 374, 857
- [90] Trenti, M., Hoggie, D. C., & Hut, P. 2007, MNRAS, 374, 344
- [91] Vallisneri, M. 2000, Phys. Rev. Lett, 84, 3519
- [92] Wainstein, L. A., & Zubakov, V. D. 1962, "Extraction of signals from noise", Prentice-Hall, Englewood Cliffs, NJ
- [93] Wen, L. 2002, ApJ, 598, 419
- [94] Wiseman, A. G. 1992, Phys. Rev. D, 46, 1517

Chapter 4

Spin Distribution Following Minor Mergers and the Effect of Spin on the Detection Range for Low-Mass-Ratio Inspirals

We compute the probability distribution for the spin of a black hole following a series of minor mergers with isotropically distributed, non-spinning, inspiraling compact objects. By solving the Fokker-Planck equation governing this stochastic process, we obtain accurate analytical fits for the evolution of the mean and standard deviation of the spin distribution in several parameter regimes. We complement these analytical fits with numerical Monte-Carlo simulations in situations when the Fokker-Planck analysis is not applicable. We find that a $\sim 150 M_{\odot}$ intermediate-mass black hole that gained half of its mass through minor mergers with neutron stars will have dimensionless spin parameter $\chi = a/M \sim 0.2 \pm 0.08$. We estimate the effect of the spin of the central black hole on the detection range for intermediate-mass-ratio inspiral (IMRI) detections by Advanced LIGO and extreme-mass-ratio inspiral (EMRI) detections by LISA. We find that for realistic black hole spins, the inclination-averaged Advanced-LIGO IMRI detection range may be increased by up to 10% relative to the range for IMRIs into non-spinning intermediate-mass black holes. For LISA, we find that the detection range for EMRIs into $10^5 M_{\odot}$ massive

black holes (MBHs) is not significantly affected by MBH spin, the range for EMRIs into $10^6 M_\odot$ MBHs is affected at the $\lesssim 10\%$ level, and EMRIs into maximally spinning $10^7 M_\odot$ MBHs are detectable to a distance ~ 25 times greater than EMRIs into non-spinning black holes. The resulting bias in favor of detecting EMRIs into rapidly spinning MBHs will play a role when extracting the MBH spin distribution from EMRI statistics.

4.1 Introduction

A growing body of evidence from observations, numerical simulations, and comparisons between the two, suggests the existence of a population of intermediate-mass black holes with masses in the $M \sim 10^2 - 10^4 M_\odot$ range (e.g., Miller & Colbert [9] and references therein). These intermediate-mass black holes may capture compact objects (stellar-mass black holes or neutrons stars) and merge with them [17, 10, 11, 13, 14, 3, 4, 15, 7]. In addition to adding to the black-hole mass, the merging compact objects will also contribute their orbital angular momentum to the spin angular momentum of the central black hole, leading to the evolution of the black-hole spin through a sequence of such minor mergers.

We might expect the typical spin of a black hole to be low if a significant fraction of its mass has been added via minor mergers with compact objects whose angular momentum at plunge is distributed isotropically. The angular momentum imparted to the black hole of mass M by a compact object of mass m is $L_{\text{obj}} \propto mM$. (We include only the orbital angular momentum, not the spin angular momentum of the compact object, since the latter is lower than the former by a factor of order m/M , which we assume to be small for minor mergers.) This causes the dimensionless spin parameter of the hole $\chi \equiv S_1/M^2 = a/M$ to change by $\sim L_{\text{obj}}/M^2 \propto m/M$. After $N \sim M/m$ such mergers, necessary for the hole to grow to mass M , the typical dimensionless spin parameter of the hole will be $\chi \propto (m/M)\sqrt{N} \sim \sqrt{m/M}$.

As discussed by Miller [8] and Hughes & Blandford [6], the angular momenta of black holes that grow through minor mergers undergo a damped random walk. The

damping comes about because retrograde orbits, which subtract angular momentum from a black hole, plunge from a last stable orbit (LSO) at a higher radius than prograde orbits, so more angular momentum is subtracted following retrograde inspirals than is added following prograde ones.

In this chapter, we make an analytical approximation to the spin change induced by a minor merger and solve the Fokker-Planck equation to obtain the evolution of the spin probability distribution [6]. (We use a simpler one-dimensional version of the Fokker-Planck equation than Hughes & Blandford [6], since we are interested only in the evolution of the magnitude of the spin, not its direction.) We find that for black holes with $\chi \gg \sqrt{m/M}$, the spin χ evolves proportionally to $M^{-2.63}$ as the mass grows via minor mergers (rather than M^{-2} , which would be the case without damping). We determine the asymptotic values of the expected mean of the spin distribution and its standard deviation in the limit of infinitely many minor mergers: $\bar{\chi} \rightarrow \sqrt{1.5m/M}$ and $\sigma \rightarrow \sqrt{0.7m/M}$. We also describe the evolution of the spin distribution in other parameter regimes, e.g., when $\sqrt{m/M} \gg \chi \gg m/M$.

Our Fokker-Planck analysis fails when the mass ratio m/M is not sufficiently low, so for those cases we resort to Monte-Carlo numerical simulations. We find that if the mass of the central black hole grows from $M = 5m$ to $M = 10m$ by capturing five objects of equal mass m , the mean spin of the resulting black hole is $\bar{\chi} \approx 0.5$, nearly independent of its initial spin (Miller obtained similar results [8]). However, if the central black hole grows from $M = 50m$ to $M = 100m$ (e.g., a $M = 70 M_{\odot}$ black hole growing to $M = 140 M_{\odot}$ by capturing fifty $m = 1.4 M_{\odot}$ neutron stars), its resulting spin is rather low, $\chi \sim 0.2 \pm 0.08$.

The combination of the spin of the central black hole and the inclination of the inspiraling object's orbit can have a significant effect on the gravitational-wave signal from a low-mass-ratio inspiral. We compute the increase in the Advanced-LIGO detection range for intermediate-mass-ratio inspirals (IMRIs) due to the spin of the central black hole. We find that the detection range, averaged over orbital inclinations, may increase by $\sim 3 - 10\%$ relative to the range for inspirals into non-spinning black holes for the expected values of black hole mass and spin. We provide an

approximate expression for the dependence of the Advanced-LIGO IMRI detection range on spin [see Eq. (4.24)]. We also compute the change in the LISA extreme-mass-ratio-inspiral (EMRI) detection range due to the spin of the massive black hole. We find that the range for inspirals into $M = 10^5 M_\odot$ black holes is nearly independent of their spin, because the frequency at the last stable orbit (LSO) is away from the minimum of the LISA noise curve. On the other hand, the inclination-averaged detection range for IMRIs into rapidly spinning $M = 10^7 M_\odot$ black holes is ~ 25 times greater than into non-spinning ones. The detection volumes are proportional to the cube of the range. This will create a bias in favor of detecting inspirals into rapidly spinning black holes, which in turn will have consequences for the extraction of massive-black-hole spin function from LISA EMRI statistics.

This chapter is organized as follows. In Sec. 4.2, we provide the background for our calculation of the spin evolution via minor mergers. In Sec. 4.3, we describe analytical solutions of the Fokker-Planck equation for spin evolution. (In Appendix 4.6, for reference we show a quick informal derivation of the Fokker-Planck equation.) In Sec. 4.4, we describe Markov-Chain numerical simulations of spin evolution. In Sec. 4.5, we evaluate the dependence of the detection ranges for low-mass-ratio inspirals averaged over orbital inclination angles on the spin of the massive body, in the context of both Advanced LIGO and LISA.

4.2 Spin Evolution

We assume that the distribution of the orbital inclination angle ι relative to the central black hole's spin is isotropic at capture. Here ι is defined via

$$\cos \iota = \frac{L_z}{\sqrt{L_z^2 + Q}}, \quad (4.1)$$

L_z is the object's orbital angular momentum in the direction of the black hole's spin, and Q is the Carter constant. We further assume that the inclination angle ι remains approximately constant over the inspiral [5], so the distribution of inclinations at the

LSO is also isotropic, $\Pr(\cos \iota) = 1/2$.

In the low-mass-ratio limit, the amount of angular momentum radiated in gravitational waves during the plunge and ringdown is smaller by a factor of $\sim m/M$ than the angular momentum at the LSO. Therefore, we assume that the merging object contributes its orbital angular momentum at the LSO to the angular momentum of the black hole. The spin of the black hole after a minor merger, χ' , is related to the original spin χ via

$$\chi' \approx \frac{1}{(M+m)^2} \sqrt{(\chi M^2 + L_z)^2 + Q}, \quad (4.2)$$

where m is the mass of the small object, M is the mass of the hole, and we assume $m \ll M$.

The constants of motion L_z and Q at the LSO can be obtained as a function of ι by demanding that the potential R and its first and second derivatives in r are zero at the LSO (see Chapter 33 of [12]):

$$\begin{aligned} R &= [E(r^2 + \chi^2 M^2) - L_z \chi M]^2 - (r^2 - 2Mr + \chi^2 M^2) [m^2 r^2 + (L_z - \chi M E)^2 + Q], \\ R &= 0, \quad \frac{dR}{dr} = 0, \quad \frac{d^2 R}{dr^2} = 0 \quad \text{at LSO.} \end{aligned} \quad (4.3)$$

It is possible to make analytic approximations to the values of L_z and Q at the LSO based on appropriately averaging the analytically known constants of motion at the LSO for prograde and retrograde equatorial orbits (cf. Eq. (9) of [6]). In particular, for $\chi \ll 1$, the plunging object's dimensionless ‘‘total angular momentum’’ is given by

$$\hat{L} = \frac{\sqrt{L_z^2 + Q}}{Mm} \approx Mm\sqrt{12} \left[1 - \frac{1}{2} \left(\frac{2}{3} \right)^{3/2} \chi \cos \iota \right], \quad (4.4)$$

where we correct a mistake in Eq. (4) of [8]. Then L_z and Q follow from Eq. (4.1):

$$L_z = \cos \iota \sqrt{L_z^2 + Q}; \quad Q = \sin \iota \sqrt{L_z^2 + Q}. \quad (4.5)$$

4.3 Fokker-Planck Equation for Spin Evolution

The black-hole spin evolution is a stochastic process. The probability distribution function of a stochastic process, however, can be described by a deterministic equation, the Fokker-Planck equation (see Appendix 4.6 for a quick derivation):

$$\frac{\partial}{\partial t} f(x, t) = -\frac{\partial}{\partial x} [\mu(x, t)f(x, t)] + \frac{1}{2} \frac{\partial^2}{\partial x^2} [\sigma^2(x, t)f(x, t)], \quad (4.6)$$

where $\mu = \langle dx \rangle / dt$ is the mean drift and $\sigma^2 = \langle (dx)^2 \rangle / dt$ is the stochastic variance. In this Section, we derive approximate analytical solutions to the Fokker-Planck equation in several interesting parameter regimes.

For simplicity, assume that all merging objects have the same mass m . We parametrize the mass of the black hole by a dimensionless “time” parameter $t = M/m$. The change in the spin χ after a merger follows from Eq. (4.2):

$$d\chi = \frac{1}{(t+1)^2} \sqrt{\chi^2 t^4 + \hat{L}^2 t^2 + 2\chi \hat{L} t^3 \cos \iota} - \chi. \quad (4.7)$$

We can compute \hat{L} at plunge as a function of χ and $\cos \iota$ by solving Eqs. (4.3), then substituting the result into Eq. (4.7) to obtain $d\chi$ as a function of t , χ , and $\cos \iota$. Although this process is simple in principle, such a numerical computation makes it impossible to obtain analytic expressions for $\langle d\chi \rangle$ and $\langle (d\chi)^2 \rangle$, which are necessary if we wish to solve the Fokker-Planck equation. (Here, brackets denote averaging over $\cos \iota$.)

We could, of course, try to obtain empirical analytic fits to the numerical solutions for $\langle d\chi \rangle$ and $\langle (d\chi)^2 \rangle$, but it turns out that there is a simpler approach. The approximate formula for \hat{L} given in Eq. (4.4) is valid only when $\chi \ll 1$; when $\chi \sim 1$, Eq. (4.4) overestimates \hat{L} by as much as 40%. Remarkably, however, using this incorrect approximation for \hat{L} in Eq. (4.7) generally yields very accurate expressions for $\langle d\chi \rangle$ for a wide range of χ . So long as $\chi t \gg 1$ (i.e., $\chi \gg m/M$), an expansion of Eq. (4.7) to the first order in $1/(\chi t)$ yields the following simple analytic expression

for the mean drift in χ :

$$\mu(\chi, t) = \frac{\langle d\chi \rangle}{dt} = \frac{\chi}{t} \left(-2 - \frac{4\sqrt{2}}{9} \right) + \frac{4}{\chi t^2}. \quad (4.8)$$

This expression is accurate to about 1% for all values of χ so long as $\chi t \gtrsim 10$. Similarly, the analytic expression for the stochastic variance of the spin is

$$\sigma^2(\chi, t) = \frac{\langle (d\chi)^2 \rangle}{dt} = \frac{4}{t^2} \left(1 + \frac{4\sqrt{2}\chi^2}{9} - \chi^2 \right). \quad (4.9)$$

This expression underestimates the variance by $\gtrsim 10\%$ for very high spins, but is generally accurate to a few percent for lower spins which are expected as a consequence of minor mergers in the Advanced LIGO setting.

We can now substitute Eqs. (4.8) and (4.9) into the Fokker-Planck equation for the probability evolution (4.6) to obtain

$$\begin{aligned} \frac{\partial}{\partial t} f(\chi, t) &= -\frac{\partial}{\partial \chi} \left[\frac{\chi}{t} \left(-2 - \frac{4\sqrt{2}}{9} + \frac{4}{\chi^2 t} \right) f(\chi, t) \right] \\ &+ \frac{1}{2} \frac{\partial^2}{\partial \chi^2} \left[\frac{4}{t^2} \left(1 + \frac{4\sqrt{2}\chi^2}{9} - \chi^2 \right) f(\chi, t) \right]. \end{aligned} \quad (4.10)$$

This is a one-dimensional equation unlike the three-dimensional equation derived in [6], since we choose to focus on the evolution of the magnitude of the spin, not its direction. Still, this is a rather complicated equation that does not easily separate. Fortunately, for many applications it is not necessary to solve the complete equation.

Equation (4.10) was derived under the assumption $\chi t \gg 1$. If we further assume that $\chi^2 t \gg 1$ (i.e., $\chi \gg \sqrt{m/M}$), then the mean spin evolution is dominated by

$$\frac{d\bar{\chi}}{dt} \approx a \frac{\bar{\chi}}{t}, \quad (4.11)$$

where $a \equiv -2 - 4\sqrt{2}/9 \approx -2.63$. (This result can also be obtained directly from

Eq. (4.8).) Thus, the mean spin evolves according to

$$\bar{\chi} \approx \bar{\chi}_0 \left(\frac{t}{t_0} \right)^a \approx \bar{\chi}_0 \left(\frac{M_0}{M} \right)^{2.63} \quad (4.12)$$

(compare with Eq. (26) of [6], where the exponent is approximated by 2.4).

If the assumption $\chi^2 t \gg 1$ is not satisfied, and instead $\chi^2 t \ll 1$, but $\chi t \gg 1$ so that Eq. (4.10) still holds, the evolution of the probability function may be approximated as

$$\frac{\partial f(t, \chi)}{\partial t} = -\frac{\partial}{\partial \chi} \left(\frac{4f(t, \chi)}{\chi t^2} \right) + \frac{1}{2} \frac{\partial^2}{\partial \chi^2} \left(\frac{4f(t, \chi)}{t^2} \right). \quad (4.13)$$

This equation can be solved by separation of variables: $f(t, \chi) = T(t)X(\chi)$, where the solution for T is $T(t) = \exp(-k/t)$, X is the solution to

$$2\chi^2 X'' - 4\chi X' + 4X - k\chi^2 X = 0, \quad (4.14)$$

and k is a constant. The mean spin grows roughly as

$$\bar{\chi} \sim \sqrt{\frac{2}{t_0} - \frac{2}{t}}, \quad (4.15)$$

so after $t \gtrsim 2t_0$ (i.e., after the black hole captures half its mass via minor mergers), $\chi^2 t \gtrsim 1$.

The spin growth and spin decay terms in Eq. (4.10) cancel when the spin is approximately equal to

$$\bar{\chi} \rightarrow \sqrt{\frac{4}{-at}} \approx \sqrt{\frac{1.5}{t}}. \quad (4.16)$$

(Compare with Miller [8], who estimated the mean spin to be $\sqrt{2}\sqrt{(m/M)} = \sqrt{2/t}$ based on numerical simulations.)

We can estimate the second moment of the probability distribution by approximating the solution to Eq. (4.10) by a Gaussian (as suggested by Miller [8]):

$$f(\chi, t) = \frac{1}{\sqrt{2\pi}\sigma} \exp \left[-\frac{(\chi - \bar{\chi}(t))^2}{2\sigma^2(t)} \right]. \quad (4.17)$$

(A Gaussian turns out to be a good approximation except at small $\bar{\chi}$, when the tails at $\chi > \bar{\chi}$ are larger than those at $\chi < \bar{\chi}$.) Substituting this Gaussian into Eq. (4.10), keeping only the lowest-order terms in $t\chi$, and setting $\chi = \bar{\chi}$, we obtain

$$-\frac{1}{\sigma} \frac{d\sigma}{dt} = -\frac{a}{t} - \frac{2}{t^2\sigma^2}(1 + b\bar{\chi}^2), \quad (4.18)$$

where $b \equiv 4\sqrt{2}/9 - 1$. If $\sigma^2 t \gg 1$, then σ evolves in the same way as $\bar{\chi}$ when $\chi^2 t \gg 1$:

$$\sigma \approx \sigma_0 \left(\frac{t}{t_0}\right)^a \approx \sigma_0 \left(\frac{M_0}{M}\right)^{2.63}. \quad (4.19)$$

What if $\sigma^2 t \ll 1$? This might be the case of interest if, say, the initial spin of a black hole created during some process is known precisely, and we wish to estimate future spin evolution through minor mergers. In this case, the second term on the right-hand side of Eq. (4.18) dominates, and if $\bar{\chi}$ is small or does not change significantly, σ grows according to

$$\sigma \approx \sqrt{4(1 + b\bar{\chi}^2) \left(\frac{1}{t_0} - \frac{1}{t}\right) + \sigma_0^2}. \quad (4.20)$$

In either case, σ asymptotes to the solution

$$\sigma \rightarrow \sqrt{\frac{2(1 + b\bar{\chi}^2)}{-at}}. \quad (4.21)$$

For large t , $\sigma \sim \sqrt{2/(-at)} \approx \sqrt{0.7/t}$; Miller [8] estimated σ to be $\sqrt{(m/M)}/\sqrt{2} = \sqrt{1/(2t)}$ based on numerical simulations.

Lastly, consider the case when $\chi t \lesssim 1$. In this case the orbital angular momentum of the plunging object is comparable to the spin angular momentum of the black hole, and Eq. (4.10) is incorrect, since it was derived under the assumption $\chi t \gg 1$. If the black hole is initially non-spinning or has spin $\chi \lesssim 1/t$, however, a single minor merger will bring its spin to $\chi \sim \sqrt{12}/t$ according to Eq. (4.7). This case can be treated with a Monte-Carlo numerical simulation as described in the next section.

4.4 Spin Evolution via Monte Carlo Simulations

We have carried out Monte Carlo simulations of spin evolution through minor mergers in order to confirm the analytical estimates presented above, based on the approximate Fokker-Planck equation. Our simulations also allow us to access the small- t regime where the Fokker-Planck approach is not valid, but where our physical approximations for low-mass-ratio inspirals still hold. Since these simulations were performed numerically, there was no need to make analytical approximations to $d\chi$ following a merger; instead, we solved Eqs. (4.3) directly and obtained $d\chi$ via Eq. (4.7).

In Figure 4.1 we plot the spin distribution of a black hole of mass $t = M/m = 10$ that started out with either spin $\chi = 0.1$ or $\chi = 0.9$ at $t = M/m = 5$ before growing via minor mergers. This corresponds, for example, to an intermediate-mass black hole that grows from $M = 50 M_\odot$ to $M = 100 M_\odot$ by capturing $m = 10 M_\odot$ black holes. The distributions for both values of initial spin are roughly Gaussian, although with shorter-than-Gaussian tails (we plot the actual Monte-Carlo histogram for the $\chi = 0.9$ case for comparison with a fitted Gaussian). We see that for these small values of t , the initial value of the spin is largely forgotten after the black hole captures half of its mass through minor mergers. The means of the spin at $t = 10$ are $\bar{\chi} = 0.49$ for the initially slowly-spinning hole and $\bar{\chi} = 0.51$ for the initially rapidly-spinning hole. The standard deviations at $t = 10$ are $\sigma = 0.17$ for initial spin $\chi = 0.1$ and $\sigma = 0.18$ for initial spin $\chi = 0.9$ (the initial standard deviations are zero in both cases, i.e., the initial spins are presumed to be precisely determined). These results agree with Fig. 1 of [8]. Because the values of t involved are so small, the Fokker-Planck equation (4.10) does not apply: at $t = 5$, the angular momentum of the inspiraling object at the LSO is comparable to or larger than the spin angular momentum of the black hole even for large initial black hole spins.

In Figure 4.2 we plot the spin distribution for a black hole of mass $t = M/m = 100$ that started out at $t = M/m = 50$ at either spin $\chi = 0.1$ or $\chi = 0.9$ before growing via minor mergers. This corresponds, for example, to an intermediate-mass black hole that grows from $70 M_\odot$ to $140 M_\odot$ by capturing $M = 1.4 M_\odot$ neutron stars. The

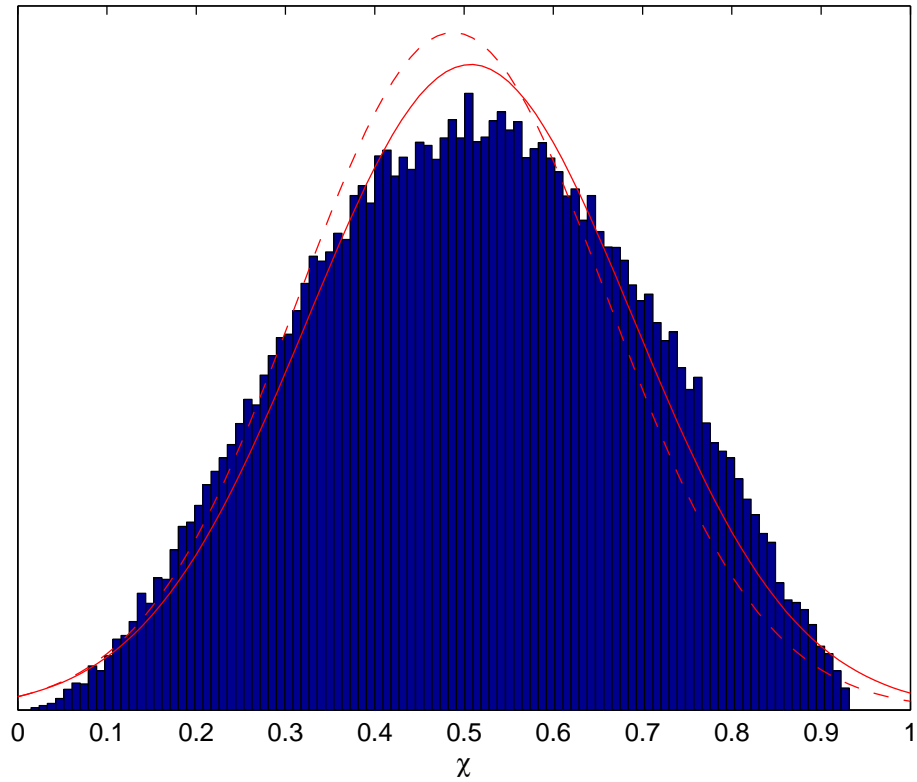


Figure 4.1: Monte-Carlo predictions for the black-hole spin distribution following black-hole growth via minor mergers from $t = M/m = 5$ to $t = M/m = 10$. The histogram shows the spin distribution at $t = 10$ for a black hole with initial spin $\chi = 0.9$, and the solid curve is a Gaussian fit to that distribution. The dashed curve is a Gaussian fit to the spin distribution at $t = 10$ for a black hole that has initial spin $\chi = 0.1$ at $t = 5$.

means of the spin at $t = 100$ are $\bar{\chi} = 0.162$ for the initially slowly-spinning hole and $\bar{\chi} = 0.233$ for the initially rapidly-spinning hole. The final spin in the initially rapidly-spinning case decreases as $\bar{\chi} \sim \chi_0(t/t_0)^{-2}$, rather than $\bar{\chi} \sim \chi_0(t/t_0)^{-2.63}$ as predicted by Eq. (4.12). That is because the spin begins to approach the asymptotic value of $\bar{\chi} \approx \sqrt{1.5/t} \approx 0.12$ as predicted by Eq. (4.16), and the rate of spin evolution decreases because $\chi^2 t$ is no longer much greater than one. The initially slowly-spinning case does not quite satisfy $\chi t \gg 1$, so the Fokker-Planck analysis is suspect; however, Eq. (4.15), relevant since $\chi^2 t < 1$ in this case, provides a roughly accurate estimate of spin growth. The standard deviations at $t = 100$ are $\sigma = 0.066$ for initial spin $\chi = 0.1$ and $\sigma = 0.084$ for initial spin $\chi = 0.9$; the predicted asymptotic value of the standard deviation according to Eq. (4.21) is $\sigma = 0.087$. The mass ratios considered in this paragraph may be plausible for intermediate-mass-ratio inspirals into intermediate-mass black holes that would be detectable with Advanced LIGO [7].

Finally, we perform a Monte-Carlo simulation of the evolution of a spin distribution from $t = 1100$ to $t = 1200$ where the starting mean spin is $\bar{\chi} = 0.72$ and the starting standard deviation is $\sigma = 0.016$. In this case, $\chi^2 t \gg 1$ holds throughout the evolution, so this example can be viewed as a test of our Fokker-Planck analysis. Based on Eq. (4.12), we expect the spin at $t = 1200$ to decrease to $\bar{\chi} = 0.57$; in fact, we find $\bar{\chi}(t = 1200) = 0.58$. Since $\sigma^2 t \ll 1$, we expect the standard deviation to grow via Eq. (4.20) to $\sigma = 0.022$ at $t = 1200$; in fact, $\sigma(t = 1200) = 0.021$.

The Fokker-Planck analysis should give excellent results in the regime of very large t , such as those corresponding to minor mergers of stellar-mass compact objects with $\sim 10^6 M_\odot$ massive black holes in galactic centers. (The extreme-mass-ratio inspirals preceding such minor mergers are an interesting class of potential LISA sources [16].) On the other hand, if a large range of t must be covered, Monte-Carlo simulations become expensive. Thus, the Monte-Carlo numerical methods and Fokker-Planck analysis can be viewed as complementary techniques.

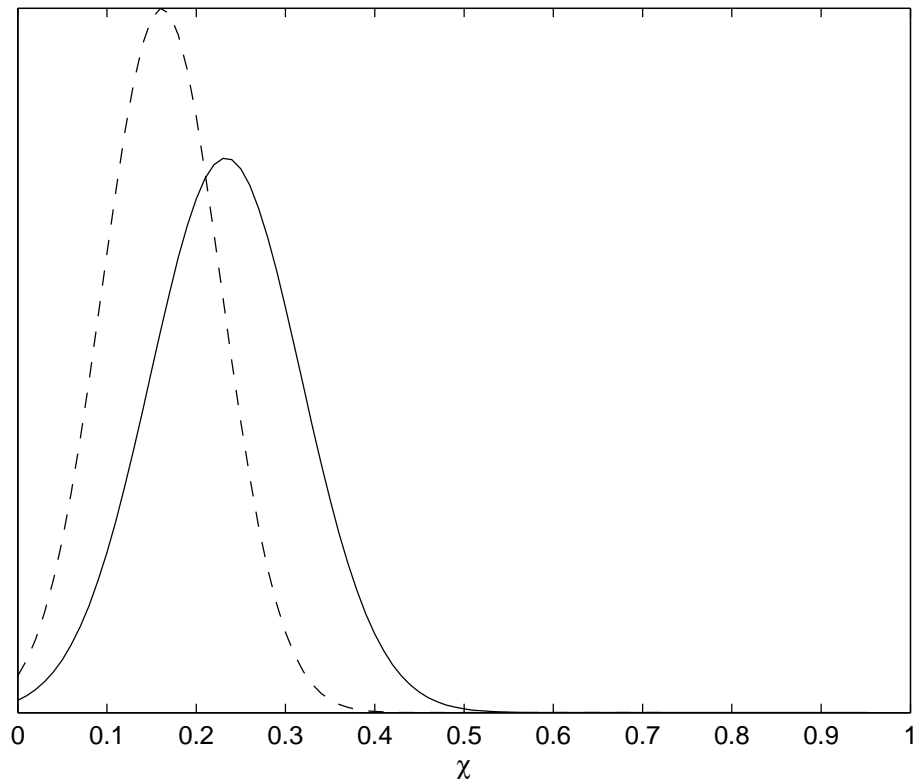


Figure 4.2: Monte-Carlo black-hole spin distribution following black hole growth via minor mergers from $t = M/m = 50$ to $t = M/m = 100$. The spin distribution for a black hole with initial spin $\chi = 0.9$ is shown with a solid curve, and one for initial spin $\chi = 0.1$ is shown with a dashed curve.

4.5 Effect of Black-Hole Spin on Detection Ranges for Low-Mass-Ratio Inspirals

The frequency of the last stable orbit before plunge is strongly influenced by the black-hole spin and the orbital inclination. Prograde inspirals into rapidly spinning black holes will have much higher LSO frequencies than inspirals into non-spinning black holes or polar inspirals into spinning black holes of the same mass, while retrograde inspirals into rapidly spinning black holes will have lower LSO frequencies. For example, for a maximally spinning Kerr black hole, the frequency of the LSO of a retrograde equatorial inspiral is twice lower than for a polar orbit, while the LSO frequency of a prograde equatorial inspiral is six times higher than for a polar orbit. Even for a more moderately spinning black hole with $\chi = 0.4$, there is almost a factor of two difference between LSO frequencies for prograde and retrograde inspirals.

The signal-to-noise ratio (SNR) for the detection of gravitational waves from inspirals depends on where the LSO frequency falls on the noise power spectral density curve of the detector. Although some inclination angles will increase SNR and others will decrease it, we might generally expect that average detection range for inspirals into spinning black holes will be higher than into non-spinning ones. (“Average” refers to averaging over the isotropically distributed orbital inclination angles of the inspiraling object.) This is because of the cubic dependence of the detection volume on detection range, which is proportional to SNR: if, say, 10% of all inspirals have their SNR boosted by a factor of three, these will be seen three times further and the detection volume for these kinds of inspirals will go up by a factor of 27, so the average volume in which detections can be made will increase by a factor of ~ 3 , and the average detection range will grow by the cube root of 3.

Conversely, this average detection range increase can manifest itself as a bias in favor of detecting inspirals into rapidly spinning black holes rather than slowly spinning ones. Thus, a numerical estimate of the detection range increase due to black hole spin is useful for determining whether a high fraction of rapidly spinning black holes among detected inspirals is an indication of the prevalence of such black

holes in the universe, or whether this is merely a selection effect.

We use the simple scaling

$$|\tilde{h}(f)^2| \propto f^{-7/3} \quad (4.22)$$

for the frequency-domain gravitational wave. The square of the signal-to-noise ratio ρ^2 is proportional to

$$\rho^2 \propto \int_{f_{\min}}^{f_{\max}} \frac{|\tilde{h}(f)^2|}{S_n(f)} df \propto \int_{f_{\min}}^{f_{\max}} \frac{f^{-7/3}}{S_n(f)} df. \quad (4.23)$$

Here, $S_n(f)$ is the noise power spectral density of the detector, f_{\max} is the frequency of gravitational waves from the last stable orbit, and f_{\min} is the low-frequency cutoff for the detector for Advanced LIGO, where $f_{\min} = 10$ Hz, or the frequency of gravitational waves one year before plunge for LISA. We set f_{\max} equal to twice the orbital frequency at the LSO, which we obtain numerically as a function of the black-hole mass M and spin χ and of the orbital inclination angle $\cos \iota$ by solving Eq. (4.3).

The distance to which an event can be seen is proportional to SNR, ρ , so the detection volume is proportional to ρ^3 . Therefore, we average ρ^3 , computed via Eq. (4.23), over the different inclinations $\cos \iota$ (uniformly distributed through the range $[-1, 1]$) in order to compute the expected increase in the detection volume for a given values of χ , and then take the cube root to compute the increase in the average detection range.

We have computed detection ranges for Advanced LIGO using this method with the noise power spectral density $S_n(|f|)$ taken from [2]. Fig. 4.3 shows our computed ratio between (i) the average Advanced-LIGO detection range for intermediate-mass-ratio inspirals into black holes of a given mass and spin and (ii) the detection range for IMRIs into Schwarzschild black holes with the same mass. For low spins $\chi \lesssim 0.4$, which are typical for intermediate-mass black holes of *sim*100 – 200 solar masses that gained a significant fraction of their mass via minor mergers, we can approximate the

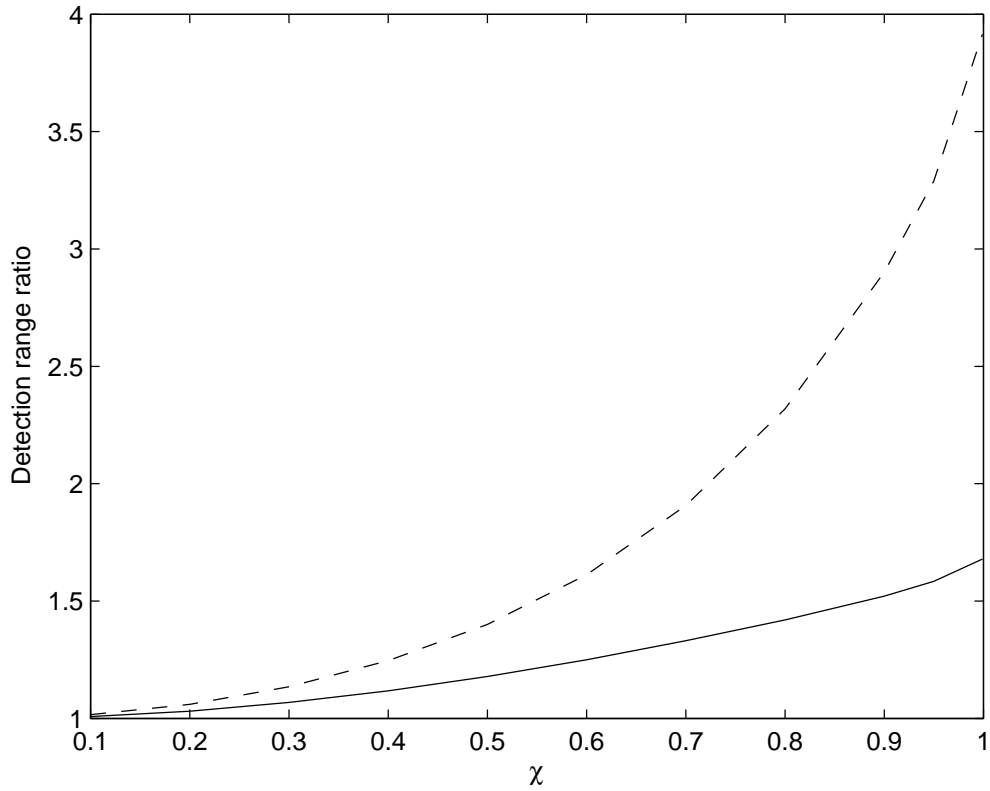


Figure 4.3: The ratio between the inclination-averaged Advanced-LIGO detection range for intermediate-mass-ratio inspirals into Kerr black holes of a given spin and the detection range for IMRIs into non-spinning black holes. The solid curve represents black holes with mass $M = 100 M_{\odot}$; the dashed curve, mass $M = 200 M_{\odot}$.

detection range increase due to the inclusion of central black hole spin as

$$\frac{\text{Range}_{\text{spin}}}{\text{Range}_{\text{no-spin}}} \sim 1 + 0.6\chi^2 \left(\frac{M}{100 M_{\odot}} \right). \quad (4.24)$$

This is the ratio of detection ranges; the ratio of detection volumes is a cube of this ratio.

The effects of cosmological redshift are not significant for Advanced-LIGO IMRIs when the black-hole spin is small. Even prograde equatorial inspirals of neutron stars into $M = 100 M_{\odot}$ black holes spinning at $\chi = 0.9$ are only detectable to $z \approx 0.2$ at an SNR threshold of 8. The cosmological redshift has the same effect as increasing the black-hole mass, so including redshift increases the ratio of detection volumes at higher spins. For the purposes of including redshift in Fig. 4.3, the inspiraling object mass was set to $m = 1.4 M_{\odot}$ and a detection threshold of $\text{SNR} = 8$ was assumed.

The results described here do not include higher-order ($m \neq 2$) harmonics of the orbital frequency. Higher harmonics are not significant when black-hole spins are small, since in that case they affect both the spinning and the non-spinning rates roughly equally, and so the ratio does not change. However, for high values of spin, the ratios would probably drop somewhat relative to those given in Fig. 4.3, since including higher-frequency harmonics would contribute more to increasing the detection range for inspirals into non-spinning holes than into rapidly holes with prograde orbits (cf. Fig. 6 of [7]).

We also compute the dependence of the LISA EMRI detection range on the massive black hole spin. We consider EMRIs of $m = 10 M_{\odot}$ objects into $M = 10^5 M_{\odot}$, $M = 10^6 M_{\odot}$, and $M = 10^7 M_{\odot}$ massive black holes. We assume that a detection is possible at an SNR threshold of 30. (Setting the threshold to 15 changes the results at the 10–20% level.) Cosmological redshift must be included for LISA EMRIs since they can be seen to $z \sim 1 - 2$. This means we must specify the inspiraling object mass and the SNR detection threshold, since these are necessary to determine the cosmological redshift of the most distant detectable source.

LISA EMRIs only sweep through a fraction of the frequency band during the

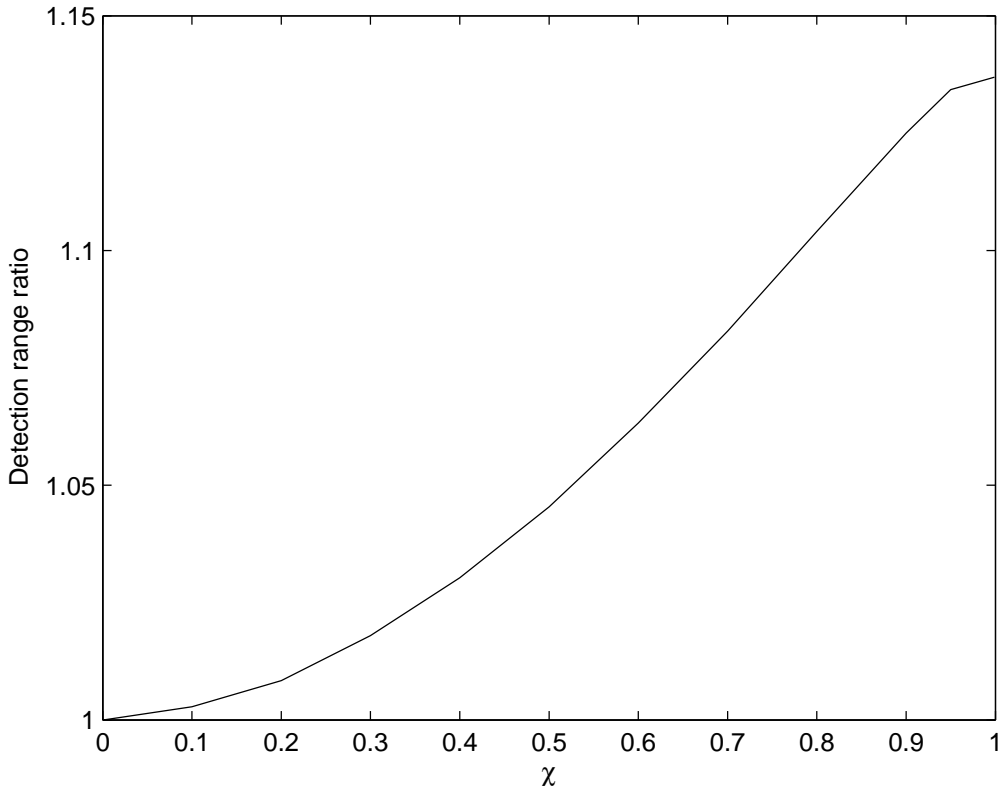


Figure 4.4: The ratio between LISA detection ranges (at SNR= 30) for extreme-mass-ratio inspirals of $m = 10 M_{\odot}$ compact objects into Kerr black holes of mass $M = 10^6 M_{\odot}$ and a given spin vs. non-spinning black holes.

observation time. Therefore, f_{\min} for LISA is set not by the detector threshold, but by the frequency of the gravitational waves emitted one year before plunge. We compute f_{\min} by evolving the gravitational-wave frequency back in time from plunge for one year using the prescription of Barack & Cutler (Eqs. (28) and (29) of [1]).

For $M = 10^5 M_{\odot}$, the spin of the black hole is almost irrelevant: once we average over orbital inclinations, the spin affects the detection range at a level of at most a few percent. This is because at these low masses, most of the SNR comes from the portion of the inspiral at much higher radii than the LSO, so the exact frequency of the LSO does not play a very significant role (cf. Fig. 8 and associated discussion in [16]).

Figure 4.4 shows the dependence of the average EMRI detection range on the

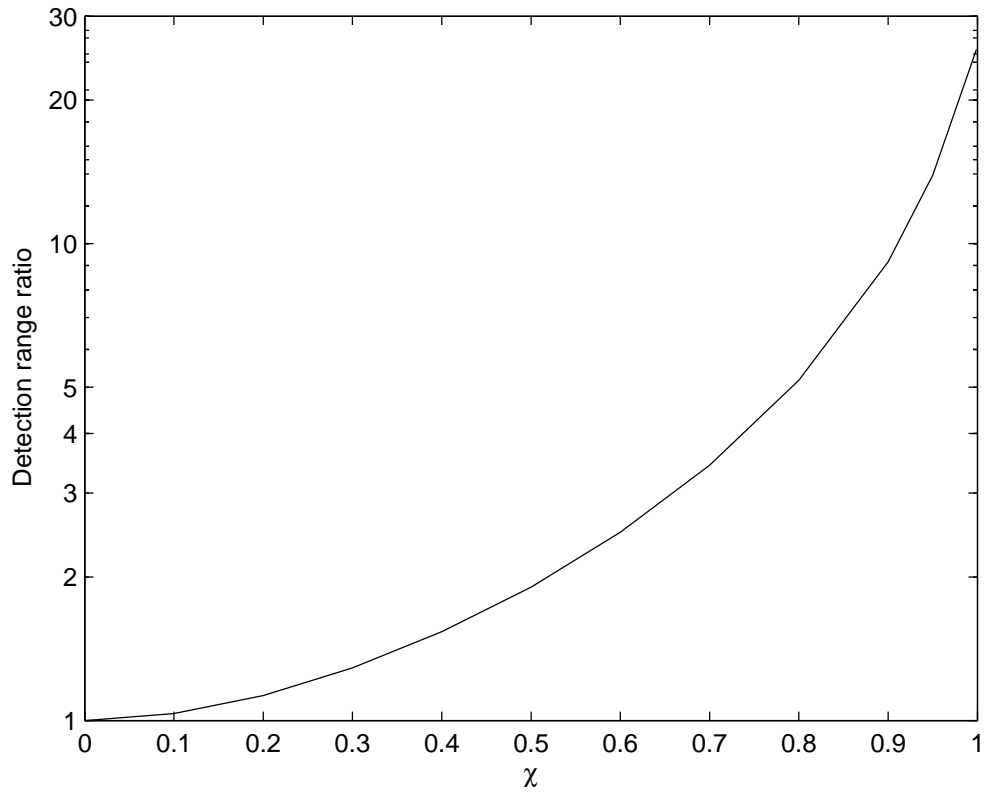


Figure 4.5: The ratio between LISA detection ranges (at SNR= 30) for extreme-mass-ratio inspirals of $m = 10 M_{\odot}$ compact objects into Kerr black holes of mass $M = 10^7 M_{\odot}$ and a given spin vs. non-spinning black holes.

massive-black-hole spin for $M = 10^6 M_\odot$. The average detection range for EMRIs into rapidly spinning black holes of mass $M = 10^6 M_\odot$ is $\sim 13\%$ larger than for EMRIs into non-spinning black holes. For $M = 10^7 M_\odot$, the detection range for EMRIs into rapidly spinning black holes is increased by a factor of ~ 25 over those into non-spinning black holes, as shown in Fig. 4.5. This greater sensitivity to black hole spin is expected, since for these massive black holes most of the SNR comes from the cycles near the LSO. However, this should not be taken to mean that inspirals into rapidly spinning $M = 10^7 M_\odot$ black holes are likely to dominate LISA EMRI observations. Figures 4.4 and 4.5 show detection range ratios only; the inclination-averaged detection range for an EMRI into a maximally spinning $M = 10^7 M_\odot$ black hole is actually less than the detection range for an EMRI into a non-spinning $M = 10^6 M_\odot$ black hole. On the other hand, this large ratio does mean that there is a strong detection bias in favor of rapidly spinning black holes, which must be taken into account when statistics of EMRI observations are inverted to gather information about the massive-black-hole spin distribution.

4.6 Appendix A. Fokker-Planck equation

Suppose a one-dimensional random process X_t is described by the stochastic differential equation

$$dX_t = \mu(X_t, t)dt + \sigma(X_t, t)dW_t, \quad (4.25)$$

where W_t is a Wiener process, and μ and σ are the mean and standard deviation of dX_t in time dt : the Itô rules for the expectation values are

$$E[dX_t] = \mu(X_t, t)dt; \quad E[dX_t^2] = \sigma^2(X_t, t)dt. \quad (4.26)$$

Let $g(X_t)$ be any function; then

$$\frac{d}{dt}E[g(X_t)] = \frac{d}{dt} \left[\int_{-\infty}^{\infty} g(x)f(x, t)dx \right] = \int_{-\infty}^{\infty} g(x) \frac{\partial}{\partial t} f(x, t)dx, \quad (4.27)$$

where x is the real value to which the map $X_t : \Omega \rightarrow R$ maps, and $f(x, t)$ is the probability function.

On the other hand,

$$\begin{aligned} dE[g(X_t)] &= E[g(X_{t+dt}) - g(X_t)] \approx E \left[\frac{\partial g(X_t)}{\partial X_t} dX_t + \frac{1}{2} \frac{\partial^2 g(X_t)}{\partial X_t^2} dX_t^2 \right] \quad (4.28) \\ &= \int_{-\infty}^{\infty} \left[\frac{\partial g(x)}{\partial x} \mu(x, t) dt + \frac{1}{2} \frac{\partial^2 g(x)}{\partial x^2} \sigma^2(x, t) dt \right] f(x, t) dx, \end{aligned}$$

where the last equality follows from applying the Itô rules. Performing the integration by parts and recalling that $f(x, t)$ and $\partial f(x, t)/\partial x$ must go to zero as $x \rightarrow \pm\infty$ in order for f to be normalizable, and dividing the result by dt , we find:

$$\frac{d}{dt} E[g(X_t)] = \int_{-\infty}^{\infty} g(x) \left\{ -\frac{\partial}{\partial x} [\mu(x, t) f(x, t)] + \frac{1}{2} \frac{\partial^2}{\partial x^2} [\sigma^2(x, t) f(x, t)] \right\} dx. \quad (4.29)$$

We can now equate the results of Eq. (4.27) and (4.29). Since the integrals must be equal for *any* $g(x)$, it follows that the integrands are equal, i.e.,

$$\frac{\partial}{\partial t} f(x, t) = -\frac{\partial}{\partial x} [\mu(x, t) f(x, t)] + \frac{1}{2} \frac{\partial^2}{\partial x^2} [\sigma^2(x, t) f(x, t)]. \quad (4.30)$$

This is the Fokker-Planck equation.

Bibliography

- [1] Barack, L. & Cutler, C. 2004, *Phys. Rev.* **D69**, 082005
- [2] Fritschel, P. 2003, arXiv:gr-qc/0308090
- [3] Gültekin, K., Miller, M. C., & Hamilton, D. P. 2004, *ApJ*, 616, 221
- [4] Gültekin, K., Miller, M. C., & Hamilton, D. P. 2006, *ApJ*, 640, 156
- [5] Hughes, S. A. 2000, *Phys. Rev.* **D61**, 084004
- [6] Hughes, S. A. & Blandford, R. D. 2004, *ApJ*, 585, L101
- [7] Mandel, I., Brown, D. A., Gair, J. R., Miller, M. C. 2007, submitted to *ApJ*, arXiv:0705.0285
- [8] Miller, M. C. 2002, *ApJ*, 581, 438
- [9] Miller, M. C., & Colbert, E. J. M. 2004, *IJMPD*, 13, 1
- [10] Miller, M. C., & Hamilton, D. P. 2002a, *MNRAS*, 330, 232
- [11] Miller, M. C., & Hamilton, D. P. 2002b, *ApJ*, 576, 894
- [12] Misner, C. W., Thorne, K. S., & Wheeler, J. A. *Gravitation* (Freeman, San Francisco, 1973)
- [13] Mouri, H., & Taniguchi, Y. 2002a, *ApJ*, 566, L17
- [14] Mouri, H., & Taniguchi, Y. 2002b, *ApJ*, 580, 844

- [15] O'Leary, R. M., Rasio, F. A., Fregeau, J. M., Ivanova, N., & O'Shaughnessy, R. 2006, *ApJ*, 637, 937
- [16] Amaro-Seoane, P., Gair, J. R., Freitag, M., Miller, M. C., Mandel, I., Cutler, C. J., Babak, S. 2007, submitted to *CQG*, arXiv:astro-ph/0703495
- [17] Taniguchi, Y., Shioya, Y., Tsuru, T. G., & Ikeuchi, S. 2000, *PASJ*, 52, 533

Chapter 5

Observable Properties of Orbits in Exact Bumpy Spacetimes

We explore the properties of test-particle orbits in “bumpy” spacetimes — stationary, reflection-symmetric, asymptotically flat solutions of Einstein equations that have a non-Kerr (anomalous) higher-order multipole-moment structure but can be tuned arbitrarily close to the Kerr metric. Future detectors should observe gravitational waves generated during inspirals of compact objects into supermassive central bodies. If the central body deviates from the Kerr metric, this will manifest itself in the emitted waves. Here, we explore some of the features of orbits in non-Kerr spacetimes that might lead to observable signatures. As a basis for this analysis, we use a family of exact solutions proposed by Manko & Novikov which deviate from the Kerr metric in the quadrupole and higher moments, but we also compare our results to other work in the literature. We examine isolating integrals of the orbits and find that the majority of geodesic orbits have an approximate fourth constant of the motion (in addition to the energy, angular momentum and rest mass) and the resulting orbits are tri-periodic to high precision. We also find that this fourth integral can be lost for certain orbits in some oblately deformed Manko-Novikov spacetimes, leading to ergodic motion. However, compact objects will probably not end up on these chaotic orbits in nature. We compute the

location of the innermost stable circular orbit (ISCO) and find that the behavior of an orbit in the approach to the ISCO can be qualitatively different depending on whether the location of the ISCO is determined by the onset of an instability in the radial or vertical direction. Finally, we compute periapsis and orbital-plane precessions for nearly circular and nearly equatorial orbits in both the strong and weak field, and discuss weak-field precessions for eccentric equatorial orbits.

Originally published as Jonathan R. Gair, Chao Li, and Ilya Mandel, 2008.

Phys. Rev. D 77 024035. Preprint available online at <http://arxiv.org/abs/0708.0628>.

5.1 Introduction

The space-based gravitational-wave detector LISA is expected to detect gravitational waves generated during the inspirals of stellar-mass compact objects (white dwarfs, neutron stars or black holes) into supermassive bodies in the centres of galaxies — extreme-mass-ratio inspirals (EMRIs). LISA could detect gravitational waves from these systems for several years prior to the plunge of the compact object into the central body and hence observe several hundred thousand waveform cycles. Such observations will provide an exquisite probe of the strong gravity region close to supermassive central bodies (see [1] for a review). In principle, the emitted gravitational waveform encodes the multipole structure of the spacetime outside the central object [2]. One of the hopes for LISA EMRI observations is to extract this spacetime structure from the data and use it to test whether the central objects are indeed Kerr black holes, as we suppose, or something else [2, 3]. (Intermediate-mass-ratio inspirals detectable by Advanced LIGO may reveal the spacetime structure outside intermediate-mass central bodies with more modest precision [4].)

For a Kerr black hole, the spacetime is uniquely determined by the mass and angular momentum of the hole and all higher multipole moments depend on these in

a simple way

$$M_l + iS_l = M(i\chi M)^l. \quad (5.1)$$

Here M_l and S_l are the l 'th mass and current multipole moments of the gravitational field, M is the mass of the black hole and χ is its dimensionless spin parameter, $\chi \equiv S_1/M^2 \equiv a/M$. As a consequence of relation (5.1), if the quadrupole or higher multipole moments of a supermassive body are measured from an EMRI observation and these are inconsistent with the values predicted by its mass and spin, the body cannot be a Kerr black hole with a vacuum exterior. The “no-hair” theorem states that, in pure gravity, any quasi-stationary, vacuum and asymptotically flat spacetime containing an event horizon and with no closed timelike curves exterior to the horizon must be described by the Kerr metric [5, 6]. If the Cosmic Censorship Conjecture is correct, all astrophysical singularities will be enclosed by a horizon. It is therefore most likely that the supermassive central bodies which are observed to inhabit the nuclei of most galaxies are indeed Kerr black holes. However, LISA should be able to test this assumption. Alternatives to Kerr black holes include “dirty” Kerr black holes with external masses (e.g., an accretion disk), exotic supermassive stars such as boson stars [7], and naked singularities. “Hairy” black hole solutions are also allowed when gravity is coupled to other fields, e.g., a Yang-Mills field (these solutions have been shown to be unstable to perturbations [8]) or a Skyrme field [9] (stability to generic perturbations is an open question). Sufficiently accurate measurements may allow us to distinguish between these possibilities.

In order to prepare us to interpret LISA observations of EMRIs, to identify any deviations from Kerr that are manifest in the waveforms and even to facilitate detection of inspirals into highly non-Kerr spacetimes, we need to understand how these deviations influence the emitted gravitational waveforms. In an extreme-mass-ratio inspiral, the timescale for the orbital inspiral due to radiation of energy and angular momentum is generally much longer than the orbital timescale. We can therefore approximate the inspiral as quasi-static, by assuming the inspiraling object is always nearly on a geodesic orbit of the spacetime, and evolving the parameters determining

this geodesic slowly over the inspiral (this is usually referred to as the “adiabatic approximation” in the literature [10] since the fluxes of energy and angular momentum used to evolve the sequence of geodesics are computed by assuming the object is on an exact geodesic of the spacetime). In this slow-inspiral limit, the emitted waveforms depend sensitively on the properties of the geodesic orbits in the spacetime — the dominant frequency components in the gravitational waveform at any moment are harmonics of the orbital frequencies of the underlying geodesic. We can thus understand some of the main consequences of deviations from the Kerr metric by examining the effect of such deviations on test particle orbits in the spacetime. By considering a spacetime with an arbitrary set of multipole moments, Ryan [2] demonstrated that, for nearly circular and nearly equatorial orbits, the periapsis and orbital-plane precessions encoded all of the multipole moments at different orders in a weak field expansion.

A multipole moment decomposition is not very practical, however, since an infinite number of multipoles are required to characterize the Kerr spacetime. For this reason, Collins & Hughes [11] and Glampedakis & Babak [12] took a different approach and explored test particle dynamics in “bumpy” spacetimes, which were constructed as first-order perturbations of the Schwarzschild and Kerr spacetimes respectively and therefore could be made arbitrarily close to Schwarzschild/Kerr by dialing a parameter to zero. Collins & Hughes coined the phrase “bumpy” black hole to describe these spacetimes. In their case, the presence of stresses exterior to the black hole meant that the horizon could be preserved in the presence of the black hole deformation without violating the no-hair theorem. In the present case, this name is not strictly applicable since the spacetimes we consider are not black holes at all, but rather naked singularities not enclosed by an event horizon. However, the term “bumpy” black hole is still a good one to describe how the spacetime appears to an observer away from the central object.

One drawback of the perturbative approach is that the perturbation is not necessarily small close to the central body, and so the first-order perturbation theory used to construct the spacetime breaks down. As a result, the perturbative solutions may

only be used relatively far from the central object. In this work, we therefore take an alternative approach and consider the properties of orbits and inspirals in a family of spacetimes that are exact solutions of the vacuum field equations of relativity and which include the Kerr and Schwarzschild spacetimes in a certain limit. We use a family of spacetimes that were derived by Manko & Novikov [13]. As exact solutions, the spacetimes are valid everywhere and can thus be used to probe the orbital dynamics in the strong-field as well as the weak-field. The family has many free parameters, which can be chosen to make the multipole moments of the spacetime match those of the Kerr spacetime up to a certain order, and then deviate at higher order. In this paper, we choose to make the multipole moments deviate at the mass quadrupole order and higher, by varying a single parameter, although the formalism generalizes to other types of deviation. We use this family of spacetimes as a test-bed for an exploration of various observable consequences of deviations from the Kerr metric, but we compare to previous work in the literature as we proceed.

The main new results of the current work are as follows. By studying the properties of orbits in the strong field of the spacetime, we find that most geodesics in the spacetime appear to have a fourth isolating integral of the motion, in addition to the energy, angular momentum and rest mass that are guaranteed by the stationarity and axisymmetry of the metric. The corresponding orbits are triperiodic to high accuracy. This was not guaranteed, since the separability of the geodesic equations in Kerr and corresponding existence of a fourth integral (the Carter constant) was unusual. Additionally, we find that for some oblate perturbations of the Kerr spacetime, there are regions of the spacetime in which there appears to be no fourth integral, leading to ergodic motion. If observed, ergodicity would be a clear ‘smoking-gun’ for a deviation from Kerr. Ergodic motion has been found in other exact relativistic spacetimes by other authors, although these investigations were not carried out in the context of their observable consequences for EMRI detections. Sota, Suzuki and Maeda [14] described chaotic motion in the Zipoy-Voorhees-Weyl and Curzon spacetimes; Letelier & Viera [15] found chaotic motion around a Schwarzschild black hole perturbed by gravitational waves; Guéron & Letelier observed chaotic motion in a black hole space-

time with a dipolar halo [16] and in prolate Erez-Rosen bumpy spacetimes [17]; and Dubeibe, Pachon, and Sanabria-Gomez found that some oblate spacetimes which are deformed generalizations of the Tomimatsu-Sato spacetime could also exhibit chaotic motion [18]. The new features of our current results are the presence of potentially ergodic regions for a wider range of magnitudes of the perturbation, and an examination of whether the ergodic regions are astrophysically relevant. We find that, in the context of an EMRI, the ergodic regions exist only very close to the central body and these regions are probably not astrophysically accessible, at least in the Manko-Novikov spacetime family.

We also look at the properties of the last stable orbit for circular equatorial inspirals. The frequency of this orbit will be a gravitational-wave observable, and depends significantly on the magnitude of any deviations from Kerr. For certain choices of the quadrupole perturbation, we find that the last stable orbit is defined by the onset of a vertical instability, rather than the radial instability which characterizes the last stable orbit in Kerr. This is a qualitative observable that could be another ‘smoking-gun’ for a deviation from Kerr.

Finally, we look at the periapsis and orbital-plane precession frequencies. We do this primarily for nearly circular and nearly equatorial orbits, since these can be characterized in a gauge invariant way in terms of the orbital frequency measured by an observer at infinity. Although such precessions were computed by Ryan [2], his results only apply in the weak-field. We find results that are consistent with Ryan’s in the weak-field, but also explore the properties of precessions in the strong-field and find they depend significantly on the nature and location of the last stable orbit. Collins & Hughes [11] and Glampedakis & Babak [12] did explore strong-field precessions, but they did so as a function of spacetime coordinates, rather than observable quantities as we use here. The perturbative spacetimes are also not totally applicable in the vicinity of the last stable orbit, so our results are more generally applicable. We also briefly discuss precessions for eccentric equatorial orbits in the weak-field and how this is relevant for LISA observations.

The paper is organized as follows. In Sec. 5.2, we introduce our chosen family

of spacetimes, describe some properties of these solutions and discuss our approach to computing geodesics in the spacetimes. In Sec. 5.3 we analyze geodesics in these bumpy spacetimes and use Poincaré maps to identify the presence of an effective fourth integral of the motion. We show that most orbits are regular and triperiodic, but also demonstrate the onset of ergodic motion in certain oblately deformed spacetimes. In Sec. 5.4 we find the last stable orbit for circular equatorial orbits and discuss its properties. In Sec. 5.5 we report our results on the periapsis precession and orbital-plane precession in these spacetimes. Finally, in Sec. 5.6 we summarize our results and discuss further extensions to this work. This paper also includes two appendices, in which we present results demonstrating ergodic motion in Newtonian gravity (Section 5.7) and an expansion of the precessions in the weak-field (Section 5.8). Throughout this paper we will use units such that $c = G = 1$.

5.2 Bumpy Black Hole Spacetimes

In this section, we briefly summarize the Manko-Novikov metric [13]. This is the test metric for which we will explore the dynamics of orbits in Sections 5.3–5.5. The Manko-Novikov metric is an exact stationary, axisymmetric solution of the vacuum Einstein equations that allows for deviations away from the Kerr spacetime by a suitable choice of parameters characterizing the higher-order multipole moments. The presence of these deviations destroys the horizon, so this is no longer a black-hole spacetime. However, its geometry is very similar to that of a Kerr black hole with additional anomalous multipole moments until close to the expected horizon location. We choose a subclass of the Manko-Novikov metric, parametrized by a parameter β . For $\beta = 0$, the metric corresponds to the usual Kerr metric. (In the notation of [13], our parametrization corresponds to setting $\alpha_2 = \beta$ and $\alpha_n = 0$ for all $n \neq 2$).

This subclass of the Manko-Novikov metric can be described by a Weyl-Papapetrou line element in prolate spheroidal coordinates as (cf. Eq. (1) of [13]):

$$ds^2 = -f(dt - \omega d\phi)^2 + k^2 f^{-1} e^{2\gamma} (x^2 - y^2) \left(\frac{dx^2}{x^2 - 1} + \frac{dy^2}{1 - y^2} \right) + k^2 f^{-1} (x^2 - 1)(1 - y^2) d\phi^2, \quad (5.2)$$

where (cf. Eqs. (9, 10, 12, 13 of [13]):

$$f = e^{2\psi} A/B, \quad (5.3a)$$

$$\omega = 2ke^{-2\psi} CA^{-1} - 4k\alpha(1 - \alpha^2)^{-1}, \quad (5.3b)$$

$$e^{2\gamma} = \exp\left(2\gamma'\right) A(x^2 - 1)^{-1}(1 - \alpha^2)^{-2}, \quad (5.3c)$$

$$A = (x^2 - 1)(1 + ab)^2 - (1 - y^2)(b - a)^2, \quad (5.3d)$$

$$B = [x + 1 + (x - 1)ab]^2 + [(1 + y)a + (1 - y)b]^2, \quad (5.3e)$$

$$C = (x^2 - 1)(1 + ab)[b - a - y(a + b)] + (1 - y^2)(b - a)[1 + ab + x(1 - y)], \quad (5.3f)$$

$$\psi = \beta R^{-3} P_2, \quad (5.3g)$$

$$\begin{aligned} \gamma' &= \frac{1}{2} \ln \frac{x^2 - 1}{x^2 - y^2} + \frac{9\alpha_2^2}{6R^6} (P_3 P_3 - P_2 P_2) \\ &+ \beta \sum_{\ell=0}^2 \left(\frac{x - y + (-1)^{2-\ell}(x + y)}{R^{\ell+1}} P_\ell - 2 \right), \end{aligned} \quad (5.3h)$$

$$a(x, y) = -\alpha \exp \left(-2\beta \left(-1 + \sum_{\ell=0}^2 \frac{(x - y) P_\ell}{R^{\ell+1}} \right) \right), \quad (5.3i)$$

$$b(x, y) = \alpha \exp \left(2\beta \left(1 + \sum_{\ell=0}^2 \frac{(-1)^{3-\ell}(x + y) P_\ell}{R^{\ell+1}} \right) \right), \quad (5.3j)$$

$$R \equiv (x^2 + y^2 - 1)^{1/2}, \quad (5.3k)$$

$$P_n \equiv P_n(xy/R) \quad \text{where } P_n(x) = \frac{1}{2^n n!} \left(\frac{d}{dx} \right)^n (x^2 - 1)^n. \quad (5.3l)$$

Here k , α , and β are free parameters which determine the multipole moments of this spacetime. The first few multipole moments have the following values (we correct a typo in Eq. (14) of [13] following [19]):

$$\begin{aligned} M_0 &= k(1 + \alpha^2)/(1 - \alpha^2) & S_0 &= 0 \\ M_1 &= 0 & S_1 &= -2\alpha k^2(1 + \alpha^2)/(1 - \alpha^2)^2 \\ M_2 &= -k^3[\beta + 4\alpha^2(1 + \alpha^2)(1 - \alpha^2)^{-3}] & S_2 &= 0 \\ M_3 &= 0 & S_3 &= 4\alpha k^4[\beta + 2\alpha^2(1 + \alpha^2)(1 - \alpha^2)^{-3}]/(1 - \alpha^2). \end{aligned} \quad (5.4)$$

Therefore, for a given choice of mass $M \equiv M_0$, spin $\chi \equiv S_1/M^2$ and anomalous (additional to Kerr) quadrupole moment $q \equiv -(M_2 - M_2^{\text{Kerr}})/M^3$, the three metric

parameters are:

$$\alpha = \frac{-1 + \sqrt{1 - \chi^2}}{\chi}, \quad k = M \frac{1 - \alpha^2}{1 + \alpha^2}, \quad \beta = q \frac{M^3}{k^3}. \quad (5.5)$$

A given choice of M , χ and q uniquely defines the metric. With this definition of q , a choice $q > 0$ represents an oblate perturbation of the Kerr metric, while $q < 0$ represents a prolate perturbation. A spacetime is oblate if it has $M_2 < 0$, e.g., for Kerr $M_2 = -\chi^2$. When we say a prolate/oblate perturbation we mean a perturbation that makes the spacetime more prolate/oblate relative to Kerr. In particular, for $-\chi^2 < q < 0$ the spacetime is still oblate, although it has a prolate perturbation relative to the Kerr metric. We note that taking $q \neq 0$ changes all higher moments from their Kerr values, so these solutions deviate not only in the mass quadrupole moment but also in the current octupole moment, the mass hexadecapole moment etc.

To present our results, we find it useful to display them in terms of cylindrical coordinates ρ , z and ϕ . These are related to the prolate spheroidal coordinates x , y by [19]

$$\rho = k(x^2 - 1)^{1/2}(1 - y^2)^{1/2}, \quad z = kxy, \quad (5.6)$$

and the line element in cylindrical coordinates is

$$ds^2 = -f(dt - \omega d\phi)^2 + f^{-1} [e^{2\gamma}(dz^2 + d\rho^2) + \rho^2 d\phi^2]. \quad (5.7)$$

5.2.1 Spacetime Properties

The Manko-Novikov spacetimes are vacuum and have the multipolar structure given in Eq. (5.4). As a consequence of the no-hair theorem, the spacetimes must therefore either lack an event horizon or contain closed timelike curves exterior to a horizon. In fact, both of these statements are true. The central singularity is enclosed by a partial horizon at coordinates $\rho = 0$, $|z| \leq 1$. However, this horizon is broken in the equatorial plane by a circular line singularity at $x = 1$, $y = 0$ ($\rho = z = 0$) [20]. For $\chi = 0$ the spacetime is otherwise regular, but for $\chi \neq 0$, the spacetimes contain

both an ergosphere and a region where closed timelike curves exist. The structure of the spacetimes is quite similar to that of the $\delta = 2$ Tomimatsu-Sato spacetime, as described in [21]. The boundary of the ergosphere is determined by the condition $g_{tt} = 0$. Inside this region, timelike observers cannot be at rest. Such a region is entirely physical, and also exists in the Kerr spacetime, where it is of interest since it allows energy extraction via the Penrose process. We show the location of the ergosphere for $\chi = 0.9$ and various choices of q in the top panel of Figure 5.1. The shape of the ergosphere is more complicated when $q \neq 0$, having a multiple lobed structure. This structure is also qualitatively different depending on the sign of q — for $q > 0$ there are three separate ergoregions, one of which intersects the equatorial plane, one which is entirely above the equatorial plane and one which is entirely below; for $q < 0$ there are only two regions, one of which is entirely above the equatorial plane and one of which is entirely below.

For a metric of this type, the region where closed timelike curves (CTCs) exist is determined by the condition $g_{\phi\phi} < 0$. In the bottom panel of Figure 5.1 we show points where $g_{\phi\phi}$ changes sign for the same choices of q and $\chi = 0.9$. Particles orbiting inside the CTC region are moving backward in time. This is not inconsistent with relativity, but CTC zones are sometimes regarded as unphysical. A spacetime with no CTC zone can be constructed by adding an inner boundary in the spacetime, and just using the portion of the Manko-Novikov solution exterior to that boundary.

The CTC zone again has a multiple lobed structure and is different depending on the sign of q . We note in particular that for $q < 0$ the ergosphere does not intersect the equatorial plane, although the CTC region does. For $q > 0$ both regions intersect the equatorial plane, and the outermost edge of the CTC region is inside the ergoregion.

5.2.2 Geodesic Motion

Geodesic motion in an arbitrary spacetime is described by the second order equations

$$\frac{d^2 x^\alpha}{d\tau^2} = -\Gamma_{\beta\gamma}^\alpha \frac{dx^\beta}{d\tau} \frac{dx^\gamma}{d\tau}. \quad (5.8)$$

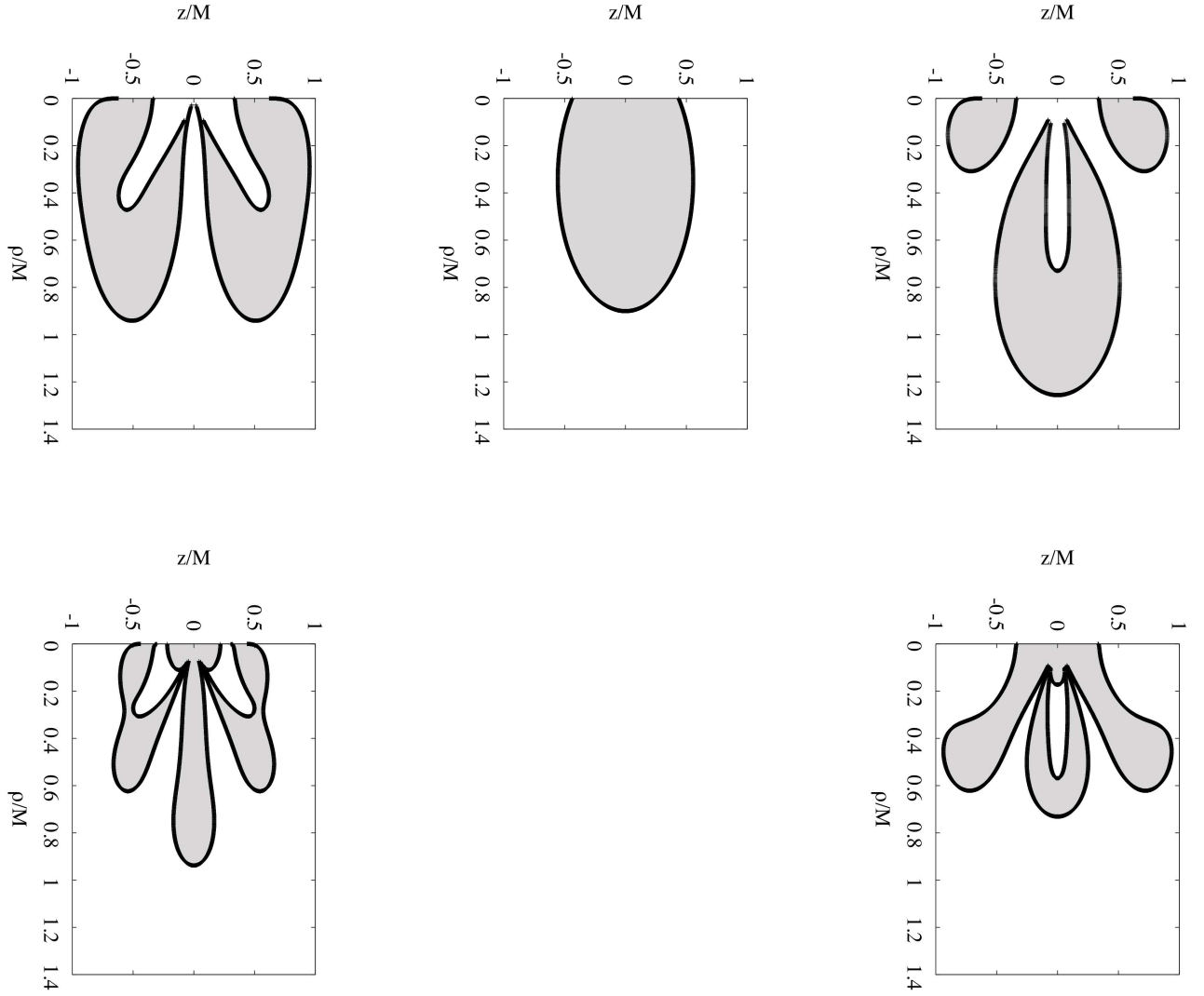


Figure 5.1: Spacetime structure for $\chi = 0.9$. The upper row shows zeros of g_{tt} for $q = -1$ (left column), $q = 0$ (middle column) and $q = 1$ (right column). This defines the boundary of the ergoregion of the spacetime. The region with $g_{tt} > 0$ is shaded. The bottom row shows points where $g_{\phi\phi}$ changes sign for the same values of q , and the region where $g_{\phi\phi} < 0$ is shaded. This defines the region where closed timelike curves exist. The middle bottom panel is empty since there is no such region in the Kerr spacetime. The shape of the two boundaries is qualitatively the same for other values of q with the same sign, although both regions grow as $|q|$ is increased.

where the connection coefficients $\Gamma_{\beta\gamma}^\alpha$ are given by

$$\Gamma_{\beta\gamma}^\alpha = \frac{1}{2}g^{\alpha\mu}(g_{\mu\beta,\gamma} + g_{\mu\gamma,\beta} - g_{\beta\gamma,\mu}). \quad (5.9)$$

The spacetimes we are interested in are axisymmetric and time-independent and the metric correspondingly has two ignorable coordinates — t and ϕ . There are therefore two constants of geodesic motion: the energy E and the z -component of angular momentum L_z , which are given by

$$E = -g_{tt}\dot{t} - g_{t\phi}\dot{\phi}, \quad L_z = g_{t\phi}\dot{t} + g_{\phi\phi}\dot{\phi}, \quad (5.10)$$

where a dot $\dot{}$ denotes the derivative with respect to proper time τ . Another first integral of the motion can be obtained from conservation of the rest mass of the orbiting particle:

$$-1 = g_{\alpha\beta}\dot{x}^\alpha\dot{x}^\beta. \quad (5.11)$$

In practice, we numerically integrate the second-order geodesic equations (5.8) rather than use these first integrals, and we use the constancy of E , L_z and $g_{\alpha\beta}\dot{x}^\alpha\dot{x}^\beta$ as cross-checks to verify the quality of our numerical results. The results reported below typically show the conservation of these quantities to a few parts in 10^{10} over the time of integration; see Fig. 5.2. We compute the connection coefficients analytically from expressions for the metric functions f , ω and γ defined in Eqs. (5.3). The only difficulty arises at points where a metric component $g_{\mu\nu}$ vanishes and its inverse $g^{\mu\nu}$ diverges. When this occurs, we analytically factor out the terms that tend to zero to avoid issues in numerical integration. To perform the numerical integration we write the coupled system of four second-order ordinary differential equations (5.8) in first-order form and integrate numerically in C++ via the Bulirsch-Stoer method.

Some general properties of geodesic motion can be understood by using the first integrals (5.10)–(5.11). The energy and angular momentum conservation equations (5.10) can be used to write \dot{t} and $\dot{\phi}$ in terms of E , L_z , ρ and z :

$$\dot{t} = \frac{Eg_{\phi\phi} + L_zg_{t\phi}}{g_{t\phi}^2 - g_{tt}g_{\phi\phi}}; \quad \dot{\phi} = \frac{-Eg_{t\phi} - L_zg_{tt}}{g_{t\phi}^2 - g_{tt}g_{\phi\phi}}. \quad (5.12)$$

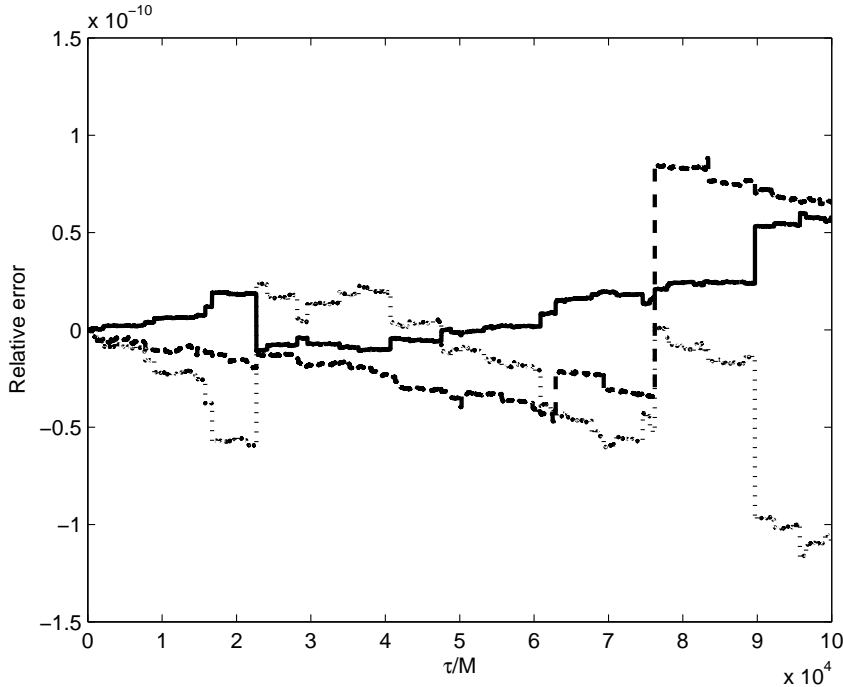


Figure 5.2: The fractional errors in energy E (solid line), angular momentum L_z (dashed line), and the quantity $g_{\alpha\beta}\dot{x}^\alpha\dot{x}^\beta$ (dotted line) accumulated over 1700 orbits of a geodesic with $E = 0.92$ and $L_z = 2.5M$ in a spacetime with spin $\chi = 0.9$ and anomalous quadrupole moment $q = 0.95$.

These expressions can be substituted into Eq. (5.11) to give

$$\frac{e^{2\gamma(\rho,z)}}{f(\rho,z)} (\dot{\rho}^2 + \dot{z}^2) = \frac{E^2}{f(\rho,z)} - \frac{f(\rho,z)}{\rho^2} [L_z - \omega(\rho,z)E]^2 - 1 \equiv V_{\text{eff}}(E, L_z, \rho, z). \quad (5.13)$$

The motion in ρ and z may thus be thought of as motion in the effective potential V_{eff} . In particular, since the left hand side of Eq. (5.13) is strictly positive or zero, motion can only exist in regions where $V_{\text{eff}} \geq 0$. Finding the zeros of the effective potential therefore allows us to find allowed regions of the motion. As an illustration, we show the zeros of the effective potential in Figure 5.3 for the simple case of the Kerr metric with spin parameter $\chi = 0.9$, energy $E = 0.95$ and angular momentum $L_z = 3M$. There are two regions of allowed motion — one region at larger radius that corresponds to bound orbits, and another region at very small radii that corresponds to rising and plunging orbits.

We now turn our attention to the Manko-Novikov spacetime with $q \neq 0$. For

spacetimes with $\chi = 0$, and for spacetimes with $\chi \neq 0$ and $q < 0$ (prolate perturbation of the Kerr metric at large radii), the addition of the perturbation does not fundamentally change the nature of the effective potential – there are still two bounded regions, one attached to the origin corresponding to rising and plunging orbits and one at larger radii corresponding to bound orbits. The shapes of these regions change as $|q|$ is increased and if $|q|$ is increased sufficiently at fixed E and L_z the two regions merge, so that all allowed orbits can reach the origin. Even after this has occurred, there appear to be two types of orbit in the single allowed region – those that rise and plunge and those that undergo many periods of radial oscillation. We don't know if the latter remain non-plunging forever in principle. In practice, perturbations due to external material or radiation reaction may cause bound orbits to diffuse onto plunging orbits over time. For fixed $q < 0$, the two allowed regions also change shape as the energy and angular momentum are varied. In particular, the plunging region connected to the singularity at $\rho = 0$, $|z| \leq 1$ develops a multi-lobed structure. For sufficiently large $|q|$ and sufficiently low E and L_z , two of these lobes can touch in the equatorial plane. This leads to the existence of circular, equatorial orbits that are unstable to vertical perturbations, which we will encounter again in Section 5.4.

For $\chi \neq 0$ and $q > 0$ (oblate perturbation of the Kerr metric at large radii), the behavior is qualitatively different. For any arbitrarily small $|q|$, an additional allowed region appears in the effective potential, which is bounded away from $\rho = 0$ and therefore corresponds to bound orbits. For small $|q|$ this new region is very close to $\rho = 0$. The other two allowed regions still exist, and merely change shape as the value of $|q|$ is increased. The additional bound region is always outside the region where closed timelike curves (CTCs) exist, and is therefore in the portion of the spacetime that can be regarded as physical. However, in the plane $z = 0$ the outermost edge of the CTC region touches the innermost edge of the region of bound motion. This additional region also extends inside the spacetime ergosphere.

We consider as an example the case with $\chi = 0.9$ and $q = 0.95$. The zeros of the effective potential V_{eff} are plotted in Figure 5.4 for geodesics with energy $E = 0.95$ and

angular momentum $L_z = 3M$. In this figure there are three distinct allowed regions as described above: (i) a foliated “plunging” region connected to $\rho = 0$, where all orbits rapidly plunge through the horizon (this region also intersects the CTC region); (ii) an inner bound region, which is located between $\rho/M \approx 0.72$ and $\rho/M \approx 2.12$ for the chosen values of E and L_z ; and (iii) an outer bound region between $\rho/M \approx 2.39$ and $\rho/M \approx 13.6$. We show the trajectory of a typical orbit in the outer region. This has a regular pattern of intersections throughout the (ρ, z) plane, which is characteristic of an orbit with an approximate fourth integral.

If $|q|$ is increased from the value shown in Figure 5.4, the two regions of bound motion eventually merge. When this first occurs, the “neck” joining the regions is extremely narrow. Geodesics exist which can pass through the neck, but this requires extreme fine tuning. As $|q|$ is further increased, the neck gradually widens and eventually disappears. At that stage, the single allowed region for bound orbits has a similar shape to the outer region of Figure 5.4.

These general properties of the effective potential seem to be common to all spacetimes with $q > 0$ and $\chi \neq 0$. More relevant for the EMRI problem is to fix q and χ and to vary E and L_z . For $E = 1$ and sufficiently large L_z , there are two regions of allowed motion bounded away from the origin, in addition to the plunging zone connected to the singularity at $\rho = 0$, $|z| \leq 1$. The outermost of the allowed regions stretches to infinity and contains parabolic orbits. The inner region of bounded motion is the analogue of the inner bound region described above and lies very close to the central object. If the angular momentum is decreased, while keeping $E = 1$, the two non-plunging regions get closer together and eventually merge to leave one allowed region that stretches to infinity. For fixed $E < 1$ the behavior is qualitatively the same, except that for $L_z \gg M$ there is no outer region (there is a maximum allowed angular momentum for bound orbits of a given energy, as in the Kerr spacetime). As L_z is decreased, the outer region for bound motion appears and then eventually merges with the inner region. Decreasing L_z further eventually causes the bound region to merge with the plunging region. At fixed L_z , if there are two distinct non-plunging allowed regions for $E = 1$, these regions do not merge as E is decreased, but the outer

region eventually disappears (there is a minimum allowed energy for orbits of a given angular momentum, as in the Kerr spacetime). If there is only one non-plunging region for $E = 1$, then as E is decreased, this region eventually splits into two allowed regions, and the outer region eventually disappears as E is decreased further. The properties are similar for all $\chi \neq 0$, but decreasing χ with the other parameters fixed tends to bring the two allowed regions of motion closer to merger with one another.

5.3 Isolating Integrals

The isolating integrals given by the conservation equations (5.10)–(5.11) do not completely describe the motion, since the motions in ρ and z are coupled. Thus, solution of the geodesic equations requires use of the second order form of those equations (5.8). However, it was demonstrated by Carter [22] that in the Kerr spacetime there is a fourth isolating integral for geodesic motion, the Carter constant, which arises as a constant of separability of the Hamilton-Jacobi equation and was later shown to be associated with a Killing tensor in the spacetime. Carter found the form of all metrics that were both Schrödinger and Hamilton-Jacobi separable. Imposing the further requirement that the metric be a solution of the vacuum Einstein-Maxwell equations leads to the Kerr metric as the only spacetime of this form that does not include a gravomagnetic monopole. Thus, the separability of the equations in Kerr is somewhat fortuitous and we would not expect that the fourth integral would be preserved when we add an anomalous quadrupole moment as we do here. As a consequence, the properties of geodesics might be expected to be somewhat different, and might even be ergodic. As mentioned in the introduction, ergodic geodesic motion has been found in other relativistic spacetimes by several other authors [14, 15, 16, 17, 18].

A fourth integral of the motion essentially gives another relationship between $\dot{\rho}^2$ and \dot{z}^2 . Combining this with the effective potential equation (5.13) allows us to eliminate \dot{z}^2 for instance and hence obtain an expression for $\dot{\rho}^2$ as a function of ρ and z only. Similarly we can obtain an expression for \dot{z}^2 as a function of ρ and z .

A standard way to examine equations of motion and look for ergodicity is to plot

a Poincaré map. This involves integrating the equations of motion and recording the value of ρ and $\dot{\rho}$ every time the orbit crosses a plane $z = \text{constant}$. From the preceding arguments, if a fourth integral exists, the value of $\dot{\rho}$ will be a function only of ρ and z (the function could be multi-valued, depending on the order at which the velocities appear in the constants of motion). Therefore such a map must show a closed curve. Similarly, if the Poincaré map of an orbit shows a closed curve for every value of z , then this defines a relationship between $\dot{\rho}$, ρ and z which is then an effective fourth integral of the motion. The Poincaré analysis thus provides a means to identify whether an effective fourth integral exists or the motion is apparently “chaotic”. In the latter case, the absence of the integral would be manifested on the Poincaré maps as space-filling trajectories rather than closed curves.

The absence of a full set of isolating integrals does not necessarily mean that all orbits will exhibit full-blown chaos. For some initial conditions, orbits may show obvious signs of ergodicity, while for other initial conditions in the same spacetime, orbits may appear to behave in an integrable fashion, suggesting that an approximate additional invariant exists. Although this behavior may appear surprising at first glance, it is consistent with the predictions of the KAM theorem and with many known examples of chaotic behavior. (The KAM theorem, due to Kolmogorov, Arnold and Moser, states that if the Hamiltonian of a system with a full set of integrals of motion is analytically weakly perturbed, then phase-space motion in the perturbed system will be confined to the neighborhoods of invariant tori in phase space, except when angle-variable frequencies of the unperturbed system are nearly commensurate, in which case motion will be chaotic [23].)

As an illustration, we show in Figure 5.5 the Poincaré map for geodesic motion along orbits with three different initial conditions in the Kerr spacetime with the same E , L_z and χ as Figure 5.3. The Poincaré maps are all closed curves, consistent with the existence of the fourth isolating integral, the Carter constant. In Section 5.7 we present results for motion under gravity in a Newtonian quadrupole-octupole potential and demonstrate the existence of both regular and ergodic orbits. This example serves to put the relativistic results described here in a Newtonian context.

5.3.0.1 Poincaré Maps for the Manko-Novikov spacetimes

The regularity properties of geodesics appear to be highly correlated with the nature of the effective potential as described in the previous section. For spacetimes with $\chi = 0$ and those with $\chi \neq 0$ but $q < 0$, all orbits appear to be regular, i.e., they show closed Poincaré maps similar to those in Figure 5.5. These are the spacetimes in the Manko-Novikov family that have effective potentials which are qualitatively the same as the Kerr case.

For $q > 0$, the effective potential can have two allowed regions for bound motion. What is striking is that, whereas orbits in the outer allowed bound region (which corresponds to the allowed region in the $q = 0$ limit) appear to be regular, with closed Poincaré maps, those in the inner allowed region appear chaotic. In Figures 5.6 and 5.7 we show Poincaré maps for one orbit in each of the outer and inner regions of the effective potential illustrated in Figure 5.4 ($q = 0.95$, $E = 0.95$, $L_z = 3M$). Orbits in the outer region show closed Poincaré maps, suggesting that the motion is regular or very nearly so and has an approximate fourth invariant of the motion. This is reinforced by the projection of the orbit onto the ρ - z plane, which was shown in Fig. 5.4. The geodesic shows a regular grid pattern, with four possible velocities at each point, corresponding to $\pm|\dot{\rho}|$ and $\pm|\dot{z}|$. If these orbits do not have a true invariant, the regularity of the Poincaré map suggests that it may still be possible to find an algebraic expression for an approximate constant of the motion.

Orbits in the inner region, by contrast, seem to fill up all possible points in a subdomain of the allowed parameter space (with $V_{\text{eff}} > 0$) and are therefore apparently ergodic in this subdomain. It seems likely, in view of the KAM theorem, that all orbits in the spacetime are strictly speaking chaotic, and no true isolating integral exists, but in the outer region there is a quantity that is nearly invariant along the orbits [4]. Either the thickness of the region mapped out by the chaotic motion is small, or the time over which ergodicity manifests itself is very long. From an observational standpoint, whether the motion is actually regular or whether only an approximate invariant exists is irrelevant, since the timescale over which ergodicity would manifest

itself in the waveform would be much longer than the time during which the orbiting object moves on an approximate geodesic.

It is unusual, given that chaotic and nearly regular regions are generally interspersed in most KAM theorem applications [23], that we find the family of geodesics is divided into two distinct regions such that geodesics in one region are ergodic while those in the other exhibit nearly regular orbital dynamics. We have been unable to find any strongly ergodic geodesics in the outer region, or any non-ergodic geodesics in the inner region. As described in the previous section, adjusting the orbital parameters can cause the two allowed regions to merge. When this first occurs, the two regions are connected by a very narrow neck. The narrowness of the neck means that extreme fine tuning is required to get a geodesic to pass through the neck. By choosing initial conditions in the neck, and integrating forwards and backwards in time, we obtained orbits that traversed the neck once and found that the motion was apparently ergodic while in the inner region, but apparently regular in the outer region. This behavior is consistent with the predictions of the KAM theorem, but observationally the fact that the orbits in the outer region are technically ergodic does not matter as long as they appear regular on long timescales. We were unable to find an orbit that traversed the neck more than once. Further adjustment of the orbital parameters causes the neck to widen and eventually disappear. At that stage, most of the orbits appear to be regular, but orbits that pass very close to the inner edge of the merged region (i.e., close to the CTC zone) have not been fully investigated.

An alternative explanation of these results [24] is that the geodesic equations are numerically unstable in the inner region, and therefore small numerical round-off errors in the integration routines are driving the orbits away from their true values. Once again, this distinction is not relevant observationally. An astrophysical system harboring an EMRI will not be isolated. The gravitational perturbations from distant stars etc. will serve the same role in perturbing the orbits as numerical errors might on a computer. The end result — that the orbit is apparently ergodic — is the same.

5.3.0.2 Frequency Component Analysis

The above conclusions are supported by a frequency-domain analysis of the ρ and z motion in the two regions. The absolute values of Fourier transforms of $\rho(t)$ and $z(t)$ are plotted in Figures 5.8 and 5.9. Fig. 5.9 shows an absence of clearly identifiable frequency peaks for geodesics in the inner region, a result consistent with full-blown chaos. By contrast, Fig. 5.8 shows discrete frequency peaks in the outer region. Generally such frequency peaks, corresponding to harmonics of a few fundamental frequencies, occur in problems with a full set of isolating integrals. We find that the frequency components measured for the ρ and z motion in the outer region can be represented as low order harmonics of two fundamental frequencies at a high level of precision (1 part in 10^7 for the first ~ 10 harmonics). This multi-periodicity of the geodesics implies that the gravitational waveforms will also be multi-periodic. Indeed, we find that an approximate gravitational waveform, constructed using a semi-relativistic approximation for the gravitational-wave emission (as used to construct Kerr EMRI waveforms in [25]), is also tri-periodic (the third frequency arises from the ϕ motion since the observer is at a fixed sky location). The absolute value of the Fourier transform of the $h_+(t)$ component of this gravitational waveform is also plotted in Fig. 5.8 and is clearly multi-periodic. This periodicity has important consequences for data analysis and parameter extraction.

5.3.0.3 Comparison to Other Results

Our results are consistent with previous work by other authors who have found chaotic geodesic motion in various spacetimes. Generally, chaotic motion only occurs in the strong-field region close to the central object, and for a limited range of geodesic parameters. As an example, Guéron and Letelier [17] found chaos in a prolate Erez-Rosen spacetime, which represented a deformation of a Schwarzschild black hole. They demonstrated that, for a particular value of the energy and angular momentum, when the deformation parameter had a value $k_2 = -5$, there was a single allowed region of bounded motion, but for $k_2 = -5.02$ the region split into two separate regions. After the split, orbits in the inner region appeared chaotic while those

in the outer region appeared regular. For the merged region, orbits that passed into the inner part also appeared ergodic while those that were purely in the outer part looked regular. This is qualitatively very similar to what we have found in the Manko-Novikov spacetime, although we find chaotic motion only when $\chi \neq 0$, while Guéron and Letelier presented examples for both a perturbed non-spinning black hole and a spinning black hole. As a test of our codes, we repeated Guéron and Letelier’s calculation and found consistent results. As well as providing another example of chaos for relativistic geodesics, the results here show some new features. In particular, the inner allowed region appears for any $q > 0$ and as far as we have been able to ascertain the motion is always ergodic in that region. This contrasts to the spacetime considered by Guéron and Letelier, in which chaotic motion exists only for a small range of k_2 (by the time k_2 has increased to $k_2 = -5.1$, the motion is no longer apparently ergodic). Previous authors have also not considered the issue of accessibility of the ergodic region to stars, and we discuss that in the next sub-section.

Sota et al. [14] discussed what might cause chaos in relativistic geodesic motion, and suggested that it might arise either due to a change in the signs of the eigenvalues of the Weyl tensor, which would lead to “local instability” or due to the presence of homoclinic orbits. The Manko-Novikov spacetimes do contain homoclinic orbits, but Sota et al. [14] found that this only led to chaos in non-reflection symmetric spacetimes, so this explanation probably does not apply here. We have not explored the properties of the eigenspace of the Weyl tensor for these spacetimes, but “local instability” could be a plausible explanation for our results. The CTC region of the Manko-Novikov spacetime might also be causing the ergodicity. The region where ergodic motion occurs touches the CTC region at a single point, so the singular behavior of the metric as the CTC region is approached might explain the observed behavior, either by causing a region of “local instability” or through some other mechanism.

We note that in the regime where chaos occurs, the perturbation to the Kerr metric cannot be regarded as purely quadrupolar, but the deviations in the higher multipole moments are also significant. This is similar to the Newtonian result described in

Section 5.7 since we find chaos in the Newtonian quadrupole-octupole potential but not a pure quadrupole potential. The relativistic results are somewhat different, however, since we find chaos only for $\chi \neq 0$, so for these spacetimes we also need a non-zero current dipole moment to observe chaotic behavior.

5.3.0.4 Accessibility of the Ergodic Domain

While the existence of ergodic motion is mathematically interesting, an important question for EMRIs that has not been addressed so far is whether ergodicity could ever be observed in nature. In other words, is it possible, during the course of an inspiral, for a captured object to find itself on an ergodic geodesic?

In typical astrophysical scenarios, the inspiraling compact object will start out far away from the central body with energy close to 1 [1]. Unless the angular momentum is very small (which in the Kerr spacetime would represent an object on a plunging orbit), this will correspond to an orbit in the outer region of allowed motion if two regions exist, so the orbit will initially be regular. As the star inspirals, the energy and angular momentum will gradually change and this causes the separation between the outermost point of the inner region of bound motion and the innermost point of the outer region, $\Delta\rho$, to change. For example, when $E = 0.99$ and $L_z = 4.33M$ in a Manko-Novikov spacetime with $\chi = 0.9$, and $q = 0.95$, we find that $\Delta\rho/M \approx 6.4$. When $E = 0.95$ and $L_z = 3M$ in the same spacetime, the separation between regions is only $\Delta\rho \approx 0.27M$. For sufficiently small choices of energy and angular momentum (e.g., $E = 0.92$ and $L_z = 2.5M$) only a single region remains. This suggests that the two regions will come closer together as energy and angular momentum are radiated away during an inspiral, until they eventually merge. We conjecture that $d(\Delta\rho)/dt$ is always negative; that is, the two regions are always merging rather than separating. To test this conjecture, we must explore the behavior of $\Delta\rho$ along an extreme-mass-ratio inspiral characterized by slowly evolving E and L_z .

To do this, we use an approximate scheme to evolve the energy and angular momentum during an inspiral. Our scheme is based on combining exact relativistic expressions for the evolution of orbital elements with approximate post-Newtonian

formulae for energy and angular-momentum fluxes. This scheme was previously devised to describe EMRIs into Kerr black holes [27] and has been shown to give reliable results in that context. For the current calculation, we must augment the fluxes with an additional post-Newtonian term to represent the effect of the anomalous quadrupole moment q on the evolution of energy and angular momentum. A Kerr black hole has quadrupole moment $M_2/M^3 = -\chi^2$. It is the quadrupole moment that leads to the lowest order terms in χ^2 in the expressions for the energy and angular momentum radiated during an inspiral. Therefore, to include the excess quadrupole moment, we just change the χ^2 terms in the flux expressions to $\chi^2 + q$, while leaving the lower order terms unchanged (this approach was also used in [26]). We then numerically find the roots of the effective potential $V_{\text{eff}} = 0$ in the equatorial plane at various times and compute the evolution of $\Delta\rho$ along the inspiral.

The result of one such computation of $\Delta\rho$ is plotted in Fig. 5.10. That figure corresponds to an inspiral in a spacetime with $\chi = 0.9$, and $q = 0.95$. The inspiral starts out at $\rho = 100M$ with an orbital inclination of 60 degrees and initial eccentricity $e = 0.8$ (these orbital parameters correspond to $E \approx 0.9982$ and $L_z \approx 5.0852M$) and proceeds until plunge. The separation between the inner and outer bounded regions gradually shrinks, until the two regions merge (on the plot, this is shown as $\Delta\rho = 0$). Afterward, the bounded regions remain joined until eventually merging with the plunging region.

We have found the same qualitative behavior described above for a wide range of parameter choices. Therefore, in all these cases, our conjecture is true — the inspiraling object can never find itself in the isolated inner region where all orbits appear to be ergodic. We should point out, however, that we have carried out this numerical investigation only for a range of specific choices of χ , q , and initial orbital parameters, and have used an approximation to the energy and angular momentum radiated during an inspiral. This is therefore not a definitive proof that chaotic motion can never be observed in the course of an inspiral in the Manko-Novikov spacetime.

Assuming this evolution really is typical, there are two important consequences. Firstly, an inspiraling object can never end up in the inner of two allowed regions of

bound motion, where ergodic motion is prevalent. Secondly, inspirals always start out in a phase where the motion is regular. This is very important, since it will allow the systems to be detected in this early inspiral stage by gravitational-wave detectors using matched filtering or a time-frequency analysis. The inspiraling object will eventually end up in the merged region formed after the two regions of bounded motion converge. Both ergodic and regular geodesics exist in that region, so in principle the particle could find itself on an ergodic orbit. However, most orbits in the merged region appear to be regular so it would require fine tuning to put the object onto such a geodesic (e.g., the “neck traversing” geodesics discussed earlier). It thus seems unlikely that this would occur in practice.

Although these results apply only to the Manko-Novikov family of spacetimes, the conclusions are consistent with other examples of chaotic geodesics in relativity. For instance, in the prolate Erez-Rosen spacetime considered in [17], if an object had arrived in the region where ergodic motion is observed during the course of an inspiral, its orbital energy and angular momentum would have been larger earlier in the inspiral. However, if either the energy or angular momentum is increased from the values that give ergodic motion, the effective potential changes so that it has only one allowed region, which includes “escape zones” connected to the central singularity. All geodesics in such a zone plunge into the central object in a short time so an astrophysical inspiral could not persist through that zone. We deduce that for that spacetime as well the ergodic region is inaccessible to objects captured at large distances.

If there was some other mechanism that could put an inspiraling object onto an ergodic geodesic, there is the question of how the ergodicity could be identified in practice. Detection of EMRIs will rely on matched filtering or possibly time-frequency techniques [1]. In either case, it will probably not be possible to identify the gravitational radiation as being emitted from an ergodic orbit, but only that radiation from a regular orbit has ceased. It is clear from Figure 5.9 that during an ergodic phase, the emitted power is spread among many harmonics, which will consequently not be individually resolvable. This radiation will increase the broadband power in

our detector, whereas if the orbit had plunged the radiated power would rapidly die away. However, the energy released during a typical EMRI is comparatively low, so it is unlikely that we could identify the presence of such broadband power over the instrumental noise. Therefore, the chances are that we will not be able to distinguish observationally between an inspiral that “ends” at a transition into an ergodic phase and one which ends by plunging into a black hole.

One potentially observable signature of ergodicity would be an inspiral that turned “off” and “on” as it progressed through ergodic phases interspersed with regular phases. This would occur if the object could move into and out of the inner ergodic region during an inspiral, but the preceding analysis indicates that this shouldn’t happen. An object on a “neck-traversing” geodesic would also show this behavior. However, the periods where the orbit is ergodic serve to randomise the phase of the orbit in the regular periods. A signal of this type would only be observable if each apparently regular phase could be individually resolved with enough signal-to-noise ratio. This would require a very narrow “neck” in order to trap the orbit for many cycles in the regular zone. However, fine tuning of the energy and angular momentum is necessary to make the neck very narrow, so if an object was on such an orbit, the neck would be widening rapidly as energy and angular momentum were radiated away. In practice, it is doubtful that sufficient signal-to-noise would accumulate to allow a detection to be made before the neck widened too much.

We conclude that, for astrophysically relevant inspirals in the Manko-Novikov spacetime family, an object would probably not end up on an ergodic geodesic. If some other mechanism conspired to put an object on such an orbit, it is unlikely that we would be able to identify this in gravitational-wave observations. If these findings carry over to a more generic class of spacetimes, then chaotic motion is merely a mathematical curiosity which is unlikely to manifest itself practically or be important for gravitational-wave data analysis considerations.

5.4 Last Stable Orbit

During an inspiral into a Kerr black hole, an EMRI will evolve quasi-statically through a sequence of near-geodesic orbits as orbital energy and angular momentum are radiated away. There is a minimum energy (which is dependent on angular momentum) for which bound orbits exist. When the inspiral reaches that separatrix, the object will rapidly plunge into the central body. The gravitational radiation emission undergoes a transition at this point, and so the frequency of this last stable orbit is in principle another quantity that is observable from the detected gravitational waves. For a Kerr inspiral, the ‘transition’ is a rapid die-off in the gravitational-wave emission as the particle plunges into the black hole. If the central object is not a black-hole, the radiation may persist for longer after the last stable orbit is passed [7], but there will still be a significant qualitative change in the emitted radiation as the orbit changes suddenly at that point. We focus on the innermost stable circular equatorial orbit in this analysis, since this is well defined in these spacetimes.

5.4.1 Circular Equatorial Orbits

The geodesic equations for an arbitrary spacetime (5.8) may be written in the alternative form

$$\frac{d}{d\tau} \left(g_{\mu\alpha} \frac{dx^\alpha}{d\tau} \right) = \frac{1}{2} \partial_\mu g_{\nu\sigma} \frac{dx^\nu}{d\tau} \frac{dx^\sigma}{d\tau}. \quad (5.14)$$

For a circular-equatorial orbit in an axi- and reflection-symmetric spacetime of the form (5.7), $d\rho/d\tau = dz/d\tau = d^2\rho/d\tau^2 = 0$; hence the ρ -component of the geodesic equation (5.14) gives

$$\partial_\rho g_{\phi\phi} \dot{\phi}^2 + 2\partial_\rho g_{t\phi} \dot{t} \dot{\phi} + \partial_\rho g_{tt} \dot{t}^2 = 0 \quad (5.15)$$

in which a dot denotes $d/d\tau$ as before. We can thus express the azimuthal frequency as observed at infinity $\Omega_\phi = \dot{\phi}/\dot{t}$ in the form

$$\Omega_\phi = \frac{-\partial_\rho g_{t\phi} \pm \sqrt{(\partial_\rho g_{t\phi})^2 - \partial_\rho g_{tt} \partial_\rho g_{\phi\phi}}}{\partial_\rho g_{\phi\phi}}, \quad (5.16)$$

where the $+/-$ signs are for prograde and retrograde orbits respectively. In the equatorial plane, the right-hand side is a function of the spacetime parameters and ρ only, so given a particular choice of azimuthal frequency Ω_ϕ , Eq. (5.16) can be inverted to determine the value of ρ such that a circular orbit at that ρ has frequency Ω_ϕ .

Equation (5.10) provides another relation between \dot{t} and $\dot{\phi}$, from which we can deduce

$$\dot{t} = \left(-g_{tt} - 2\Omega_\phi g_{t\phi} - \Omega_\phi^2 g_{\phi\phi}\right)^{-\frac{1}{2}} \quad (5.17)$$

and then the energy and angular momentum equations (5.10) give us E and L_z as a function of ρ for circular equatorial orbits.

5.4.2 Innermost Stable Circular Orbit

The location of the innermost stable circular orbit (ISCO) in the equatorial plane can be found using the effective potential (5.13). Circular equatorial orbits are located at simultaneous zeros and turning points of V_{eff} , where $V_{\text{eff}} = \partial V_{\text{eff}}/\partial\rho = \partial V_{\text{eff}}/\partial z = 0$. As we will see in Section 5.5 the second derivatives of V_{eff} determine the frequencies of small oscillations about the circular orbit. For the circular orbit to be stable, we need the orbit to sit at a local maximum of V_{eff} , i.e., we require $\partial^2 V_{\text{eff}}/\partial\rho^2$ and $\partial^2 V_{\text{eff}}/\partial z^2$ to be negative. In the following we will use $\tilde{V}_{\rho\rho}(\rho)$ ($\tilde{V}_{zz}(\rho)$) to denote the value of $\partial^2 V_{\text{eff}}/\partial\rho^2$ ($\partial^2 V_{\text{eff}}/\partial z^2$) evaluated for the circular equatorial orbit at radius ρ . For the Kerr spacetime, $\tilde{V}_{zz}(\rho) < 0$ at all radii, but $\tilde{V}_{\rho\rho}(\rho)$ has a single root at a critical radius ρ_{ISCO} . This tells us that the orbit becomes radially unstable at that point, which defines the ISCO. For $\chi = 0$, $\rho_{\text{ISCO}} \approx 4.90M$, while for $\chi = 0.9$, $\rho_{\text{ISCO}} \approx 1.25M$ for prograde orbits and $\rho_{\text{ISCO}} \approx 7.705M$ for retrograde orbits. Note that ρ is a cylindrical Weyl coordinate, which is why these results differ from the familiar black-hole ISCO radii, which are normally quoted in Boyer-Lindquist coordinates.

For the Manko-Novikov solutions with $\chi = 0$, the shape of the functions $\tilde{V}_{\rho\rho}(\rho)$ and $\tilde{V}_{zz}(\rho)$ does not change significantly as q is increased with $q > 0$ — $\tilde{V}_{zz}(\rho) < 0$ everywhere and $\tilde{V}_{\rho\rho}(\rho) = 0$ has a single solution that defines the ISCO. However,

as $|q|$ is increased with $q < 0$, there is a transition in behavior at $q \approx -0.163$. For larger values of $|q|$ with $q < 0$, the function $\tilde{V}_{\rho\rho}(\rho)$ has two zero-crossings. Thus, in addition to the radially-stable circular orbits at large radii, we find additional such orbits exist very close to the central singularity. If $|q|$ is increased still further, the two roots converge at $q \approx -0.654$ and for $q < -0.654$ radially stable orbits exist at all values of ρ . However, at the point where the second branch of the radial roots appears, there is also a transition in the shape of $\tilde{V}_{zz}(\rho)$, so that there are now orbits which are vertically unstable. For $q < -0.163$, the ISCO is defined by this vertical instability, rather than the radial instability characteristic of the Kerr spacetime, and Manko-Novikov spacetimes with $q > 0$. In the range $-0.654 < q < -0.163$, there are two regimes where stable circular orbits exist — an outer zone with $\rho > \rho_{\text{ISCO}}$, and an inner zone with $\tilde{\rho}_{\text{ISCO}} < \rho < \rho_{\text{OSCO}}$ (we use “OSCO” to indicate “outermost stable circular orbit” and $\tilde{\rho}_{\text{ISCO}}$ to denote the ISCO for the inner set of circular orbits). The energy and angular momentum of an orbit at the “OSCO” are greater than the energy and angular momentum at the ISCO of the outer zone, ρ_{ISCO} . Thus, an object inspiraling from large distances on a circular equatorial orbit will reach ρ_{ISCO} and plunge into the central body, rather than finding itself in the inner range of circular orbits. Compact objects could only find themselves in the inner range if they came in on an eccentric/inclined orbit and then radiated away energy and angular momentum in exactly the right proportions. It is therefore unlikely that this inner zone would be populated in practice. However, any object on a circular equatorial orbit in this inner zone would reach $\tilde{\rho}_{\text{ISCO}}$ and then plunge into the central body.

In Figure 5.11 we show the location of the ISCO as a function of q for spacetimes with $\chi = 0$. We also show the orbital frequency at the ISCO as a function of q , computed using Eq. (5.16). For spacetimes with spin, the behavior is qualitatively similar, but there are now two ISCO radii, corresponding to prograde and retrograde orbits respectively. We show results for a spin of $\chi = 0.9$ in Figure 5.12. We note that the ISCO radius is always outside the boundary of the causality-violating region of the spacetime. For $\chi \neq 0$ and $q > 0$, the ISCO radius is determined by the point at which the outer allowed region for bound motion (which is a single point for a circular

equatorial orbit) merges with the inner allowed region. In that case when the object reached the ISCO it would undergo a transition onto an eccentric/inclined geodesic.

The value of the ISCO frequency depends not only on q but also M and χ . However, as we shall discuss in the next section, it is possible to measure these other parameters using precessions measured when the orbit is in the weak-field. Thus, the ISCO frequency is a powerful probe of the nature of the spacetime since it can be very different even for comparatively small deviations from Kerr.

5.5 Periapsis and Orbital-Plane Precessions

In Section 5.3 we saw that astrophysically relevant orbits in the Manko-Novikov spacetime are multi-periodic to high precision. In such cases, there is no smoking-gun signature that indicates the presence of “bumpiness” in the spacetime. Instead, the imprint of the spacetime bumpiness will be observationally apparent in the location of the last stable orbit, as discussed in the previous section, and in the following ways: (1) in the three fundamental frequencies of the gravitational waves generated while the inspiraling object is on an instantaneous geodesic orbit; (2) in the harmonic structure of the gravitational-wave emission, i.e., the relative amplitudes and phases of the various harmonics of the fundamental frequencies; and (3) in the evolution of these frequencies and amplitudes with time as the object inspirals. A full analysis of the accuracies that could be achieved in observations would involve computing gravitational waveforms in the bumpy spacetimes, performing a Fisher-Matrix analysis to account for parameter correlations, and comparing to a similar analysis for Kerr. That is beyond the scope of this paper. However, we can examine the first of these observational consequences by comparing the fundamental frequencies between the bumpy and Kerr spacetimes.

The complication in such an analysis is to identify orbits between different spacetimes. Identifying orbits by the ρ and z coordinates is not gauge-invariant, since the meaning of these coordinates depends on the spacetime structure. Identifying orbits via the energy and angular momentum is gauge-invariant, but these quantities are

not directly measurable observationally. However, circular orbits in the equatorial plane of the spacetime are characterized by a single observable — the azimuthal frequency of the orbit. We can use this frequency to identify circular equatorial orbits in different spacetimes.

Precession frequencies are absent in exactly circular equatorial orbits. However, if the circular orbit is perturbed radially, it will undergo small oscillations at the radial epicyclic frequency, which is characteristic of the periapsis precession frequency at that radius. Likewise, if the orbit is perturbed vertically it will undergo small oscillations at the vertical epicyclic frequency, which is characteristic of the orbital-plane precession frequency at that radius. We thus compare these epicyclic frequencies, as a function of the circular orbital frequency, between Kerr and bumpy spacetimes. This comparison was employed by Ryan, who used it to derive his theorem stating that all spacetime multipole moments are encoded in the gravitational waves generated by nearly-circular, nearly-equatorial EMRIs [2].

An eccentric equatorial orbit can be characterized by two observables — the orbital frequency and the periapsis precession frequency. These two frequencies can therefore be used to identify orbits in different spacetimes (provided there is an orbit with corresponding frequencies in the Kerr metric). Likewise, the orbital-plane precession frequency can be used to identify inclined orbits between spacetimes¹. With such an identification, differences in the multipole structure of the spacetime will show up only in the relative amplitudes of the harmonics and in the evolution of the fundamental frequencies over the inspiral. We will discuss this some more at the end of this section, but a full analysis requires treatment of inspiral in an arbitrary spacetime and is beyond the scope of the current paper.

¹The ‘orbital-plane’ is not well defined in the strong field. However, we know the gravitational waves should be triperiodic and, in the weak-field, the three periods correspond to the orbital period and the two precessions. When we refer to ‘orbital-plane precession frequency’ we really mean the frequency component of the orbit that corresponds to orbital-plane precession in the weak-field. This will be the frequency of the vertical motion, averaged over many orbits.

5.5.1 Epicyclic Frequencies

The frequency of epicyclic motion can be derived by perturbing a circular, equatorial orbit in either the radial or vertical direction. The second order geodesic equations (5.8) for z and ρ take the form

$$\begin{aligned} \frac{d}{d\tau} \left(2g_{XX} \frac{dX}{d\tau} \right) &= \partial_X g_{tt} \left(\frac{dt}{d\tau} \right)^2 + 2\partial_X g_{t\phi} \left(\frac{dt}{d\tau} \right) \left(\frac{d\phi}{d\tau} \right) + \partial_X g_{\phi\phi} \left(\frac{d\phi}{d\tau} \right)^2 \\ &\quad + \partial_X g_{\rho\rho} \left(\frac{d\rho}{d\tau} \right)^2 + \partial_X g_{zz} \left(\frac{dz}{d\tau} \right)^2. \end{aligned} \quad (5.18)$$

Here X denotes either ρ or z . The dependence on $dt/d\tau$ and $d\phi/d\tau$ can be eliminated by using the energy and angular momentum conservation equations to express these in terms of E , L_z , ρ and z , as in Eq. (5.12). Using this form of the equations we can take a circular, equatorial orbit, $\rho = \rho_0$, $z = 0$, and perturb it either in the radial direction, $\rho = \rho_0 + \delta\rho$, $z = 0$, or in the vertical direction, $\rho = \rho_0$, $z = \delta z$. Considering the equations of motion at leading order in the small orbital perturbation, it is easy to see that the frequencies of these small epicyclic oscillations are given by

$$\begin{aligned} \left(\frac{g_{\phi\phi}E - g_{t\phi}L_z}{g_{tt}g_{\phi\phi} - g_{t\phi}^2} \right)^2 \Omega_X^2 &= \\ \frac{1}{2g_{XX}} \frac{\partial}{\partial X} &\left(\frac{\partial_X g_{tt} (g_{\phi\phi}E - g_{t\phi}L_z)^2 + 2\partial_X g_{t\phi} (g_{\phi\phi}E - g_{t\phi}L_z) (g_{tt}L_z - g_{t\phi}E)}{(g_{tt}g_{\phi\phi} - g_{t\phi}^2)^2} \right) \\ &+ \frac{1}{2g_{XX}} \frac{\partial}{\partial X} \left(\frac{\partial_X g_{\phi\phi} (g_{tt}L_z - g_{t\phi}E)^2}{(g_{tt}g_{\phi\phi} - g_{t\phi}^2)^2} \right) \end{aligned} \quad (5.19)$$

As before, X denotes either ρ (for the radial epicyclic frequency Ω_ρ) or z (for the vertical epicyclic frequency Ω_z). The same result can be derived starting from the effective potential equation (5.13): the frequencies are given by $\Omega_X^2 = -(1/2)\partial^2 V_{\text{eff}}/\partial X^2$ evaluated at the circular orbit.

5.5.2 Precessions

We are interested in precessions rather than the epicyclic frequency. We define the *periapsis precession* as the number of cycles by which the periapsis advances per

radial period (i.e., over one complete epicyclic oscillation). Likewise, the *orbital-plane precession* is defined as the number of cycles by which the azimuthal angle to the highest point of the orbit advances during one vertical oscillation. These precessions, which we denote by p_X , are related to the epicyclic frequencies, Ω_X , by

$$p_X = \frac{\Omega_\phi}{\Omega_X} - 1. \quad (5.20)$$

The behavior of the precessions can be understood in terms of what happens in the weak-field, far from the black hole, and in the strong-field, close to the ISCO. In the weak-field it is possible to derive expressions for the precessions as functions of the orbital frequency. This was originally done for nearly circular, nearly equatorial orbits by Ryan [2], who demonstrated that the various spacetime multipole moments enter the precession rate expansion at different orders of $(M\Omega_\phi)^\alpha$. This was the basis for a theorem that, in principle, the weak-field precessions can be used to extract the lowest order spacetime multipole moments. The weak-field expansion of the precessions is summarised in Section 5.8.

In the strong-field, we find that one or the other precession diverges at a certain frequency. This frequency corresponds to the frequency of the ISCO. To understand what is happening, we use the effective potential (5.13) and consider radial oscillations. For the energy and angular momentum corresponding to the circular equatorial orbit at radius $\rho = \rho_c$, the effective potential in the equatorial plane takes the form $V_{\text{eff}}(\rho, z = 0) = -\tilde{V}(\rho)(\rho - \rho_-)(\rho - \rho_c)^2$. Here $\tilde{V}(\rho)$ is a function that is strictly positive for $\rho > \rho_-$. The radius ρ_- is the other solution to $V_{\text{eff}}(\rho, z = 0) = 0$, and $\rho_- < \rho_c$. As the ISCO is approached, the effective potential develops a point of inflection at the location of the turning point rather than a maximum since $\rho_- \rightarrow \rho_c$. The epicyclic frequency for radial oscillations is $\Omega_\rho^2 = \tilde{V}(\rho_c)(\rho_c - \rho_-)$, which thus tends to zero as the ISCO is approached. The corresponding periapsis precession diverges. The radius ρ_- corresponds to an unstable circular orbit, and associated with any unstable circular orbit is a bound, eccentric orbit that has an infinite period — the object comes in from larger radii, and asymptotically approaches the radius of the circular

orbit. This is referred to as a “homoclinic” orbit, or as a “zoom-whirl” orbit in the EMRI literature. As the ISCO is approached, a small perturbation from the location of the circular orbit will put the object onto an orbit that is close to the homoclinic orbit associated with the unstable circular orbit. Hence, it takes a very long time for the object to complete a radial oscillation, but it is moving rapidly in the azimuthal direction the whole time, building up a large periapsis precession.

This understanding leads us to expect the precession to diverge at the location of the ISCO, and this divergence should be like $(\rho_c - \rho_{\text{ISCO}})^{-1/2}$, or $(\Omega_{\phi, \text{ISCO}} - \Omega_{\phi})^{-1/2}$. The above argument applies to an ISCO defined by a radial instability (as in the Kerr metric). As we saw in Section 5.4, the ISCO in the Manko-Novikov spacetimes can be determined by the onset of a vertical instability. In that case, the above argument still applies, but it is now the orbital-plane precession that will diverge as the ISCO is approached. This provides another potential ‘smoking-gun’ for a deviation from the Kerr metric. The divergence in the precession at the ISCO arises as a result of one of the two epicyclic frequencies going to zero. It is these frequencies that will in principle be observable in the gravitational waves. If an inspiral is observed starting in the weak-field and up until the last stable orbit (LSO), the different frequency components could be tracked, and one frequency will tend to zero as the LSO is approached. This is in principle an observable, and if it is the orbital-plane precession that goes to zero the central body cannot be a Kerr black hole. A more careful treatment of the gravitational-wave emission will be required to understand how practical it will be to make such observations.

In Figures 5.13–5.16 we show the precessions as a function of $M\Omega_{\phi}$ for a variety of values of q . In Figures 5.17–5.19 we present the same results, but now we show the differences between precessions in a bumpy spacetime with a given q and precessions in the Kerr spacetime with the same spin parameter χ : $\Delta p_X = p_X - p_X^{\text{Kerr}}$. The variable Δp_X represents the number of cycles of difference, so for instance a value of $\Delta p_{\rho} = 0.1$ means that the orbits in the two spacetimes, although having the same azimuthal frequency, would drift an entire cycle out of phase in the epicyclic radial oscillation within ten radial orbits. We do not show results for the difference in the

orbital-plane precession for $\chi = 0$, since there is no orbital-plane precession in the Schwarzschild spacetime and hence that plot would be identical to Figure 5.15.

Figures 5.13 and 5.17 show the periapsis precession $r_\rho(\Omega_\phi)$ for $\chi = 0$ while Figures 5.14 and 5.18 show the periapsis precession for $\chi = 0.9$. We see that as the value of q decreases from zero, the periapsis precession decreases relative to the corresponding value in the Kerr/Schwarzschild spacetime. By contrast, if q is increased from zero, the periapsis precession increases. In spacetimes with non-zero spin, the difference is more extreme for prograde orbits than for retrograde orbits. This is presumably because retrograde orbits do not get as close to the central object, and so do not “feel” the strong-field deviations in the bumpy metric.

For $q \geq -0.5$, the radial epicyclic frequency $\Omega_\rho(\Omega_\phi)$ approaches zero as the ISCO is approached and the periapsis precession r_ρ goes to infinity for the reasons described above. This is not true of the $q < -0.5$ spacetimes shown, since for those the ISCO is defined by a vertical instability. Figure 5.15 shows the orbital-plane precession $r_z(\Omega_\phi)$ for $\chi = 0$ and Figures 5.16 and 5.19 show the orbital-plane precession for $\chi = 0.9$. As for the case of the periapsis precession, the orbital-plane precession behaves qualitatively differently depending on the sign of q . The orbital-plane precession is greater for $q < 0$ and smaller for $q > 0$ compared to the non-bumpy value. As expected, the orbital-plane precession tends to a constant at the ISCO for $q > -0.5$, while it diverges for $q < -0.5$, since the ISCO for the latter spacetimes is defined by a vertical instability as discussed earlier.

Previous authors have looked at precessions in “bumpy” spacetimes. As mentioned above, Ryan [2] derived a weak-field expansion for the precessions. Collins & Hughes [11] looked at precessions for eccentric equatorial orbits in a perturbed Schwarzschild spacetime, and Glampedakis & Babak [12] did the same for a perturbed Kerr black hole. However, both pairs of authors did this by comparing orbits with the same coordinates, which is rather unphysical. Our results are consistent with this previous work in the weak-field, as it should be, but our calculation is the first that can be applied in the strong field, since Ryan’s work used a weak-field expansion, and the other work used perturbative spacetimes that break down close to the central

body. The behavior in the approach to the ISCO is thus a new result.

It is possible to fit the precessions as a sum of a weak-field expansion (as given in Section 5.8) plus a term $A/\sqrt{\Omega_{\phi,\text{ISCO}} - \Omega_{\phi}}$. However, only a comparatively few weak-field terms are required to give a good fit, implying that the divergence at the ISCO limits the number of multipole moments that can be recovered from such an expansion. To quantify this statement properly, we must do a full analysis, that includes the effect of inspiral, uses an instrumental noise curve to restrict the observable bandwidth and accounts for parameter correlations via the Fisher Matrix. We can do this by constructing semi-relativistic inspiral waveforms for bumpy spacetimes in the same way that has been used for Kerr inspirals [27, 25]. This is beyond the scope of the present paper. However, there are several things that we can take away from the current results — the location of the ISCO has a strong influence on precessions that could be observable, in particular the nature of the instability that defines the ISCO could be a clear indicator of a non-Kerr system; precessions can be very different in the strong field in the presence of a deviation; circular orbits with frequencies very different from the Kerr value exist in some bumpy spacetimes, so another observable signature would be that an inspiral persists at frequencies inside the Kerr ISCO.

5.5.3 Effect of Eccentricity

As discussed above, the measurement of the precessions as a function of orbital frequency for nearly circular, nearly equatorial orbits would in principle allow measurement of the spacetime multipole moments [2]. In practice, however, the precessions will only be manifest in the observed gravitational waves if the orbit is not circular and equatorial, so we need to understand how the dependence of the precessions on azimuthal frequency differs when we relax the assumption of near-circularity. In the following, we shall focus on the periapsis precession of eccentric but equatorial orbits.

The eccentricity of an orbit modifies two things — 1) the frequency associated with the periapsis precession as a function of the orbital frequency; 2) the relative amplitudes of different harmonics of these two frequencies in the observed GWs. To accurately compute the dependence of the harmonic structure on eccentricity for a

generic orbit, we need to know details of GW generation in a spacetime with arbitrary multipole moments. This is a difficult problem, so we focus on the effect of eccentricity on the periapsis precession frequency itself. We consider an eccentric equatorial orbit in the Kerr spacetime, and use Ω_ϕ to denote the average azimuthal frequency (i.e., the total advance in ϕ over one radial period, divided by the period of the radial motion). We define an orbital eccentricity, e , such that the ratio of the Boyer-Lindquist radii of the periapse, r_p , and apapse, r_a , of the radial motion is $r_p/r_a = (1 - e)/(1 + e)$. With these definitions, the periapsis precession as defined above can be found to be

$$\begin{aligned}
 p_\rho = & 3 \left(\frac{M\Omega_\phi}{(1 - e^2)^{\frac{3}{2}}} \right)^{\frac{2}{3}} - 4\chi \left(\frac{M\Omega_\phi}{(1 - e^2)^{\frac{3}{2}}} \right) + \frac{3(18 - 7e^2 + 2\chi^2)}{4} \left(\frac{M\Omega_\phi}{(1 - e^2)^{\frac{3}{2}}} \right)^{\frac{4}{3}} \\
 & - (34 - 18e^2) \chi \left(\frac{M\Omega_\phi}{(1 - e^2)^{\frac{3}{2}}} \right)^{\frac{5}{3}} + \dots
 \end{aligned} \tag{5.21}$$

where we are expanding in the weak field, $M\Omega_\phi \ll 1$. The corresponding result for a spacetime with an excess quadrupole moment can be found at lowest order by replacing the term in χ^2 with $\chi^2 + q$, since the quadrupole moment of a Kerr black hole is χ^2 as discussed earlier.

In the circular limit, $e = 0$, the expansion (5.21) allows us to extract M from the coefficient of $\Omega_\phi^{2/3}$, χ from the coefficient of Ω_ϕ , q from the coefficient of $\Omega_\phi^{4/3}$ etc. However, if we expand to lowest order in the eccentricity, e , it is clear that the effect of a small excess oblate quadrupole moment $q > 0$ could be mimicked, at leading order, by an eccentricity evolving as $e^2 = 2(M\Omega_\phi)^{-2/3}q$. The two possibilities are then distinguished by knowing how the eccentricity should evolve with $M\Omega_\phi$.

The expansion (5.21) contains redundancy, since the coefficient of $M\Omega_\phi^{5/3}$ also depends only on the lowest current moment, χ . If the eccentricity of the orbit did not evolve with time the first four terms in the expansion would determine M , χ , q and the eccentricity e , and higher terms would determine the remaining multipole moments as in the circular case. However, the eccentricity does evolve with time. In practice, we will only observe EMRIs as they evolve through a finite range of frequencies (determined by the detector sensitivity). During that period, the evolution will be

driven entirely by gravitational-wave emission. This means that we can quantify the eccentricity of the orbit by a single number — the periapse at which the eccentricity was equal to 1 if we integrated the inspiral backwards in time, assuming a purely GW driven inspiral. Specifying this parameter *and the multipole structure of the spacetime* determines the eccentricity as a function of $M\Omega_\phi$. Determining this relationship, however, requires knowing the details of GW emission in an arbitrary spacetime.

A complication arises because the ratio $M\Omega_\phi/(1-e^2)^{3/2}$ tends to a constant at the point where $e = 1$. Assuming that this occurred in the weak-field, $M\Omega_\phi/(1-e^2)^{3/2} \ll 1$, this can be seen by considering the leading order term in $de/d\Omega_\phi$ in the weak-field (see for instance [27])

$$\frac{de}{d(M\Omega_\phi)} = \frac{-(304 + 121e^2)(1 - e^2)e}{3(M\Omega_\phi)(96 + 292e^2 + 37e^4)}. \quad (5.22)$$

Denoting $X = 1 - e^2$ and expanding in the limit $M\Omega_\phi \rightarrow 0$, $X \rightarrow 1$, we find

$$\frac{dX}{d(M\Omega_\phi)} \approx \frac{2}{3} \frac{X}{M\Omega_\phi} \Rightarrow X = X_0(M\Omega_\phi)^{\frac{2}{3}} + O(\Omega_\phi^{\frac{4}{3}}) \quad (5.23)$$

in which X_0 is a constant that is related to the periapse at “capture” when $X = 0$. If the capture occurs in the strong field, the ratio $M\Omega_\phi/(1 - e^2)^{3/2}$ would still tend to a constant if we integrated backward until $e \rightarrow 1$. Although the inspiral would not be observed as $e \rightarrow 1$, that section of the inspiral does affect the portion that we can observe.

We now substitute the asymptotic behavior (5.23) into Eq. (5.21), to obtain an expansion of the periapsis precession as a function of the angular frequency in the form $p_\rho = a_0 + a_2(M\Omega_\phi)^{2/3} + a_3(M\Omega_\phi) + \dots$, where a_0, a_2, a_3 etc. are constants. In contrast to the circular case, each of these coefficients depends on all the spacetime multipole moments, so multipole extraction from the periapsis precession expansion is no longer straightforward. The reason for this qualitative difference between circular and eccentric orbits is that it is only possible to observe an eccentric inspiral over a finite range of periapse, since the orbit is captured with a certain finite periapse, while a circular orbit could inspiral from infinity. The various multipole moments

have different radial dependencies, thus if one can observe the precession frequency at any radius it makes sense that all the moments can be separately extracted, while this is more difficult if only a finite section of the spacetime is explored.

In practice, this difficulty also arises when observing a circular inspiral, since the radiation can only be detected in a certain frequency range. One can parameterize an observation by the frequency at the start of the observation, $\Omega_0 = \Omega_\phi(t = 0)$. A Taylor series expansion of the precession (see Eq. (5.41) in the Appendix) then gives

$$\begin{aligned}
p_\rho &= \left(3(M\Omega_0)^{\frac{2}{3}} - 4\chi(M\Omega_0) + \frac{3}{2}(9 + \chi^2 + q)(M\Omega_0)^{\frac{4}{3}} + \dots \right) \\
&\quad + \left(2(M\Omega_0)^{\frac{2}{3}} - 4\chi(M\Omega_0) + 2(9 + \chi^2 + q)(M\Omega_0)^{\frac{4}{3}} + \dots \right) \frac{\Omega_\phi - \Omega_0}{\Omega_0} \\
&\quad + \left(-\frac{1}{3}(M\Omega_0)^{\frac{2}{3}} + \frac{1}{3}(9 + \chi^2 + q)(M\Omega_0)^{\frac{4}{3}} + \dots \right) \left(\frac{\Omega_\phi - \Omega_0}{\Omega_0} \right)^2 + \dots \\
&= b_0 + b_1 \frac{\Omega_\phi - \Omega_0}{\Omega_0} + b_2 \left(\frac{\Omega_\phi - \Omega_0}{\Omega_0} \right)^2 + \dots \tag{5.24}
\end{aligned}$$

In this kind of expansion the multipole moments again contribute at all orders. However, provided the initial frequency $M\Omega_0 \ll 1$, the dominant piece of the constant term, b_0 , is $(M\Omega_0)^{\frac{2}{3}}$, so this term can be used to estimate M . Similarly, the dominant piece of $2b_0 - 3b_1$ is $4\chi(M\Omega_0)$, so this can be used to estimate χ , and that estimate of χ can be used to improve the estimate of M from b_0 . The dominant piece of $b_0 - b_1 + 3b_2$ is $(9 + \chi^2 + q)/2(M\Omega_0)^{\frac{4}{3}}$, so this can be used to estimate the excess quadrupole moment q and so on. In the same way, if an eccentric inspiral is observed in a regime where the initial frequency is small (and hence the frequency at capture was also small), we can use the same type of expansion and use combinations of the coefficients to successively extract each multipole moment and the initial eccentricity. To do this requires an expansion of $e^2 - e_0^2$ as a function of $\Omega_\phi/\Omega_0 - 1$. The necessary derivatives $de^2/d(M\Omega_\phi)$ are known in the weak-field, and to lowest order in the multipoles (see, for example, reference [27]). However, this calculation is somewhat involved and beyond the scope of this paper.

The above discussion indicates that the periapsis precession rate can be used on its own to measure the multipole moments from an eccentric equatorial inspiral, al-

though this is more difficult than for the circular equatorial case. However, the value of the precession is not the only observable. As mentioned earlier, the relative amplitude of the various harmonics of the orbital frequencies is a powerful probe of the orbital eccentricity. To exploit this harmonic structure we also need to know how the amplitudes of the harmonics depend on the spacetime multipole moments. However, if the deviations from the Kerr metric multipole structure are small, we could imagine using the Kerr harmonic amplitude relation to estimate the eccentricity (and inclination) of the orbit, and then use the precessions to extract the multipole structure. Proper insight can be gained using the approximate semi-relativistic waveforms described earlier or post-Newtonian expansions of the gravitational waveforms. Such an investigation will be an important extension of the current work.

5.6 Summary

In this paper we have discussed various observational signatures that could leave an imprint on an EMRI gravitational waveform if the spacetime in which the EMRI was occurring deviated from the Kerr metric. We have seen that some orbits in “bumpy” spacetimes lack a fourth integral of the motion, and appear ergodic. Geodesics in the Kerr spacetime have a complete set of integrals, so if an apparently ergodic orbit was observed it would be a clear signature of a non-Kerr central object. However, regions of ergodic motion only appear very close to the central object, in a regime which is probably inaccessible to a star inspiraling from large distances. Most astrophysically relevant orbits are regular and appear to possess an approximate fourth integral of the motion, and the orbits are tri-periodic to high accuracy. The deviations of the central body from Kerr then manifest themselves only in the changes in the three fundamental frequencies of the motion and the relative amplitude of the different harmonics of these frequencies present in the gravitational waves. For nearly circular, nearly equatorial orbits, the dependence of the precession frequencies on the orbital frequency is well fit by a combination of a weak field expansion that encodes the multipole moments at different orders, plus a term that diverges as the innermost stable circular orbit

is approached. The frequency of the ISCO and its nature (whether it is defined by a radial or vertical instability) is another observable signature of a non-Kerr central object.

To derive these results, we have focussed on a particular family of spacetimes due to Manko and Novikov [13]. However, we expect the generic features of the results in the weak field and as the ISCO is approached to be true for a wide range of spacetimes. Chaos has been found for geodesic motion in several different metrics by various authors [14, 15, 16, 17, 18]. In all cases, however, the onset of chaos was qualitatively similar to what we found here — it occurred only very close to the central object, and for a very limited range of orbital parameters. The conclusion that gravitational waves from ergodic EMRIs are unlikely to be observed is thus probably quite robust.

Precessions for spacetimes that deviate from the Kerr metric have also been considered by several authors [2, 11, 12]. Our results agree with this previous work in the weak-field as it should. However, the results in the present paper are the first that are valid in the strong-field since previous work was either based on a weak-field expansion [2] or a perturbative spacetime [11, 12]. The main feature of the precessions in the strong-field — the divergence of one of the precessions as the ISCO is approached — is expected from spacetime-independent considerations and therefore should be a general feature of inspirals in any spacetime. The present work, and earlier research [11, 12], has also considered only solutions that first differ from the Kerr metric in the mass quadrupole moment. The Manko-Novikov solutions [13] include spacetimes that first differ at higher orders. While we have not considered such solutions, we expect the generic features to be similar. The precessions will be closer to the Kerr values for a greater fraction of the inspiral, and the ISCO will be at a different frequency, but the qualitative behavior in the approach to ISCO should be the same.

The next step in understanding how gravitational-wave detectors might identify non-Kerr central objects from EMRI observations is to consider the gravitational waveforms produced during an inspiral. Any analysis should account for both param-

eter correlations and the finite bandwidth and observation time of gravitational-wave detectors by using a Fisher Matrix analysis. Glampedakis and Babak [12] constructed approximate gravitational waveforms generated by orbits in a perturbed Kerr spacetime, but they considered only waveforms from geodesics (i.e., not inspirals) and compared waveforms with the same orbital parameters. These are not observable quantities (unlike the frequency of the orbit which we used as a basis for comparison here) and such a calculation does not account for parameter correlations. Barack and Cutler [26] did a full Fisher Matrix analysis of this problem, and estimated that a LISA observation of an EMRI could measure the quadrupole moment of a body to an accuracy of 10^{-3} while simultaneously measuring the mass and spin to 10^{-4} . That calculation was based on an approximate waveform model devised to describe Kerr inspirals. The expressions governing the inspiral were modified by adding the leading order effect of a quadrupole moment to the energy and angular momentum fluxes. The waveform generation part of the algorithm was left unchanged. Although this result is a good guide, the calculation contained a number of inconsistencies. For Kerr inspirals, semi-relativistic “kludge” waveforms based on combining exact geodesic motion with approximate gravitational-wave emission formulae have proven to give accurate results [27, 25]. The same method could be used to produce waveforms for inspiral in the Manko-Novikov spacetimes, by changing the geodesic equations and augmenting the inspiral fluxes appropriately. Such an approach will not generate totally accurate gravitational waveforms, but it will reproduce the main features of the orbit — the precession frequencies, the orbital shape and the frequency of the ISCO. A study of gravitational waveforms generated in “bumpy” spacetimes will provide useful guidance for future detectors such as to what precision an observation could determine that an inspiral is an inspiral into a Kerr black hole and how well observations can distinguish different types of deviation from Kerr, e.g., an exotic central object from a naked singularity from a Kerr black hole with external matter.

5.7 Appendix A. Chaotic Motion in Newtonian Gravity

The classic example from astrophysics of a system that exhibits chaos in classical (Newtonian) gravity is the two dimensional Hénon-Heiles potential $V(r, \theta) = r^2/2 + r^3 \sin 3\theta/3$ (see [28] for example). Guéron and Letelier [16] also found chaos in the Paczyński-Witta potential ($\Phi = M/(r - r_S)$, where $r_S = 2M$ is the Schwarzschild radius) with a dipolar perturbation. Neither of these spacetimes is reflection symmetric, so for a better analogy to the relativistic spacetimes considered in this paper, we examine the Newtonian quadrupole-octupole potential

$$\Phi(\rho, z) = -\frac{M}{r} - \frac{M_2}{2r^3} \left(1 - 3\frac{z^2}{r^2}\right) + \frac{M_4}{8r^5} \left(35\frac{z^4}{r^4} - 30\frac{z^2}{r^2} + 3\right). \quad (5.25)$$

Here, M , M_2 and M_4 denote the monopole (mass), quadrupole and octupole multipole moments of the potential. Stationarity and axisymmetry ensure that energy E and angular momentum $L_z = r^2 d\phi/dt$ are conserved as usual, which leads us to the Newtonian analogue of the effective potential equation (5.13)

$$\frac{1}{2} \left(\left(\frac{dr}{dt} \right)^2 + \left(\frac{dz}{dt} \right)^2 \right) = V_{\text{eff}}(E, L_z, \rho, z) = \frac{1}{2} (E^2 - 1) - \frac{L_z^2}{2\rho^2} - \Phi(\rho, z) \quad (5.26)$$

where we have replaced the standard Newtonian energy by the relativistic expression $(E^2 - 1)/2$ for consistency with (5.13). The equation of motion in this potential takes the usual form $d^2\mathbf{r}/dt^2 = -\nabla\Phi$. If we take the multipole moments to have the values $M_2 = 2M^3$ and $M_4 = 10M^5$, and choose the angular momentum to be $L_z = 1.7M$, we find that for a range of values of the energy E , bound orbits occur quite close to the origin. For sufficiently large values of E , there is a single allowed region for motion (defined by $V_{\text{eff}} \geq 0$). Orbits in that regime appear to be regular, and show closed Poincaré maps. If the energy is reduced, the allowed region eventually splits into two separate regions, one bounded away from $r = 0$, and one connected to $r = 0$. Orbits in the outermost region after this transition exhibit ergodic behavior. In Figure 5.20 we show four plots. Two of these plots are for an orbit with $E = 0.82$, which exhibit

regular behavior. The other two are for $E = 0.81$ and exhibit ergodic behavior. We choose the initial conditions of both orbits to be $\dot{\rho} = 0 = \dot{z}$ and $\rho = 3M$, with \dot{z} determined from the assigned energy (5.26). The upper panels in the figure show the orbit in the (ρ, z) plane, and the boundary of the allowed region of motion (defined by $V_{\text{eff}} = 0$). The lower panels show Poincaré maps for the two orbits. The ergodicity of the orbit with $E = 0.81$ is quite evident from the Poincaré map. We also find that this orbit fills up the entire allowed range of ρ and z . By contrast, the regular orbit with $E = 0.82$ explores only a narrow torus in space.

A thorough examination of when ergodicity appears in this potential, as a function of energy, angular momentum and the multipole moments M_2 and M_4 is peripheral to the focus of this paper. However, the results presented here provide a Newtonian example to which we can compare the relativistic results of Section 5.3.

5.8 Appendix B. Weak Field Precessions

5.8.1 Relativistic Precession

In Boyer-Lindquist coordinates, the energy, angular momentum and rest-mass conservation equations (5.10)–(5.11) for geodesic motion in the Kerr metric can be used to derive the equation of motion in the form (see for instance [29])

$$\frac{1}{2} \left(\left(\frac{dr}{dt} \right)^2 + \Delta \left(\frac{d\theta}{dt} \right)^2 \right) = \frac{(E(r^2 + a^2) - aL_z)^2 - \Delta (r^2 + (L_z - aE)^2 + L_z^2 \cos^2 \theta + a^2 \cos^2 \theta (1 - E^2))}{2 (E((r^2 + a^2)^2/\Delta - a^2 \sin^2 \theta) - 2MaL_z r/\Delta)^2} \quad (5.27)$$

where $\Delta = r^2 - 2Mr + a^2$, and $a = M\chi$. The prograde equatorial circular orbit at radius r has energy and angular momentum

$$E = \frac{1 - 2v^2 + av^3/M}{\sqrt{1 - 3v^2 + 2av^3/M}} \quad (5.28)$$

$$L_z = rv \frac{1 - 2av^3/M + a^2v^4/M^2}{\sqrt{1 - 3v^2 + 2av^3/M}} \quad (5.29)$$

where $v^2 = M/r$. The frequency of a prograde circular orbit is given by

$$\Omega_\phi = \frac{d\phi}{dt} = \frac{\sqrt{M}}{r^{3/2} + a\sqrt{M}}. \quad (5.30)$$

The epicyclic frequencies for radial and vertical perturbations of the orbit are given by the second derivatives of the right hand side of equation (5.27) with respect to r and θ (the right hand side of Eq. (5.27) is the effective potential for the Kerr spacetime). To obtain the form of these frequencies in the weak field, we wish to expand in $1/r$. With some manipulation and keeping terms up to r^{-5} only, we obtain the expansion

$$\Omega_\rho^2 = \frac{M}{r^3} - 6\frac{M^2}{r^4} + 6\chi\frac{M^{5/2}}{r^{9/2}} - 3\chi^2\frac{M^3}{r^5} + \dots \quad (5.31)$$

$$\Omega_z^2 = \frac{M}{r^3} - 6\chi\frac{M^{5/2}}{r^{9/2}} + 3\chi^2\frac{M^3}{r^5} + \dots \quad (5.32)$$

where we use Ω_ρ, Ω_z to denote the radial and vertical epicyclic frequencies to be consistent with the results earlier in the paper. With further manipulation, expressions for the precessions, p_X , as a function of the orbital frequency, Ω_ϕ , may be derived

$$\begin{aligned} p_\rho &= 3(M\Omega_\phi)^{\frac{2}{3}} - 4\chi(M\Omega_\phi) + \frac{3}{2}(9 + \chi^2)(M\Omega_\phi)^{\frac{4}{3}} - 34\chi(M\Omega_\phi)^{\frac{5}{3}} \\ &\quad + \frac{1}{2}(135 + 67\chi^2)(M\Omega_\phi)^2 + \dots \end{aligned} \quad (5.33)$$

$$p_z = 2\chi(M\Omega_\phi) - \frac{3}{2}\chi^2(M\Omega_\phi)^{\frac{4}{3}} + 8\chi^2(M\Omega_\phi)^2 + \dots \quad (5.34)$$

Results for retrograde orbits may be obtained by the substitutions $\chi \rightarrow -\chi$, $\Omega_\phi \rightarrow -\Omega_\phi$ and $L_z \rightarrow -L_z$ in the above expressions (NB $\Omega_\phi < 0$ for retrograde orbits, so $-\Omega_\phi$ is equivalent to $|\Omega_\phi|$).

5.8.2 Precession due to a Quadrupole Moment

The precession induced by a quadrupole moment can be derived using the Newtonian quadrupole potential

$$\Phi = -\frac{M}{r} - \frac{1}{2}\frac{Q}{r^3}\left(1 - 3\frac{z^2}{r^2}\right). \quad (5.35)$$

Here $r = \sqrt{x^2 + y^2 + z^2}$ is the distance from the origin, z is the vertical coordinate and we will use $\rho = \sqrt{x^2 + y^2}$ to denote the cylindrical polar radial coordinate. The

radial equation of motion in this potential takes the form

$$\frac{1}{2} \left(\frac{d\rho}{dt} \right)^2 = E - \frac{L_z^2}{2\rho^2} + \frac{M}{r} + \frac{1}{2} \frac{Q}{r^3} \left(1 - 3 \frac{z^2}{r^2} \right) \quad (5.36)$$

and the energy, angular momentum and orbital frequency of a circular, equatorial orbit with radius ρ are

$$\begin{aligned} E &= \frac{Q}{4\rho^3} - \frac{M}{2\rho} \\ L_z &= \sqrt{M\rho + \frac{3Q}{2\rho}} \\ \Omega_\phi &= \sqrt{\frac{M}{\rho^3} + \frac{3Q}{2\rho^5}} \end{aligned} \quad (5.37)$$

Differentiating Eq. (5.36) twice with respect to ρ and z , we find the epicyclic frequencies take the form

$$\Omega_\rho^2 = \frac{M}{\rho^3} - \frac{3}{2} Q \frac{M}{r^5} + \dots \quad (5.38)$$

$$\Omega_z^2 = \frac{M}{\rho^3} + \frac{3}{2} Q \frac{M}{r^5} + \dots \quad (5.39)$$

Hence we derive the precession frequencies

$$\begin{aligned} p_\rho &= -\frac{3}{2} \frac{Q}{M^3} (M\Omega_\phi)^{\frac{4}{3}} + \dots \\ p_z &= \frac{3}{2} \frac{Q}{M^3} (M\Omega_\phi)^{\frac{4}{3}} + \dots \end{aligned} \quad (5.40)$$

The lowest order form of these expressions was also given in Collins and Hughes [11], although they expressed the precession in terms of a radial coordinate, rather than the observable Ω_ϕ . We also use a slightly different definition for the quadrupole moment Q so that it is consistent with $Q = \chi^2 M^3$ for the Kerr metric. As we would expect, the leading-order terms in these expressions agree with the leading order terms in χ^2 in the Kerr expressions.

Combining this result with Eq. (5.34), we obtain the weak-field precessions for the

Manko-Novikov solution with spin parameter χ and excess quadrupole moment q

$$\begin{aligned}
 p_\rho &= 3(M\Omega_\phi)^{\frac{2}{3}} - 4\chi(M\Omega_\phi) + \frac{3}{2}(9 + \chi^2 + q)(M\Omega_\phi)^{\frac{4}{3}} - 34\chi(M\Omega_\phi)^{\frac{5}{3}} \\
 &\quad + \frac{1}{2}(135 + 67\chi^2 + 39q)(M\Omega_\phi)^2 + \dots \\
 p_z &= 2\chi(M\Omega_\phi) - \frac{3}{2}(\chi^2 + q)(M\Omega_\phi)^{\frac{4}{3}} + (8\chi^2 - 3q)(M\Omega_\phi)^2 + \dots \quad (5.41)
 \end{aligned}$$

In the above, the lowest order term that is omitted is the order at which the excess current quadrupole moment would first contribute. This result is also given in Ryan [2], although he quotes an expression for $\tilde{\Omega}_\rho/\Omega_\phi$, where $\tilde{\Omega}_\rho$ is equal to $\Omega_\phi - \Omega_\rho$. Our result is consistent with his once this is taken into account. We note that some of the terms in expression (5.41) come from relativistic corrections to the effect of the quadrupole moment. These cannot be derived using only the results quoted in this appendix, but are given in Ryan's paper [2].

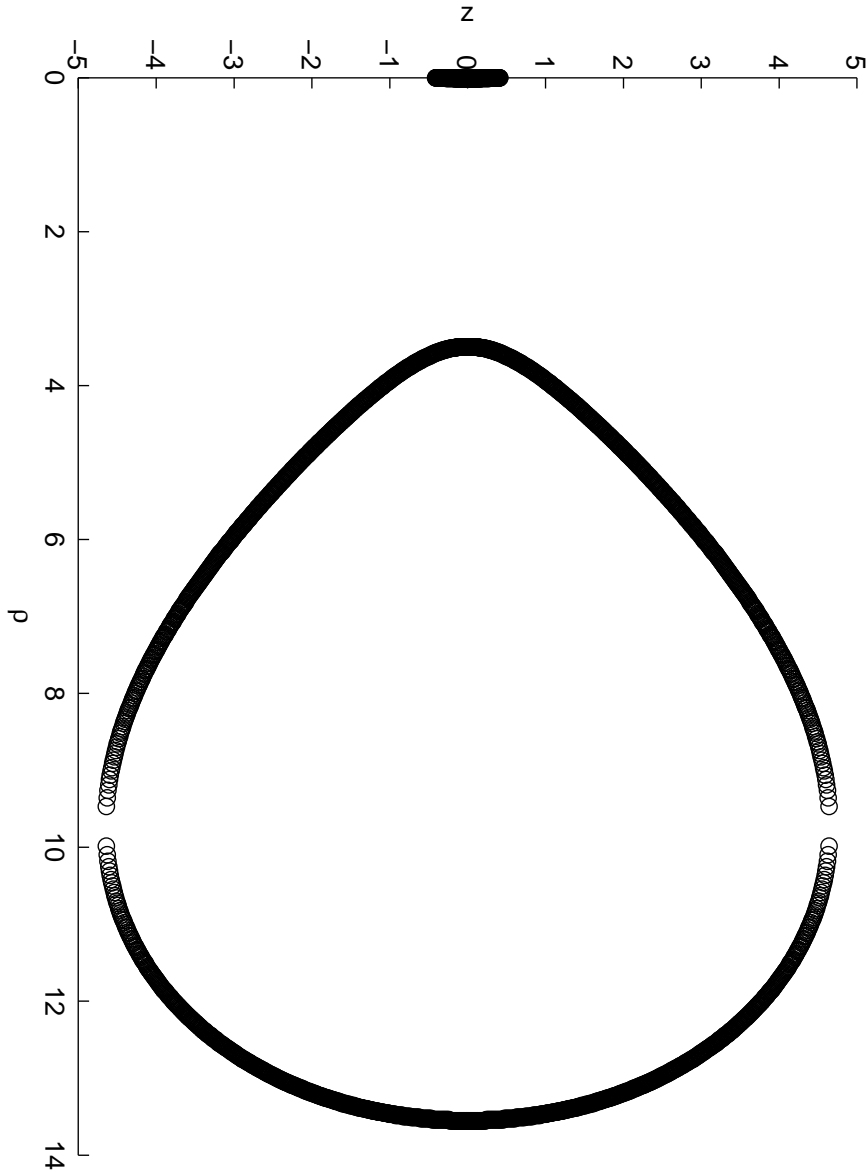


Figure 5.3: Effective potential for geodesic motion around a Kerr black hole, with $E = 0.95$, $L_z = 3M$ and $\chi = 0.9$. The curves indicate zeros of the effective potential. Allowed orbits are found in the small region around $\rho = 0$, $z = 0$ (rising and plunging orbits) or in the region containing $\rho = 10$, $z = 0$ (bound orbits).

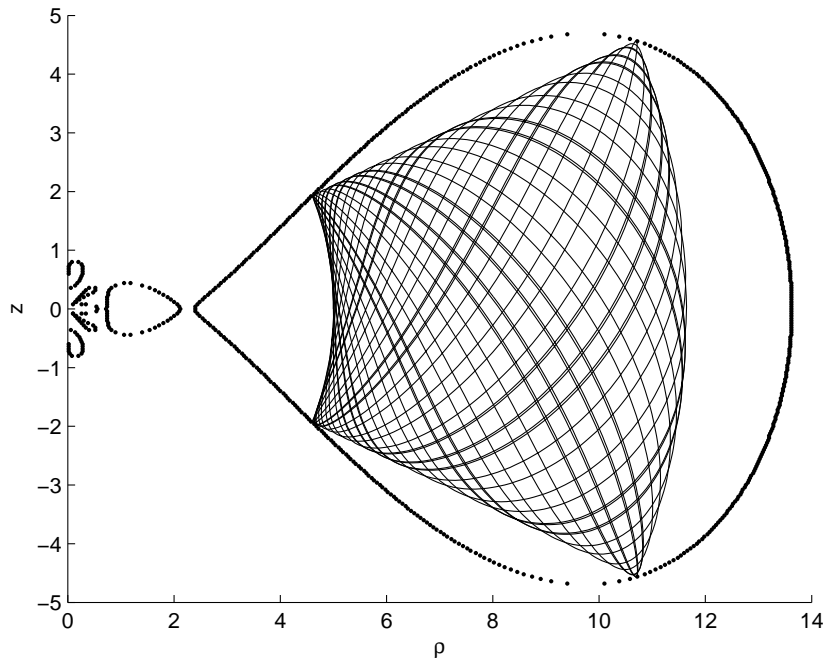


Figure 5.4: Effective potential for geodesic motion around a bumpy black hole with $\chi = 0.9$, $q = 0.95$, $E = 0.95$, and $L_z = 3M$. The thick dotted curves indicate zeros of the effective potential. The trajectory of a typical geodesic in the outer region is shown by a thin curve. The regular pattern of self-intersections of the geodesic projection onto the $\rho - z$ plane indicates (nearly) regular dynamics.

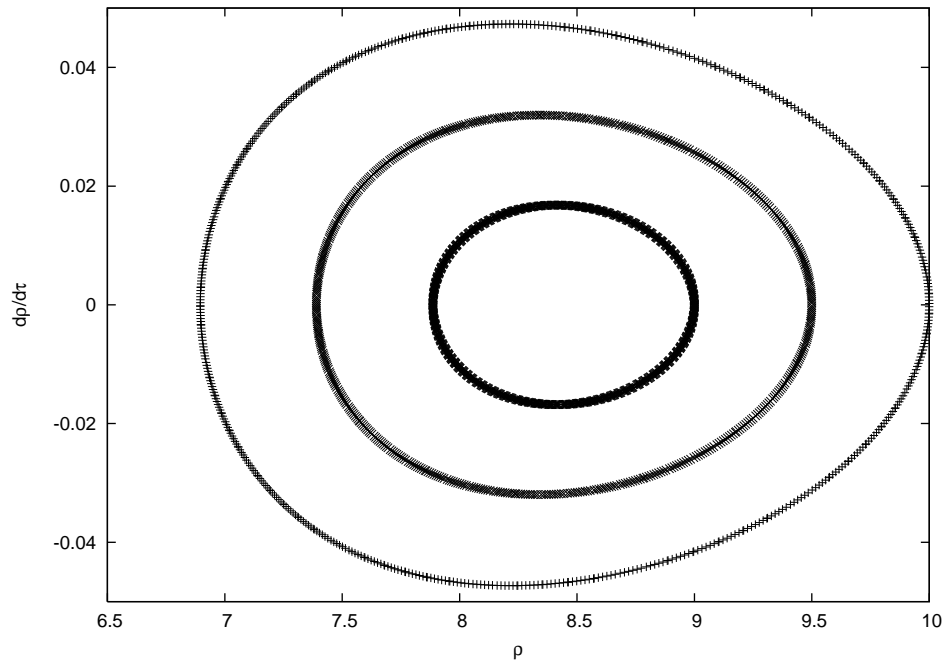


Figure 5.5: Poincaré map showing $d\rho/d\tau$ vs ρ for crossings of the $z = 0$ plane for a sequence of orbits in the outer allowed region of the Kerr spacetime with $E = 0.95$, $L_z = 3M$ and $\chi = 0.9$. The closed curves indicates the presence of a fourth isolating integral, which we know to be the Carter constant.

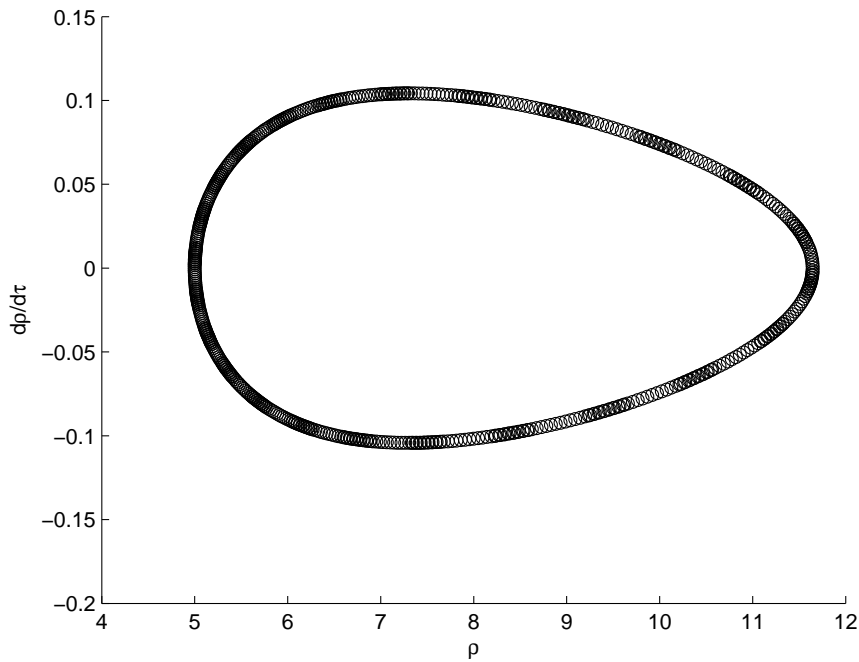


Figure 5.6: Poincaré map for a geodesic in the outer region of Fig. 5.4.

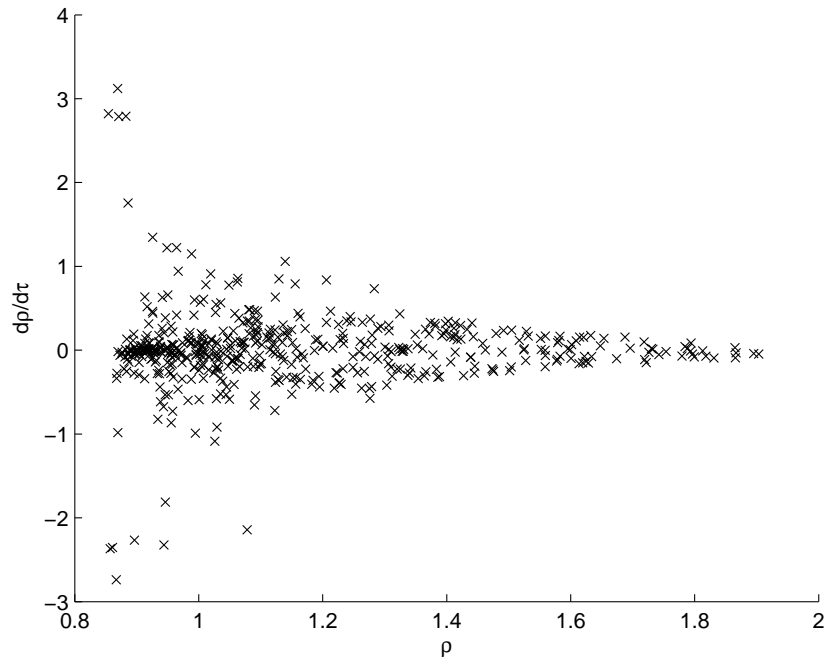


Figure 5.7: Poincaré map for a geodesic in the inner region of Fig. 5.4.

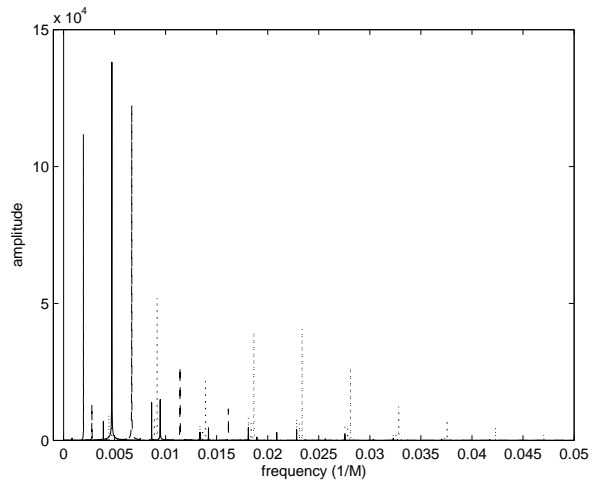


Figure 5.8: Absolute values of the Fourier transforms of $\rho(t)$ (solid line), $z(t)$ (dashed line), and the gravitational wave component $h_+(t)$ (dotted line) in the frequency domain for an orbit in the outer region of Fig. 5.4. The frequency is displayed in units of $1/M$; the amplitude scaling is arbitrary.

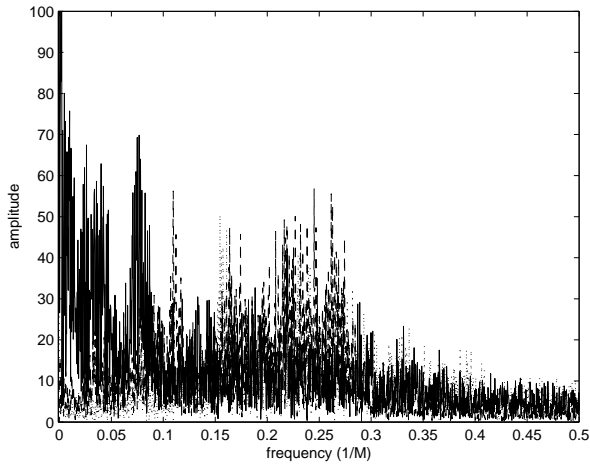


Figure 5.9: Absolute values of the Fourier transforms of $\rho(t)$ (solid line), $z(t)$ (dashed line), and the gravitational wave component $h_+(t)$ (dotted line) in the frequency domain for an orbit in the inner region of Fig. 5.4. The frequency is displayed in units of $1/M$; the amplitude scaling is arbitrary.

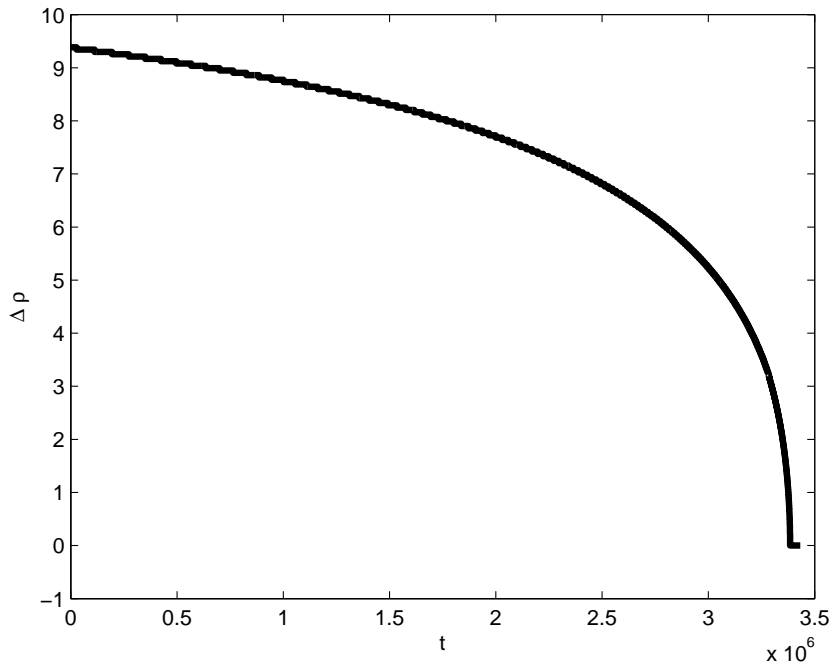


Figure 5.10: The evolution of the separation $\Delta\rho$ between the inner and outer bounded regions in the equatorial plane along an inspiral in a Manko-Novikov spacetime with $\chi = 0.9$ and $q = 0.95$. $\Delta\rho = 0$ means that the two regions have merged and there is a single bounded region.

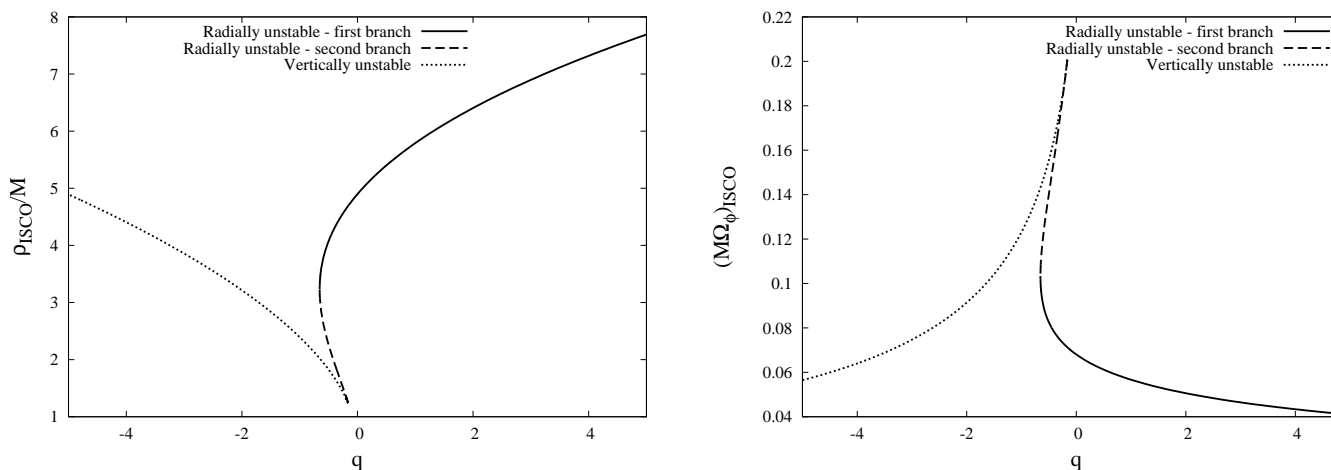


Figure 5.11: Properties of the equatorial ISCO in spacetimes with $\chi = 0$, as a function of q . We show the ρ coordinate of the ISCO (left panel) and the dimensionless frequency of the orbit at the ISCO (right panel). As described in the text, the ISCO radius has three branches, depending on whether it is determined by one of the two branches of radial instability or the branch of vertical instability. These branches are indicated separately in the diagram. For values of q where all three branches are present, the dashed line denotes the “OSCO” and the dotted line denotes $\tilde{\rho}_{\text{ISCO}}$ as discussed in the text. Allowed orbits lie above the curve in the left panel, and below the curve in the right panel.

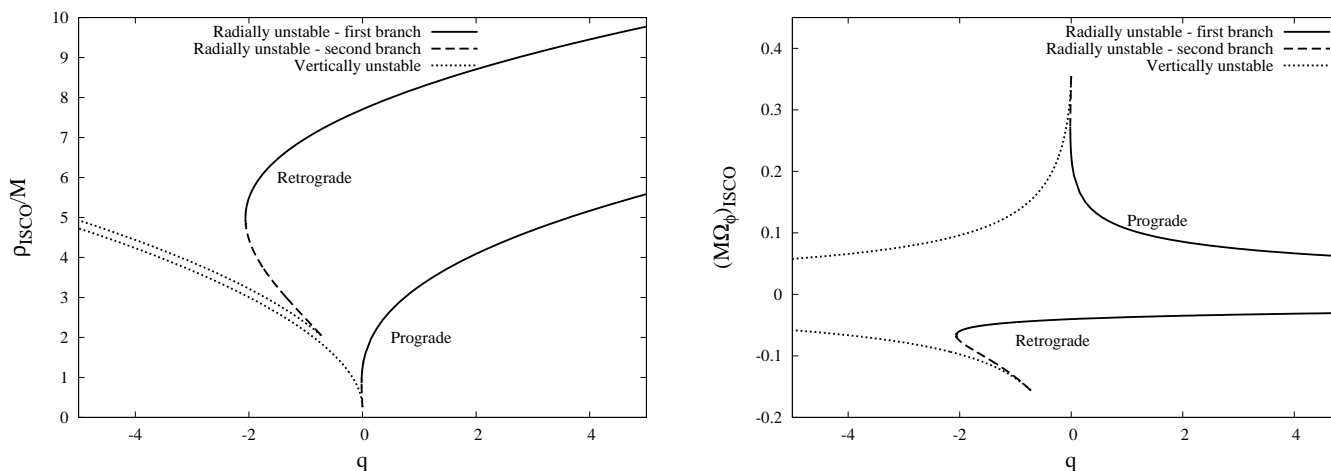


Figure 5.12: As Figure 5.11, but now for a spin of $\chi = 0.9$. There are now two ISCO curves, one for prograde orbits and one for retrograde orbits. The allowed range of orbital frequencies is given by the region in between the two curves in the right hand panel.

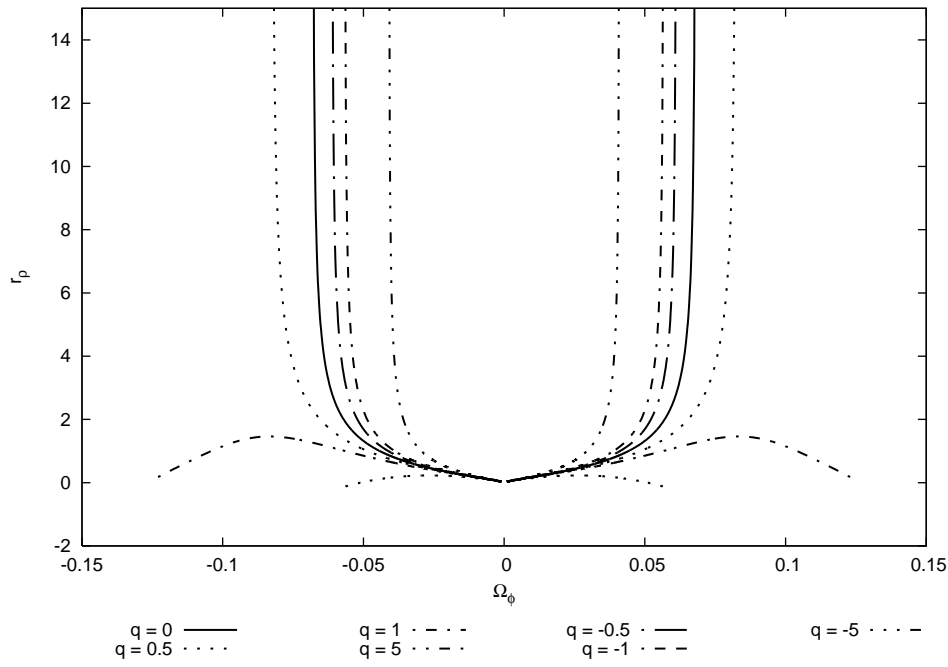


Figure 5.13: Periapsis precession p_ρ versus azimuthal frequency Ω_ϕ for $\chi = 0$ and various values of q .

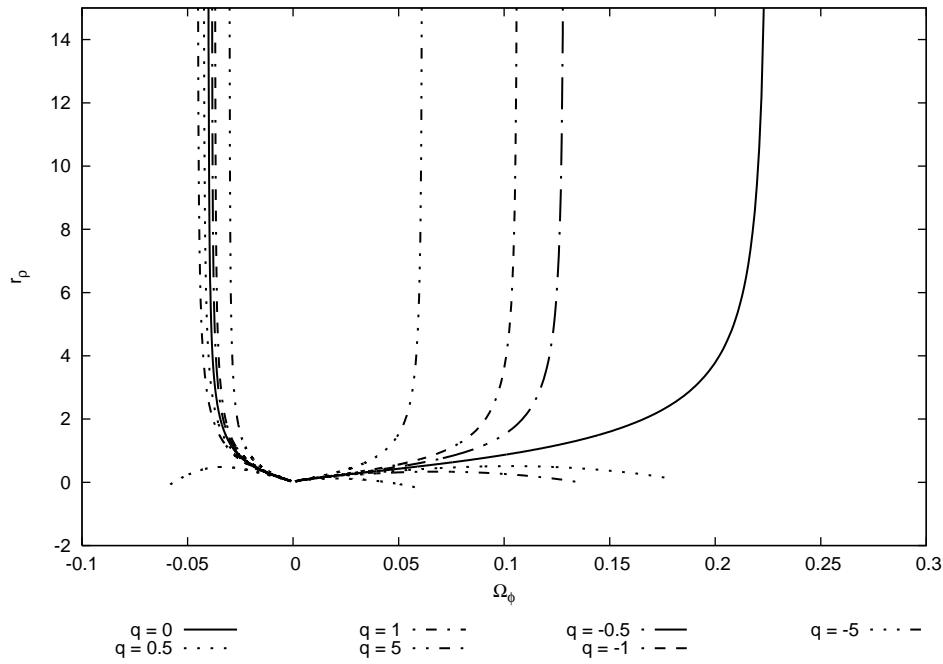


Figure 5.14: Periapsis precession p_ρ versus azimuthal frequency Ω_ϕ for $\chi = 0.9$ and various values of q .

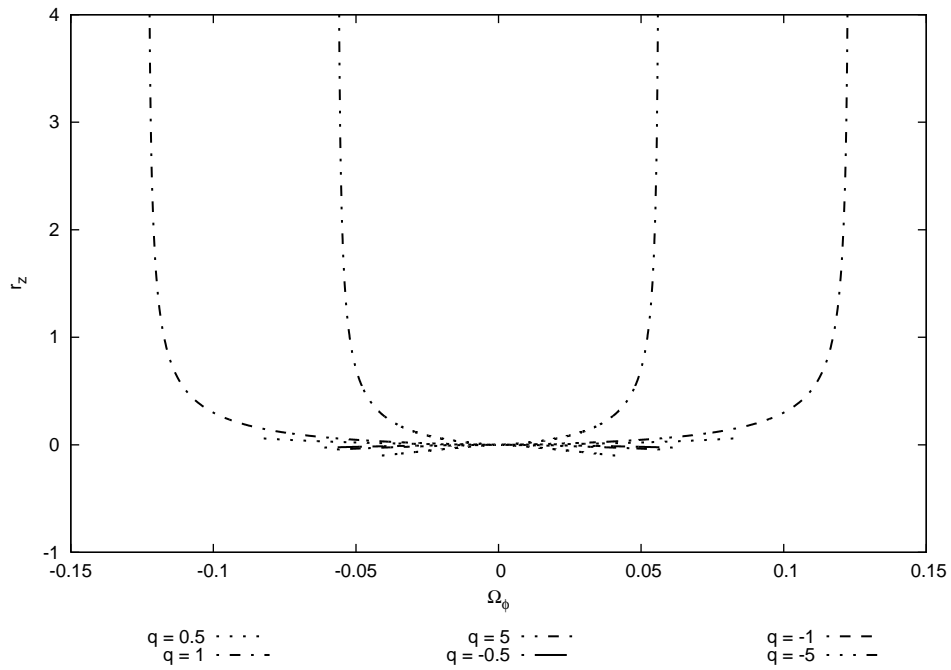


Figure 5.15: Orbital-plane precession p_z versus azimuthal frequency Ω_ϕ for $\chi = 0$ and various values of q . We do not show the case $q = 0$ here, since there is no orbital-plane precession in Schwarzschild.

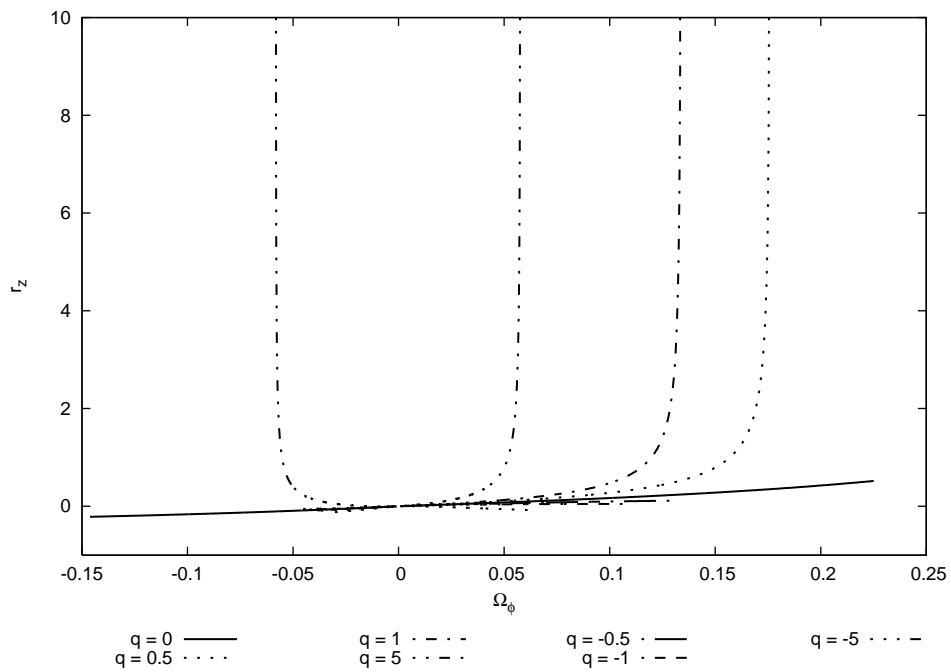


Figure 5.16: Orbital-plane precession p_z versus azimuthal frequency Ω_ϕ for $\chi = 0.9$ and various values of q .

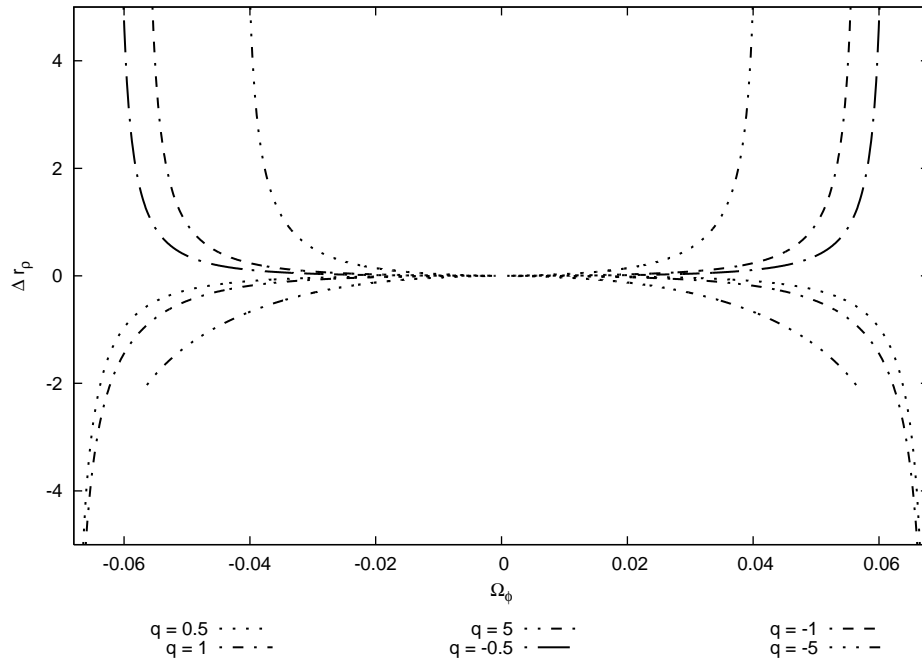


Figure 5.17: Difference between periapsis precessions in a bumpy spacetime with $\chi = 0$ and the Schwarzschild spacetime, $\Delta p_\rho(\Omega_\phi, q) = p_\rho(\Omega_\phi, q) - p_\rho(\Omega_\phi, q = 0)$.

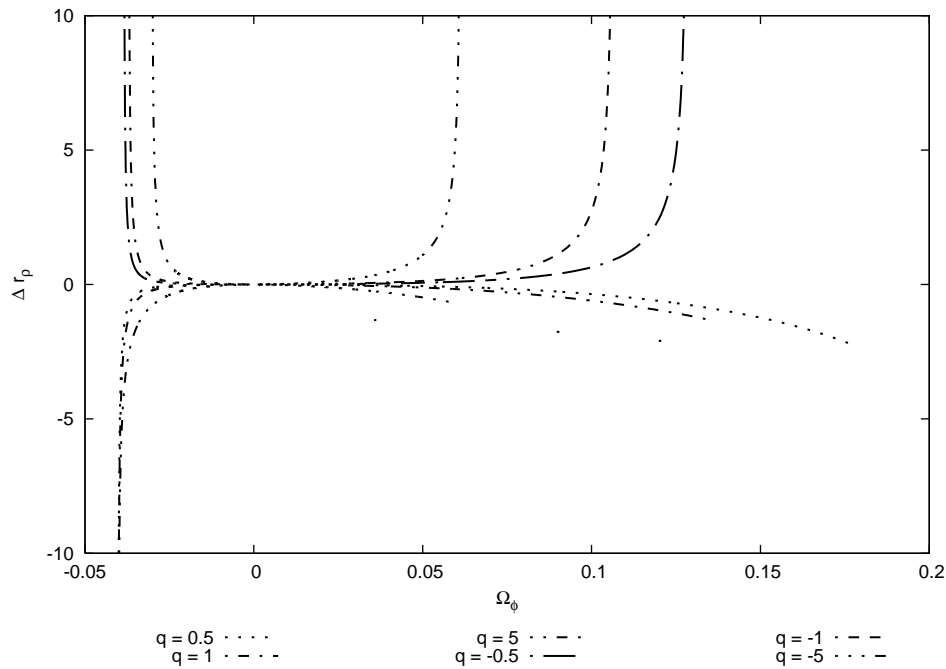


Figure 5.18: Difference between periapsis precessions in a bumpy spacetime with $\chi = 0.9$ and the Kerr spacetime with $\chi = 0.9$, $\Delta p_\rho(\Omega_\phi, q) = p_\rho(\Omega_\phi, q) - p_\rho(\Omega_\phi, q = 0)$.

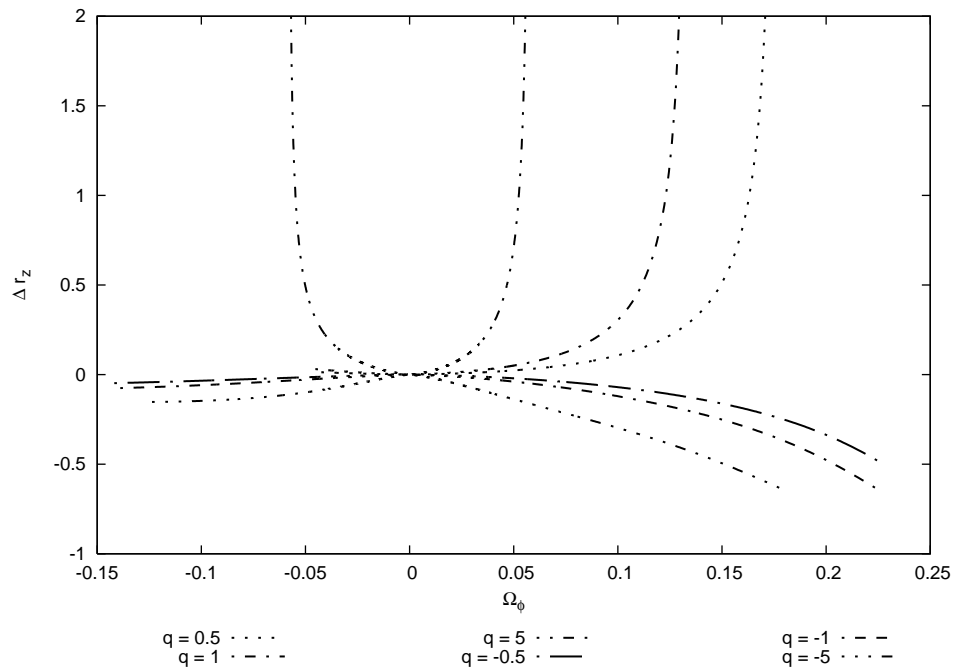


Figure 5.19: Difference between orbital-plane precessions in a bumpy spacetime with $\chi = 0.9$ and the Kerr spacetime with $\chi = 0.9$, $\Delta p_z(\Omega_\phi, q) = p_z(\Omega_\phi, q) - p_z(\Omega_\phi, q = 0)$.

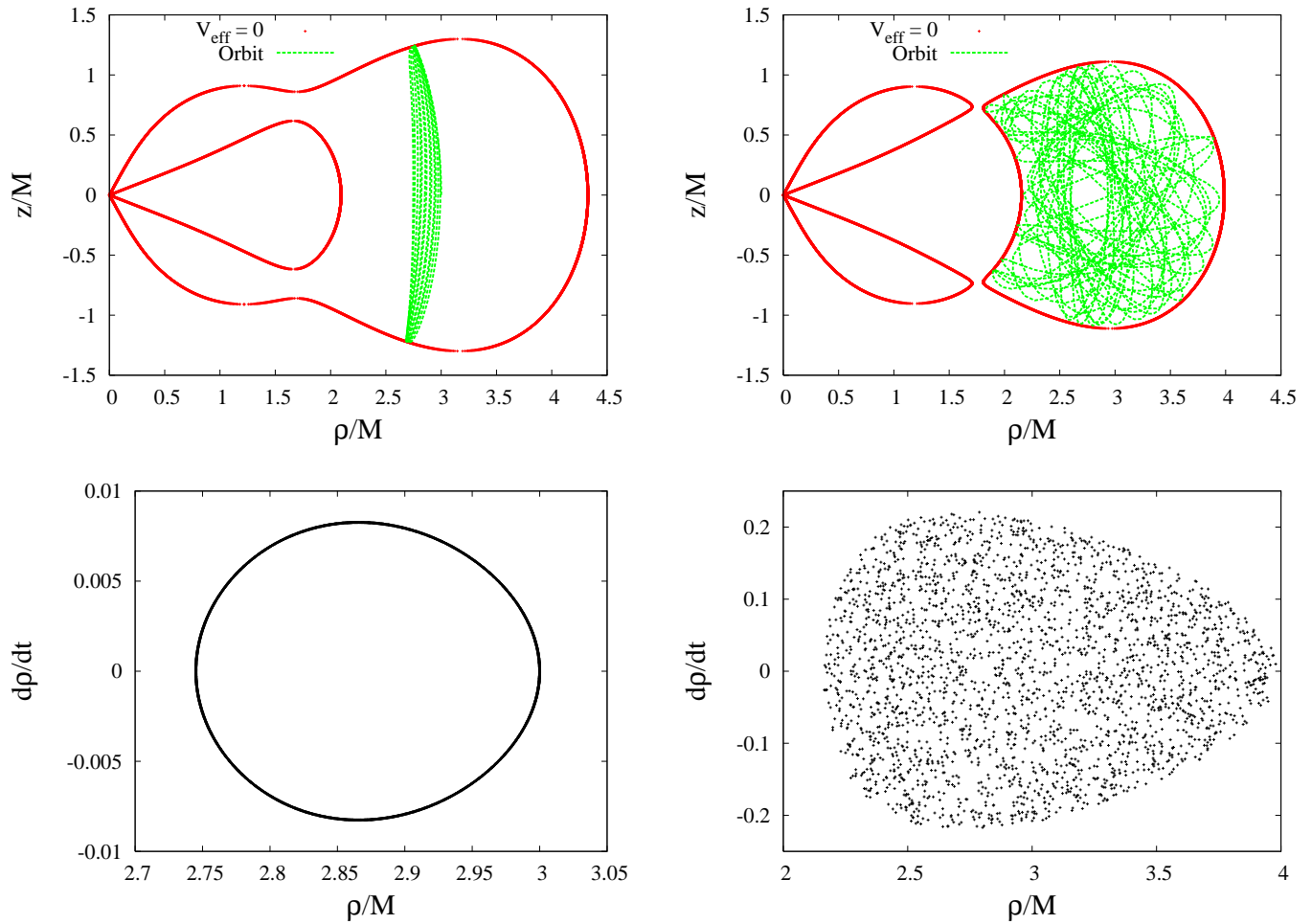


Figure 5.20: Example of onset of chaos in the Newtonian quadrupole-octupole potential (5.25). All plots are for orbits which start with $\dot{\rho} = 0 = \dot{z}$, $\rho/M = 3$ and have specific angular momentum $L_z = 1.7M$. The left hand panels are for energy $E = 0.82$, while the right hand panels have energy $E = 0.81$. The top two plots show zeros of the effective potential, $V_{\text{eff}} = 0$, as defined by equation (5.26), and the paths followed by the orbits in the (ρ, z) plane. The bottom two plots are Poincaré maps for crossings of the $z = 0$ plane in each case.

Bibliography

- [1] Amaro-Seoane, P., Gair, J. R., Freitag, M., Miller, M. C., Mandel, I., Cutler, C. J., Babak, S. 2007. Accepted by *Class. Quant. Grav.*, arXiv:astro-ph/0703495
- [2] Ryan F. D. 1995. *Phys. Rev. D***52** 5707
- [3] Hughes, S. A. 2006. In *Laser Interferometer Space Antenna: 6th International LISA Symposium*, vol. 873 of *American Institute of Physics Conference Series*, pp. 233-240, arXiv:gr-qc/0608140
- [4] Brown, D. A., Brink, J., Fang, H., Gair, J. R., Li, C., Lovelace, G., Mandel, I., and Thorne, K. S. 2007. Accepted by *Phys. Rev. Lett.*, arXiv:gr-qc/0612060
- [5] Carter, B. 1971. *Phys. Rev. Lett***26**, 331.
- [6] Robinson, D. C. 1975. *Phys. Rev. Lett***34**, 905.
- [7] Kesden, M., Gair, J. R., and Kamionkowski, M. 2005. *Phys. Rev. D***71**, 044015, arXiv:astro-ph/0411478
- [8] Straumann, N., and Zhou, Z. 1990. *Phys. Lett. B***243**, 33.
- [9] Droz, S., Heusler, M., and Straumann, N. 1991. *Phys. Lett. B***268**, 371.
- [10] Hughes, S. A., Drasco, S., Flanagan, E. E., and Franklin, J. 2005. *Phys. Rev. Lett***94** 221101.
- [11] Collins, N. A. & Hughes, S. A. 2004. *Phys. Rev. D***69**, 124022, arXiv:gr-qc/0402063

- [12] Glampedakis, K. & Babak, S., 2006. *Class. Quant. Grav.* **23**, 4167, arXiv:gr-qc/0510057
- [13] Manko, V. S. & Novikov, I. D. 1992. *Class. Quant. Grav.* **9**, 2477
- [14] Sota, Y., Suzuki, S. & Maeda, K. 1996, *Class. Quant. Grav.* **13** 1241.
- [15] Letelier, P. S. & Viera, W. M. 1997, *Class. Quant. Grav.* **14** 1249.
- [16] Guéron, E. & Letelier, P. S. 2001, *A&A* **368** 716.
- [17] Guéron, E. & Letelier, P. S. 2002. *Phys. Rev. E* **66** 046611,
- [18] Dubeibe, F. L., Pachon, L. A., Sanabria-Gomez, J. D. 2007. *Phys. Rev. D* **75**, 023008, arXiv:gr-qc/0701065
- [19] Fang, H. 2007. Ph.D. thesis, California Institute of Technology
- [20] Brink, J. 2007. Private communication
- [21] Kodama, H. & Hikida, W. 2003, *Class. Quant. Grav.* **20** 5121.
- [22] Carter B. 1968. *Comm. Math. Phys.* **10**, 280
- [23] Tabor M. 1989. Chapter 3.4 of *Chaos and integrability in nonlinear dynamics: an introduction*, (John Wiley & Sons, New York)
- [24] Brink, J. 2007. In preparation
- [25] Babak, S., Fang, H., Gair, J. R., Glampedakis, K., Hughes, S. A. 2007. *Phys. Rev. D* **75**, 024005, arXiv:gr-qc/0607007
- [26] Barack, L. & Cutler, C. 2007 *Phys. Rev. D* **75** 042003, arXiv:gr-qc/0612029
- [27] Gair, J. R. & Glampedakis, K. 2006. *Phys. Rev. D* **73** 064037, arXiv:gr-qc/0510129v2
- [28] Contopoulos, G. 2002. *Order and Chaos in Dynamical Astronomy* (Berlin: Springer).

- [29] Chandrasekhar, S. 1983, *The Mathematical Theory of Black Holes* (London: Clarendon Press)

Chapter 6

Detection and Science Applications of Intermediate- and Extreme Mass-Ratio Inspirals into Massive Black Holes

Black hole binaries with extreme ($\gtrsim 10^4 : 1$) or intermediate ($\sim 10^2 - 10^4 : 1$) mass ratios are among the most interesting gravitational wave sources that are expected to be detected by the proposed Laser Interferometer Space Antenna. These sources have the potential to tell us much about astrophysics, but are also of unique importance for testing aspects of the general theory of relativity in the strong field regime. Here we discuss these sources from the perspectives of astrophysics, data analysis, and applications to testing general relativity, providing both a description of the current state of knowledge and an outline of some of the outstanding questions that still need to be addressed.

This chapter contains excerpts from a review that was published by Pau Amaro-Seoane, Jonathan R. Gair, Marc Freitag, M. Coleman Miller, Ilya Mandel, Curt J. Cutler, and Stanislav Babak in *Classical and Quantum Gravity* 24 (2007). A preprint of the full paper is available online at <http://arxiv.org/abs/astro-ph/0703495>.

6.1 Background

Our understanding of the central regions of galaxies has advanced rapidly during the past few years, not least due to major advances in high angular resolution instrumentation at a variety of wavelengths. Observations carried out with space-borne telescopes, such as the Hubble Space Telescope (HST), and from the ground, using adaptive optics, have allowed the study of the kinematics of stars or gas in regions reaching down to milli-pc for the Milky Way and to sub-pc scales for more distant galaxies. One remarkable conclusion is that dark compact objects, most probably massive black holes (MBHs), with a mass $\mathcal{M}_\bullet \simeq 10^6 - 10^9 M_\odot$, are present at the centre of most of the galaxies for which such observations can be made. A deep link exists between the central MBH and the host galaxy. This is exemplified by the discovery of correlations between \mathcal{M}_\bullet and global properties of the spheroid, the tightest correlation being with its velocity dispersion, the so-called $\mathcal{M}_\bullet - \sigma$ relation [103]. The central part of a galaxy, its *nucleus*, consists of a cluster of a few 10^7 to a few 10^8 stars surrounding the MBH, with a size of a few pc. The nucleus is understandably expected to play a major role in the interaction between the MBH and the host galaxy. In the nucleus, one finds stellar densities in excess of 10^6 pc^{-3} and relative velocities of order a few 100 km s^{-1} to a few 1000 km s^{-1} . In these exceptional conditions and unlike anywhere else in the bulk of the galaxy, collisional effects come into play. These include 2-body relaxation, i.e., mutual gravitational deflections, and genuine contact collisions.

The stars and the MBH interact in two primary ways. Firstly, stars can produce gas to be accreted on to the MBH, through normal stellar evolution, collisions or disruptions of stars by the strong central tidal field. These processes may contribute significantly to the mass of the MBH [78, 37]. Tidal disruptions trigger phases of bright accretion that may reveal the presence of a MBH in an otherwise quiescent, possibly very distant, galaxy [53, 46]. Secondly, stars can be swallowed whole if they are kicked directly through the horizon (referred to as *direct plunges*) or inspiral gradually due to the emission of gravitational waves (GWs). The latter process, known

as an “*Extreme Mass Ratio Inspiral*” (EMRI) is one of the main sources expected for the future space-borne GW detector LISA (Laser Interferometer Space Antenna) [30, 101]. For the last stages of an EMRI to produce GWs in the frequency domain to which LISA will be most sensitive, i.e., 0.1mHz–100 mHz [67], the mass of the MBH must be between $\sim 10^4 M_\odot$ and $\sim 10^7 M_\odot$. Only compact stars, i.e., white dwarfs, neutron stars, stellar mass black holes or, possibly, the Helium cores of giant stars can produce EMRI signals detectable at extra-galactic distances. Main-sequence stars are either not compact enough to withstand the tidal forces in the vicinity of the MBH or not massive enough to produce waves of large enough amplitude. Predictions for the expected number of EMRI detections that LISA will make are rather uncertain but lie in the range of a few to a few thousand.

On the other hand, numerical simulations of young dense clusters show that runaway collisions due to mass segregation can produce central stars with masses $\sim 10^{2-4} M_\odot$ [86, 50, 87, 38]. Such a star might undergo collapse and form a so-called intermediate-mass black hole (IMBH) with $M \sim 10^{2-4} M_\odot$. It has also been proposed that globular clusters can capture the compact remnant of a zero-metallicity population III star [1]. A cluster harbouring an IMBH which starts relatively close to the central MBH of the host galaxy will sink to the centre in a few million years, and will eventually release its central IMBH due to tidal stripping of the cluster [33]. A first-order estimate of the event rate of this process leads to a few detectable coalescences of IMBHs with MBHs per year in the universe [76] but even if only one of these events occurs during the LISA mission, the signal-to-noise ratio by the end of the inspiral would be so high [57, 29, 49] that it would be visible in a time-frequency spectrogram of the LISA data, without having to resort to matched filtering [76]. The mass ratio of such a merger would typically be $10^{3-4} : 1$ –we shall refer to it as an “*Intermediate Mass Ratio Inspiral*” (IMRI) for obvious reasons.

The LISA mission is scheduled to fly in about 10 yrs and critical design choices which will affect the ability to detect E/IMRIs will be made soon. It is important to produce robust estimates for the rates and typical orbital parameters of these events as input for the development of search algorithms. Such search algorithms

must have the capability to extract science information out of the complex LISA data stream, which will contain many thousands of overlapping resolvable signals, plus astrophysical backgrounds from millions of more distant sources.. The readiness of data analysis for the LISA mission will be assessed on an equal footing with the hardware so it is essential that data analysis strategies are finalised in the near future.

Detection of EMRIs with LISA is difficult (in discussions of data analysis, we will generally use the term EMRIs to refer to both EMRIs and IMRIs since most of the discussion applies to both types of inspirals, except for those obvious cases when we discuss differences between the two). A typical signal will be very weak, lying buried in instrumental noise and in the gravitational wave foreground created by nearby Galactic white dwarf binaries. The signals are long-lived, typically being observable for several years prior to plunge, which in principle allows the EMRIs to be detected by matched filtering. Matched filtering employs a bank of templates that describes signals with all possible parameters within the expected range. Unfortunately, the large parameter space of possible EMRIs makes the number of templates required for such a search computationally prohibitive. Over the past few years, several alternative algorithms have been developed — a semi-coherent matched filtering algorithm, time-frequency search algorithms and Markov Chain Monte Carlo techniques. The results are promising, but more work needs to be done before we will have an optimal algorithm for EMRI detection. The correspondingly higher signal-to-noise ratios of IMRIs make detection of those events somewhat easier, but it is still a challenging task.

In Section 6.2.1 we describe the existing algorithms and outstanding challenges for EMRI/IMRI detection. The search algorithms require models of EMRI waveforms. In principle, the extreme mass ratio means that the waveforms can be computed using black hole perturbation theory. However, this formalism is not fully developed and will be computationally expensive once it is. Various alternative waveform models are currently being developed and used for scoping out EMRI detection. We will describe these various models and necessary future developments of them in Section 6.2.2.

If we do detect many EMRI/IMRI events, we will be able to do some very inter-

esting science. EMRI observations will provide measurements of the masses and spins of black holes to an accuracy which is not accessible by other astronomical observations. This will tell us about the properties and growth of black holes in the nearby universe. EMRIs also provide a means to probe general relativity in the strong-field regime close to astrophysical black holes. The extreme mass ratio ensures that over many orbits the inspiralling object acts essentially like a test-body moving in the space-time of the central body. The emitted gravitational waves encode a map of the space-time. If we can decode that map, then we will be able to test the belief that massive compact objects in the centres of galaxies are indeed Kerr black holes. Carrying out this mapping is difficult, but is the focus of much current research. We summarise current results in Section 6.3 and discuss some outstanding questions in this area.

In Section 6.4 we discuss the scientific benefits of LISA observations of EMRI/IMRI events. This section takes the form of answers to five broad questions that were the focus of discussions at the LISA EMRI workshop hosted by the Albert Einstein Institute in Golm, Germany in September, 2006. Finally, in Section 6.5 we provide a summary of the main topics in the paper.

6.2 EMRI detection

6.2.1 Data analysis algorithms

A typical EMRI signal will have an instantaneous amplitude an order of magnitude below the LISA's instrumental noise and (at low frequencies) as many as several orders of magnitude below the gravitational wave foreground from Galactic compact binaries. This makes detection a rather difficult problem. However, the signals are very long lived, and will be observed over more than 10^5 cycles, which in principle allows the signal-to-noise-ratio (SNR) to be built up over time using matched filtering. Estimates of the number of important parameters in EMRI evolution range from 7 to 15. Even taking a number at the lower end of this range, the naive expectation is that $N \sim 10^{35}$ templates would be needed to carry out a fully coherent matched

filtering search [43]. This is far more than can reasonably be searched with realistic computing resources. Several alternative approaches to EMRI detection that will be computationally feasible have been investigated. These will be able to detect signals with matched filtering $\text{SNR} \gtrsim 20$. By comparison, in a fully coherent search, the SNR required for detection is $12 - 14$, to ensure a reasonable false alarm rate when searching such a huge number of templates.

LISA data analysis is further complicated by the richness of the LISA data stream. The motion of LISA in its orbit creates amplitude and phase modulation of the signals and we have to employ time-delay interferometry techniques [3, 102] in order to remove the laser frequency noise. Time-delay algorithms applied to the Doppler readouts lead to a rather complicated response function which depends on the frequency and sky position of the source under investigation. It is expected that the detection rates for EMRIs will fall somewhere between a few tens and a few thousands [10, 43, 56]. Additionally, the LISA data will be very strongly coloured by gravitational wave signals from the foreground of white dwarf binaries in our galaxy ($\sim 10^7$ sources which create confusion noise at frequencies below a few millihertz [54, 16, 80, 35]) and signals from a handful of merging supermassive black hole binaries which might have SNR as high as a few thousand [112, 34, 97]. All these signals will overlap in time and frequency. To illustrate this complexity we have simulated a LISA frequency Doppler shift measurement with ~ 27 million Galactic binaries, 1 EMRI and 1 inspiralling MBH binaries. The power spectral density of each separate source and the total envelope is presented in Figure 6.1. This Figure is primarily illustrative, but it appears that the EMRI signals will be overwhelmed by the signals from the MBH mergers. However, it should be possible to identify and remove the high signal-to-noise ratio MBH merger signals from the data stream before searching for the EMRI signals, so the situation is not as bad as it may at first appear.

6.2.1.1 Current status

To date, three algorithms for detection of EMRIs in LISA data have been considered.

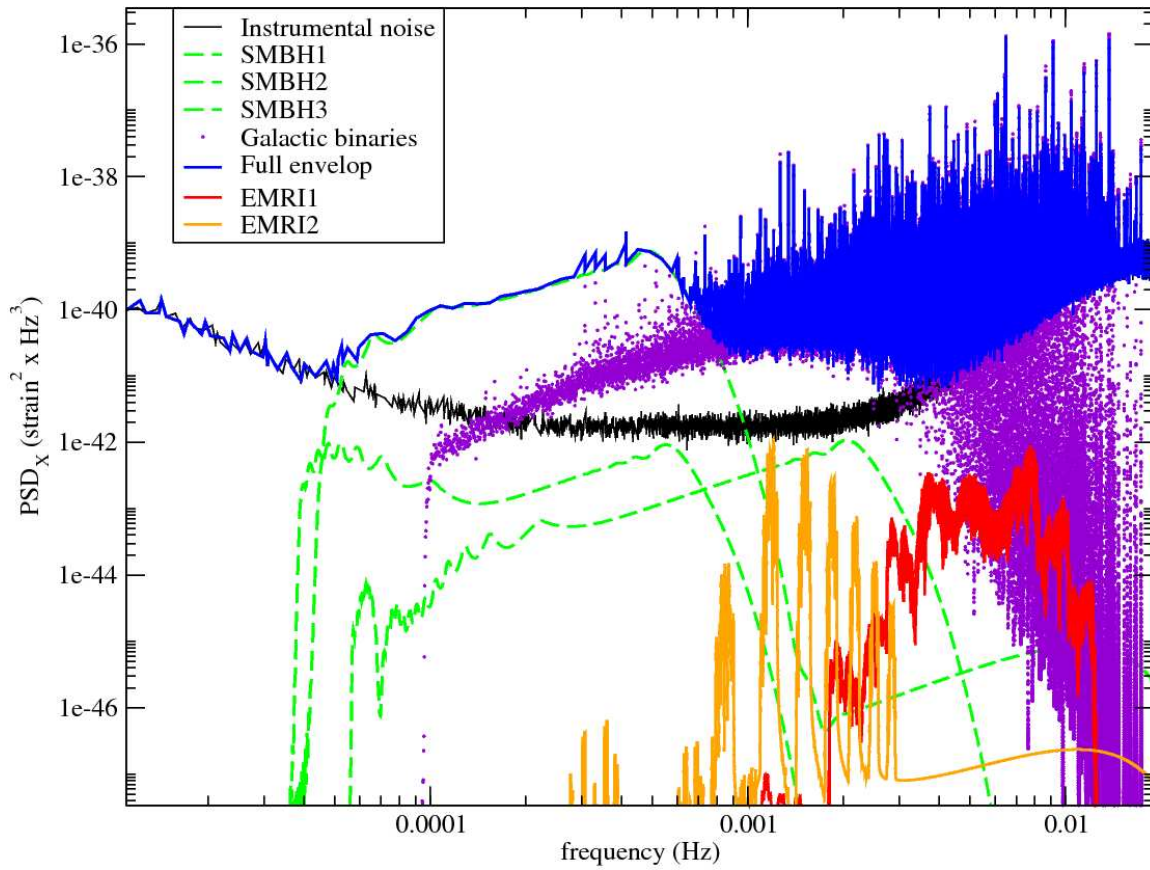


Figure 6.1: Power spectral density of one of the unequal arm Michelson TDI channel. It contains 1 MBH inspirals at luminosity distances of 3.3 Gpc and 1 EMRI at luminosity distances of 2.3 Gpc. The duration of the EMRI was taken to be one and a half years. The galactic binary realisation used here was drawn from the distribution described in [80].

The first is a semi-coherent algorithm, which uses a first coherent matched filtering stage to search for ~ 3 -week sections of EMRIs, followed by a second stage where the power is summed incoherently along trajectories through these sections that correspond to inspirals. This algorithm could detect EMRIs at redshift $z \sim 1$, which translates to tens to hundreds of LISA events, depending on the intrinsic astrophysical rate [43]. The preliminary analysis of this algorithm made only limited efforts to optimise its performance. It is likely that optimisation, such as the addition of extra stages in the hierarchy, will be able to further improve the reach of search, but this has not yet been explored.

A second approach is to use time-frequency methods, i.e., divide the data stream into segments of a few weeks in length, perform a Fourier transform on each and then analyse the resulting spectrogram. A simple method that looks for unusually bright pixels in binned versions of this spectrogram could detect typical EMRI signals at about half the distance of the semi-coherent search, but at a tiny fraction of the computational cost [109, 42]. An improved method that considers clustering of bright pixels in the binned spectrograms (the Hierarchical Algorithm for Clusters and Ridges), has slightly further reach, and also more potential for parameter extraction [41]. While more work needs to be done, template-free techniques could detect as many as one tenth of the EMRI sources in the data stream. A typical spectrogram for an EMRI signal is presented in Fig. 6.2 for which the amplitude of the signal at plunge was normalised to one.

The third approach that has been explored is to use Markov Chain Monte Carlo (MCMC) techniques. The MCMC approach essentially carries out fully coherent matched filtering, but does so in an intelligent way, reducing the number of waveform templates that have to be considered. MCMC methods are being explored extensively for application to all aspects of LISA data analysis [27, 105, 110]. In the context of the EMRI search, the MCMC approach has been found to work well when searching for a simple model EMRI signal in a short stretch of LISA data [98]. The exact reach of the MCMC search has not yet been properly assessed. Given infinite computing resources, the MCMC would eventually return the posterior probability function for

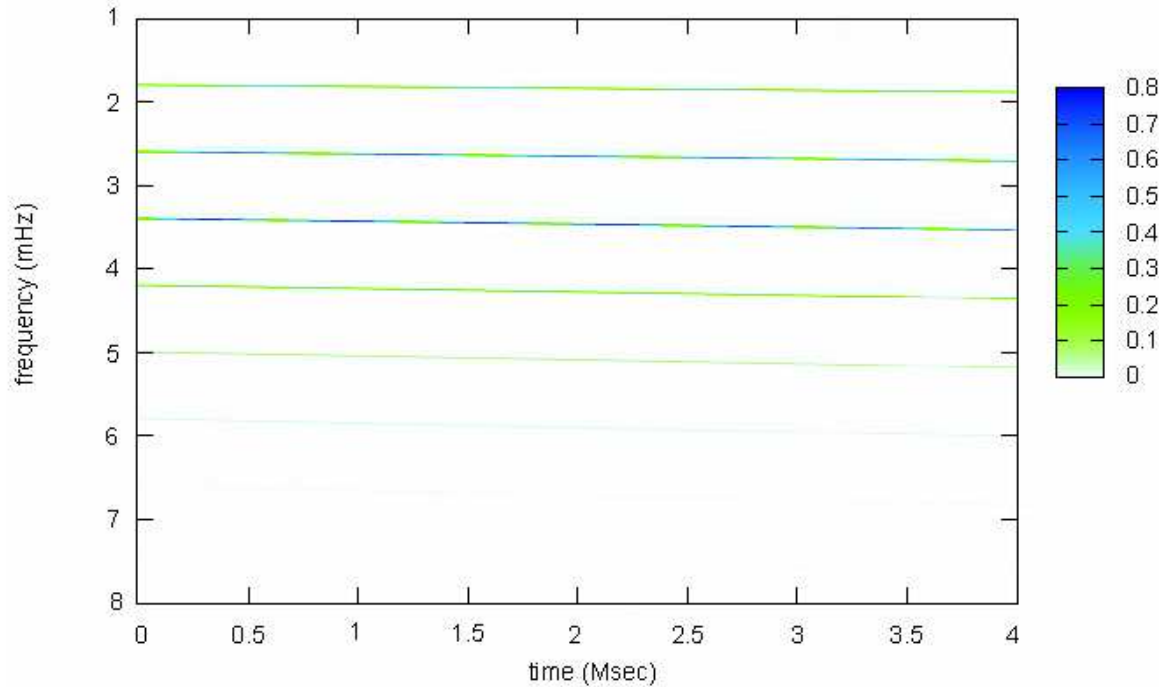


Figure 6.2: Spectrogram of the signal from an EMRI on an inclined and eccentric orbit. One can see several harmonics modulated by orbital precession and LISA’s orbital motion.

the source parameters. The ability to correctly identify sources then depends on the shape of this posterior, which depends on both the signal-to-noise ratios of the sources and the structure of the waveform template space. These are the same properties that determine the detection limit of a fully-coherent matched filtering search, so it is plausible that an MCMC search with infinite computing power could achieve the same range as the fully coherent matched filtering approach. However, the MCMC suffers from the same computational constraints as the fully coherent search, and these will limit the ability of an MCMC search to sample the posterior. Peaks in the posterior will have to be larger to be detected, and sources will have to be correspondingly closer. For these reasons, it is not possible to say how the performance of the MCMC and the semi-coherent method will compare in practice, although this should become clear over the next several years.

6.2.1.2 Outstanding challenges

The results quoted above for the various search algorithms were obtained using a vastly simplified model of LISA — searching for a single EMRI event in coloured Gaussian noise. However, as already mentioned, the LISA data stream will actually be source-dominated and in order to detect EMRIs we might first need to clear the data of signals from MBH binaries and from resolvable Galactic binaries. As many as 10^4 Galactic binaries with frequencies above a few mHz will be individually resolvable [35] and hopefully removed. Estimates suggest there could be tens of coalescing MBH binaries observed each year during the mission lifetime [97]. LISA could also see as many as several hundred individually resolvable EMRI events [43] plus a confusion background generated by distant EMRI signals [10]. In the work on EMRI searches, the confusion background from unresolvable compact binaries has been included in an approximate way, but no account has been made of the effect of interference from the thousands of resolvable sources that will be present in the data. Research on the problem of resolving individual sources in the rather complex LISA data is under way within the Mock LISA Data Challenge effort [4, 5].

Some of the questions that need to be addressed are as follows:

- How do the three existing algorithms perform when applied to data streams containing two, ten or a hundred EMRI events? How does the performance degrade when there are other sources, e.g., a MBH merger signal, in the data stream? The semi-coherent and MCMC algorithms are likely to be better at handling confusion than the time-frequency approach, since the former methods use matched filtering. Time-frequency analyses will not be readily able to cope with many sources of comparable brightness that intersect in the time-frequency plane. Work needs to be done to quantify these statements.
- If existing algorithms for the extraction of compact binaries and supermassive black hole mergers from the data stream are used on a data stream including one or more EMRI signals, how is the EMRI signal affected? Can the process of “cleaning” other sources be modelled merely as an alteration in the noise prop-

erties of the data stream? This will answer the important question of whether it is necessary to fit simultaneously for all the sources in the data, or whether the parameters of the different source types can be estimated sequentially, before following up with a global fit and refinement of the parameters. Another concern here is how well we can model MBH merger signals — the mismatch between the true signal and the theoretical model could result in rather high residuals.

- Markov Chain Monte Carlo (MCMC) techniques in principle can search for multiple types of source in the data stream, but how well do they perform when searching for compact binaries, supermassive black hole mergers and EMRIs in the same data set? How quickly does the chain converge? How complex is the likelihood function with many different source types in the data stream? It has recently been shown that MCMC based methods can detect MBH inspirals in the presence of a Galactic WD binary foreground to a very high accuracy [28], which gives reason to hope that this problem will be surmountable.
- What are the computational costs of the various approaches? Which of them are computationally feasible? As mentioned earlier, fully coherent matched filtering is impossible due to the large number of templates required to tile the whole parameter space. The semi-coherent algorithm was designed to make maximum use of expected computational resources, and 3 weeks was estimated to be the longest possible “snippet” length under that assumption. Markov Chain Monte Carlo techniques provide a more computationally efficient way to search high-dimensional parameter spaces. The MCMC search for a simplified EMRI in 1 month of data described in [98] required the evaluation of $\sim 10^7$ chain states in order to determine the parameters of a source which had $\text{SNR} \sim 10$. This is fairly typical of the number of states required to accurately recover the posterior in searches for small numbers of sources [28]. However, the exact number of states required will depend on the number of sources in the data (typically a linear scaling), the complexity of the waveform space and

the SNRs of the various sources. This will likely increase the requirement by several orders of magnitude, although the MCMC should be able to obtain reasonable estimates of the parameters of the loudest sources using many fewer than the $\sim 10^{35}$ templates required to cover the whole parameter space in a fully coherent matched filtering search [43]. However, the template at each one of these Markov chain states still needs to be evaluated as the chain runs. The templates thus either need to be generated “on-the-fly” or a bank of templates needs to be generated in advance. For the former, we would need quick methods to generate EMRI waveforms, such as the kludge models. For the latter, we are back to the necessity that the entire parameter space be covered with EMRI templates. This is unlikely to be computationally practical, and even if it were, the overhead associated with accessing such a huge database would be prohibitively high. Thus, computational costs will have to be considered very carefully when devising the final EMRI search.

The final EMRI search will most likely include a combination of the three approaches described above, and perhaps some new techniques. The search is likely to be hierarchical, using inaccurate but quick techniques to get estimates of the source parameters before refining with more computationally intensive methods. It is likely that the searches for different types of LISA source will be somewhat integrated with one another, although one possible approach might be to estimate the parameters for each source type separately, before unifying everything in a final global fit.

There are various “non-standard” channels for EMRI formation that may produce comparable numbers of inspirals as the standard picture. A binary tidal separation or the capture of the core of a giant star would tend to lead to an EMRI on a circular orbit. The formation of stars in a disc would tend to lead to an EMRI on a circular and equatorial orbit. These special types of orbit have less free parameters than a generic EMRI. It might therefore be worthwhile having three EMRI data analysis pipelines, focused on circular-equatorial, circular-inclined and eccentric-inclined orbits respectively. The reduction in the parameter space in the restricted cases will probably not be sufficient to allow fully coherent matched filtering to be carried out,

but it will allow considerably longer segments to be used in the first stage of a semi-coherent search. Moreover, the threshold SNR required for detection of a source will be reduced (since there are far fewer templates in which a false alarm could be found), increasing the range of the search. It will be important to find out to what distance a well-tuned search algorithm targeting circular or circular-equatorial EMRIs can make a detection, but this has not yet been explored thoroughly.

No algorithms have been examined explicitly in the context of IMRI detection, although the above algorithms for EMRI detection can all be applied. For the matched filtering algorithms, the complication is the need for waveform models, which will be discussed in more detail below. The time-frequency algorithms can see IMRI events further away, since they are intrinsically brighter, so this might be a good method to use, but it will depend on the distance to the nearest likely event. As search techniques for EMRIs and MBH mergers are further developed in the future, they can be expanded to encompass a search for IMRIs.

6.2.2 Source modelling

Most of the data analysis algorithms outlined above require models of the source waveforms. Waveform templates will also be essential for parameter estimation once sources have been detected. Templates for EMRIs could be constructed in several ways which we discuss here.

6.2.2.1 Current status

Post-Newtonian expansion The post-Newtonian expansion in powers of velocity v/c converges poorly when $v/c \gtrsim 0.3$ [19]. Unlike comparable-mass inspirals, which only spend a few cycles in the regime where the post-Newtonian approximation breaks down, IMRIs and EMRIs may spend thousands to millions of cycles in this regime. Therefore, this expansion is not useful for EMRI or IMRI waveform modelling.

Numerical relativity Solving Einstein's equations numerically on a computer has proven to be a very difficult task, but significant progress has been made in the

past year. Several groups have now successfully modelled the last orbit, merger and ring-down of a comparable mass binary system [90, 7, 22, 21]. Numerical techniques are essential for modelling the highly non-linear dynamics during the last few orbits and merger of a comparable mass system. However, numerical techniques are not fast enough to evolve the large number of cycles necessary for EMRI waveforms. In addition there are technical problems which make numerical methods unreliable as one goes to higher mass ratios. Fortunately, in EMRI systems the extreme mass ratio makes it possible to produce templates accurate over many cycles by perturbative methods expanding in the mass ratio, so numerical relativity is not needed in this context.

Self-force waveforms The extreme mass ratio in an EMRI system allows the waveform to be obtained by perturbation theory. The inspiralling object can be regarded as a small perturbation on the background space-time of the central black hole, except very close to the small object. In the vicinity of the small object, the space-time can be regarded as a point mass moving under the influence of an external tidal field due to the central body. Matching these two regimes allows one to obtain an expression for the self-force acting on the small body as a result of its motion in the space-time. This self-force can be thought of as arising from gravitational radiation being generated by the small object, reflecting off the curvature of the background space-time and then subsequently acting on the small body. The mathematical theory of this self-force interaction has been developed over the past ten years (see the review [85] and references therein). In principle, the self-force formalism will provide accurate EMRI waveforms that can be used for source characterisation. However, evaluation of the self-force is computationally difficult. Recently, a new scheme was proposed [12] which has produced results for the self-force acting on circular orbits in the Schwarzschild space-time [13]. However, it is computationally expensive to generate the self-force acting even at a single point in an orbit. A generic *inspiral* trajectory and waveform from a particle evolving as a result of the self-force is still some way in the future.

Adiabatic inspiral waveforms Evaluation of the self-force acting at every point on the orbit is necessary to include the ‘conservative’ piece of the self-force, i.e., the piece that modifies the orbit, but does not dissipate energy, E , angular momentum, L_z , or Carter constant, Q , (a generalised angular momentum squared which is the third integral of the motion for orbits in the Kerr space-time). However, the radiative piece of the self-force can be determined more easily, by solving the perturbation equations for the background space-time, with a source that represents a particle moving on a geodesic of this background. This reduces to integrating the Teukolsky equation [99, 100]. Solutions of the Teukolsky equation encapsulate radiation at infinity in a single equation for the Weyl scalar ψ_4 :

$$\psi_4 = \frac{1}{2}(\ddot{h}_+ - i\ddot{h}_\times). \quad (6.1)$$

The Teukolsky solution also determines the orbital averaged rates of change of the orbital constants — $\langle dE/dt \rangle$, $\langle dL_z/dt \rangle$, $\langle dQ/dt \rangle$ — from which the value of these constants a short period of time later can be determined. This allows the construction of ‘adiabatic waveforms’ [62] — a sequence of geodesics can be found that represent an inspiral, by solving the Teukolsky equation for a given geodesic, then computing the energy, angular momentum and Carter constant loss rate for that geodesic, neglecting oscillatory terms which average to zero over the orbital period. These are then used to determine the next geodesic in the sequence. The corresponding gravitational waveforms generated on each geodesic orbit can then be stitched together to give an adiabatic inspiral waveform. This procedure works provided the timescale over which the orbit is changing is long compared to the orbital period, i.e., the evolution is adiabatic. For special classes of orbits — eccentric equatorial and circular inclined — the rate of change of the orbital constants is determined by energy and angular momentum balance. It is possible to extract from ψ_4 (6.1) the gravitational waveform near the horizon and near infinity, and hence the amount of energy and angular momentum being carried by the waves down the horizon and out to infinity. Equating the loss of energy and angular momentum of the orbit to the sum of the energy and

angular momentum fluxes near the horizon and near infinity determines the orbital evolution. This simplification meant that adiabatic inspirals were determined several years ago for both of these special classes of orbit [48, 58], although the stitching together of waveforms has only been done for circular inclined orbits [59]. Recently, ‘snapshot’ waveforms and energy/angular momentum fluxes have also been generated for generic geodesics in the Kerr space-time [31]. Generic geodesics in Kerr have the third integral of the motion, the Carter constant, in addition to the energy and the polar component of the orbital angular momentum. It was originally thought that evaluation of the self-force would be required to correctly evolve the Carter constant. However, it was recently shown that the evolution of the Carter constant can also be determined from the same Teukolsky coefficients that are needed for computing the energy and angular momentum fluxes [77, 95, 96].

This should allow the construction of generic adiabatic waveform templates in the near future. Adiabatic waveforms are accurate except for the omission of the conservative piece of the self-force. There is some debate in the literature about how important this omission will be [32, 88]. However, the adiabatic waveforms may be accurate enough over a timescale of a few weeks that they can be used for source detection via the semi-coherent algorithm. They may also perhaps find a role in source characterisations and are somewhat less computationally expensive to generate than full self-force waveforms.

“Kludge” waveforms The adiabatic waveforms, although accurate, are still computationally intensive to compute. For the purposes of scoping out data analysis algorithms for the detection of EMRIs with LISA, it is necessary to generate waveforms in large numbers, e.g., to count the number of templates needed to cover the whole parameter space with sufficiently high overlap. Perturbative waveforms did not fit this requirement, which led to the development of two families of approximate, “kludge” waveforms, that capture the main features of true EMRI waveforms but are much quicker and easier to generate.

The first family of kludge waveforms use an “analytic kludge” (AK). They are

based on waveforms representing emission from a particle on a Keplerian orbit, as given by Peters and Mathews [83, 82]. The waveform is augmented by imposing relativistic precession of the orbital periapsis and orbital plane, plus inspiral (in an analogous way to how the adiabatic waveforms include inspiral). The precession and inspiral rates are taken from post-Newtonian results. These waveforms are described in [9]. The AK approach is “analytic” since analytic expressions are known for the Peters and Mathews waveforms. This makes the AK waveforms very quick to evaluate. However, they are not particularly accurate in the latter stages of inspiral, since a Keplerian orbit with precessions is not a good approximation to a true Kerr geodesic close to the central black hole.

The second family of kludge waveforms attempts to address this failing by using a true geodesic orbit for the inspiralling particle. The geodesic equations have to be integrated numerically, so the second family is labelled the “numerical kludge” (NK). The procedure to compute a numerical kludge waveform has two stages. Firstly, a phase-space inspiral trajectory is constructed, i.e., the sequence of geodesics that an inspiral passes through, by integrating prescriptions for the evolution of the three constants of the motion — energy, angular momentum and Carter constant. An initial prescription for this evolution based on post-Newtonian expansions of the Teukolsky function [49] was found to exhibit pathologies in certain regimes. By imposing consistency corrections and augmenting the evolution with higher order post-Newtonian terms and fits to solutions of the Teukolsky equation, a considerably improved prescription for the inspiral has now been obtained [40]. This current inspiral prescription is accurate until very close to the end of the inspiral for circular orbits. It is less accurate for eccentric orbits, but it should be possible to improve this in the future now that Teukolsky data for generic orbits is available. Once a phase space trajectory has been obtained, the Kerr geodesic equations can be numerically integrated, with the time-dependent constants of the motion inserted. The trajectory of the inspiralling particle through the Kerr background is then obtained. The second stage of the NK construction is to construct a waveform based on this trajectory. This is done by identifying the Boyer-Lindquist coordinates of the particle trajectory with spherical

polar coordinates in flat space, and applying a weak field gravitational wave emission formula to the pseudo-flat space trajectory. NK waveforms have been constructed using the standard flat space quadrupole radiation formula, the quadrupole-octupole formula [15] and the Press formula [89], which is derived for fast-motion but weak field sources. All three prescriptions perform well when compared to more accurate, adiabatic waveforms, but there is little gain from using the Press formula in preference to the quadrupole-octupole expression [6].

AK waveforms are not particularly “faithful” as EMRI templates, i.e., an AK waveform with a given set of parameters does not have high overlap (noise weighted inner product) with a more accurately computed waveform with the same set of parameters. However, they do capture the main features of EMRI waveforms, which has made them a useful tool for scoping out the semi-coherent algorithm [43] and other studies. They may also be quite “effectual” templates, i.e., for any real EMRI waveform, there may be an AK waveform *with different parameters* that has a high overlap with that waveform. The AK family of waveforms may thus play some role in the final analysis of LISA data. The NK waveforms are not only effectual but very faithful, because they are built around true Kerr geodesics. For orbits with periapsis greater than $\sim 5M$ (in geometrical units, where M is the mass of the central black hole), the NK waveforms have overlaps in excess of 95% with waveforms computed via solution of the Teukolsky equation. With further improvements (outlined below), the NK waveforms are likely to be very useful tools in LISA data analysis, not only for source detection but also for approximate source identification before subsequent follow-up with more accurate templates. In Figure 6.3 we show a snapshot of NK EMRI waveform. This figure serves as an illustration of the structure of the signal.

6.2.2.2 Outstanding challenges

None of these approaches to source modelling is as yet fully developed. In the case of the self-force formalism, recent progress has been significant, and the self-force acting on particles in circular orbits in the Schwarzschild space-time has been computed [13]. However, this is only for a small selection of circular orbits. The work must then be

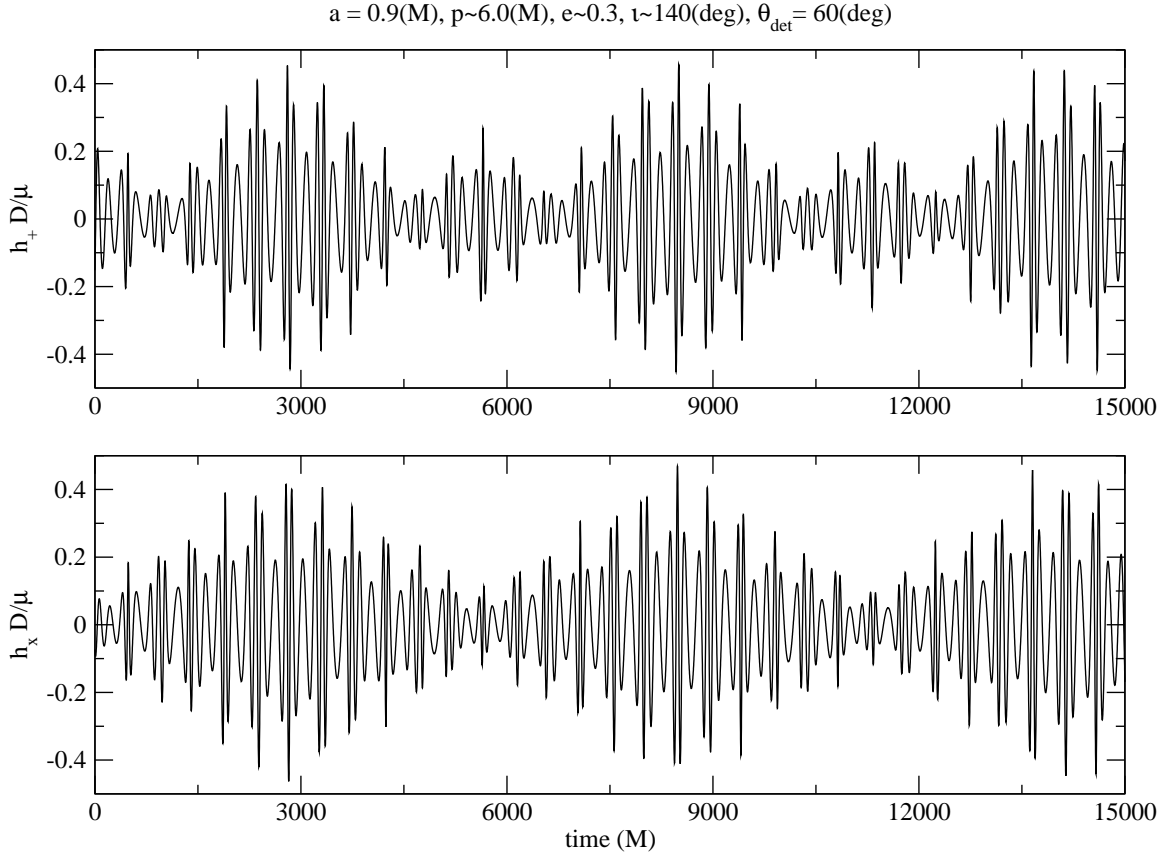


Figure 6.3: The two polarisations of an NK EMRI waveform with a mass ratio of 10^{-7} . The GW amplitude is measured in units of the mass of the compact object over distance (μ/D) and time is measured in units of MBH mass M . The eccentricity is ~ 0.3 , the semi-latus rectum $p \sim 12M$, the inclination of the plane to the MBH spin axis is 140 degrees and the detector (observer) is 30 degrees above the azimuthal plane.

extended to eccentric orbits in the Schwarzschild space-time, then to circular equatorial orbits in the Kerr space-time before finally moving onto eccentric-equatorial and ultimately eccentric-inclined orbits in Kerr. Although this is a non-trivial progression, it should be achieved within the next five to ten years. By the time LISA flies, it is likely that codes will exist to compute self-force based waveform templates for arbitrary orbits. However, these are likely to be computationally expensive, which is why it is necessary to pursue the alternative models.

Adiabatic waveforms are at a more advanced stage of completion. All that remains is to compute the evolution of the Carter constant for generic orbits, using the results of [77], and to “stitch together” waveforms for generic inspiral orbits. There are no technical challenges remaining, although computational cost is an issue. Generic adiabatic inspiral waveforms should be available within one to two years. Understanding their range of validity may take longer, without self-force templates to compare them against. However, the consideration of conservative corrections outlined below will be important for developing this understanding.

The NK waveforms can also be improved. One of the reasons that the performance degrades for small periapsis is that the kludge waveforms do not include tail contributions, i.e., back-scattering of the radiation from the background geometry. It should be possible to include this in an approximate way, which is likely to improve the NK performance for orbits close to the central black hole. Additionally, the inspiral prescription can be improved by fitting functions to Teukolsky data for generic orbits. The current inspiral prescription [40] includes fits to Teukolsky data for circular inclined orbits, and the resulting inspiral trajectories agree very well for that class of orbit. It is likely that similar accuracy can be obtained for generic orbits in a similar way. Finally, the NK waveforms can be augmented by inclusion of conservative corrections. The conservative correction to the phase evolution of an EMRI is already known in post-Newtonian theory to 3.5 \mathcal{PN} order. By considering asymptotic observables, namely the rate of change of the orbital, periapsis precession and orbital plane precession frequencies as functions of those three frequencies, it is in principle possible to compute the necessary conservative corrections for inclusion

in the NK model. This was demonstrated for the simple case of circular equatorial orbits in Schwarzschild in [6]. Although the conservative effects could be included this way only up to a certain \mathcal{PN} order, it is quite plausible that this will suffice, since conservative effects contribute most significantly to the phase evolution in the weak field [88], where the \mathcal{PN} expansion is valid.

This last improvement of the NK model is potentially important, since an issue that needs to be understood before LISA flies is how much conservative effects can influence the emitted waveform. If conservative effects are not significant, then a combination of kludge and adiabatic waveforms will be able to identify the parameters of EMRI sources in the LISA data stream with quite high accuracy. If conservative effects are important, the degree to which these waveform families can constrain the parameter space will be significantly reduced. Although self-force calculations are now at the point of computing conservative corrections, this has only been done to date for circular orbits in Schwarzschild. It is unlikely that generic conservative corrections from self-force calculations will be available in the near future. The \mathcal{PN} fitting procedure outlined above will provide approximate results on a much shorter timescale. This should allow the contribution to the phasing of each \mathcal{PN} order in the conservative correction to be assessed, which will give some insight into the importance of including conservative effects. Moreover, the procedure for including the \mathcal{PN} conservative corrections in the NK model can also be used to include these effects in the adiabatic waveforms.

As these developments and improvements to each family of waveforms proceed, we will be able to address three primary groups of questions of great importance:

- What is the computational cost of evaluating waveforms of each type (self-force, adiabatic, kludge)? How many self-force templates could be generated in a reasonable time for a follow-up analysis? How accurately would kludge/adiabatic templates therefore have to constrain the source parameters prior to the self-force analysis?
- What is the overlap of kludge, adiabatic and self-force templates with one an-

other? How accurately, therefore, can kludge and adiabatic templates determine the source parameters, assuming we consider “faithful” searches only? Can we compute sufficiently many self-force waveforms to determine parameter mappings between the families, i.e., can we allow the search to be only effectual?

- What is the most computationally efficient way to detect and identify a source, assuming we are using a multi-stage search employing kludge, adiabatic and self-force templates at different stages of this search? What limit on parameter extraction accuracy is set by computational constraints on our search? Is this limit much worse than the theoretically achievable parameter measurement accuracy?

The answers to the first and second itemised points may be incompatible, i.e., we may not be able to determine the parameters of the source sufficiently accurately using kludge or adiabatic templates to allow a self-force follow-up with reasonable computational cost. In this case, we would have to live with a potentially larger error in our source parameters, as mentioned in the third item.

In the above, we have focused on the modelling of waveforms from EMRIs. However, another outstanding challenge is to develop models for IMRI waveforms. To date, no models have been developed explicitly for IMRIs, although existing models for other systems can be easily applied. An IMRI (mass ratio $\sim 1 : 1000$) lies somewhere between the inspiral of two comparable mass black holes (a CMRI, mass ratio $\sim 1 : 1$) and an EMRI system (mass ratio $\sim 1 : 10^6$). For a comparable mass system, the masses and spins of both components are important, but the system spends very few cycles in the regime where the velocity of the components is close to the speed of light. The waveforms can thus be accurately computed from post-Newtonian expansions. In an EMRI system, the number of cycles spent in the high-velocity regime (scaling as one over the mass ratio) is 10^6 times higher, so the post-Newtonian expansion is not reliable, but the extreme mass ratio allows construction of accurate waveforms from perturbation theory. An IMRI is somewhere in between, spending 1000 times longer than a CMRI in the high-velocity regime, but 1000 times less than

an EMRI. Post-Newtonian results will not be fully reliable for an IMRI, since they spend so many cycles with $v \sim c$. However, perturbative results are not fully reliable either, since they are linearised in the mass ratio and thus omit terms at higher order in m/M (where m is the mass of the inspiraling object and M is the mass of the central body). In addition, at present we do not have \mathcal{PN} waveforms that include both spins of the two bodies and orbital eccentricity, both of which could be non-negligible for IMRIs.

How quickly do higher-order mass-ratio corrections become important? For simplicity, we consider circular equatorial orbits, but the following arguments apply generally. Higher order mass ratio corrections fall into two categories: (i) corrections to the frequency for an orbit at fixed radius (these corrections arise from the conservative piece of the self-force and from spin-orbit interactions due to the spin of the smaller body) and (ii) corrections to the inspiral rate. Corrections to the frequency enter at $O(m/M)$, e.g., the spin of the small object is of order m^2 and leads to a spin-orbit coupling force at this order, with resulting acceleration at order m [81]. However, observationally, we cannot measure the radius of the orbit, only the orbital frequency, so to lay out accurate templates we in fact need the rate of change of orbital frequency as a function of the observable orbital frequency (half the frequency of the fundamental gravitational wave harmonic). Higher-order mass-ratio corrections just modify the rate of change of orbital frequency as a function of orbital frequency (as discussed for conservative self-force corrections in [6]). These corrections occur at order m/M above leading order (which itself is $O(m/M)$ since inspiral arises from radiation reaction). A change $\Delta\dot{f}$ in the inspiral rate $d(Mf)/d(t/M)$ leads to a $\Delta N \sim \Delta\dot{f}(T/M)^2$ change in the number of cycles over a dimensionless observation time T/M . If the observation time was fixed, this increases like $O((m/M)^2)$, and therefore is much bigger for IMRIs than EMRIs. However, LISA has a fixed frequency bandwidth, and so above a certain mass ratio, inspirals will be observed over a fixed range of frequency. In that limit, the effective observation time is proportional to the number of cycles in a fixed frequency range, $T/M \sim M/m$, which suggests higher order corrections to \dot{f} lead to a phase shift $\Delta N \sim (m/M)^2(T/M)^2 \sim 1$, independent of mass ratio.

This argument indicates that perturbative waveform templates will become worse as the mass ratio increases, but at some point the errors will stabilise. Of course, the argument above sweeps many things under the carpet. The orbital frequency is not the only observable, and we have ignored the changes to the GW energy spectrum in the above argument. We have also not considered the size (or post-Newtonian order) of the various corrections to the rate of change of frequency. This argument can be quantified somewhat by using post-Newtonian models. It is possible to compute the overlap of a \mathcal{PN} waveform, linearised in mass ratio, with the full \mathcal{PN} waveform. This calculation will indicate the relative importance of including higher-order mass ratio terms in perturbative models, even though the \mathcal{PN} models are not reliable as EMRI templates. Using a leading order \mathcal{PN} model, describing the last three years of inspiral of two non-spinning bodies, with central MBH mass of $10^6 M_\odot$, the mismatch between the linearised and full waveforms increases from 0.001% (when $m = 0.5 M_\odot$) to 0.01% ($m = 1.4 M_\odot$) to 1% ($m = 10 M_\odot$) to 15% ($m = 100 M_\odot$) to 18% ($m = 1000 M_\odot$). This is consistent with the above argument. For lower mass central black holes, the mismatches are likely to be higher since the plunge frequency is correspondingly higher. There is also likely to be a significant increase in the mismatch when spin is included.

In summary, perturbative templates without higher order mass ratio corrections or spin-orbit coupling corrections will probably not be good enough as IMRI templates. However, it might be possible to construct “Kludge” IMRI templates by including post-Newtonian spin-orbit and other corrections in the current kludge EMRI models (in the same way that conservative corrections are currently being included). This needs further investigation.

6.3 Testing relativity theory

One of the potentially exciting payoffs from EMRI and IMRI observations made by LISA is the ability to test aspects of relativity theory. The high mass ratio ensures the small object acts like a test particle moving in the background space-time of the central black hole. The emitted gravitational waves trace out the orbit of the particle,

which in turn encodes a map of the space-time [92]. EMRI events are comparatively “clean” systems, and we know what this map should look like if the inspiral is an inspiral into a Kerr black hole. Decoding the map then allows us to measure the parameters of the system to high precision. However, if the inspiral deviates from what we expect — an inspiral, described by General Relativity, of a compact object falling in vacuum into a Kerr black hole — we should be able to see this deviation in the emitted gravitational waves.

6.3.1 Current status

Conceptually, tests of a theory fall into two general categories: comparisons of rival theories (which theory is best supported by the data?) and tests of consistency (are the data consistent with a given theory?).

6.3.1.1 Comparisons of rival theories

Currently there are no really plausible rivals to general relativity; rival theories have either been ruled out, or, like Brans-Dicke, can be dialled arbitrarily close to general relativity by adjustment of extra parameters (and so could never be ruled out even if GR were completely correct). Moreover, to test an alternative theory, we need to be able to compute gravitational waveforms for EMRIs in that alternative theory to compare against EMRI gravitational waves from Relativity. This is a very challenging problem both theoretically and computationally.

Constraining the parameter space that rival theories can occupy can be a useful exercise, since it is a measure of how close to General Relativity the true theory must lie. It is possible to compute the leading-order correction to the gravitational wave phasing for inspiralling objects in Brans-Dicke theory. Work on this has suggested that LISA observations of neutron stars inspiralling into $\sim 10^2\text{--}10^4 M_\odot$ black holes could put meaningful constraints on the Brans-Dicke parameter and on the mass of the graviton [111, 17]. The theoretical waveforms used for this work were rather simple and ignored important effects such as orbital plane precession due to spin-orbit coupling. It is known that parameter estimation accuracies for MBH binaries

improve significantly when spin-orbit coupling is included [107, 66], so the current results are probably conservative. However, it is unclear whether the astrophysical rate is sufficiently high that LISA will be likely to see any of the “optimal” events for such an analysis ($1.4M_{\odot} + 10^3M_{\odot}$). Moreover, developing highly accurate waveforms under alternative theories is difficult, and the constraints that I/EMRI observations will be able to impose on the parameter space will probably not be significantly tighter than existing results. For these reasons, most research to date has focussed on the second type of test — tests of consistency.

6.3.1.2 Tests of consistency within General Relativity

A simple example of a consistency test would be to divide an observed EMRI signal into several consecutive pieces, and show that the best-fit parameters from each piece were consistent with each other, within the error bars. This would already be a very strong test of the theory. The complication in regarding EMRI observations as consistency tests is that taking GR to be the correct theory of gravity is not the only assumption that goes into generating the waveform. We assume also that the system is vacuum and that the central body is described by the Kerr metric. Without requiring an alternative theory, we can regard EMRI observations as testing the premise that massive compact objects in our universe are Kerr black holes, rather than some other exotic object (e.g., a boson star or naked singularity) that is still consistent with Relativity. Any axisymmetric, vacuum space-time in Relativity can be decomposed into mass (M_l) and current (S_l) multipole moments [45, 52] and it was demonstrated by Ryan [92] that these multipole moments are redundantly encoded in gravitational wave observables, namely the periaapsis precession frequency, the orbital plane precession frequency and the gravitational wave energy spectrum for nearly circular, nearly equatorial orbits. If an object is enclosed by a horizon and there are no time-like curves exterior to the horizon, then the object must be a Kerr black hole (this is the “no-hair” theorem), and all of its multipole moments are determined by

the mass and spin of the black hole [52]

$$M_l + iS_l = M (ia)^l, \quad (6.2)$$

where M is a black hole’s mass and a is the reduced spin of the black hole $a = S_1/M$. If three moments of the space-time are extracted from the gravitational wave emission, these can be checked for consistency with (6.2). A boson star with large self-interaction (one viable alternative to an MBH) is uniquely characterised by three multipole moments [93], so if four moments are extracted from the gravitational wave emission, the boson star model could also be ruled out. This idea of measuring multipole moments is sometimes referred to as “testing the no-hair property” (one sometimes hears the variation “testing the no-hair theorem”, but this is obviously sloppy wording, since a true mathematical theorem cannot be invalidated by any experimental test). Objects with non-Kerr values of higher multipole moments within general relativity would have to be exotic stars or naked singularities. The no-hair theorem applies only in Relativity, thus non-Kerr values of the higher multipole moments could also arise if the object is a black hole, but Relativity is the wrong theory of gravity. If, for example, the quadrupole moment of the massive object was found to differ from that of a Kerr black hole, this could, therefore, have several explanations. We will discuss this in more detail later.

A significant amount of work has been done on quantifying how well LISA could measure multipole moments and carry out these sorts of tests. Ryan [94] considered a general axisymmetric space-time, decomposed into multipole moments and found that a LISA observation of a nearly circular, nearly equatorial EMRI could measure the mass quadrupole moment to an accuracy of $\Delta M_2/M^3 \sim 0.0015 - 0.015$, depending on the source parameters. Ryan’s approach is somewhat unwieldy, however, since an infinite number of multipole moments are present in the Kerr space-time. The multipole expansion is essentially an expansion in $1/r$, where r is the distance from the black hole. LISA will mostly observe EMRIs that are deep in the strong field region, very close to the black hole and in that regime all the multipole moments

will be important. Extracting multipole moments one at a time is therefore a rather inefficient way to characterise a Kerr black hole. Collins and Hughes [26] were the first to suggest an alternative approach to LISA observations — regarding the observation as a null-hypothesis test of the assumption that the EMRI is a Kerr EMRI. By constructing space-times that are close to Kerr, which Collins and Hughes called “bumpy black holes”, it is possible to quantify how large a deviation from the Kerr space-time could be present while leaving the signal observationally consistent with a Kerr inspiral [60]. This approach is preferable, since the Kerr space-time can then be recovered exactly by dialing a small parameter to zero, so we do not lose much sensitivity to the events that we expect to see by using detection templates with an additional bumpy parameter. Collins and Hughes constructed a static space-time that deviates from the Schwarzschild space-time by a small amount. They did this by using the Weyl metric and adding a perturbation that represents a pure mass quadrupole asymptotically. They found that the azimuthal frequency of equatorial orbits with the “same parameters” differed by 0.01% (for an orbital periapsis of $\sim 50M$) – 10% (for periapsis of $\sim 6M$) when a quadrupole moment perturbation $Q = 0.01M^3$ was added.

Babak and Glampedakis [47] carried out a similar calculation for stationary space-times that deviated from Kerr by a small amount, which they constructed using the Hartle-Thorne approach. They not only considered orbital frequencies, but also constructed kludge waveforms and found that in the presence of a $\sim 10\%$ deviation in the quadrupole moment of the space-time, the overlap could degrade by 25% over the radiation reaction timescale for typical LISA events. In both these analyses, the results were not directly relevant to observations, since they took no account of the fact that some of the differences in the waveforms could be mimicked by changing the orbital parameters (Babak and Glampedakis did comment on this fact in their paper, however). Recently, Barack and Cutler [11] have done an analysis accounting for parameter correlations, using a waveform model constructed by including a term representing a non-Kerr value of the quadrupole moment of the central black hole into their analytic kludge [9]. They find that LISA could measure the quadrupole

moment, $Q = -S^2/M$, of the central black hole to an accuracy $\Delta Q/M^3 \sim 10^{-3}$, while simultaneously measuring the mass and spin to an accuracy of $\sim 10^{-4}$. We note that spinning boson stars typically have quadrupole moments ten to a hundred times larger than Kerr black holes of the same mass and spin [93]. This provides an indication of the accuracies required to do meaningful tests.

The research described above concerns extracting information about the spacetime multipole structure from the inspiral part of the waveform. If a ringdown was also detected, the ringdown frequencies can also be used to measure the multipole structure of the ringing object [18]. EMRI-induced ringdowns are unlikely to be detected with sufficient signal-to-noise ratio, but IMRI-induced ringdowns could plausibly be used for such a test. However, more work needs to be done to quantify this, in particular to compute ringdown frequencies for non-Kerr supermassive objects. Moreover, in general the constraints on the multipole moments obtained from the inspiral will be tighter than those obtained from the ringdown due to the large number of wave cycles that can be observed over the inspiral.

There is an analogous source to EMRIs that might be detected by ground-based gravitational wave detectors, namely the inspiral of a stellar mass neutron star or black hole into a $\sim 100M_\odot$ IMBH (a “LIGO IMRI”). The event rate for such inspirals is somewhat uncertain (see [55, 84, 71] for discussion and further references). However, if they are detected, these sources have the potential to probe the strong-field regime with more modest accuracy than LISA’s EMRIs, and would be observed by Advanced LIGO, i.e., a few years before LISA EMRI events are observed. A significant amount of work has gone into studying these sources [20], and this work also applies to LISA EMRI/IMRI events. Some of the applicable results include the generalisation of Ryan’s results [92] to more generic cases. Ryan considered only nearly circular, nearly equatorial orbits and ignored the effect of tidal coupling. The generalisation to eccentric but nearly equatorial orbits is straightforward, although the generalisation to arbitrary orbits is difficult [20, 68]. An extension of Ryan’s theorem to tidal coupling tells us that this coupling is also encoded in (and could be extracted from) the gravitational wave observables [20, 69]. The inspiralling object distorts the horizon

surrounding the central object and orbital energy is lost to gravitational radiation flowing into the horizon as well as out to infinity. These interactions with the horizon can be modelled as a tidal interaction, and characterised in terms of energy being lost to the central body through tidal dissipation. In broad terms, the multipole moments of the space-time can be extracted from observations of the periapsis and orbital plane precession rates, and from these the rate at which energy is being radiated to infinity can be determined. The rate at which energy is being lost from the orbit can also be measured, by observing the change of the orbital frequency with time. The difference between these two energy fluxes gives the flux of energy going into the central body, which is a measure of the strength of the tidal interaction, and tells us about the structure of the central object [20].

In another aspect of this effort to study EMRIs, Gair *et al.*[44] have studied the properties of geodesics in other classes of “bumpy” space-times. This work has considered two types of nearly Kerr space-times — exact solutions in the family of Manko and Novikov [72] that deviate from Kerr in the quadrupole and higher moments, and perturbative solutions constructed via solving the Teukolsky equation and then applying the Chrzanowski-Ori procedure to recover the metric [25]. As mentioned before, the geodesics in the Kerr space-time possess three integrals of the motion, because the Kerr space-time is one of a special class of GR solutions for which the Hamilton-Jacobi equation is separable [23] and Q arises as the separation constant. Space-times that deviate from Kerr, even by a small amount, may not be of separable form, and therefore there is no guarantee that the geodesics will possess a full set of integrals. However, it turns out that the majority of geodesics in most of the space-times considered in [44] have an approximate third invariant, and the geodesics are tri-periodic to high accuracy: the waveform phase evolution can be decomposed in terms of harmonics of three fundamental frequencies to an accuracy of one part in 10^7 or better. This means that Ryan’s theorem can be applied, and deviations from Kerr show up only in the differences in precession and inspiral rates. However, in a small subset of cases, the geodesics show apparently ergodic motion, with no well defined frequency structure. Although this makes the sources difficult to detect, observations

of ergodic dynamics would be a clear signature that the space-time was not simply Kerr. This is unlikely in practice since the ergodic motion only appears for orbits that are very close to the central object, and this is a regime that is probably not accessible in an inspiral that begins with the capture of a star on a highly eccentric orbit some distance from the central object.

6.3.2 Outstanding challenges

There are several questions that still need to be addressed before LISA will be able to carry out tests of General Relativity. These include:

- What are the imprints of deviations from Kerr on the waveforms generated by EMRIs on generic orbits? As described above, we have a partial answer to this question already. However, the only work so far that includes the effect of radiation reaction on generic orbits is [11], which uses a very simple model. With further research, it should be possible to make general statements about how deviations from Kerr manifest themselves in the EMRI signal, and how the deviations correlate with other parameters. We want to understand how adding greater complexity in the family of deviations from Kerr causes the determination of other parameters to degrade, e.g., whether a Kerr EMRI could also be well described by a “bumpy” Kerr EMRI with different parameters. In [94], Ryan found that by adding arbitrary multipole moments (up to M_{10}), the accuracy with which the mass of the large body could be determined in an observation degraded from one part in 10^6 to one part in 3, although most of this degradation was due to the inclusion of moments up to S_5 . This is a known problem in data analysis: introducing more parameters (especially if they are small) causes effective “noise” in the parameter space. This would also apply if we wanted to use EMRI observations to also test alternative theories of gravity. Testing everything simultaneously would yield very poor constraints, since there would likely be correlations between, for example, a non-zero Brans-Dicke parameter and an anomalous quadrupole moment. Thus, it might be

necessary to decide *a priori* which deviations from Relativity we most want to constrain in order to produce useful statements.

- Are there any “smoking gun” signatures for deviations from Kerr? For instance, ergodicity in the orbits — which “nearly Kerr” space-times admit ergodic orbits, and can a star end up on these orbits in practice? What are the observational signatures?

- Can matter external to the massive object (e.g., an accretion disc, or other stars) perturb the EMRI orbit sufficiently to leave a measurable imprint on the emitted gravitational waves? How would we detect or recognise such a system? Some work has already been done to estimate the effects of an accretion disc [24, 79, 14], which suggests that these effects are unlikely to be measurable unless the accretion disc is very massive. Such massive discs might be found around MBHs accreting at or near their Eddington limit, i.e., in active galactic nuclei. Star formation in the disc of such systems might lead to EMRI events. In a normal nucleus, accretion could happen if a lot of material was recently dumped in the vicinity of the MBH by, for example, the disruption of a star or a gas cloud. However, such events occur very infrequently [108]. If a very tight binary, consisting of a main sequence star and a compact object, were to inspiral into a $10^6 M_{\odot}$ MBH, the MS star would be disrupted at a distance of $\sim 2 \times 10^{-6}$ pc from the MBH. Most of the bound stellar material would be accreted within a few years [104, 74] but it would take $100 - 10^4$ years for the compact object to complete its inspiral. Therefore it seems unlikely that the material of the disrupted companion can either perturb the EMRI or create a clear-cut electromagnetic precursor to it. Nonetheless, if there is a small possibility that such a system could in principle be observed, it is important that we know how to detect it and recognise it, not least because an EMRI interacting with a massive accretion disc might lead to an electromagnetic counterpart. An EMRI with a counterpart is a powerful cosmological probe, so it is valuable to maximise our chances of seeing such events.

Finally, we note that if two EMRIs were occurring simultaneously, this would almost certainly leave a measurable imprint on the emitted gravitational waves. However, this is very unlikely as well. A compact binary of mass m_{bin} tight enough to survive tidal separation down to a distance R of the MBH, would have to have a timescale for (self-)merger by GW emission, τ_{merge} , smaller than $\tau_{\text{merge}} < \tau_{\text{insp}}(\mathcal{M}_{\bullet}/m_{\text{bin}})^{2/3}$, where τ_{insp} is the timescale for inspiral into the MBH on a circular orbit of radius R . Therefore there cannot be any significant number of binaries tight enough to survive until the last ~ 100 years of inspiral. If the binary disrupts earlier it is likely that both stars will find themselves on orbits with vastly different inspiral times and when the faster-inspiralling one becomes detectable the other will still be too dim. However, the distant EMRI might cause a detectable orbital perturbation on its ex-companion and this has to be assessed.

- How do we interpret deviations from Kerr if they are observed? There could be several explanations — there could be material external to the black hole; alternatively, the massive object could be some exotic star with a non-singular distribution of matter (e.g., a boson star); yet another possibility is that the massive object is a naked singularity, which would disprove the cosmic censorship conjecture, but would not contradict the no-hair theorem. How could we distinguish these possibilities in an observation? Over a long (\sim year) observation, it should be relatively straightforward to distinguish the effect of material outside the black hole (an “external” quadrupole perturbation) from a change in structure of the central object (an “internal” quadrupole perturbation), since the effect would accumulate differently over the course of an inspiral. The existence/location of a horizon might be determined from gravitational wave observations. While an inspiral into a Kerr black hole would undergo a rapid plunge from the innermost stable circular orbit followed by a ring-down, an inspiral into a boson star may continue to produce inspiral-like waves after the compact object crosses the stellar surface. The signal-to-noise ratio generated during the

plunge and ringdown for an EMRI will be small, so this will almost certainly not be observed. However, if a signal persisted after the “plunge”, this might be detected by building up the signal-to-noise over several waveform cycles. Thus, we might be able to say whether a signal is still “present” or “absent”, although the resolution of the time at which the signal became absent would not be very high. A horizon could be inferred by comparing the approximate time of plunge with the plunge time predicted based on parameters measured in the early part of the inspiral. If a horizon is found to be absent, the object might be an extended mass distribution (e.g., a boson star) or a naked singularity. If emission after the object’s path started to intersect the boson star material was observed with sufficiently high signal-to-noise, the features of this emission might allow us to distinguish between these two possibilities [63]. Only if the massive object were found to have a non-Kerr quadrupole moment that was not due to the presence of exterior matter *and* a horizon would there be firm evidence that the system did not have the no-hair property; however, proving that any horizon completely surrounds the body and that no closed time-like curves exist in the exterior may be impractical. While these ideas give us some hope that interpretation will be possible, further research is needed on all of these topics.

- How do we detect deviations from GR in practice? The need to use matched filtering for EMRI detection makes it difficult to detect signals that look very different from our template models. It also makes it hard to detect small deviations in the model. The simplest thing we can do is to look only for inspirals into Kerr black holes. If our observations are consistent with this model, then we have tested the theory to high precision. The existing research programme then allows us to make statements such as “this observation is consistent with a Kerr inspiral, with agreement in the quadrupole moment to $x\%$ ”. To do this in practice we would perform Monte Carlo simulations to find the maximum “ x ” such that the gravitational waveform emitted during an inspiral into a non-Kerr

object with a quadrupole moment that differed by x from the Kerr value still had sufficiently high overlap (for a suitable definition of “high”) with a waveform emitted during an inspiral into a Kerr black hole with some (not necessarily the same) parameters. A more sophisticated analysis could look at segments of the inspiral separately, and check for consistency in the parameters estimated for each segment. We could also look for characteristic signatures of a deviation from Kerr, for instance a transition from regular to ergodic motion in the orbits or the existence/location of the horizon inferred by the plunge time. This might be done by dividing the end of the inspiral into short segments, in which the signal should have SNR large enough so that we can say with high confidence whether the signal is present or absent. The resolution of the plunge time is thus likely to be poor. If the EMRI is close enough to be loud ($\text{SNR} \gtrsim 50$), it might be possible to detect the signal in a time-frequency analysis. This would not only make it easier to measure things like the plunge point, but would allow us to detect signals that deviate significantly from Kerr inspirals. Finally, it might be possible to do a more generic analysis using templates parametrised by space-time multipole moments, e.g., the family employed by Ryan [94]. Such a technique would not be particularly sensitive to Kerr inspirals, but if it was used in conjunction with a matched filtering search for Kerr EMRIs it might be a useful diagnostic. As EMRI data analysis techniques are developed, techniques for space-time mapping will need to be properly explored.

6.4 EMRI science

It is clear from the discussion of EMRI detection above that, while much is already known, there is still some work to be done before LISA flies. However, the scientific payoffs if we detect and characterise a large number of EMRI events could be very significant. From a single EMRI observation, we can measure the parameters of the system to very high precision [9]. The mass and spin of the central black hole, the mass of the inspiralling object, and the orbit’s eccentricity (at some fiducial instant) can

all be determined to a part in 10^4 , typically, while the cosine of the orbit's inclination angle (roughly, the angle between the MBH's spin vector and the orbital angular momentum of the CO) can typically be determined to $\sim 10^{-3}$ – 10^{-2} . The luminosity distance to the source can be measured to an accuracy of $\sim 5\%$, and the sky position to a resolution of 10^{-3} sr (a few square degrees). The accuracies achievable with LISA IMRI observations should be significantly better. In addition, for each of these observed systems we will be able to test the black hole hypothesis to high accuracy (e.g., constrain the mass quadrupole moment to a fraction of a percent), as described in Section 6.3.

LISA may detect as many as several hundred EMRIs out to a redshift of $z \sim 1 - 2$ [8, 43]. The first estimates of signal-to-noise ratios for EMRIs were done by Finn and Thorne [36]. They considered circular equatorial inspirals only, and found that at a distance of 1Gpc, one year before plunge, the inspiral of a $10M_{\odot}$ object into a rapidly spinning 10^6M_{\odot} black hole would have signal-to-noise ratio of ~ 100 in a gravitational wave frequency bandwidth equal to the frequency. To obtain EMRI rate estimates, updated signal-to-noise ratios were computed for inclined and eccentric orbits, using kludged waveforms [40, 6] and including a more accurate model of the LISA response provided by the Synthetic LISA simulator [106]. Table 6.1 shows the results of those calculations — the signal to noise ratio of a variety of systems at a fiducial distance of 1Gpc [8, 43]. These signal to noise ratios assume that the LISA mission lasts five years and that the satellite is fully functional for the whole time, so that the optimal combination of TDI data streams can be used. These results are consistent with Finn and Thorne [36] when one accounts for the gravitational wave bandwidth remaining one year from plunge, the fact that Finn and Thorne compute the SNR in one LISA Michelson channel only and the fact that these orbits are eccentric.

To translate these SNRs into a maximum detectable distance, we first need to specify a detection threshold. The estimated detection threshold for the semi-coherent algorithm described earlier is ~ 30 , although optimisation of this method may be able to reduce this threshold somewhat. A GW source at a redshift z with masses M and m looks like the same type of gravitational wave source at a Euclidean distance equal

M/M_\odot	m/M_\odot	SNR at 1Gpc	z_{max}	$M_i/M_\odot(z_{max})$	$m_i/M_\odot(z_{max})$
3×10^5	0.6	18	0.13	2.7×10^5	0.53
	10	73	0.44	2.1×10^5	6.9
	100	620	2.5	8.5×10^4	29
1×10^6	0.6	30	0.21	8.3×10^5	0.50
	10	210	1.0	4.9×10^5	4.9
	100	920	3.5	2.2×10^5	22
3×10^6	0.6	25	0.17	2.6×10^6	0.51
	10	270	1.3	1.3×10^6	4.4
	100	1500	5.2	4.8×10^5	16

Table 6.1: This table shows the signal-to-noise ratio (SNR) at a distance of 1Gpc for systems with a variety of observed masses M and m . Also shown is the maximum redshift at which such a source could be detected, z_{max} , and the intrinsic masses of the system, $M_i = M/(1+z_{max})$ and $m_i = m/(1+z_{max})$, that a source at redshift z_{max} would need to have in order to have apparent red-shifted masses M and m . The SNRs were computed assuming the optimal TDI combination of LISA data streams could be constructed for five years of observation. All sources have MBH spin of $S/M^2 = 0.8$, inclination of 45° and eccentricity at plunge of 0.25. The waveforms were computed using the numerical kludge model [40, 6] and the LISA response was included using the Synthetic LISA simulator [106]. These results were used for computing event rate estimates using the semi-coherent search [43].

to the luminosity distance to redshift z , $D_L(z)$, but with red-shifted masses $(1+z)M$ and $(1+z)m$. Table 6.1 also shows the redshift at which the source would have SNR of 30 (computed by setting $\text{SNR}(1\text{Gpc})/30 = D_L(z)/1\text{Gpc}$) and the intrinsic masses M_i and m_i that a source at that redshift would have to have in order to give the appropriate observed masses. This Table serves to illustrate the typical distances to which sources can be detected.

The mass red-shifting makes the process of computing the range for a given source a more complicated procedure than a simple linear distance scaling. Figures 6.4 and 6.5 show preliminary results of a more careful calculation [39]. The plots show contours of constant “detectable lifetime” for circular-equatorial EMRI sources as a function of the mass of the central black hole. The figures plot the intrinsic mass of the MBH on the x-axis, and redshift on the y-axis. The lines on the plot are contours of equal observable lifetime, τ . A source will be detectable only if the signal-to-noise ratio accumulated over the LISA mission exceeds the necessary threshold (assumed

to be 30 for this plot). This requirement will only be satisfied if the source is in a certain range of phases of the inspiral at the moment that LISA starts taking data. The observable lifetime is the length of that acceptable range of phases, as measured at the source. If EMRIs of this type start once every T years in any galaxy, the expected observed number of events would be τ/T per galaxy. For Figure 6.4, we consider only prograde inspirals into a central black hole with spin $a = 0.99$ and plot contours for various values of τ . In Figure 6.5 we show $\tau = 1\text{yr}$ contours for various black hole spins (NB a negative spin indicates a retrograde inspiral into a black hole with spin of the same magnitude). In both plots we have assumed a constant mass for the compact object of $10M_{\odot}$, and are considering circular-equatorial inspirals only. These results were computed using the flux data tabulated in Finn and Thorne [36], assuming a five-year LISA observation that uses both Michelson channels, averaging over the sky position and orientation of the source, and taking the LISA noise spectral density as given in [9], with the assumption that the white-dwarf background has been subtracted using five years of LISA data. It is clear from this figure that we can see EMRI events out to fairly large distances, but that this distance is very spin dependent. There is also a significant spin-dependence of the mass to which LISA has maximal reach. The fraction of the total energy radiated that is radiated in a circular-equatorial inspiral between a Boyer-Lindquist radius r and plunge at the innermost stable circular orbit, r_{isco} , effectively depends on spin only through the ratio r/r_{isco} . The ISCO radius decreases as the black hole spin increases, and the total energy radiated increases. This means that inspirals into rapidly spinning black holes radiate more energy, having, therefore, higher total signal-to-noise ratios, and this radiation is emitted at higher frequencies for a given central black hole mass. LISA will be most sensitive to systems that radiate most of their energy in the detector's optimal sensitivity range of $\sim 3\text{--}10\text{mHz}$. The frequency of the radiation decreases as the black hole mass increases, but increases as the spin increases. The mass that ensures radiation at $\sim 5\text{mHz}$ will, therefore, be larger for higher black hole spins, as illustrated in the figure. It is also clear from Figure 6.5 that the sensitivity to low mass central black hole systems is effectively independent of spin. For these systems,

LISA will observe the middle part of the inspiral, while the final plunge occurs at higher frequencies that are out of band. LISA will, therefore, observe a phase of the inspiral where the radius is large, at which distances the orbit does not “feel” the effect of the black hole spin.

These results illustrate the LISA range to typical EMRIs, but are only for circular-equatorial orbits, and assume a simplified model of the LISA response. Eccentric orbits in general will lose more energy in the LISA band, and hence should have larger signal-to-noise ratio. Treating the LISA data stream more carefully, using a TDI analysis (e.g., by using Synthetic LISA to include the response function [106]), will also tend to increase the signal-to-noise, especially for sources that generate significant radiation at high frequencies. These general expectations are supported by the results in Table 6.1 and by further calculations using numerical kludge waveforms [40, 6] for eccentric-inclined orbits.

For all of the systems that LISA can see, we will obtain accurate parameter estimates. LISA will thus provide data on a large sample of black holes in the relevant mass and redshift range, which can be used for astrophysics. For the discussion sessions at the meeting that inspired this review, we divided the scientific questions on the astrophysical benefits and consequences of LISA EMRI and IMRI observations into five categories. We summarise these in the following sections, along with an outline of the answers that LISA might give us.

6.4.1 What can we learn from the characterisations of EMRI/IMRI dynamics, i.e., the observed eccentricities etc. of the orbits?

The observed eccentricities will carry information about the capture mechanism: significant eccentricities are indicative of the direct capture scenario via two-body relaxation, while negligible eccentricities suggest capture via binary tidal disruption or, possibly, tidal stripping of giants (such captures occur at a higher periapsis and have time to circularise before entering the LISA band). The orbital inclination is also informative: random inclinations are expected in the standard scenario with a spher-

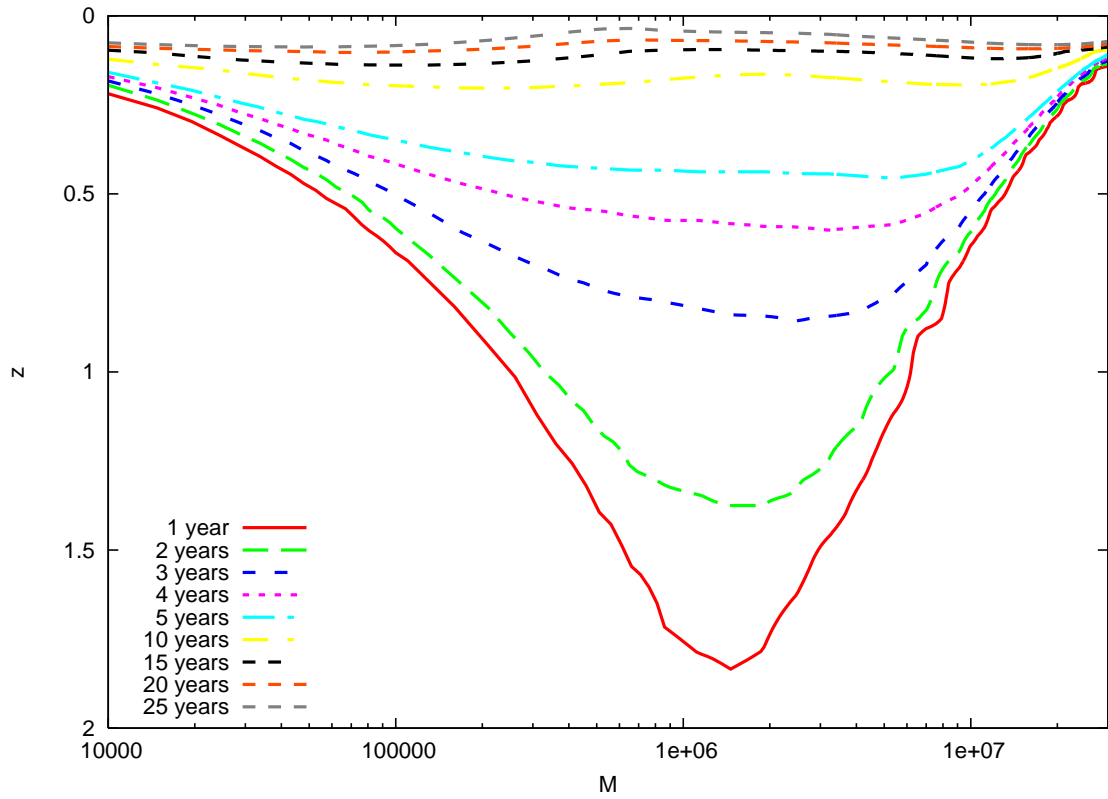


Figure 6.4: Contours of constant “detectable lifetime” (as defined in the text) for the circular-equatorial inspiral of a $10M_\odot$ black hole into an MBH with spin $a = 0.99$, as a function of MBH mass M and redshift z .

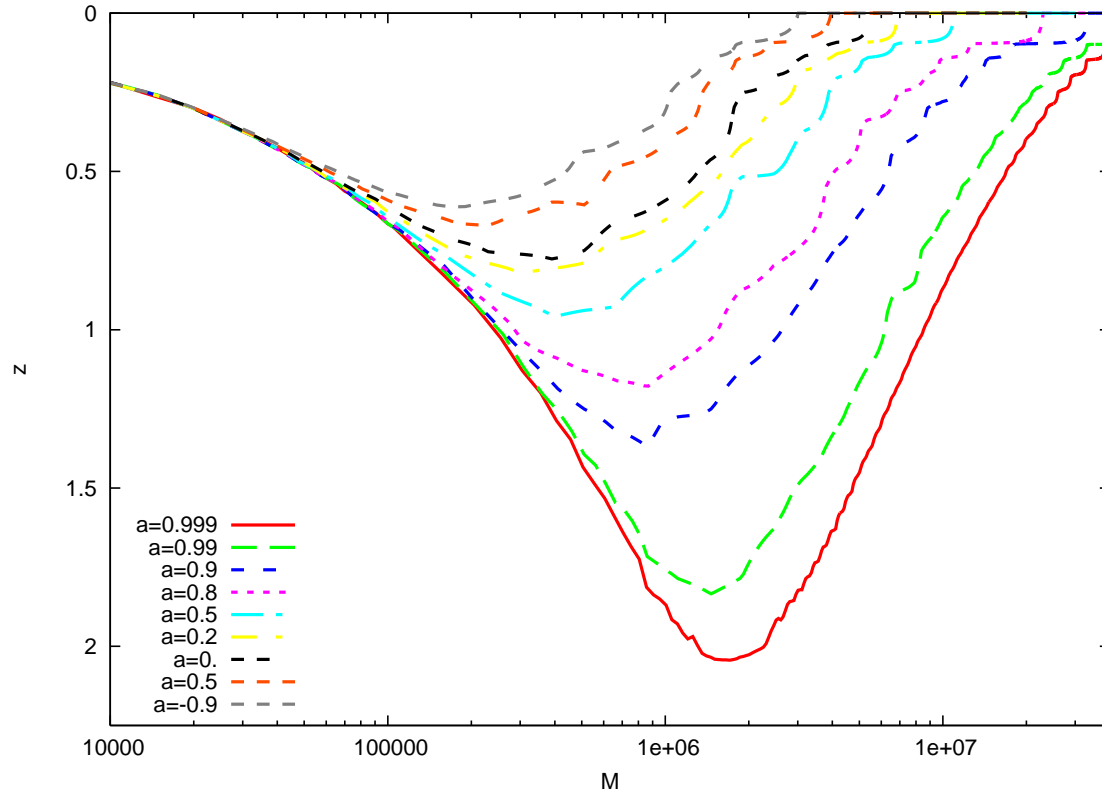


Figure 6.5: As for Figure 6.4, this figure shows contours of constant “detectable lifetime”, τ , for the circular-equatorial inspiral of a $10M_{\odot}$ black hole into an MBH. Here we show $\tau = 1$ year contours for several different spins of the central black hole, as labelled in the key. Negative spins indicate retrograde circular-equatorial inspirals into black holes of the same spin magnitude.

ical cluster, while formation in the disc would be manifested by a significant fraction of EMRIs having near-zero inclinations (although this could be made more complicated by disc warpage). The event rates themselves would be interesting, although it may be very difficult to deconvolve the various uncertain parameters that influence event rates (e.g., the MBH density and mass function, the density and distribution of compact objects near the MBH, etc.).

6.4.2 What can we learn about the inspiralling compact objects from EMRIs/IMRIs?

We will learn the CO mass to fractional accuracy $\sim 10^{-4}$. From the distribution of masses we will obtain information about the relative numbers of the WD, NS, and BH populations close to the MBH (within ~ 0.01 pc). Although it is difficult to deconvolve mass segregation from the initial mass function or from the mass-dependence in capture rates, unexpected results such as the under-representation of more massive COs could be very intriguing. If BHs with masses in the range $20 - 1000M_{\odot}$ are found, this is already an important discovery, since such objects are not yet firmly known to exist (and, if $1000M_{\odot}$ IMBHs do exist, it is not clear how well they can sink to the centre). Even the precise measurement of the mass of a few stellar BHs (in the range $3 - 20M_{\odot}$) would be of great interest to constrain models of stellar evolution and collapse. CO spins will probably not be measurable for EMRIs, but we guess they might be measurable to $\lesssim 10\%$ for IMRIs. This would tell us about the formation mechanism for IMRIs (has mass been accumulated mostly via accretion, or via mergers?), just as for the MBH spin.

6.4.3 What can we learn about the MBHs from EMRIs/IMRIs?

From

EMRIs/IMRIs, we will learn the masses and spins of MBHs to fractional accuracy $\sim 10^{-4}$. Rapid spins will imply that much of the MBH mass was built up by gas accretion from a disc (unless the gas arrives in randomly oriented events [64, 65, 91]), moderate spins will imply the MBH was built as a result of a major merger

of comparable-mass black holes [61, 75], while low spins will imply the MBH was mostly built from a sequence of minor mergers with smaller objects coming in from random directions (since then the spin angular momentum increases only in a random-walk fashion). The boundaries that separate these three spin regimes are somewhat uncertain. Spins $S/M^2 > 0.9$ are undoubtedly “high”, but lower spins might also arise from accretion. The spins resulting from major mergers depend on the magnitude and direction of the spins of the two components prior to merger and could be anywhere in the range $0.4 \lesssim S/M^2 \lesssim 0.9$. Spins $S/M^2 < 0.2$ are undoubtedly “low”, but the boundary between this regime and the major merger regime is unknown. Once again, decoding the spin observations must be done carefully. The prograde inspiral of a black hole into a rapidly spinning MBH has much greater SNR at a given distance than a retrograde inspiral or an inspiral into a MBH of lower spin. Our observations will therefore be weighted towards more rapidly spinning black holes. Since we can compute the relative SNR of systems with different spins, it will not be too difficult to account for bias when interpreting the observations, but this must be done carefully.

6.4.4 What can we learn about cosmology and early structure formation from EMRIs/IMRIs?

An EMRI or IMRI observation will give a very accurate measure of the luminosity distance to a source, but not an independent value for the redshift at which the source is located. However, it is possible that an electromagnetic counterpart to an EMRI event will be observed (the sky position accuracy of a few square degrees, although poor, is not beyond the reach of survey telescopes). The EMRI will be observed for sufficiently long before plunge that the plunge time can be accurately estimated, and advance warning of the moment of coalescence supplied to other telescopes. However, it is not entirely clear what mechanisms could give rise to an electromagnetic signature at coalescence that would be sufficiently bright to be seen at cosmological distances. If we were lucky, and a single EMRI event was observed with an electromagnetic counterpart, it would provide an estimate of the Hubble constant that is not tied to the local distance scale. We could thus measure the Hubble constant to $\sim 2\%$,

compared to the current systematic error from the Hubble Key Project of $\sim 10\%$. With N observations, the error decreases like $1/\sqrt{N}$.

The inspiral of a $10 M_{\odot}$ object into a $10^5 - 10^6 M_{\odot}$ MBH should be detectable to a redshift of about 2, corresponding to a time when the Universe was less than 4 Gyr old. Although MBH-MBH mergers are visible to much larger redshift, offering the potential to probe the whole early history of MBH formation and growth, there are considerable uncertainties about their predicted detection rate [51, 73, 112, 97]. Also the merger rate for LISA-detectable systems probably peaks at $z > 2$. EMRIs therefore offer an alternative and complementary way to probe the relatively late evolution of MBHs with masses below a few $10^6 M_{\odot}$.

6.4.5 How can EMRIs/IMRIs be used to test GR, or (assuming GR is correct) that the central massive object is a Kerr BH?

As discussed above, what we can perform are consistency checks (i.e., is the signal consistent with GR predictions?) or compare the Kerr null hypothesis to straw man alternatives. In the simplest case, if we find that the observed EMRI waveforms agree with the models predicted by GR, for reasonable physical parameters, this would be an impressive verification of the theory. Matching strong-field EMRI waveforms to one cycle in 10^5 will be compelling evidence in support of GR. Beyond this, one can further check consistency in the EMRI by checking, for example, that different pieces of the waveform yield the same consistent estimates for the physical parameters of the system. This amounts to verifying the consistency of relativity in the strong field region in the immediate vicinity of MBHs, a regime in which it has not been verified to date (though one hopes this regime will be probed by LIGO before LISA flies, albeit with less accuracy). These consistency checks are not testing the theory against an alternative; however, this is familiar from other areas of physics. For instance, in particle physics, tests of the standard model are not based on comparison with serious rivals: one measures that the W mass or top quark mass is roughly where it is predicted, and this is trumpeted as a substantial validation of the theory. Also,

the idea of embedding GR/Kerr predictions in a somewhat larger, phenomenological theory (e.g., with non-zero graviton mass, or non-standard quadrupole moment for the BH), is similar to the current status of GR tests with binary pulsars, in which the orbital motion is first fit to a phenomenological set of Keplerian and post-Keplerian parameters, and radio astronomers then show that the fitted values are consistent with the predictions of GR (twenty years ago binary pulsar measurements killed a host of alternatives to GR, but now that they are dead, radio astronomers are also stuck with demonstrating consistency with GR).

One important issue is whether, if systems that differ from the Kerr hypothesis exist, we will actually be able to detect them, given that our data analysis will rely on matched filtering. As mentioned above, if the deviations are small, this will not be a problem, since the source will remain consistent with our templates for long enough to be detected. The point at which deviations start to appear will then be a probe of the nature of the deviations present (e.g., the existence/location of a horizon as determined by the frequency of plunge, if any). If the deviations are large, then matched filtering might fail entirely, and we would have to rely on a source being close enough to show up in a time-frequency analysis or other template-free technique.

If we see a single event that differs from the Kerr model, this will be very weak evidence against the black hole hypothesis (no doubt many possible explanations would appear in the literature over time). If every observation differed, then the evidence would be difficult to refute. Explaining the observations would be a difficult, but extremely interesting task.

6.5 Conclusions

Black hole binaries with large mass ratios are uniquely important sources for planned space-based gravitational wave detectors such as LISA. These EMRIs or IMRIs will provide information about the stellar dynamics of galactic nuclei that will be difficult, if not impossible, to obtain any other way. Single events will yield precise measurements of the masses and spins of supermassive black holes in a mass range extremely

difficult to observe electromagnetically. In addition, the high mass ratios mean that inspiral events will map the space-time around black holes and test predictions of general relativity in the strong field. These enticing prospects have led to a recent surge in interest in the astrophysical, general relativistic, and data analysis aspects of EMRIs and IMRIs, and we have given here an overview the state of the art in these three areas. Although much analytical and numerical work remains, the level of progress in the last few years suggests that when LISA flies in roughly a decade, the community will be ready to maximise the scientific return from observations of these events.

Currently, the most discussed mechanism for the production of EMRIs involves the gradual evolution of the orbits of stellar-mass black holes and other compact objects via two-body relaxation. The estimated rates for a galaxy such as the Milky Way are in the range of $\sim 10^{-8} - 10^{-6} \text{ yr}^{-1}$. The further technical development of N -body codes will be essential to reducing the uncertainty of these rates, as well as to proper inclusion of effects such as mass segregation and resonant relaxation. There are additional qualitatively different mechanisms that have been proposed recently, including tidal separation of binary stellar-mass black holes, and formation or capture of black holes in accretion discs around the MBH, that could lead to an increase in the estimated EMRI rate. In addition, whereas standard EMRIs are likely to have high eccentricity and random inclination in the LISA frequency range, tidal separations would lead to circularised orbits with random inclination, and disc processes to circularised orbits in the spin plane of the MBH. The distinct waveforms from these different mechanisms suggest that they will be distinguishable in data, and hence will carry important information about different properties in galactic nuclei.

Detection of EMRI and IMRI signals in the LISA data stream is a difficult task. In Section 6.2.1 we described three existing algorithms for EMRI detection and discussed some of the outstanding issues in EMRI data analysis. The current algorithms might be able to detect as many as several hundred EMRIs in the LISA data stream — the reach of the best searches (semi-coherent and Markov Chain Monte Carlo) is out to $z \sim 1 - 2$. However, the performance of each of these algorithms has so far

been analysed only for the detection of a single EMRI in noisy data. The LISA data stream will be source-dominated, and the need to simultaneously identify and extract all these signals puts severe demands on data analysis algorithms. Understanding how to extract EMRIs in the presence of source confusion is the key data analysis issue that must be addressed in the future.

Several of the proposed data analysis algorithms employ some variant of matched filtering, for which models of the signals present in the data must be known. The extreme mass ratio means that accurate EMRI waveform templates can be constructed using black hole perturbation theory. However, this is computationally intensive. Various approximate EMRI waveform models have been developed, and these were described in Section 6.2.2. Comparison to perturbative results suggests that these models might be good enough for LISA data analysis, but more work needs to be done. A key uncertainty is in the computational costs. A plausible data analysis strategy would use an approximate waveform model to get estimates for the source parameters, before carrying out a follow up search with more accurate waveforms. This hierarchical approach is subject to constraints on computing power. It may turn out that it is not possible to constrain the source parameters with sufficient accuracy in the first stage of the search to perform the follow-up search in a reasonable time. If that is the case, we will end up with larger errors on observed source parameters, but this needs to be quantified as waveform models are further developed in the future. Modelling of IMRI waveforms has not yet been considered in detail. While EMRI or comparable mass binary models or a combination of the two might be applied, this needs further investigation.

One of the key science goals of EMRI observations is to test general relativity theory in the strong field. The extreme mass ratio means that the inspiralling object effectively acts like a test-body in the space-time of the central object. The emitted gravitational waves encode a map of the space-time of the central object. If we can decode that map, we will be able to tell to high precision if the central body is indeed a Kerr black hole, or some other object. Understanding how LISA will be able to test relativity in practice is a subject of much current research, which we

summarised in Section 6.3. The main outstanding issues include producing waveforms for generic inspirals in bumpy (modified Kerr) space-times to test detection and data analysis strategies; finding efficient ways to search for deviations from a Kerr black hole; and interpreting such deviations to determine their origin (e.g., an accretion disc around a Kerr black hole, a boson star, a naked singularity with non-Kerr higher-order multipole moments).

If we do manage to detect many EMRI and IMRI events with LISA, we stand to learn a lot about astrophysics, and we summarise some of this discovery space in Section 6.4. The EMRI eccentricity distribution can tell us about the capture mechanisms, while the distribution of inclinations can shed light on whether compact objects are formed in a disc around the central black hole. The distribution of compact object masses could provide information on their populations, and any IMRI detection would be exciting in demonstrating that intermediate-mass black holes exist. Spin measurements of massive black holes will enlighten our understanding of their formation history. If any electromagnetic counterparts to EMRIs are observed, it could yield an improved measurement of the Hubble constant. EMRIs could also be used to confirm whether massive objects are indeed Kerr black holes, as generally assumed, and to test strong-field general relativity.

Bibliography

- [1] Amaro-Seoane, P., Freitag, M., Rasio, F. A. and Miller, M. C. (2007). *In preparation*.
- [2] Amaro-Seoane, P., Kupi, G., and Fregeau, J. M. (2006). *To be submitted*
- [3] Armstrong J W, Estabrook F B and Tinto M 1999 *ApJ* **527** 814.
- [4] Arnaud K A, Babak S, Baker J G, Benacquista M J, Cornish N J, Cutler C, Larson S L, Sathyaprakash B S, Vallisneri M, Vecchio A and Vinet J-Y 2006 in Proceedings of the Sixth International LISA Symposium, preprint gr-qc/0609105.
- [5] Arnaud K A, Babak S, Baker J G, Benacquista M J, Cornish N J, Cutler C, Larson S L, Sathyaprakash B S, Vallisneri M, Vecchio A and Vinet J-Y 2006 in Proceedings of the Sixth International LISA Symposium, preprint gr-qc/0609106.
- [6] Babak S V, Fang H, Gair J R, Glampedakis K and Hughes S A 2006 *Phys. Rev. D* accepted, preprint gr-qc/0607007
- [7] Baker J G, Centrella J, Choi D-I, Koppitz M and van Meter J 2006 *Phys. Rev. D* **73** 104002
- [8] Barack, L., Creighton, T., Cutler, C., Gair, J., Larson, S., Phinney, E. S., Thorne, K. S., and Vallisneri, M. (2003). available on-line at <http://www.tapir.caltech.edu/listwg1/EMRI/LISTEMRIreport.pdf>.
- [9] Barack, L. and Cutler, C. (2004). *Phys. Rev. D*, 69(8):082005.
- [10] Barack L and Cutler C 2004 *Phys. Rev.D* **70** 122002

- [11] Barack L and Cutler C 2007 preprint gr-qc/0612029
- [12] Barack L and Lousto C O 2005 *Phys. Rev. D* **72** 104026
- [13] Barack, L. and Sago, N. (2007).preprint gr-qc/0701069
- [14] Barausse, E., Rezzolla, L., Petroff, D. and Ansorg, M. (2007). preprint gr-qc/0612123
- [15] Bekenstein J D 1973 *Astrophys. J.* **183** 657
- [16] Bender, P. L. and Hils, D. (1998).*Bulletin of the American Astronomical Society* 30:844
- [17] Berti, E., Buonanno, A. and Will, C. M., 2005, *Phys. Rev. D* 71:084025
- [18] Berti E, Cardoso V and Will C M 2006 *Phys. Rev. D* **73** 064030
- [19] Brady P R, Creighton J D E and Thorne K S, 1998, *Phys. Rev. D* **58** 061501
- [20] Brown D A, Fang H, Gair J R, Li C, Lovelace G, Mandel I and Thorne K S 2006 *Phys. Rev. Lett.* submitted
- [21] Brüggmann B, Gonzalez J A, Hannam M, Husa S, Spehake U, Tichy W, 2006, gr-qc/0610128
- [22] Campanelli M, Lousto C O, Marronetti P and Zlochower Y 2006 *Phys. Rev. Lett.* **96** 111101
- [23] Carter B 1968 *Comm. Math. Phys.* **10** 280
- [24] Chakrabarti, S. K. (1996).*Phys. Rev. D* 53:2901
- [25] Chrzanowski P L 1975 *Phys. Rev. D* **11** 2042
- [26] Collins N A and Hughes S A 2004 *Phys. Rev. D* **69** 124022.
- [27] Cornish N J and Crowder J 2005 *Phys. Rev. D* **72** 043005.

- [28] Cornish N J and Porter E K 2006 preprint gr-qc/0612091.
- [29] Cutler C., Thorne K. S., 2002, preprint gr-qc/0204090.
- [30] Danzmann K et al, *LISA – Laser Interferometer Space Antenna, Pre-Phase A Report*, Max-Planck-Institute für Quantenoptic, Report MPQ 233 (1998)
- [31] Drasco S and Hughes S A 2006 *Phys. Rev. D* **73** 024027
- [32] Drasco S, Flanagan E E and Hughes S A 2005 *Class. Quantum Grav.***22** S801
- [33] Ebisuzaki, T., Makino, J., Tsuru, T. G., Funato, Y., Portegies Zwart, S., Hut, P., McMillan, S., Matsushita, S., Matsumoto, H., and Kawabe, R. (2001). *ApJ Lett.*, 562:L19–L22.
- [34] Enoki, M., Inoue, K. T., Nagashima, M. and Sugiyama, N. (2004). *ApJ* 615:19
- [35] Farmer A J and Phinney E S, 2003, Mon. Not. Roy. Astron. Soc. **346** 1197
- [36] Finn, L. S., and Thorne, K. S. (2000). *Phys. Rev. D* 62:124021.
- [37] Freitag, M. and Benz, W. (2002). *A&A*, 394:345–374.
- [38] Freitag M., Gürkan M. A., Rasio F. A., 2006, MNRAS, 368, 141
- [39] Gair, J. R., 2007, in preparation
- [40] Gair J R and Glampedakis K 2006 *Phys. Rev. D* **73** 064037
- [41] Gair, J. R. and Jones, G. J. (2007). *Class. Quantum Grav.*, 27:1145
- [42] Gair J R and Wen L, *Class. Quantum Grav.***22** S1359 (2005)
- [43] Gair J R, Barack L, Creighton T, Cutler C, Larson S L, Phinney E S and Vallisneri M 2004 *Class. Quantum Grav.***21** S1595
- [44] Gair J R, Li C, Mandel I 2008 *Phys. Rev. D***77** 024305
- [45] Geroch R 1970 *J. Math. Phys.* **11** 2580

- [46] Gezari, S., Halpern, J. P., Komossa, S., Grupe, D., and Leighly, K. M. (2003). *ApJ*, 592:42–51.
- [47] Glampedakis K and Babak S 2006 *Class. Quantum Grav.***23** 4167
- [48] Glampedakis K and Kennefick D 2002 *Phys. Rev. D* **66** 044002
- [49] Glampedakis K, Hughes S A and Kennefick D 2002 *Phys. Rev. D* **66** 064005
- [50] Gürkan, M. A., Freitag, M., and Rasio, F. A. (2004). *ApJ*, 604.
- [51] Haehnelt, M. G. (1994). *MNRAS*, 269:199.
- [52] Hansen R O 1974 *J. Math. Phys.* **15** 46
- [53] Hills, J. G. (1975). *Nature*, 254:295–298.
- [54] Hils, D., Bender, P. L. and Webbink, R. F. (1990). *ApJ* 360:75
- [55] Hopman, C. and Alexander, T. (2005). *ApJ*, 629:362–372.
- [56] Hopman, C. and Alexander, T. (2006b). *ApJ Lett.*, 645:L133–L136.
- [57] Hughes, S. A. (2001). *Phys. Rev. D*, 64:4004.
- [58] Hughes S A 2000 *Phys. Rev. D* **61** 084004
- [59] Hughes S A 2001 *Phys. Rev. D* **64** 064004
- [60] Hughes S A 2005 in the Proceedings of the Sixth International LISA Symposium, gr-qc/0608140
- [61] Hughes S A and Blandford R D 2003 *Astrophys. J.* **585** L101–L104
- [62] Hughes S A, Drasco S, Flanagan E E and Franklin J 2005 *Phys. Rev. Lett.* **94** 221101
- [63] Kesden M, Gair J R and Kamionkowski M 2005 *Phys. Rev. D* **71** 044015
- [64] King, A. R. and Pringle, J. E. (2006). *MNRAS*, 373:L90–L92.

- [65] King, A. R. and Pringle, J. E. (2007). preprint, astro-ph/0701679.
- [66] Lang, R. N., and Hughes, S. A., 2006, *Phys. Rev. D* 74:122001
- [67] Larson, S. L., Hiscock, W. A., and Hellings, R. W. (2000). *Physical Review D*, 62:062001.
- [68] Li C 2007 in preparation
- [69] Li C, and Lovelace G, 2007, *gr-qc/ 0702146*.
- [70] Mandel I 2007 *arXiv:0707.0711*
- [71] Mandel, I., Brown, D. A., Gair, J. R. and Miller, M. C. (2007). *arXiv:0705.0285*
- [72] Manko V S and Novikov I D 1992 *Class. Quantum Grav.***9** 2477
- [73] Menou, K., Haiman, Z., and Narayanan, V. K. (2001). *ApJ*, 558:535–542.
- [74] Menou, K. and Quataert, E. (2001). *ApJ Lett.*, 562:L137–L140.
- [75] Miller, M. C. (2002). *ApJ*, 581:438–450.
- [76] Miller, M. C. (2005). *ApJ*, 618:426–431.
- [77] Mino Y 2003 *Phys. Rev. D* **67** 084027
- [78] Murphy, B. W., Cohn, H. N., and Durisen, R. H. (1991). *ApJ*, 370:60–77.
- [79] Narayan, R. (2000). *ApJ*, 536:663.
- [80] Nelemans G, Yungelson L R, Portegies Zwart S F and Verbunt F 2001 *A&A* bf 365 491.
- [81] Papapetrou A 1951 *Proc. R. Soc. A* **209** 248
- [82] Peters P C 1964 *Phys. Rev.* **136** B1224
- [83] Peters P C and Mathews J 1963 *Phys. Rev.* **131** 435

- [84] Pfahl, E. 2005, *ApJ*, 626, 849
- [85] Poisson, E., *Living Rev. Relativity* 7, (2004), 6.[Online article]: cited on 7/11/2006, <http://www.livingreviews.org/lrr-2004-6>
- [86] Portegies Zwart S. F., McMillan S. L. W., 2000, *ApJ Lett.*, 528, L17
- [87] Portegies Zwart S. F., Baumgardt H., Hut P., Makino J., McMillan S. L. W., 2004, *Nat*, 428, 724
- [88] Pound A, Poisson E and Nickel B G 2005 *Phys. Rev. D* **72** 124001
- [89] Press W H 1977 *Phys. Rev. D* **15** 965
- [90] Pretorius F 2005 *Phys. Rev. Lett.* **95** 121101
- [91] Rees, M. J. and Volonteri, M. (2007). to appear in Proc. IAU Symp. 238, "Black Holes: from stars to galaxies - across the range of masses", astro-ph/0701512.
- [92] Ryan F D 1995 *Phys. Rev. D* **52** 5707
- [93] Ryan F D 1997 *Phys. Rev. D* **55** 6081
- [94] Ryan F D 1997 *Phys. Rev. D* **56** 1845
- [95] Sago N, Tanaka T, Hikida W and Nakano H 2005 *Prog. Theor. Phys.* **114** 509
- [96] Sago N, Tanaka T, Hikida W, Ganz K and Nakano H 2005 *Prog. Theor. Phys.* **115** 873
- [97] Sesana A, Haardt F, Madau P and Volonteri M 2005 *Astrophys. J.* **623** 23
- [98] Stroeer A, Gair J R and Vecchio A. 2006. Proceedings of 6th LISA Symposium. *gr-qc/0605227*
- [99] Teukolsky S A 1973 *Astrophys. J.* **185** 635
- [100] Teukolsky S A and Press W H 1974 *Astrophys. J.* **193** 443

- [101] Thorne, K. S. (1998). In Wald, R. M., editor, *Black Holes and Relativistic Stars*, page 41.
- [102] Tinto, M. and Dhurandhar, S. (2005), *Living Rev. Relativity* **8**, 4. [Online article]: cited on 7/11/2006, <http://relativity.livingreviews.org/Articles/lrr-2005-4/>
- [103] Tremaine, S., Gebhardt, K., Bender, R., Bower, G., Dressler, A., Faber, S. M., Filippenko, A. V., Green, R., Grillmair, C., Ho, L. C., Kormendy, J., Lauer, T. R., Magorrian, J., Pinkney, J., and Richstone, D. (2002). *ApJ*, 574:740–753.
- [104] Ulmer, A. (1999). *ApJ*, 514:180–187.
- [105] Umstätter R, Christensen N, Hendry M, Meyer R, Simha V, Veitch J, Vigeland S and Woan G 2005 *Phys. Rev. D* **72** 022001
- [106] Vallisneri, M. (2005). *Phys. Rev. D* 71:022001
- [107] Vecchio, A., 2004, *Phys. Rev. D* 70:042001
- [108] Wang, J. and Merritt, D. (2004). *ApJ*, 600:149–161.
- [109] Wen L and Gair J R, *Class. Quantum Grav.* **22** S445 (2005)
- [110] Wickham E D L, Stroeer A and Vecchio A. 2006. *gr-qc/0605071*
- [111] Will, C. M., and Yunes, N., 2004, *Class. Quantum Grav.* 21:4367
- [112] Wyithe, J. S. B. and Loeb, A. (2003). *ApJ*, 590:691

Chapter 7

The Geometry of a Naked Singularity Created by Standing Waves Near a Schwarzschild Horizon, and its Application to the Binary Black Hole Problem

The most promising way to compute the gravitational waves emitted by binary black holes (BBHs) in their last dozen orbits, where post-Newtonian techniques fail, is a *quasistationary approximation* introduced by Detweiler and being pursued by Price and others. In this approximation the outgoing gravitational waves at infinity and downgoing gravitational waves at the holes' horizons are replaced by standing waves so as to guarantee that the spacetime has a helical Killing vector field. Because the horizon generators will not, in general, be tidally locked to the holes' orbital motion, the standing waves will destroy the horizons, converting the black holes into naked singularities that resemble black holes down to near the horizon radius. This paper uses a spherically symmetric, scalar-field model problem to explore in detail the following BBH issues: (i) The destruction of a horizon by the standing waves. (ii) The accuracy with which the resulting naked singularity resembles a black hole. (iii) The conversion of the standing-wave spacetime (with a destroyed horizon) into a space-

time with downgoing waves by the addition of a “radiation-reaction field”. (iv) The accuracy with which the resulting downgoing waves agree with the downgoing waves of a true black-hole spacetime (with horizon). The model problem used to study these issues consists of a Schwarzschild black hole endowed with spherical standing waves of a scalar field, whose wave frequency and near-horizon energy density are chosen to match those of the standing gravitational waves of the BBH quasistationary approximation. It is found that the spacetime metric of the singular, standing-wave spacetime, and its radiation-reaction-field-constructed downgoing waves are quite close to those for a Schwarzschild black hole with downgoing waves — sufficiently close to make the BBH quasistationary approximation look promising for non-tidally-locked black holes.

Originally published as Ilya Mandel, 2005. Phys. Rev. D 72, 084025.

Preprint available online at <http://arxiv.org/abs/gr-qc/0505149>.

7.1 Introduction and Summary

It is very important, in gravitational astronomy, to have accurate computations of the gravitational waves from the inspiral of a black hole binary [1]. However, computing these waves is extremely challenging: for the last ≈ 25 cycles of inspiral waves, post-Newtonian approximations fail [2], and numerical relativity can not yet evolve the full dynamical equations in this regime¹. It appears that the best hope for accurately computing the BBH inspiral waves is by a quasi-stationary approximation [3, 4]. In this approximation, the energy and angular momentum of the binary are conserved by the imposition of standing gravitational waves, and the spacetime has a helical Killing vector field. The standing-wave radiation required to keep the orbit stationary is computed by demanding that the energy contents of the gravitational waves (GW) be minimized [4].

¹Numerical relativity has made great progress since this research was published, so this statement is no longer accurate.

Standing-wave radiation consists of a sum of ingoing and outgoing radiation at infinity, and downgoing and upgoing radiation at the black-hole horizons. The physical spacetime, with purely outgoing waves at infinity and downgoing waves at the horizons, can be recovered from the standing-wave spacetime by adding a perturbative radiation-reaction field [5]. The solution for the BBH inspiral consists of a series of quasi-stationary solutions that evolve from one to another via energy and angular momentum loss triggered by the radiation-reaction field. The waves measured at a detector can be deduced from this sequence of quasistationary solutions.

The black holes comprising the binary are tidally locked if their horizon generators are static in the frame co-rotating with the orbit. In the tidally locked case, the metric perturbations necessary to keep the black holes on a stationary orbit are static in the co-rotating frame, and the black holes can be regarded as having bifurcate Killing horizons (both a past horizon and a future horizon).

In reality, the black holes are not tidally locked. Their mutual tidal forces are not strong enough to maintain locking during the inspiral. In the absence of tidal locking, the standing waves of the standing-wave approximation destroy the black-hole horizons: the downgoing waves destroy the past horizon by building up an infinite energy density at the past horizon, and the upgoing waves destroy the future horizon. Therefore, we expect that forcing the orbit to be stationary via the addition of standing gravitational waves will strip the Kerr black holes of their horizons and leave naked singularities in their place [6].

Despite this radical change in the character of the orbiting bodies, it is reasonable to expect that the standing-wave solution will give a quite accurate approximation to the true physical black-hole spacetimes everywhere except very near the black-hole horizons. In order to verify or refute this expectation, it is necessary to explore the nature of the singularities created by the standing gravitational waves and to test how well the physical solution with true black holes can be extracted from the standing-wave solution with naked singularities.

As a first step in such an exploration, we consider in this paper a simple model problem designed to give insight into the nature of the singularities generated by

the standing gravitational waves, and the accuracy with which the physical, BBH spacetime can be recovered from the standing-wave, singularity-endowed spacetime.

Our model problem is a single, spherically symmetric black hole that is converted into a naked singularity by spherical standing waves of a scalar field.

We begin our analysis in Sec. 7.2 by describing the mapping between the BBH problem, into which we seek insight, and our spherical, scalar-field model problem. In particular, we deduce what should be the range of scalar-field amplitudes and frequencies in order to mock up the gravitational waves of the BBH problem.

Then in Sec. 7.3, we construct and explore the standing-wave spacetime for our spherical model problem. We initially treat the standing-wave scalar field as residing in the unperturbed Schwarzschild spacetime of the black hole, and we use Regge-Wheeler first-order perturbation theory to compute the scalar-energy-induced deviations of the hole's metric from Schwarzschild. The metric perturbations consist of a static component and a component varying in time at twice the scalar-field frequency (see Fig. 7.2 below). The oscillatory component is smaller than the static one and higher-order harmonics of both the field and the metric are strongly suppressed.

The static metric perturbation grows divergently as one approaches the Schwarzschild horizon — an obvious indication of the horizon's destruction by the standing-wave stress-energy. To explore the structure of the resulting naked singularity, in Sec. 7.3.2 we abandon perturbation theory and switch to the fully nonlinear, coupled Einstein equations and scalar-field equations. To simplify the analysis, we focus solely on the static part of the singularity's metric; we do this by time averaging the scalar stress-energy tensor before inserting it into the fully nonlinear Einstein equations. We solve the resulting equations numerically to obtain the spacetime geometry outside the singularity. The geometry's embedding diagram (Fig. 7.3 below) and the redshift seen by a distant observer (Fig. 7.4 below) show that the spacetime remains nearly Schwarzschild outside the Schwarzschild horizon, but deviates strongly from Schwarzschild at $r \approx 2M$ and below. (Here M is the mass of the hole-like singularity and we use geometrized units $c = G = 1$ everywhere in this paper.) Above $r = 2M$, the standing-wave spacetime is very nearly identical to the Schwarzschild spacetime

down to radii that are well inside the inner edge of the effective potential (Fig. 7.5). Below $r = 2M$, radial distance changes far more slowly than areal radius; i.e., g_{rr} tends to 0 as $r \rightarrow 0$. The redshift seen by an external observer rises rapidly when the emitter falls inside $r = 2M$. However, a signal from the singularity at $r = 0$ may be infinitely redshifted or infinitely blueshifted, depending on the choice of scalar field parameters.

In Sec. 7.4 we turn to the model spherical spacetime that mocks up our desired BBH solution: the spacetime of a Schwarzschild black hole with downgoing scalar waves. Not surprisingly, the metric perturbations induced by the downgoing scalar-wave energy are those of the Vaidya solution of Einstein's equations — a slowly growing black hole with a smooth, non-singular future horizon. This spacetime is well approximated, for short time intervals, by the Schwarzschild solution with (constant) Schwarzschild mass equal to the instantaneous Vaidya mass.

Finally, in Sec. 7.5 we demonstrate that by adding a perturbative radiation-reaction field to the standing-wave solution, a downgoing solution to the scalar-wave equation can be recovered. We explore the level of agreement between these downgoing waves that live in the singularity-endowed standing-wave spacetime and the downgoing waves in the Schwarzschild approximation to the Vaidya spacetime. The agreement (for details see Sec. 7.5 and Fig. 7.6 below) is rather good for scalar-wave amplitudes and frequencies that mock up the BBH problem — sufficiently good to give optimism that the standing-wave approximation will give accurate gravitational waveforms for the final stages of binary-black-hole inspiral.

7.2 The Mapping Between the BBH Problem and our Model Scalar-Field Problem

In our exploration of the quasistationary, standing-wave approximation for black-hole binaries we shall study several spherically symmetric spacetimes, each endowed with a standing-wave scalar field. In Sec. 7.3.1 the spacetime will be Schwarzschild, or Schwarzschild with first-order gravitational perturbations generated by the scalar-

field stress-energy tensor. In Sec. 7.3.2 the spacetime will be that of a naked singularity generated by the coupled, time-averaged Einstein-scalar-field equations. In this section we shall identify the parameter regime relevant to gaining insight from these spacetimes into the binary black hole problem.

In each of these spherical spacetimes, the scalar field must be a solution to the wave equation:

$$\square\Phi = \frac{1}{\sqrt{-g}}(\sqrt{-g}g^{\alpha\beta}\Phi_{,\alpha})_{,\beta} = 0, \quad (7.1)$$

where $g_{\alpha\beta}$ is the spacetime metric with the interval

$$ds^2 = f(r,t)dt^2 + g(r,t)dr^2 + r^2(d\theta^2 + \sin^2\theta d\phi^2). \quad (7.2)$$

We assume that the scalar field is monochromatic with frequency ω , and we write it in the form

$$\Phi = \Re\left(\frac{\Psi(r)e^{-i\omega t}}{r}\right), \quad (7.3)$$

where $\Re()$ denotes the real part and the phase was set by the choice of the zero of time t .

The scalar field Φ serves as the source of curvature in the Einstein equations,

$$G_{\alpha\beta} = 8\pi T_{\alpha\beta}, \quad (7.4)$$

where the stress-energy tensor depends on the scalar field according to

$$T_{\alpha\beta} = \frac{1}{4\pi}\Phi_{,\alpha}\Phi_{,\beta} - \frac{1}{8\pi}g_{\alpha\beta}\Phi_{,\mu}\Phi^{,\mu} \quad (7.5)$$

(cf. Eq. (20.66) of [7] or Eq. (A.11) of [8]).

We can re-write equations (7.4) and (7.5) in a simpler form via the Ricci tensor:

$$R_{\alpha\beta} = 2\Phi_{,\alpha}\Phi_{,\beta}. \quad (7.6)$$

Relevant ranges for the scalar-field frequency and amplitude are determined by the binary black hole problem we are modeling. Suppose that the black holes in the binary have equal mass M , and let a be their radial separation. Since we are

interested in the late inspiral, where the post-Newtonian methods fail, the desired range of parameters should correspond to $6 \lesssim a/M \lesssim 15$ [2].

The Keplerian orbital frequency of the black holes is

$$\Omega = \frac{1}{M} \sqrt{\frac{2}{(a/M)^3}}. \quad (7.7)$$

The gravitational wave frequency is twice the Keplerian frequency, and we set our scalar-field frequency equal to the GW frequency:

$$\omega = 2\Omega = \frac{2}{M} \sqrt{\frac{2}{(a/M)^3}}. \quad (7.8)$$

The power going down a black hole due to the orbital motion of its companion is approximately

$$P_{GW} = \frac{32}{5} M^4 \mu^2 \Omega^6, \quad (7.9)$$

where μ is the mass of the companion [9, 10]. Although the calculations in Refs. [9, 10] underlying Eq. (7.9) were carried out under the assumption $\mu \ll M$, we will use Eq. (7.9) to approximate the power for equal mass black holes, $\mu = M$. This approximation is not too worrisome because we are interested in the general features of the scalar-field model, which roughly corresponds to the interesting range of BBH separations, rather than in the quantitative results for this model. We select the scalar-field amplitude by demanding that its energy density near the horizon equal the GW energy density there:

$$\frac{dE}{dV} \approx \frac{P_{GW}}{4\pi(2M)^2}. \quad (7.10)$$

(In the spirit of this approximate analysis we here ignore the gravitational blueshift of the energy.) By equating this energy density to the value of T_{00} at the horizon, computed by inserting Eq. (7.3) into Eq. (7.5), we obtain the scalar-field amplitude inside the peak of the effective potential:

$$\Psi_{in} = \sqrt{\frac{64}{5}} \left[\frac{1}{(a/M)} \right]^3 M. \quad (7.11)$$

Using equations (7.8) and (7.11), we can compute the desired scalar-field frequency and amplitude for the boundaries of the region of interest:

$$a = 6M \Rightarrow \omega \approx 0.19/M, \Psi_{in} \approx 0.017M; \quad (7.12a)$$

$$a = 15M \Rightarrow \omega \approx 0.049/M, \Psi_{in} \approx 0.0011M. \quad (7.12b)$$

7.3 Standing-Wave Scalar Field

We now turn to the standing-wave scalar-field spacetime that mocks up the spacetimes of the BBH standing-wave approximation. The metric of this spacetime has the form of Eq. (7.2) and the standing-wave scalar field follows from Eq. (7.3):

$$\Phi = \frac{\Psi(r) \cos \omega t}{r}, \quad (7.13)$$

where $\Psi(r)$ is now real.

We shall treat the standing-wave scalar field twice via two different simplifying assumptions. First, in Sec. 7.3.1, we will consider the scalar field perturbatively; its wave equation will be that of the Schwarzschild spacetime, and its stress-energy will generate first-order perturbations of the metric away from Schwarzschild. Then in Sec. 7.3.2, we will consider the fully nonlinear Einstein-scalar-field spacetime but with the scalar stress-energy averaged over time to make the metric static.

7.3.1 Perturbative standing-wave solution

7.3.1.1 Perturbative formalism for the standing-wave spacetime

In our first approach, the lowest-order solution for the scalar field is computed by solving the wave equation (7.1) in the Schwarzschild background with the metric

$$\begin{aligned} ds^2 &= g_{\alpha\beta}^B dx^\alpha dx^\beta \\ &= -(1 - 2/r) dt^2 + \frac{1}{1 - 2/r} dr^2 + r^2 d\Omega^2, \end{aligned} \quad (7.14)$$

where we rescale so that $M = 1$. The wave equation simplifies as follows (cf. Eq. (32.27b) of [7]):

$$\frac{d^2\Psi}{dr^{*2}} = \left[-\omega^2 + (1 - 2/r)\frac{2}{r^3} \right] \Psi, \quad (7.15)$$

where r^* is the Regge-Wheeler tortoise coordinate [11],

$$r^* = r + 2 \ln(r/2 - 1). \quad (7.16)$$

Because ω^2 dominates the right hand side of Eq. (7.15) both far from the horizon ($r \gg 2$) and very near the horizon, the scalar field will oscillate with a nearly constant frequency ω in those regions. In between, where the effective potential

$$V(r^*) = (1 - 2/r)(2/r^3), \quad (7.17)$$

is significant, there is an intermediate transitional region (see Fig. 7.1). (In this paper we mention several times “the inner edge of the peak of the effective potential”; we define this inner edge to be the radius at which the effective potential drops to one percent of its maximum value at the peak.)

Since we are approaching the problem perturbatively, we are interested in some small metric perturbation $h_{\alpha\beta}$ on top of the background metric $g_{\alpha\beta}^B$ of Eq. (7.14) that would yield the curvature corresponding to the stress-energy tensor of the scalar field:

$$g_{\alpha\beta} = g_{\alpha\beta}^B + h_{\alpha\beta}. \quad (7.18)$$

Linearizing in $h_{\alpha\beta}$, this metric gives the Ricci tensor

$$R_{\alpha\beta} = R_{\alpha\beta}^B + \frac{1}{2} \left(h_{\mu\alpha|\beta}{}^\mu + h_{\mu\beta|\alpha}{}^\mu - h_{\alpha\beta|\mu}{}^\mu - h_{|\alpha\beta} \right), \quad (7.19)$$

where $h = h_\mu{}^\mu$ and $|$ represents the covariant derivative in the background metric $g_{\alpha\beta}^B$. For the Schwarzschild background metric, $R_{\alpha\beta}^B = 0$.

We are interested only in spherically symmetric perturbations. A gauge transformation brings additional simplification, so $h_{\alpha\beta}$ can be written in the following simple

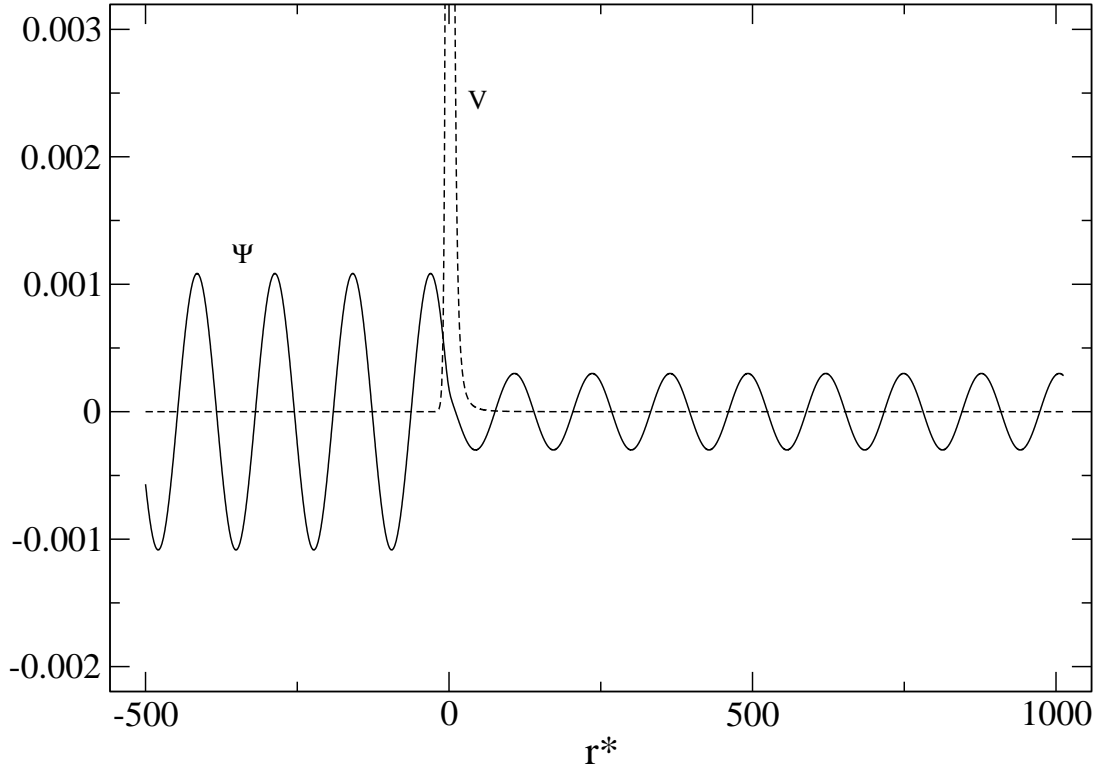


Figure 7.1: The standing-wave scalar field in a Schwarzschild background (solid curve) and the effective potential (dashed curve) for angular frequency $\omega = 0.049$.

Regge-Wheeler form:

$$h_{\alpha\beta} = \begin{pmatrix} (1 - 2/r)H_0(t, r) & 0 & 0 & 0 \\ 0 & \frac{H_2(t, r)}{1-2/r} & 0 & 0 \\ 0 & 0 & 0 & 0 \\ 0 & 0 & 0 & 0 \end{pmatrix}. \quad (7.20)$$

(Compare with Eq. (13) of [11] for the case $L = 0$.)

We can now substitute $h_{\alpha\beta}$ given by Eq. (7.20) into Eq. (7.19) to compute the

perturbed Ricci tensor:

$$R_{tt} = -\frac{1}{2} \frac{\partial^2}{\partial t^2} H_2 \quad (7.21a)$$

$$-\frac{r-2}{2r^3} \left[(2r-1) \frac{\partial}{\partial r} H_0 + \frac{\partial}{\partial r} H_2 + r(r-2) \frac{\partial^2}{\partial r^2} H_0 \right];$$

$$R_{tr} = \frac{1}{r} \frac{\partial}{\partial t} H_2; \quad (7.21b)$$

$$R_{rr} = \frac{r^2}{2(r-2)^2} \frac{\partial^2}{\partial t^2} H_2 + \frac{1}{2r(r-2)} \quad (7.21c)$$

$$\times \left[3 \frac{\partial}{\partial r} H_0 + (2r-3) \frac{\partial}{\partial r} H_2 + r(r-2) \frac{\partial^2}{\partial r^2} H_0 \right];$$

$$R_{\theta\theta} = H_2 + \frac{r-2}{2} \frac{\partial}{\partial r} H_0 + \frac{r-2}{2} \frac{\partial}{\partial r} H_2. \quad (7.21d)$$

Inserting expressions (7.21) for $R_{\alpha\beta}$ into the Einstein equations (7.6), one obtains a set of rather complicated PDE's containing both spatial and time derivatives to the second order. However, we expect that the equations can be further simplified because of additional consistency conditions imposed on Φ by the wave equation (7.15). Indeed, after adding the R_{tt} and R_{rr} equations with appropriate coefficients to remove the second derivatives in both t and r , and using $R_{\theta\theta} = 0$ to relate H_0 to H_2 , we obtain the following set of first-order ODE's for H_0 and H_2 :

$$\frac{\partial H_2}{\partial r} = -\frac{H_2}{r-2} + \frac{r^3}{(r-2)^2} \Phi_{,t} \Phi_{,t} + r \Phi_{,r} \Phi_{,r}; \quad (7.22a)$$

$$\frac{\partial H_0}{\partial r} = -\frac{\partial H_2}{\partial r} - \frac{2}{r-2} H_2. \quad (7.22b)$$

These far simpler equations can be shown to produce no spurious solutions; in fact, together with the wave equation (7.15), they are equivalent to the second-order PDE system (7.21) & (7.6).

7.3.1.2 First-order metric perturbations due to the standing-wave scalar field

In the scalar-field ansatz (7.13) we assumed $\Phi \propto \cos \omega t$. Therefore, the driving term on the right hand side of Eq. (7.22a) will have static components as well as components oscillating in time at the frequency 2ω . Because there is no mixing of

terms with distinct time signatures in equations (7.22), these terms may be treated separately:

$$H_2(t, r) = H_2^{stat}(r) + H_2^{cos}(r) \cos 2\omega t; \quad (7.23a)$$

$$H_0(t, r) = H_0^{stat}(r) + H_0^{cos}(r) \cos 2\omega t. \quad (7.23b)$$

(There is no $\sin 2\omega t$ term with our particular choice of the scalar-field phase.)

For $r \gg 2$ analytical approximations for H_0 and H_2 are easy to obtain because the scalar field is particularly simple there:

$$\Phi \approx (\Psi_0/r) \cos(\omega r^*) \cos(\omega t), \quad (7.24a)$$

where Ψ_0 is the scalar-field amplitude as $r \rightarrow \infty$. Inserting this into Eqs. (7.22), we readily compute, at large r :

$$H_2^{stat}(r) \approx \frac{1}{2}\omega^2\Psi_0^2 - \frac{\Psi_0^2}{4r^2} - \frac{\Psi_0^2 \cos 2\omega r^*}{4r^2}; \quad (7.24b)$$

$$H_2^{cos}(r) \approx -\frac{\Psi_0^2}{4r^2} - \frac{\Psi_0^2 \cos 2\omega r^*}{4r^2} - \frac{\Psi_0^2 \omega \sin 2\omega r^*}{4r}; \quad (7.24c)$$

$$H_0^{stat}(r) \approx -\omega^2\Psi_0^2 \ln r + \frac{\Psi_0^2 \cos 2\omega r^*}{4r^2}; \quad (7.24d)$$

$$H_0^{cos}(r) \approx \frac{\Psi_0^2 \cos 2\omega r^*}{4r^2} + \frac{\Psi_0^2 \omega \sin 2\omega r^*}{4r}. \quad (7.24e)$$

The static components of H_2 and H_0 are non-vanishing at infinity, and H_0^{stat} actually diverges. This indicates that, due to the energy contained in the scalar field, the spacetime is not asymptotically flat. However, this bad behavior at infinity is an artifact of our model problem and is irrelevant to the issues we are studying in this paper.

A more significant issue for the binary black hole problem is the contribution of the additional energy stored in standing gravitational waves inside the orbit of a companion to the effective mass seen by the companion and the resulting change in the companion's angular velocity. Translating this issue into the language of our

model problem, we ask for the energy stored in standing waves of the scalar field inside the radius a and the value of the metric perturbation H_0 there. For scalar field amplitude and frequency corresponding to the inner boundary of the region of interest $a = 6M$ [Eq. (7.12a)], the energy stored in the standing waves of the scalar field between $r = 2.01M$ and $r = 6M$ (obtained by integrating R_{00}) is $E \approx 10^{-4}M$ and $H_0(r = 6M) \approx 10^{-5}$ [cf. Eqs. (7.24)]. For scalar field parameters corresponding to the outer boundary of the region of interest $a = 15M$ [Eq. (7.12b)], the energy stored in the scalar waves between $r = 2.01M$ and $r = 15M$ is $E \approx 10^{-8}M$ and $H_0(r = 15M) \approx 10^{-8}$. This suggests that the presence of standing waves should not significantly affect the determination of the angular velocity of the binary or the gravitational wave frequency.

We can read off from Eqs. (7.24) the ratios of the oscillatory and static components of the metric perturbations at large r . They are

$$\left| \frac{H_2^{cos}}{H_2^{stat}} \right| \approx \frac{1}{2\omega r} \quad (7.25a)$$

and

$$\left| \frac{H_0^{cos}}{H_0^{stat}} \right| \approx \frac{1}{4\omega r \ln r}; \quad (7.25b)$$

thus, the static components dominate far from the horizon.

Equations (7.24) can be used to set initial conditions for the metric perturbations at some large r , allowing for a numerical solution to Eqs. (7.22) from there down to the horizon, $r = 2$. The resulting solution, plotted in Fig. 7.2, indicates that static components continue to dominate near the horizon.

Near the horizon (inside the effective-potential peak), the scalar field has the form

$$\Phi \approx (\Psi_{in}/2) \cos \omega r^* \cos \omega t, \quad (7.26a)$$

where Ψ_{in} is the scalar-field amplitude as $r \rightarrow 2$. Inserting this approximation into Eq. (7.22a) and averaging the right-hand side leads to the following rough estimate

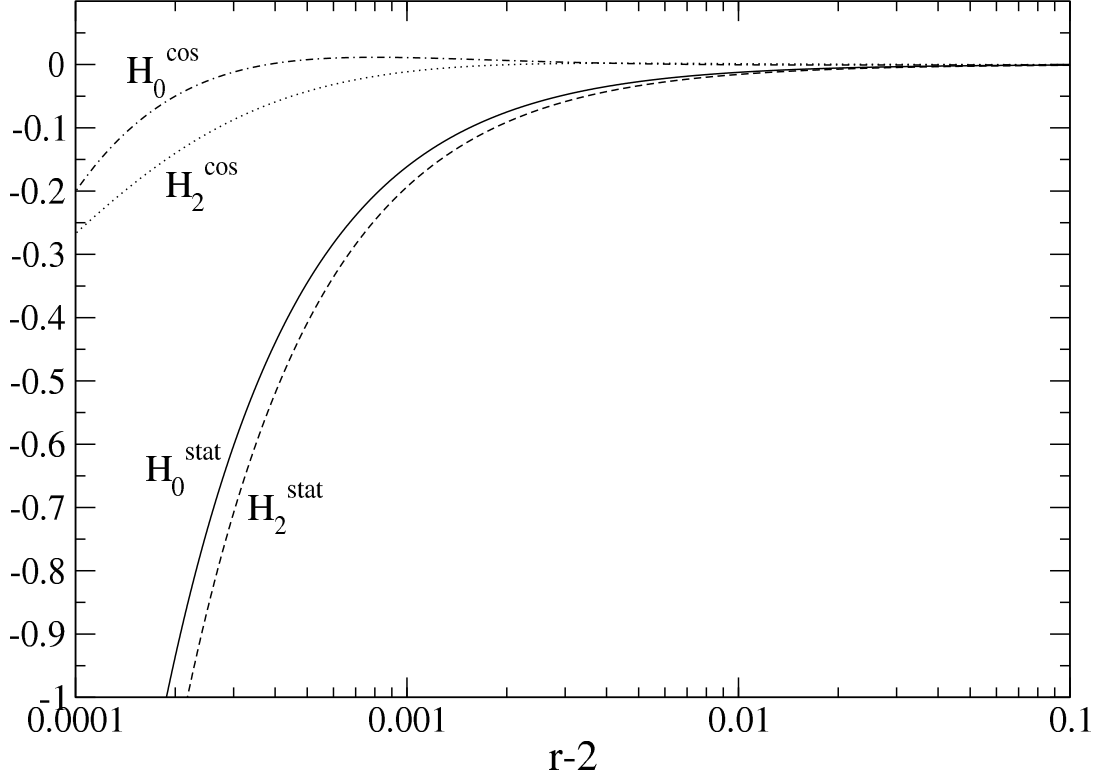


Figure 7.2: Metric perturbations for a standing-wave scalar field in a Schwarzschild background with angular frequency $\omega = 0.19$ and amplitude $\Psi_0 = 0.015$ far from the black hole, corresponding to a binary separation $a \approx 6M$, [Eq. (7.12a)].

of the magnitude of the perturbation near the horizon:

$$H_2^{stat} \approx \frac{2\omega^2 \Psi_{in}^2 \ln(r-2)}{r-2}. \quad (7.26b)$$

Inverting this formula can give a useful estimate of the distance from the horizon where the perturbation reaches a particular value; the estimate turns out to be accurate to within a factor of two.

Although it appears that the metric perturbation diverges at the expected location of the horizon, our perturbative solution is not trustworthy in this regime for several reasons in addition to the obvious one of violating the perturbative assumption $H_0, H_2 \ll 1$:

1. We ignored the *back reaction*, i.e., the feedback of the metric perturbation into

the wave equation. Using the Schwarzschild metric in place of the more accurate perturbed metric in the wave equation, that is, using the approximate Eq. (7.15) in place of the exact Eq. (7.1), is equivalent to an error in the scalar-field frequency $\Delta\omega/\omega \approx O(H)$, which produces phase offsets in the scalar field when the wave equation is integrated numerically.

2. We linearized the Ricci tensor in the perturbations, neglecting higher-order $O(H^2)$ effects. In contrast to the linearized equations (7.22) for H_2 and H_0 , the nonlinear perturbative equations are:

$$\frac{\partial H_2}{\partial r} = -\frac{H_2(1+H_2)}{r-2} + \frac{r^3}{(r-2)^2} \frac{(1+H_2)^2}{1-H_0} (\Phi_{,t})^2 + r(1+H_2)(\Phi_{,r})^2; \quad (7.27a)$$

$$\frac{\partial H_0}{\partial r} = (1-H_0) \left[-\frac{1}{1+H_2} \frac{\partial H_2}{\partial r} - \frac{2H_2}{r-2} \right]. \quad (7.27b)$$

Linearization introduces local errors of order H into the Einstein equations. However, the errors can build up globally when the equations are integrated to obtain a numerical solution. The errors produced by linearizing the Ricci tensor (the differences between solutions to the linearized and nonlinear Einstein equations without back reaction in the wave equation) have the same order of magnitude in the parameter range of interest as the errors produced by neglecting *back reaction* (the differences between solutions to the nonlinear Einstein equations depending on whether wave equation (7.15) or (7.1) is used).

3. We ignored higher harmonics of the scalar field and of the metric perturbations that would arise from the back reaction. However, these higher harmonics are suppressed by additional factors of $H \propto \Psi^2$: whereas the static and $\cos 2\omega t$ components of H are quadratic in Ψ , higher-order harmonics of frequency $2n\omega$ are proportional to Ψ^{2n} for $n > 1$.

7.3.2 Time-averaged fully nonlinear standing-wave solution

To explore the behavior of the standing-wave spherical scalar field and the spherical metric near and inside the expected location of the horizon, we solve the fully

nonlinear coupled Einstein-scalar-field equations including full back reaction in the wave equation. To simplify our solution, we average the stress-energy tensor in time to remove oscillations of the scalar-field energy, so that the metric is static. This is justified by the perturbative analysis above, which demonstrates that metric components oscillating in time are smaller than static metric components and largely decouple from them.

7.3.2.1 Formalism for nonlinear solution with back reaction

We write the static spherically symmetric metric in the form

$$ds^2 = -e^{\beta(r)+\alpha(r)} dt^2 + e^{\beta(r)-\alpha(r)} dr^2 + r^2 d\Omega^2, \quad (7.28)$$

and we compute the Einstein tensor from this metric in the standard way. The Einstein tensor is diagonal and its angular components $G_{\hat{\theta}\hat{\theta}}$ and $G_{\hat{\phi}\hat{\phi}}$ are not particularly interesting because of spherical symmetry (the angular components of the Einstein equations will merely repeat the time and radial components by virtue of the contracted Bianchi identities). The careted subscripts $\hat{\mu}$ denote the orthonormal basis associated with the (t, r, θ, ϕ) coordinate system. The relevant non-vanishing terms of the Einstein tensor in the orthonormal basis are:

$$G_{\hat{t}\hat{t}} = e^{\alpha-\beta}(\beta' - \alpha')/r + (1 - e^{\alpha-\beta})/r^2, \quad (7.29a)$$

$$G_{\hat{r}\hat{r}} = e^{\alpha-\beta}(\beta' + \alpha')/r - (1 - e^{\alpha-\beta})/r^2, \quad (7.29b)$$

where $'$ denotes a derivative with respect to r , not r^* .

Substituting the Einstein tensor (7.29) and the stress-energy tensor (7.5) into the Einstein equations (7.4), we obtain:

$$\alpha' = \frac{1}{r}(e^{\beta-\alpha} - 1), \quad (7.30a)$$

$$\beta' = r e^{-2\alpha}(\Phi_{,t})^2 + r(\Phi_{,r})^2. \quad (7.30b)$$

We can now insert the standing-wave scalar-field ansatz (7.13) and time average the right hand side of Eq. (7.30b) over a complete period. For numerical analysis

it will be useful to switch to a logarithmic coordinate that changes more gradually than r in the vicinity of the Schwarzschild horizon. The following generalization of the Regge-Wheeler tortoise coordinate r^* proves convenient:

$$\frac{dr}{dr^*} = e^\alpha. \quad (7.31a)$$

In terms of this coordinate, the wave equation (7.1) simplifies to

$$\frac{d^2\Psi}{dr^{*2}} = -\omega^2\Psi + \frac{e^\alpha}{r} \frac{d\alpha}{dr^*}\Psi \quad (7.31b)$$

and the Einstein equations (7.30) with time-averaged $(\Phi_{,t})^2$ and $(\Phi_{,r})^2$ become

$$\frac{d\alpha}{dr^*} = \frac{e^\beta - e^\alpha}{r}, \quad (7.31c)$$

$$\frac{d\beta}{dr^*} = \frac{e^{-\alpha}}{2r} \left[\Psi^2\omega^2 + \left(\frac{d\Psi}{dr^*} \right)^2 \right] + \frac{\Psi^2 e^\alpha}{2r^3} - \frac{\Psi}{r^2} \frac{d\Psi}{dr^*}. \quad (7.31d)$$

7.3.2.2 Singular standing-wave spacetime

We have solved the coupled equations (7.31) numerically to high accuracy for values of the scalar-field amplitude and frequency in the range relevant to the BBH problem [Eqs. (7.12)]. Our numerical solutions are very well approximated by analytic formulae that rely on dividing space $0 < r < \infty$ into three regions. Region I is “perturbed Schwarzschild”, i.e., the region where the perturbative solution is valid ($r > 2$, $H \lesssim 0.1$). Region III describes the space very close to $r = 0$ where the $1/r$ terms diverge. Finally, the intermediate region II extends from the inner boundary of region I to the outer boundary of region III.

For sufficiently small amplitudes of the scalar field, the contributions from the *back reaction* (by which we mean the impact of the deviation of the spacetime from Schwarzschild on the solution to the wave equation) and from nonlinearity remain small until very close to $r = 2$, so that the metric can be well approximated by perturbations on top of the Schwarzschild metric. In other words, the perturbative solution developed in Sec. 7.3.1 is valid throughout region I. Indeed, for scalar-field

amplitudes and frequencies in the range of interest, the metric perturbations H_0^{stat} and H_2^{stat} derived in the previous subsection match the values of H_0 and H_2 corresponding to the complete nonlinear solution with back reaction to within 3% for $H \lesssim 0.01$.

We begin the analysis in region III, where $r \ll 1$, by assuming $e^{\beta-\alpha} \ll 1$ as $r \rightarrow 0$, which corresponds to $g_{rr} \rightarrow 0$ at $r = 0$. (This assumption, which can be deduced from the behavior of $d\beta/dr^*$ in the transition region, will be shown to be self-consistent; more importantly, it is supported by our numerical solutions.) Then, from Eq. (7.31c), $\alpha' \equiv d\alpha/dr \rightarrow -1/r$, so α is given by

$$\alpha = -\ln r + \alpha_0. \quad (7.32a)$$

Here α_0 is a constant whose value depends on the amplitude and the frequency of the scalar waves; it can be roughly approximated by

$$\alpha_0 \sim \ln(\Psi_{in}^2 \omega^2). \quad (7.32b)$$

The wave equation (7.31b) becomes

$$\begin{aligned} \Psi'' &= -\Psi\omega^2 e^{-2\alpha} - \alpha'(\Psi' - \Psi/r) \\ &= -\Psi\omega^2 e^{-2\alpha_0} r^2 + 1/r(\Psi' - \Psi/r). \end{aligned} \quad (7.32c)$$

Since we are interested in the region $r \rightarrow 0$, the last term dominates, so that the approximate solution to Eq. (7.32c) is

$$\Psi = nr + kr \ln r, \quad (7.32d)$$

where n, k are constants.

Substituting Ψ and α into Eq. (7.31d) and selecting non-vanishing terms with the highest order in $1/r$, we find that $\beta' \rightarrow k^2/(2r)$, so

$$\beta = \frac{k^2}{2} \ln r + \beta_0, \quad (7.32e)$$

where β_0 is a constant. Thus, we see that our assumption, $e^{\beta-\alpha} \ll 1$ as $r \rightarrow 0$, is

self-consistent:

$$\beta - \alpha = \left(\frac{k^2}{2} + 1 \right) \ln r + \beta_0 - \alpha_0 \rightarrow -\infty \text{ as } r \rightarrow 0, \quad (7.32f)$$

since the coefficient of $\ln r$ is always positive.

Our numerical solution in region III agrees well with the asymptotic analytical solution (7.32). For instance, the value of k obtained from matching Ψ to the form of Eq. (7.32d) agrees with the value of k obtained from matching β to Eq. (7.32e) to one part in ten thousand. Of particular interest are the metric components and the Ricci scalar, whose asymptotics for $r \rightarrow 0$ are:

$$g_{tt} = -e^{\beta+\alpha} = -e^{\beta_0+\alpha_0} r^{k^2/2-1}, \quad (7.32g)$$

$$g_{rr} = e^{\beta-\alpha} = e^{\beta_0-\alpha_0} r^{k^2/2+1}, \quad (7.32h)$$

and

$$R = R_\gamma^\gamma = 2\Phi_{,\gamma}\Phi^{,\gamma} = k^2 e^{\alpha_0-\beta_0} r^{-3-k^2/2}. \quad (7.32i)$$

The exponent of r in Eq. (7.32i) is always negative, so the Ricci curvature scalar tends to infinity as $r \rightarrow 0$, i.e., the radius of curvature vanishes at the singularity at $r = 0$, as expected. The exponent of r in Eq. (7.32h) is always positive, so g_{rr} tends to zero as $r \rightarrow 0$ according to a power law. However, the sign of the exponent of r in Eq. (7.32g) depends on the value of k , which in turn is a complicated function of the scalar-field frequency and amplitude. For some scalar field parameter values in the range relevant to the BBH problem [Sec. 7.2] $k^2/2 > 1$ and g_{tt} vanishes at the singularity; for others, g_{tt} is infinite at $r = 0$.

The nature of region II, which represents the transition from the Schwarzschild-like region I to the singularity of region III, depends strongly on the values of Ψ_0 and ω . In Schwarzschild, $\alpha = \ln(1 - 2/r)$ tends to $-\infty$ as $r \rightarrow 2$, and this is the behavior of α in the nearly Schwarzschild region I; meanwhile, in region II, as in region III, α is well approximated by

$$\alpha = -\ln r + \alpha_0. \quad (7.33a)$$

The outer boundary of region II is located at the transition between these two behaviors of α , i.e., at the minimum of α .

Substituting the approximation (7.33a) for α into the wave equation (7.31b), we obtain:

$$\frac{d^2\Psi}{dr^{*2}} = \Psi\left(-\omega^2 - \frac{e^{2\alpha_0}}{r^4}\right). \quad (7.33b)$$

Thus, the condition for the scalar field to exhibit spatial oscillations at an approximately constant amplitude is $e^{2\alpha_0}/r^4 \ll \omega^2$. The location where this condition begins to be violated forms the inner boundary of region II. Thus, region II can be said to be defined by the variation of α according to Eq. (7.33a) as in region III, and by rapid spatial oscillations of the scalar field $d\Psi/dr^* = \omega$ as in region I.

Since α_0 will be more negative for smaller amplitudes of the scalar field, we see that region II is going to be significant for small Ψ_0 , including those in the relevant range of the BBH problem. For larger values of Ψ_0 , the metric and scalar field will proceed directly from region I to region III.

When region II does exist, the amplitude and phase of the scalar field [solution of Eq. (7.33b)]

$$\Psi(r) = A(r) \cos \phi(r) \quad (7.33c)$$

will be given by

$$A = A_0\left(1 - \frac{e^{2\alpha_0}}{4r^4\omega^2} + \dots\right), \quad (7.33d)$$

$$\dot{\phi} = \omega\left(1 + \frac{e^{2\alpha_0}}{2r^4\omega^2} + \dots\right), \quad (7.33e)$$

to first order in $e^{2\alpha_0}/(r^4\omega^2)$.

Substituting expressions (7.33) for α and Ψ into the differential equation for β , Eq. (7.31d), we find that the dominant term is the first one, $d\beta/dr^* \rightarrow (1/2)e^{-\alpha_0}A^2\omega^2$, so in region II β is approximately

$$\begin{aligned} \beta &= \frac{1}{2}e^{-\alpha_0}A^2\omega^2r^* + \text{const} \\ &= \frac{1}{4}e^{-2\alpha_0}r^2A^2\omega^2 + \text{const}, \end{aligned} \quad (7.33f)$$

where the last equality comes from the integral of equation (7.31a), $r^* = e^{-\alpha_0}r^2/2 +$

const.

Embedding diagrams and redshifts may provide the best pictorial insight into our full time-averaged standing-wave scalar-field solution, including all of regions I, II and III.

Figure 7.3 shows an embedding diagram for the standing-wave spacetime:

$$\frac{dz}{dr} = \sqrt{|g_{rr} - 1|} \quad (7.34)$$

The 2-surface obtained by rotating around the vertical axis $r = 0$ has the same 2-geometry as the surface ($t = \text{const}$, $\theta = \pi/2$) in the standing-wave spacetime. At radii $r > 2$ the embedding is very nearly the same as for a Schwarzschild black hole (cf. Fig. 31.5 of [7]). For $r < 2$, the radial distance changes far more slowly than the areal radius ($0 < g_{rr} \ll 1$), so the embedding is performed in Minkowski space rather than Euclidean space: the metric is $ds^2 = -dz^2 + dr^2 + r^2d\phi^2$ rather than $ds^2 = +dz^2 + dr^2 + r^2d\phi^2$. The embedded surface asymptotes to the light cone as $r \rightarrow 0$.

Figure 7.4 depicts the redshift of light emitted at one radius and received at another, greater one, as a function of the emitting radius:

$$z = \sqrt{\frac{g_{tt}^{rec}}{g_{tt}^{em}}} - 1 \quad (7.35)$$

Figure 7.4(a) shows that, while the redshift becomes very large as $r \rightarrow 2$, it never becomes infinite there as it would for a Schwarzschild black hole. As expected, the horizon is destroyed by the standing-wave scalar field, so an observer at infinity can receive signals from any source at $r > 0$, albeit with a very large redshift for sources close to or inside the location ($r = 2$) of the Schwarzschild horizon. A blown-up view of the region $r \ll 1$ [Figure 7.4(b)] shows that the signal emitted near the singularity may be infinitely redshifted or blueshifted depending on the asymptotics of the scalar field as $r \rightarrow 0$ according to

$$z = \sqrt{g_{tt}^{rec}} e^{(\alpha_0 - \beta_0)/2} r^{-k^2/4 + 1/2} - 1. \quad (7.36)$$

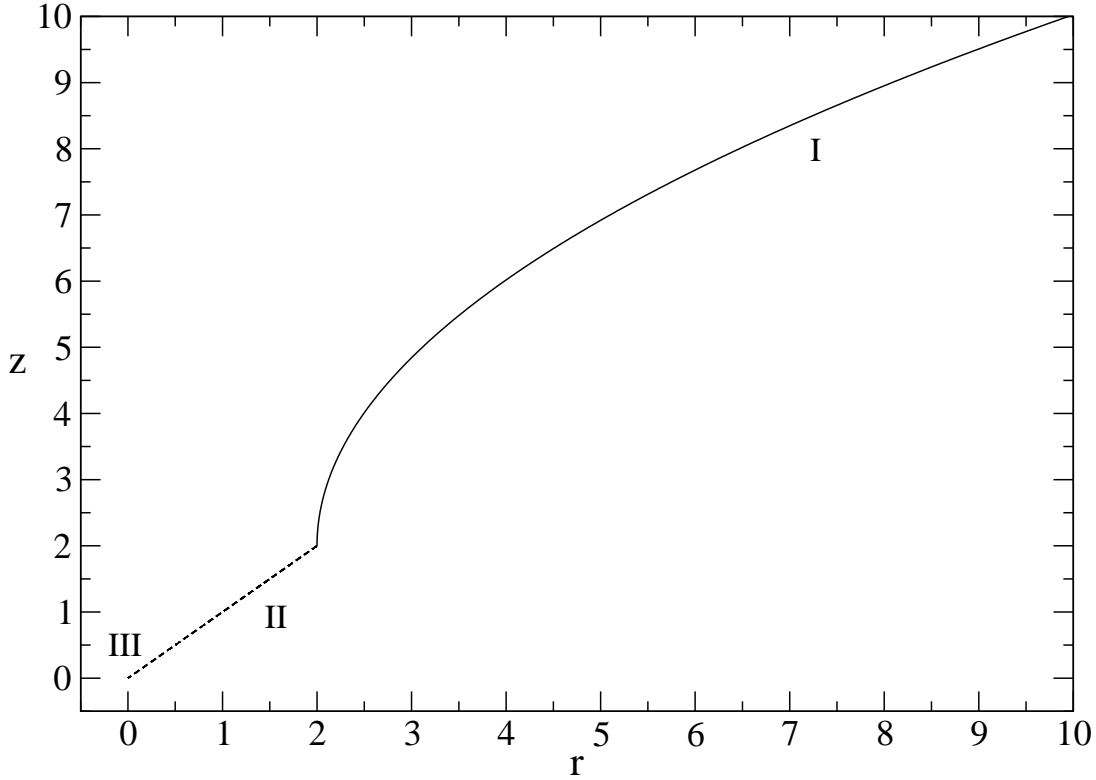


Figure 7.3: Embedding diagram for the spacetime with time-averaged standing-wave scalar field of angular frequency $\omega = 0.19$ and amplitude $\Psi_0 = 0.015$ at large radii [corresponding to the binary black hole separation $a \approx 6M$; Eq. (7.12a)]. The solid line represents embedding in Euclidean space; the dashed line, embedding in Minkowski space. Regions I, II and III are labeled on plot.

7.3.2.3 Comparison of standing-wave and Schwarzschild spacetimes

It is important to understand how the complete standing-wave spacetime with back reaction (we shall call this spacetime S) compares with the Schwarzschild spacetime (which we shall call spacetime D). We might first try to compare the metric components in the two spacetimes as functions of the radial coordinate r . Indeed, the metric components $g_{\theta\theta} = r^2$ and $g_{\phi\phi} = r^2 \sin^2 \theta$ are precisely equal in the two spacetimes when evaluated at the same location in (t, r, θ, ϕ) coordinates. Furthermore, outside the effective-potential region, the perturbation due to the scalar field is so small that the fractional difference $\delta g_{\alpha\beta}/g_{\alpha\beta} \equiv (g_{\alpha\beta}^S - g_{\alpha\beta}^D)/g_{\alpha\beta}^D$ in metric components g_{tt} and g_{rr} does not exceed 0.01% for scalar-field parameters in the range of interest. However,

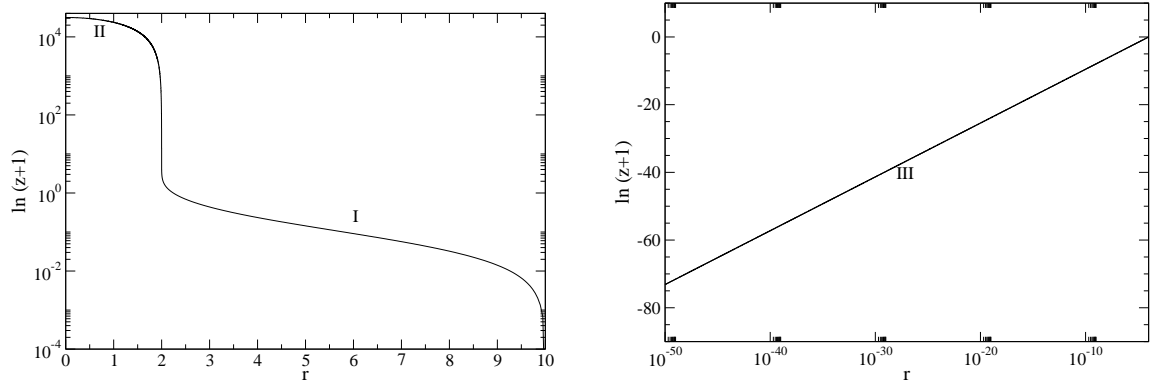


Figure 7.4: (a) Redshift $z = \delta\lambda/\lambda$ of light emitted from radius r and received by an observer at $r = 10$. (b) Redshift for an observer at $r = 0.0001$. A distant observer would see light emitted from $r = 0.0001$ redshifted by $\ln(z + 1) \approx 10^5$. These curves are drawn for the spacetime with time-averaged standing-wave scalar field that has angular frequency $\omega = 0.19$ and amplitude $\Psi_0 = 0.015$ at large radii [corresponding to the binary black hole separation $a \approx 6M$; Eq. (7.12a)].

the metric components g_{tt} and g_{rr} in S and D can differ by orders of magnitude near $r = 2$, inside the effective potential peak.

The apparent mismatch between the metric components of the two spacetimes near $r = 2$ turns out to be a consequence of a poor choice of the radial coordinate r for comparison. A much better choice is r^* : when the coordinates (t, r^*, θ, ϕ) are used for mapping between the two spacetimes S and D , the metric components agree extremely well near $r = 2$.

The fractional differences $\delta g/g$ between the g_{tt} and $g_{\theta\theta}$ components in S and D are plotted in Fig. 7.5 for scalar field parameters corresponding to binary black hole separations at the boundaries of the range of interest. Using r^* rather than r as the coordinate for comparison means that the $g_{\theta\theta}$ components no longer match perfectly; however, the fractional difference introduced remains small as $r \rightarrow 2$ and does not exceed 0.6% in the range of interest. The fractional differences in $g_{\phi\phi}$ are identical to those in $g_{\theta\theta}$ and are not plotted separately. The Regge-Wheeler tortoise coordinate r^* [Eq. (7.16)] and its generalization [Eq. (7.31a)] were defined so that $g_{r^*r^*} \equiv -g_{tt}$ in both spacetimes S and D ; therefore, the fractional differences in the values of $g_{r^*r^*}$ in S and D are the same as the fractional differences in g_{tt} .

As Fig. 7.5 shows, the fractional differences in the metrics are $\lesssim 0.02$ down to values of $r^* \sim -1000$, a location so deep inside the peak of the effective potential that it contains at least 20 near-horizon oscillations of the scalar field for frequencies and amplitudes in the BBH separation range of interest. Perhaps a more impressive way to state this is that in the (t, r^*, θ, ϕ) coordinate system, metric components of g^S and g^D match to an accuracy of 2% for all relevant scalar-field parameters down to the Schwarzschild radius $r^D - 2 < 10^{-100}$.

The fractional differences between the coefficients of the metrics g^S and g^D continue to grow approximately linearly in r^* deep inside the effective potential and reach 10% at the Schwarzschild radius $r^D - 2 \sim 10^{-3000}$, or approximately 500 scalar-field oscillations inside the effective-potential peak for scalar field parameters corresponding to BBH separation $a \approx 6M$.

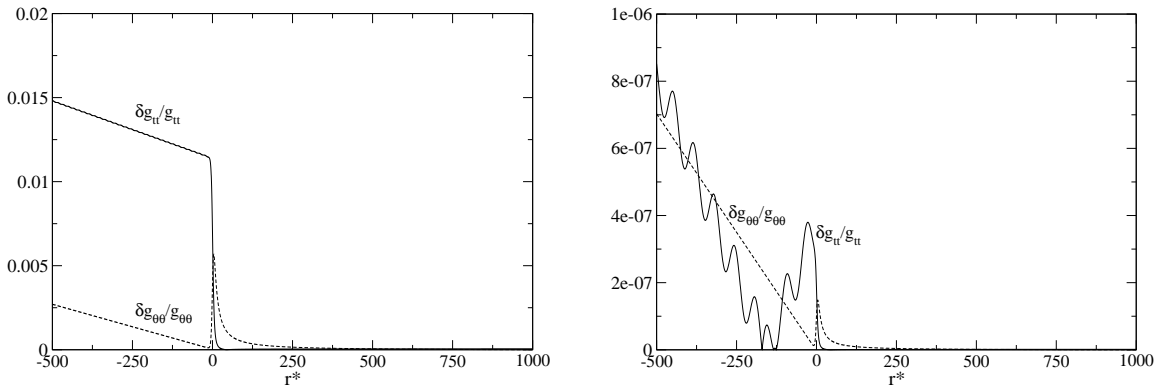


Figure 7.5: (a) Fractional differences of the metric components $g_{tt} = -g_{r^*r^*}$ (solid curve) and $g_{\theta\theta}$ (dashed curve) between Schwarzschild spacetime D and standing-wave scalar field spacetime S with scalar-wave amplitude and frequency chosen to model BBH separation $a \approx 6M$ [Eq. (7.12a)]. (b) Same quantities plotted for scalar field parameters chosen to model BBH separation $a \approx 15M$ [Eq. (7.12b)].

7.4 Downgoing Scalar Field

Having discussed, in Sec. 7.3, the standing-wave scalar-field spacetime that modeled the stationary BBH approximation, we now turn to a scalar-field spacetime that serves as a model for the physical BBH spacetime with downgoing gravitational waves at

the black-hole horizons: a nearly Schwarzschild spacetime with spherically symmetric scalar waves that are purely downgoing at $r = 2$.

For a perturbative analysis of downgoing scalar waves in Schwarzschild, the ingoing, null Eddington-Finkelstein time coordinate $v = t + r^*$ is more appropriate than the standard Schwarzschild time coordinate. Let us suppose that by the time $v = 0$ a total mass-energy $M_0 = m(v = 0)$ is located within the horizon $r = 2$. We are not particularly interested in how this mass accumulated there or how the scalar field behaved in the past; we are only interested in the times immediately following $v = 0$, and we let the scalar waves be purely downgoing and monochromatic at the horizon for $v > 0$. Then for $v > 0$ radiation is falling into the black hole at a nearly constant rate, corresponding to the energy density in the scalar field $dm/dv \approx \Psi_0^2 \omega^2 / 2$, with some small oscillations on top of the linear increase in mass. This is very similar to the Vaidya solution and, indeed, the Vaidya metric will be seen to describe the spacetime of the downgoing scalar-field solution:

$$ds^2 = - \left[1 - \frac{2m(v)}{r} \right] dv^2 + 2dvdr + r^2 d\Omega^2. \quad (7.37)$$

Near the horizon, $\Phi = (1/r) \cos \omega v$ is a purely downgoing solution to the wave equation (7.1). The only non-zero term of the Ricci tensor in Vaidya coordinates is $R_{vv} = (2/r^2)m'(v)$, where $'$ denotes the derivative with respect to v . The Einstein equations (7.6) at $r = 2$ say:

$$R_{vv} = \frac{2m'(v)}{4} = 2\Phi_{,v}\Phi_{,v} = \frac{2\Psi_0^2 \omega^2 \sin^2 \omega v}{4}. \quad (7.38)$$

Equation (7.38) is trivially integrated to obtain:

$$m(v) = M_0 + \frac{\Psi_0^2 \omega^2}{2} v - \frac{\Psi_0^2 \omega \sin 2\omega v}{4}. \quad (7.39)$$

The black-hole mass grows linearly in v at the rate $\Psi_0^2 \omega^2 / 2$ with a tiny superimposed oscillatory component. The black hole retains a smooth, non-singular future horizon.

The scalar field is purely downgoing at the horizon and approximately downgoing everywhere inside the Schwarzschild effective-potential peak. Outside the effective-

potential peak there is both a downgoing scalar field and an upgoing one, reflected off the potential. Since for small v the metric is nearly Schwarzschild [the constant Schwarzschild mass M is replaced by the $m(v)$ of Eq. (7.39)], the scalar field everywhere is given to a high accuracy by a solution to the wave equation in the Schwarzschild background subject to the purely downgoing boundary condition at the horizon. (Of course, very far from the horizon the energy contained in the intervening scalar field will act as an additional mass, but we are not interested in this region for our model problem.)

7.5 Reconstruction of Downgoing Scalar Field from Standing-Wave Scalar Field

We turn now to our scalar-wave version of adding a radiation-reaction field to a standing-wave spacetime to obtain a physical spacetime with downgoing waves at horizons and outgoing waves at infinity. For this procedure there is a substantial difference between the BBH problem and our model problem.

In the true BBH problem, the periodic standing wave (SW) solution is sourced by the black holes and corresponds to the $\frac{1}{2}$ Retarded + $\frac{1}{2}$ Advanced solution of the Green's function problem. In this case we add the non-sourced $\frac{1}{2}$ Retarded - $\frac{1}{2}$ Advanced radiation reaction (RR) solution of the linearized Einstein equations in the SW spacetime to get an approximation to the physical retarded solution [5]. At infinity, where the SW field is $\frac{1}{2}$ Outgoing + $\frac{1}{2}$ Ingoing, the boundary condition for the RR field should be set to $\frac{1}{2}$ Outgoing - $\frac{1}{2}$ Ingoing, so that their sum contains only physical outgoing waves, and similarly at the horizons the RR field will be $\frac{1}{2}$ Downgoing - $\frac{1}{2}$ Upgoing. Adding this RR field to the $\frac{1}{2}$ Downgoing + $\frac{1}{2}$ Upgoing standing waves would yield gravitational waves that are downgoing at the expected horizon locations, conforming to the expected behavior in physical black-hole spacetimes. (We do not expect the stress-energy tensor of the sum of SW and RR waves to precisely match the Einstein tensor of the SW spacetime because, of course, gravitational theory is not linear; however, it is likely that "effective linearity" holds in the sense defined by Price [4]

for the non-tidally-locked case as well as for the tidally-locked case. In a future paper we intend to explore this issue with a model that more closely resembles the BBH problem.)

The scalar-field model we are currently analyzing is not sourced: the wave equation (7.1) we used to compute the SW solution is homogeneous. There is then no perturbative homogeneous solution that is simultaneously $\frac{1}{2}$ Outgoing $- \frac{1}{2}$ Ingoing at infinity and $\frac{1}{2}$ Downgoing $- \frac{1}{2}$ Upgoing at the expected horizon location. Since at the outer boundary the problem is obviously linear for sufficiently weak scalar fields, it is easy to reconstruct the outgoing solution from the SW solution there: we simply double the outgoing component of the SW solution. The interesting case lies in the extraction of a downgoing solution near $r \approx 2$. We attempt to reconstruct the downgoing scalar field from the SW scalar field near the expected horizon by adding to the SW field a perturbative RR field that is $\frac{1}{2}$ Downgoing $- \frac{1}{2}$ Upgoing at $r \approx 2$. We then compare the sum of SW and RR fields to the purely downgoing scalar field obtained in Sec. 7.4.

As in Sec. 7.3.2, let S denote the spacetime of the complete standing-wave solution with back reaction. As discussed in the previous section, the spacetime of the downgoing scalar field is approximated to sufficient accuracy for our purposes by the Schwarzschild spacetime D .

The complete SW scalar field is a solution to the wave equation in spacetime S (in our simplified treatment of the problem, spacetime S actually corresponds to the time-averaged solution, i.e., one in which we ignore the oscillatory components of the metric). The RR field is a solution to the same wave equation in S in our model. The “reconstructed” downgoing field is, therefore, the downgoing solution to the wave equation in S . We want to compare this to the “true” downgoing field, which is the downgoing solution to the wave equation in D , i.e., in Schwarzschild.

In the region between the expected horizon location $r = 2$ and the inner edge of the peak of the effective potential, the wave equation (7.1) is dominated by

$$\frac{d^2\Psi}{dr^{*2}} \approx -\omega^2\Psi \quad (7.40)$$

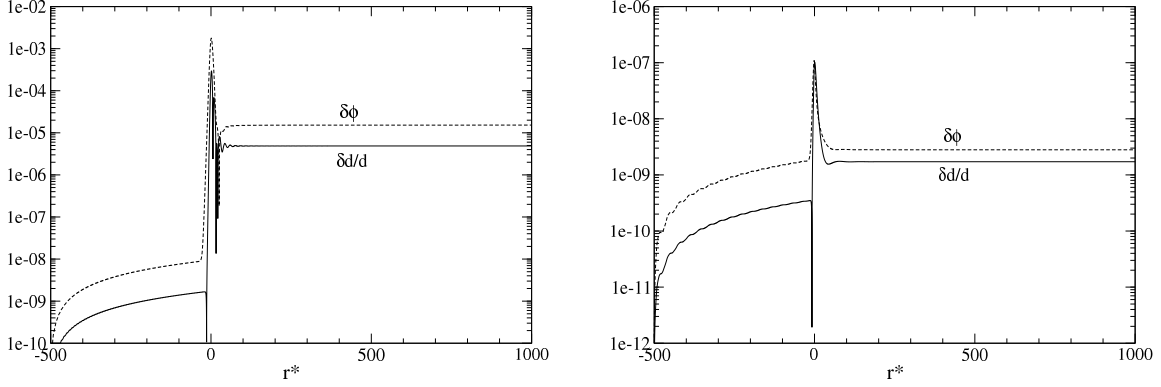


Figure 7.6: (a) The fractional difference in the amplitudes of the reconstructed scalar field and downgoing scalar field $\delta d/d \equiv (d^{SW+RR} - d^{down})/d^{down}$ (solid curve) and the phase difference between the two fields $\delta\phi_d = \phi_d^{SW+RR} - \phi_d^{down}$ (dashed curve), plotted vs. r^* . Scalar-wave amplitude and frequency chosen to model BBH separation $a \approx 6M$. (b) Same quantities plotted for scalar-field parameters chosen to model BBH separation $a \approx 15M$.

in both spacetimes S and D . Hence, the solution to the wave equation will be oscillatory in r^* with frequency ω , which makes sense on physical grounds, since ingoing light cones are $t + r^* = \text{constant}$ in both S and D . Moreover, as discussed in Sec. 7.3.2, the metrics of the two spacetimes are nearly the same in the r^* coordinate, i.e., $g^S(r^*) \approx g^D(r^*)$. This suggests that to get the scalar wave phasing to agree, we need to map between the two spacetimes using the r^* radial coordinate.

We set the boundary conditions for both the RR field in S and the downgoing field in D at a negative value of r^* chosen so that the fields are at least a few wavelengths inside the effective potential, and so that $r^S(r^*)$ is very close to $r^S = 2$ (it might actually be slightly inside $r = 2$). The SW+RR and downgoing scalar fields will match by construction at the point where the initial conditions are set. We will integrate both solutions toward larger r^* and compare the quality of the match between the two fields.

For the purposes of comparing the scalar fields in the two spacetimes, we separate the complex scalar field $\Psi(r^*)$ [the spatial factor of the complete field $\Phi(r, t) = \Re[\Psi(r^*)e^{-i\omega t}]/r$, cf. Eq. (7.3)] into upgoing and downgoing components. We define the amplitudes and phases of the upgoing and downgoing fields as follows (see below

for motivation):

$$u \equiv \frac{1}{2\omega} \left| \frac{d\Psi}{dr^*} + i\omega\Psi \right|; \quad (7.41a)$$

$$d \equiv \frac{1}{2\omega} \left| \frac{d\Psi}{dr^*} - i\omega\Psi \right|; \quad (7.41b)$$

$$e^{i\phi_u} \equiv \frac{1}{2i\omega u} \left(\frac{d\Psi}{dr^*} + i\omega\Psi \right); \quad (7.41c)$$

$$e^{i\phi_d} \equiv \frac{1}{-2i\omega d} \left(\frac{d\Psi}{dr^*} - i\omega\Psi \right). \quad (7.41d)$$

To motivate these definitions we consider the geometric optics limit, where the wave phase evolves much faster than the amplitude. In this limit, the downgoing component of the scalar field $\Psi_d \propto e^{-i\omega r^*}$ separates unambiguously from the upgoing component $\Psi_u \propto e^{i\omega r^*}$:

$$\Psi(r^*) = ue^{i\phi_u} + de^{i\phi_d}, \quad (7.42a)$$

where we use the standard approximations

$$\frac{d\phi_u}{dr^*} \cong \omega \gg \left| \frac{du}{dr^*} \right|, \quad (7.42b)$$

$$-\frac{d\phi_d}{dr^*} \cong \omega \gg \left| \frac{dd}{dr^*} \right|. \quad (7.42c)$$

Inverting Eq. (7.42a) with these approximations yields the definitions (7.41). Although the geometric optics approximations break down in the region of the effective potential, and the separation of the scalar waves into upgoing and downgoing components becomes ambiguous there because the wave speed is ill-determined outside the short-wavelength limit, expressions (7.41) are adequate for comparing scalar fields in our region of interest.

In Fig. 7.6 we show the fractional difference $\delta d/d \equiv (d^{SW+RR} - d^{down})/d^{down}$ in the amplitude of the downgoing components of the reconstructed SW + RR waves and the downgoing waves along with the phase difference $\delta\phi_d = \phi_d^{SW+RR} - \phi_d^{down}$. The two plots represent the endpoints of the range of relevant BBH separations: $a \approx 6M$ in Fig. 7.6(a) and $a \approx 15M$ in Fig. 7.6(b). Only the downgoing amplitude d and downgoing phase ϕ_d are plotted. The upgoing field components are zero to numer-

ical precision inside the effective potential and the differences between the reflected upgoing components of the “reconstructed” and “true” downgoing fields outside the effective-potential peak are similar to the differences between the downgoing field components there, $\delta u/u \sim \delta d/d$ and $\delta\phi_u \sim \delta\phi_d$.

The amplitudes and phases of the “true” downgoing field and the “reconstructed” downgoing field match to within one part in ten million from the location where the initial conditions are set (several scalar-field oscillations inside the effective potential) to the inner edge of the effective-potential peak for all BBH separations in the range of interest. Near the effective-potential peak the fractional difference in the amplitudes does not exceed 0.03% and the phase difference is less than 0.002. Outside the effective potential, the fractional difference in the amplitudes is 5 parts per million and the phase difference is less than 0.00002 for the smallest BBH separations in the range of interest.

We also compared the “reconstructed” and “true” downgoing fields very deep inside the effective potential when the field-matching initial conditions are set about 10 scalar-field oscillations inside the effective-potential peak. In this case, the amplitudes of the two fields are equal to within numerical precision and the phase difference does not exceed 3×10^{-7} down to 500 scalar-field oscillations inside the effective-potential peak. The fields begin to disagree significantly only once the naked singularity is approached in the spacetime S , at $r^S(r^*) \lesssim 0.2$ ².

²It might seem odd that the fields continue to match far deeper (at far more negative r^*) than the metrics, which begin to disagree by 10% at 500 scalar-field oscillations inside the effective-potential peak. The reason is that in the wave equation, the metric enters only into the effective-potential piece [see Eq. (7.31b)], which is so tiny throughout the region $0.2 \lesssim r^S \lesssim 2$ that even significant deviations of the standing-wave spacetime metric g^S from the Schwarzschild metric do not affect the behavior of the scalar field.

Bibliography

- [1] K. S. Thorne, in *300 Years of Gravitation*, edited by S. Hawking and W. Israel (Cambridge University Press, 1987)
- [2] P. R. Brady, J. D. E. Creighton, and K. S. Thorne, *Phys. Rev. D* **58**, 61501 (1998)
- [3] S. Detweiler, *Phys. Rev. D* **50**, 4929 (1994)
- [4] R. Price, *Class Quant. Grav.* **21**, S281-S293 (2004); Z. Andrade *et al.*, *Phys. Rev. D* **70**, 064001 (2004)
- [5] K. S. Thorne, unpublished notes, 2002
- [6] H. Friedrich, I. Rácz, and R. M. Wald, *Commun. Math. Phys.* **204**, 691 (1999)
- [7] C. W. Misner, K. S. Thorne, and J. A. Wheeler, *Gravitation* (Freeman, San Francisco, 1973)
- [8] V. P. Frolov and I. D. Novikov, *Black Hole Physics*, Fundamental Theories of Physics (Kluwer, Dordrecht, 1998)
- [9] E. Poisson and M. Sasaki, *Phys. Rev. D* **51**, 5753 (1995)
- [10] H. Fang and G. Lovelace, gr-qc/0505156
- [11] T. Regge and J. A. Wheeler, *Phys. Rev.* **108**, 1063 (1957)

Chapter 8

A Three-Stage Search for Supermassive Black Hole Binaries in LISA Data

Gravitational waves from the inspiral and coalescence of supermassive black-hole (SMBH) binaries with masses $m_1 \sim m_2 \sim 10^6 M_\odot$ are likely to be one of the strongest sources for the Laser Interferometer Space Antenna (LISA). We describe a three-stage data-analysis pipeline designed to search for and measure the parameters of SMBH binaries in LISA data. The first stage uses a time–frequency track-search method to search for inspiral signals and provide a coarse estimate of the black-hole masses m_1, m_2 and of the coalescence time of the binary t_c . The second stage uses a sequence of matched-filter template banks, seeded by the first stage, to improve the measurement accuracy of the masses and coalescence time. Finally, a Markov Chain Monte Carlo search is used to estimate all nine physical parameters of the binary (masses, coalescence time, distance, initial phase, sky position and orientation). Using results from the second stage substantially shortens the Markov Chain burn-in time and allows us to determine the number of SMBH-binary signals in the data before starting parameter estimation. We demonstrate our analysis pipeline using simulated data from the first LISA Mock Data Challenge. We discuss our plan for improving this pipeline and the challenges that will be faced

in real LISA data analysis.

Originally submitted for publication by Duncan A. Brown, Jeff Crowder, Curt Cutler, Ilya Mandel and Michele Vallisneri as a special issue article in *Class. Quantum Grav.* (2007), preprint available online at <http://arxiv.org/abs/0704.2447>.

8.1 Introduction

There is compelling evidence from electromagnetic observations that the cores of galaxies contain supermassive black holes (SMBHs) [1]. SMBH binaries can form after galactic mergers as the black holes from the individual galaxies fall to the center of the merged system and form a bound pair. Hierarchical-merger models of galaxy formation predict that SMBH binaries will be common in galaxies [2, 3] and the presence of one such binary has been inferred from X-ray measurements of the core of the galaxy NCG 6240 [4]. The evolution of an SMBH binary will eventually be driven by radiation reaction from the emission of gravitational waves (GWs) and the binary will inspiral and merge to form a single SMBH. The GWs from inspirals of SMBH binaries with component masses m in the range $m \sim 10^4\text{--}10^7 M_\odot$ will be one of the strongest sources for LISA, the planned space-based GW detector [5, 6]. The direct detection of SMBH binaries will be of wide astrophysical relevance, for example by probing the merger rates and histories of galaxies [7], or by providing cosmological standard candles [8].

Searching for SMBH binary inspiral signals is expected to be one of the more straightforward tasks in LISA data analysis. The velocities of the black holes during the inspiral are $v/c \ll 1$, and so existing post-Newtonian waveforms [9, 10] will describe the gravitational waveforms with sufficient accuracy for use as templates in a matched-filter search [11]. As such, searches for SMBH binaries in LISA data will be similar in nature to existing searches for binary–neutron-star (BNS) inspirals in ground-based GW detectors, such as the Laser Interferometer Gravitational-wave Ob-

servatory (LIGO) [12]. However, there are several key differences between LIGO and LISA binary inspiral searches. First, the LIGO pipelines are designed to search for signals with expected signal-to-noise ratios (SNRs) $\lesssim 10$, whereas the SNR of LISA SMBH binaries at distances $z \lesssim 2$ is expected to be several hundred or more. Second, the BNS signals sweep through the sensitive frequency band of ground-based detectors on timescales of order a minute, during which detector velocities and orientations can be considered as fixed to high accuracy. By contrast, LISA will be able to observe a single SMBH inspiral for weeks to months. During that time, the LISA velocity and orientation change appreciably, inducing modulations in the recorded signal. Indeed, almost all the information about an SMBH binary's sky location and orientation is encoded in these modulations. (In the ground-based case, a network of three or more widely separated detectors is required to determine a binary's sky location by triangulation between the times of arrival of the GW signals at the different detector locations.) Finally, whereas the rate of BNS inspirals in ground-based detectors makes it unlikely that multiple signals will be observed concurrently, LISA data may contain simultaneous signals from a few different SMBH binaries.

Existing search pipelines developed for ground-based observations of stellar-mass binary inspirals can achieve high detection efficiency already at SNRs ~ 10 [13, 14, 15, 16], so the task of detecting SMBH inspirals with LISA seems easy in comparison. Furthermore, since SMBH binaries at $z \sim 1$ have such high SNR, and because of LISA's relatively wider frequency band (roughly three orders of magnitude for LISA, compared to two for LIGO), it should also be possible to determine the masses and spins of the binaries with significantly higher accuracy in the LISA case than for ground-based detections. Fisher-matrix calculations suggest that, for SMBHs detected at $z \sim 1$, LISA should be able to determine the chirp mass to relative accuracy $\sim 10^{-5}$, both individual masses to $\sim 10^{-3}$ and the SMBH spins to $\sim 10^{-3}$ – 10^{-2} [17]. Indeed, the goal of our data-analysis pipeline is not only to detect the SMBH signals, but also to provide accurate measurements of the binary parameters.

Based partly on the considerations discussed above, our group has adopted the following three-stage search method. Low- z SMBH binary inspirals are so bright that

they are easily visible as tracks in time–frequency (TF) spectrograms. Therefore our first stage consists of a search for such TF tracks; the shape and location of the track yields a first estimate of the two masses, m_1 and m_2 , and the coalescence time, t_c . The second stage is a set of more refined grid-based matched-filter searches that start in a neighborhood of the best-fit parameters found in the first stage; these searches home in on more accurate values for the three parameters m_1 , m_2 and t_c . The final stage is currently a straightforward implementation of a Markov Chain Monte Carlo (MCMC) simulated-annealing search for the best-fit parameters in the full nine-dimensional parameter space (including also the binary’s luminosity distance, initial phase, inclination, polarization, ecliptic latitude and longitude).

There are a few reasons for adopting such a complicated algorithm. First, we believe that the capability of looking for TF tracks is a very useful one to develop in the LISA context: it is possible that there will be tracks that do *not* follow the expected chirping pattern, and so would not be found by more sophisticated (grid-based or MCMC) methods, even though they are visible to the eye. The track-search method also allows us to count the number of SMBH binary signals present in the data before attempting parameter estimation. Second, the grid search is useful to make sure that we do not miss any binary sources, by examining the entire parameter space. In the pipeline described here, however, we did not cover the entire parameter space in our grid search; rather, we seeded the second-stage search using the parameters obtained from the first stage. In future implementations, we intend to compare the full grid search to this method. Finally, the MCMC approach is clearly very adept at obtaining the final parameter estimates.

We have tested the performance of our SMBH binary search pipeline using data from the Mock LISA Data Challenges (MLDCs) [18, 19]. The MLDCs are a program sponsored by the LISA International Science Team to foster the development of LISA data-analysis methods and tools, and to demonstrate already acquired milestones in the extraction of science information from the LISA data output. In the MLDCs, GW signals whose parameter values are unknown to the challenge participants are embedded in synthetic LISA noise; participants are challenged to identify the signals

and extract their parameters. Challenges of increasing difficulty are being issued roughly every six months. The results from the first Challenge are summarized by Arnaud and colleagues in this volume [20]. Challenge 1 included two datasets with signals from isolated SMBH systems; we analyzed one of them. One of the goals of the MLDCs is to demonstrate that data-analysis pipelines can actually achieve the fantastic parameter measurement accuracy predicted by the Fisher-matrix analysis.

Two other differences between the ground-based and space-based cases deserve mention. First, SMBH binaries may enter the LISA band with considerable eccentricity, whereas the BNSs observed by ground-based detectors will have become essentially circular by the time they enter the observation band. Second, in the ground-based case the binary-inspiral signals are immersed in noise that originates almost entirely from the instrument, while through much of LISA’s sensitivity band the dominant noise comes from unresolved Galactic white-dwarf binaries. To keep Challenge 1 relatively simple, however, these last two complications were omitted in creating the synthetic datasets, and hence from our initial pipeline described here.

The rest of this paper is organized as follows: in sections 8.2–8.4 we describe the three stages in our SMBH binary data-analysis pipeline: a track search in the time-frequency plane, a grid-based matched filtering search, and Markov Chain Monte Carlo; in 8.5 we present the results of analyzing the MLDC dataset 1.2.1; and in 8.6 we discuss our plans for improving the pipeline to cope with issues such as binary eccentricity and the noise sources likely to be observed in real LISA data.

8.2 Stage 1: Search for Tracks in the Time–Frequency Plane

The TF spectrogram contains enough information to identify an SMBH binary inspiral at a high SNR. The techniques described below make it possible to quickly search for the presence of an SMBH binary inspiral in the signal and to get rough estimates of its parameters.

Challenge 1 includes signals from the adiabatic inspiral of a circular binary system

of nonspinning SMBHs. The frequency evolution of these inspirals is given by (7.11a) of [21] in terms of the time of coalescence t_c and the two SMBH masses m_1 and m_2 . We write it here as a function of the symmetric mass ratio $\eta = m_1 m_2 / (m_1 + m_2)^2$ and the chirp mass $M_c = (m_1 + m_2) \eta^{3/5}$, using the second-order post-Newtonian (2PN) approximation:

$$f_{\text{GW}}(t) = \frac{\eta^{3/5}}{8\pi M_c} (T_c - T)^{-3/8} \left\{ 1 + \left[\frac{743}{2688} + \frac{11}{32} \eta \right] (T_c - T)^{-1/4} - \frac{3\pi}{10} (T_c - T)^{-3/8} \right. \\ \left. + \left[\frac{1855099}{14450688} + \frac{56975}{258048} \eta + \frac{371}{2048} \eta^2 \right] (T_c - T)^{-1/2} + \mathcal{O} \left[(T_c - T)^{-5/8} \right] \right\}. \quad (8.1)$$

Here f_{GW} is the GW frequency in Hz, M_c is expressed in seconds, and T is the dimensionless time variable related to coordinate time t by $T = t \eta^{8/5} / (5M_c)$.

We create a TF map of the noisy data stream $s(t) = h(t) + n(t)$ [in fact, one of the Time-Delay Interferometry (TDI) channels $X(t)$, $Y(t)$ and $Z(t)$ provided in the MLDC datasets], sampled with timestep dt , in two passes. On the first pass, we split up the data stream into time bins of equal duration Δt . The TF spectrogram will then consist of pixels of size $\Delta t \times \Delta f$, where $\Delta f = 1/(\Delta t)$. We determine the normalized power contained in each pixel with a Fast Fourier Transform (FFT), normalizing by the power spectral density of the noise, and then find the peak frequency in each bin by searching for the loudest pixel (see below for details). The resulting set of {time, frequency} pairs allows us to search for an inspiral track on the TF map (see figure 8.1). Once such a track is identified, we make a second pass through the data, iterating through the track region with time bins of varying duration to create an improved TF map. Earlier in the track, a larger Δt helps to detect a weak signal and achieve greater frequency resolution; closer to coalescence, a smaller Δt reduces the error in estimating the rapidly chirping GW frequency.

In fact, we have made several improvements to the general approach outlined in the previous paragraph. The first set of improvements concerns the determination of the peak frequency in a given time bin. Simply searching for the loudest pixel would give frequency-determination errors of order $1/(\Delta f)$, even for a noiseless signal. Instead,

we achieve higher accuracy by modeling the bleeding of frequency into neighboring pixels: specifically, we determine the peak frequency by fitting the logarithm of power in the pixels nearest to the brightest pixel to a parabola, using zero-padding in the time domain to achieve better frequency resolution when necessary. We also apply a Hanning window to the signal prior to taking the FFT, and we overlap time bins to avoid information loss from windowing.

Another improvement concerns the variable timestep and the selection of outliers on the second pass through the data. If the peak frequencies of neighboring time bins differ by more than $2\Delta f$, we decrease Δt by a pre-set factor (say, 1.5) to reduce the sweep of frequency in each bin. If this operation fails to bring the peak frequencies closer together, we declare the data point an outlier, and skip to the next bin.

The {time, frequency} data points obtained on the second pass serve as inputs to a MATLAB least-squares fitting algorithm that extracts the inspiral parameters t_c , M_c and η by fitting these points to the model of (8.1) (see figure 8.2). Specifically, we find the values \hat{t}_c , \hat{M}_c and $\hat{\eta}$ that minimize the sum

$$\Sigma = \sum_{i=1}^N [f(t_i) - f_{\text{GW}}(t_i; t_c, M_c, \eta)]^2, \quad (8.2)$$

where the t_i are the centers of the output time bins, $f(t_i)$ are the associated frequencies, and $f_{\text{GW}}(t_i; t_c, M_c, \eta)$ is the model from (8.1).

Although one could weight the data points on the basis of the signal amplitude, such a weighting seems to carry little benefit: late in the inspiral, the increased amplitude offers greater SNR, which is however substantially offset by poorer frequency determination (due either to frequency drift within each time bin if Δt is not properly adjusted, or to low frequency resolution if it is).

Table 8.1 shows the results of the TF search on the blind Challenge dataset 1.2.1. After averaging results from the three TDI streams, we found $\hat{M}_c = 1.208 \times 10^6 M_\odot$, $\hat{\eta} = 0.17$ and $\hat{t}_c = 1.3372 \times 10^7$ s. The accuracy of these estimates is discussed in Sec. V below; suffice it to say that these first-stage results were certainly accurate enough for our purpose.

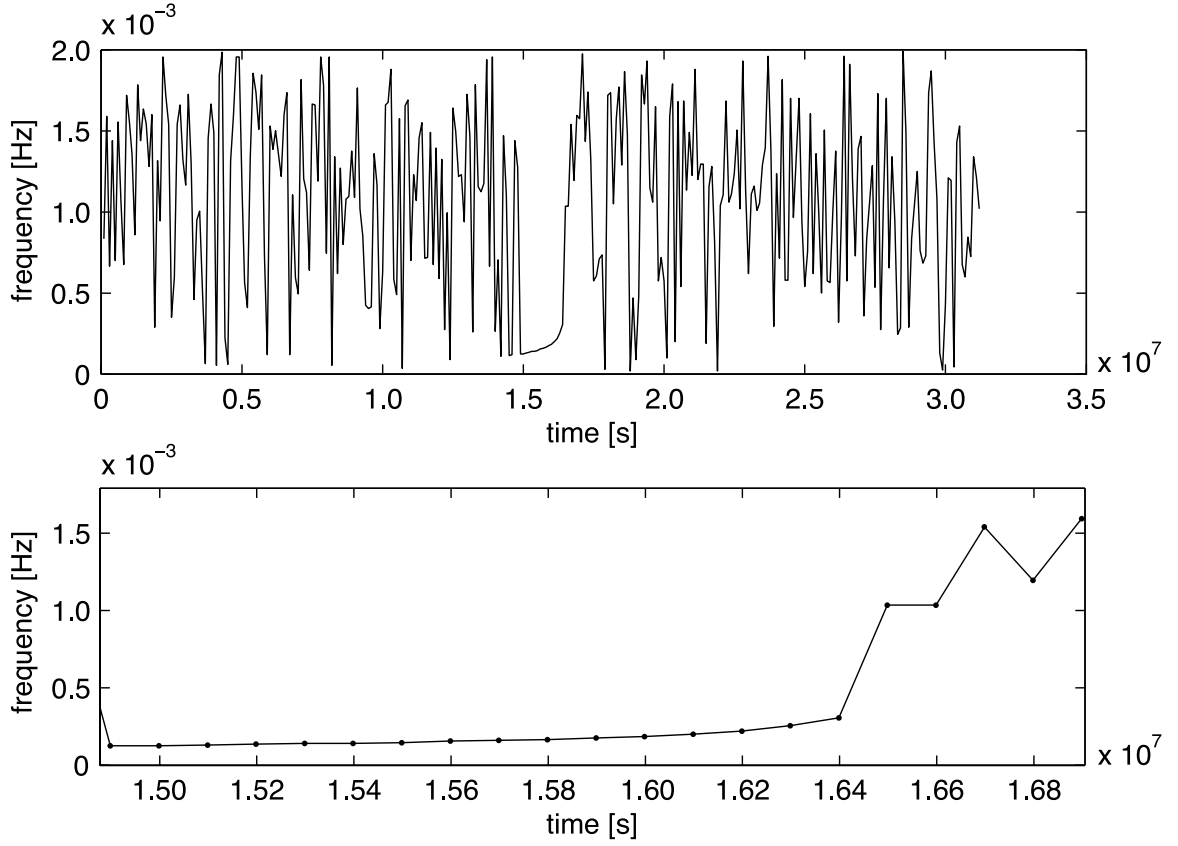


Figure 8.1: Time–frequency plot of the brightest pixel in each time bin, as computed for the X channel of Challenge 1 training set 1.2.1. The bottom plot is a blown-up version of the top plot showing the presumed track found on the first pass through the data.

Table 8.1: Parameters extracted via TF searches from the X , Y and Z channels of blind Challenge dataset 1.2.1. N is the number of data points obtained during the second pass through the data and Σ is the sum of the squares of the residuals, as defined in (8.2).

	N	$\Sigma/10^{-11}$	$M_c/(10^6 M_\odot)$	η	$t_c/(10^7 \text{ s})$
X	156	9.2	1.2096	0.182	1.3373
Y	190	9.21	1.2033	0.139	1.3370
Z	192	11.5	1.2099	0.183	1.3373

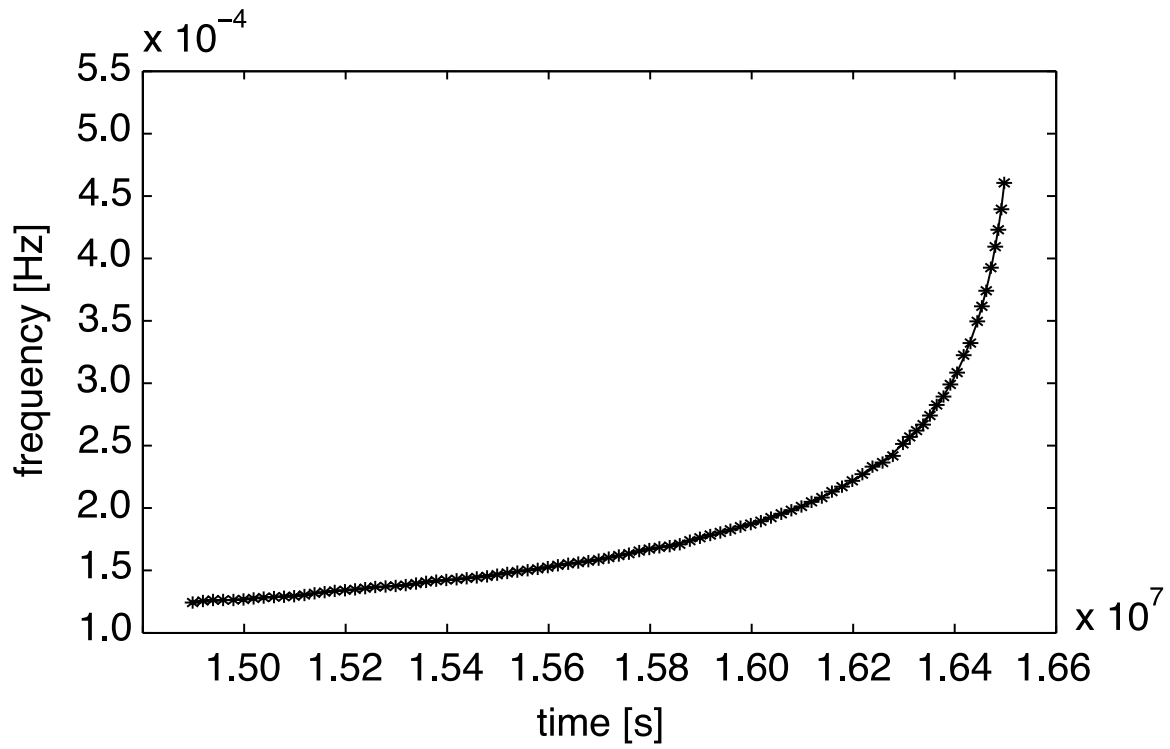


Figure 8.2: The stars represent individual points on the TF map obtained during the second pass through the data in the $X(t)$ channel of where Training Set 1.2.1. The curve is the result of fitting these points to the model (8.1).

8.3 Stage 2: Grid-Based Search

The grid-based part of the search relies on the template placement algorithm of Babak *et. al.* [13] and the FINDCHIRP matched filtering algorithm of Allen *et. al.* [14], both of which were developed for the LIGO binary neutron star searches. The basic algorithm is as follows: a grid of templates is constructed in the (m_1, m_2) plane using the metric-based square-grid placement algorithm [22, 13] implemented in the LIGO Algorithm Library (LAL) [23]¹. The fineness of the grid is specified by its minimum-match parameter MM, which is the minimum overlap between any point in the parameter space and its nearest grid-point. To implement the algorithms described in [14], we have written C code which implements the matched filtering algorithms and template generation. These C functions are then “wrapped” by the Simplified Wrapper Interface Generator (SWIG), which allows them to be called from the Python high-level programming language. This approach allows us to rapidly prototype and develop the procedure described below.

For each mass pair in the grid, we compute a (Fourier-transformed) waveform $\tilde{h}(f)$ (corresponding to coalescence at $t = 0$), using 2PN waveforms and the stationary phase approximation (SPA) [24]. We transform from $\tilde{h}(f)$ to the LISA TDI variable $\tilde{X}_h(f)$ using

$$\tilde{X}_h(f) = \sin^2(2\pi f L) \tilde{h}(f), \quad (8.3)$$

where L is the LISA arm length. Let the (Fourier transformed) data be $\tilde{X}_s(f)$; then for each template waveform $\tilde{X}_h(f)$ in our grid we use the FFT to compute the inverse Fourier transform

$$z(t) = \int \frac{\tilde{X}_s(f) \tilde{X}_h^*(f)}{S_X(f)} e^{2\pi i t f} df, \quad (8.4)$$

and we maximize $|z(t)|$ over t to estimate the time of coalescence. We identify the best-fit point in the (m_1, m_2) plane, and then repeat the search in a neighborhood of that point, with a finer grid. We do this four times, with a final minimum-match

¹Babak *et. al.* also describe a more efficient hexagonal placement algorithm, however we were unable to place templates for LISA SMBH binaries using the LAL implementation of this algorithm. We intend to work with the authors of the LAL code to resolve this.

parameter $MM = 0.995$. For Challenge 1.2.1, based on the results from the TF stage ($m_1 \approx 2.9 \times 10^6 M_\odot$ and $m_2 \approx 7.3 \times 10^5 M_\odot$), we chose our initial grid to cover the portion of the (m_1, m_2) plane satisfying $6 \times 10^5 < m_2 < m_1 < 3.2 \times 10^6 M_\odot$, with initial $MM = 0.30$.

Now, our parameter-estimation errors are dominated not by the coarseness of the grid, but by the fact that our 2PN SPA waveforms are not identical to BBH waveforms injected into the Mock LISA data, even for the same parameter values. Our 2PN SPA waveforms differ from the MLDC versions by higher-order PN terms, and do not include the modulations due to the detector motion. They are also simply cut off at the frequency of the innermost stable circular orbit (ISCO) of a test mass in the Schwarzschild spacetime, while the MLDC waveforms end with a very particular choice of taper. Therefore we do one final grid search using MLDC waveforms (again with $MM = 0.995$), and for some particular choice of the five angles $(\theta, \phi, \iota, \psi, \varphi_0)$. Although these angles are wrong, in this step the *other* features of the templates (e.g., the Doppler modulation of the frequency due to LISA’s orbit and the amplitude taper) do match those of the injected MLDC binary waveforms, and so presumably yield improved parameter estimates.

8.4 Stage 3: Markov Chain Monte Carlo

So far, the first two stages have given estimates only of the two masses and coalescence time; in addition, the stage-2 analysis was based only on the X channel. Thus, we rely on the MCMC stage to find the distance, sky location, and the polarization and inclination angles of our source. A more efficient way to do this would be to use the \mathcal{F} -statistic [25, 26] to automatically optimize over four amplitude parameters that are functions of distance, polarization, inclination and initial phase; however, we did not have time to implement this procedure for Challenge 1. Therefore our MCMC code does a brute force search over all parameters—but with the advantage that it starts in the right vicinity for the masses and coalescence time, as estimated in the first two stages.

MCMC approaches have shown promise in the extraction of GW-source parameters with LISA [27, 28, 29, 30, 31, 32]. Nevertheless, it has been suggested that, for SMBH binaries, MCMC searches over a full parameter set need to be started in a neighborhood of the correct source parameters to efficiently characterize the posterior probability density functions [28]. Since the initial search grid provided a good estimate of three parameters (the constituent masses and coalescence time t_c), and since it is trivial to extremize analytically over the luminosity distance, we were hopeful that we could determine the values of the sky location and binary orientation with a straightforward implementation of the Metropolis–Hastings Algorithm (MHA). Since time was limited and posterior distributions were not required for Challenge 1, we chose not to estimate these, but rather to use the MHA to locate the best-fit parameters.

In the MHA, a Markov chain is built by accepting a new proposed point with probability $\alpha = \min(1, H)$; H is the Hastings ratio for a jump from position \vec{x} to \vec{y} in parameter space, given by

$$H = \frac{p(\vec{y})p(s|\vec{y})q(\vec{x}|\vec{y})}{p(\vec{x})p(s|\vec{x})q(\vec{y}|\vec{x})}, \quad (8.5)$$

where $p(\vec{x})$ is the prior distribution, $p(s|\vec{y})$ is the likelihood of the parameter set \vec{y} producing the signal s , and $q(\vec{x}|\vec{y})$ is the proposal distribution used to generate the move from \vec{x} to \vec{y} . If the noise is a normal process with zero mean, the likelihood is given by

$$p(s|\vec{\lambda}) \propto \exp - (s - h(\vec{\lambda}) | s - h(\vec{\lambda})) / 2, \quad (8.6)$$

with “ $(\cdot|\cdot)$ ” the standard inner product computed with respect to the LISA instrument noise.

The Markov chain process is guaranteed to converge to the posterior probability distribution if the proposal distribution is nontrivial; however, the speed of convergence does depend on its choice. In this search we adopted two types of proposals: the first consisted of a multivariate normal distribution with jumps directed along the eigendirections of the Fisher information matrix, computed locally; the second

amounted to drawing parameters from uniform distributions. For the angular parameters, both timid and bold draws (from small or large ranges) were made to ensure we were fully exploring parameter space; for the component masses, only timid draws ($< 1\%$) were used.

Multiple concurrent chains were started using the parameter estimates obtained in stage 2. These were run on a supercomputing cluster with 3.2 GHz Intel Pentium 4 processors, using Synthetic LISA [33] to reproduce the LISA response to the SMBH binary waveforms. Each run was limited to 12 hours, providing $\sim 3,500$ steps in each of the chains. The most promising candidates at the end of the first run were used as the starting locations of a second run. At the end of the first run the best candidates had reached log likelihood values in the neighborhood of 200,000; the second run saw them increase to $\sim 205,000$. The chains converged around two points in parameter space, differing by their locations on opposite sides of the sky. This was not unexpected: dual maxima at antipodal sky positions are a well-known degeneracy for LISA sources. Our choice between the two final parameter sets was based on a visual comparison of the putative signals with the challenge dataset.

In future implementations of the pipeline, we plan to incorporate the \mathcal{F} -statistic in the MCMC stage to reduce the size of parameter space. This will increase search efficiency and relax the need to begin the search in a neighborhood of the best-fit parameters (something that will be necessary when searching for the dimmer SMBH binaries of Challenge 2). Another time-saving measure will be to start the search on a limited portion of the data stream, and then steadily increase its size. This process, called frequency annealing [34], allows a quick initial exploration of parameter space, and a careful later investigation of the exquisitely sharp likelihood peaks close to bright SMBH binaries.

8.5 Results for MLDC Challenge

As was the case for many Challenge-1 participants, the Dec. 3, 2006 submission deadline arrived before our pipeline was fully ready; nevertheless we decided to submit

our best estimates for the parameters of the blind dataset 1.2.1. This dataset consisted of the three TDI unequal-Michelson channels $X(t)$, $Y(t)$ and $Z(t)$. In stage 1 of our search, we analyzed each of these channels separately, and simply averaged the three results to arrive at the stage-one parameter estimates shown in the fourth column of table 8.2. In stage 2, only the $X(t)$ data was analyzed (partly because of time pressure). In stage 3, we analyzed two orthogonal TDI channels given by X and $(X + 2Y)/\sqrt{3}$.

The true signal parameters were made publicly available on Dec. 4, and here we briefly describe how our search fared in their recovery. The injected signal had a combined² ($A + E$) SNR of 667.734; its true physical parameters are listed in the third column of table 8.2. Our best-fit waveform matched the true waveform rather well: it had an SNR of 664.47 and its cross-correlation with the true waveform was 0.994 for the A channel and 0.996 for the E channel [35]. The quality of the fit is illustrated in figure 8.3, which compares the true $X(t)$ (produced by us from the key file) with our best-fit $X(t)$, for short time stretches near the coalescence time t_c and near the beginning of the dataset. Clearly our fit is excellent near t_c , where most of the SNR accumulates, but is much poorer at early times, when the contribution to the SNR is much lower. The lesson from the other two Michelson variables is qualitatively the same.

Our best-fit parameters are listed in the last column of table 8.2: our inferred chirp mass M_c was correct to within $\Delta M_c/M_c < 10^{-3}$, our inferred symmetric mass ratio η to within $\Delta\eta \approx 4 \times 10^{-3}$, and the error in our coalescence time was $\Delta t_c \approx 45$ s, corresponding to approximately 0.05 GW periods just before the plunge. Nevertheless, it is clear from our estimates for the *other* parameters that, instead of converging on a neighborhood of the true maximum, our MCMC code locked onto a high but secondary maximum of the posterior probability distribution. Our inferred sky position is almost at the antipodes of the actual location (i.e., our ecliptic latitude is approximately the negative of the true value, and our ecliptic longitude is off by

²In this context, A and E are the orthogonal, optimal TDI observables given by $(2X - Y - Z)/3$ and $(Z - Y)/\sqrt{3}$, as used in [20]. The third orthogonal, optimal TDI observable, T , contributes only a tiny fraction of the total SNR for these sources.

Table 8.2: True values and estimates from three steps for the challenge parameters. In stages 1 and 2 estimates were made only for parameters M_c and η (and therefore m_1 and m_2) and t_c .

Parameter	Unit	True value	Stage 1	Stage 2	Stage 3
M_c	$10^6 M_\odot$	1.2086	1.208	1.2108	01.2077
η		0.160	0.17	0.163	0.156
m_1	$10^6 M_\odot$	2.8972	2.74	2.8536	2.9652
m_2	$10^6 M_\odot$	0.7270	0.76	0.7381	0.7130
t_c	10^7 s	1.3374027	1.3372	1.3374149	1.3374072
Ecl. Lat. θ	rad	0.492	–	–	0.536
Ecl. Long. ϕ	rad	0.866	–	–	4.039
Pol. Angle ψ	rad	3.234	–	–	5.886
Init. Phase φ_0	rad	3.527	–	–	0.233
Distance D	10^9 pc	8.000	–	–	16.811
Incl. Angle ι	rad	1.944	–	–	0.617

nearly π). This was not due to a mismatch of conventions or a bug in our code; rather, it reflects the above-mentioned degeneracy between antipodal sky locations (the degeneracy becomes perfect in the low-frequency limit). The four parameters $(D, \iota, \psi, \varphi_0)$ that determine the overall complex amplitudes of the GW polarizations h_+ and h_\times were also off by factors of order one, except for our overall phase φ_0 , which was correct to within 0.004 radians (modulo π).

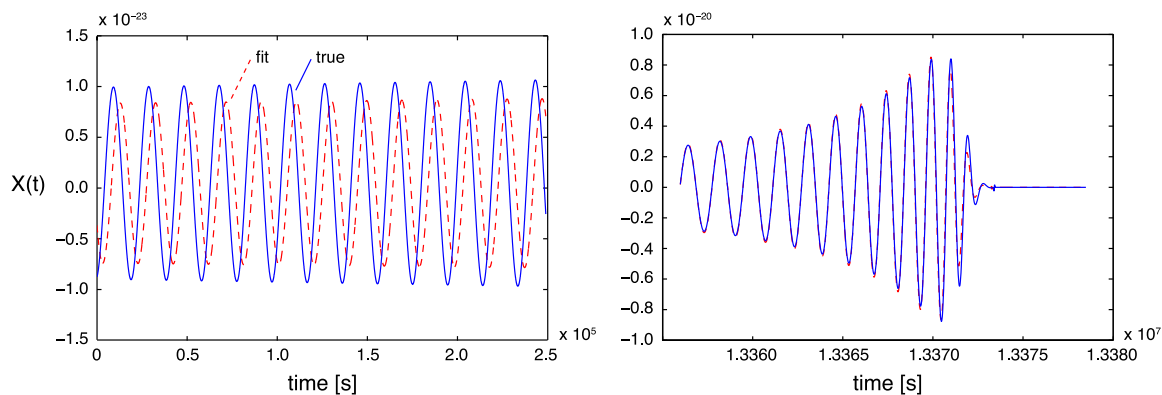


Figure 8.3: Comparison of our best-fit $X(t)$ to the true $X(t)$ for a) a short stretch of time near t_c and b) a short stretch near the beginning of the dataset. Clearly, our fit is excellent near t_c , where most of the SNR accumulates, but much poorer at early times.

It is also instructive (and reassuring) to contemplate the performance of the first two stages of our search. Stage 1 returned M_c with a fractional error $\Delta M_c/M_c < 10^{-3}$,

η to within $\sim 6\%$, and t_c to within $\sim 2 \times 10^3$ s. After stage 2, the estimated M_c was in fact slightly worse, but the errors in η and t_c were significantly reduced, to $\Delta\eta \approx 0.003$ and $\Delta t_c \approx 120$ s. This gratifying level of accuracy indicates that the coarser stages 1 and 2 were indeed accomplishing the job required of them.

8.6 Future Directions

As explained above, the most obvious improvement to our pipeline will be to recast the MCMC stage so that it maximizes the \mathcal{F} -statistic on the 5-dimensional space $(M_c, \eta, t_c, \theta, \phi)$, reducing the search-space dimensionality by three. In addition, we will extend our grid search to handle the case where the merger occurs *after* the end of the dataset (we did not compete on dataset 1.2.2 because our current grid search could not handle such mergers). This generalization should be fairly straightforward.

In the second round of Challenges (see the proceeding by Arnaud and colleagues in this volume [35]), dataset 2.2 contains signals from an entire Galaxy's worth of white-dwarf binaries, four to six SMBH binary inspirals (the exact number is not specified) with SNRs ranging from ~ 10 to ~ 2000 , and five EMRIs. Our plan is to first run our pipeline as a standalone search for the SMBH binaries, and then to join forces with Crowder and Cornish's WD binary search [32] to iteratively improve the fits provided by the two searches. Beyond that, we plan to extend the SMBH binaries search to include: 1) merger and ringdown waveforms; 2) spin-precession effects; and 3) the effects of nonzero eccentricity. For the first two items, we intend to make use of the technology already developed by the ground-based GW community. For instance, Buonanno, Chen, and Vallisneri [36] have shown how searches for binaries of spinning BHs can be made considerably more efficient by dividing the parameters into intrinsic (such as the masses) and extrinsic (such as the orientation of the orbital plane at a fiducial time), and optimizing over the extrinsic parameters semi-analytically. (This can be viewed as a generalization to spinning binaries of the \mathcal{F} -statistic analysis mentioned above.) We shall endeavour to generalize this strategy to LISA searches for SMBH binaries.

Bibliography

- [1] Krolik J H 1999. *Active Galactic Nuclei: From the Central Black Hole to the Galactic Environment* (Princeton University Press, Princeton, NJ)
- [2] Haehnelt M G and Kauffmann G 2002. MNRAS**336** L61
- [3] Volonteri M, Haardt F and Madau P 2003. ApJ**582**, 559
- [4] Komossa S *et al.* 2003. ApJ**582**, L15
- [5] Bender P L *et al.* 1998. *LISA Pre-Phase A Report* (Max-Planck-Institut für Quantenoptik, Garching, Germany)
- [6] Haehnelt M G 1998. In *Laser Interferometer Space Antenna, Second International LISA Symposium on the Detection and Observation of Gravitational Waves in Space* AIP Conf. Proc. 456 ed. Folkner, W M
- [7] Hughes S A 2002. MNRAS**331** 805
- [8] Holz D E & Hughes S A 2002. *Class. Quantum Grav.***20** S65
- [9] Arun K G, Blanchet L, Iyer B R and Qusailah M S S 2004. *Class. Quant. Grav.***21** 3771
- [10] Blanchet L, Faye G, Iyer B R and Joguet B 2002. Phys. Rev. D**65** 061501
- [11] Wainstein L A and Zubakov V D 1962. *Extraction of signals from noise*
- [12] Barish B C and Weiss R 1999. Physics Today**52**(10) 44

- [13] Babak S, Balasubramanian R, Churches D, Cokelaer T and Sathyaprakash B S 2006. *Class. Quant. Grav.***23** 5477
- [14] Allen B, Anderson W G, Brady P R, Brown D A and Creighton J D E 2005. gr-qc/0509116
- [15] Brown D A *et al.* 2004. *Class. Quant. Grav.***21** S1625
- [16] Abbott B *et al.* (LIGO Scientific Collaboration) 2007. In preparation
- [17] Lang R N and Hughes S A 2006. *Phys. Rev. D***74** 122001
- [18] Arnaud K A *et al.* (Mock LISA Data Challenge Task Force) 2006. In *Laser Interferometer Space Antenna, Sixth International LISA Symposium AIP Conf. Proc. 873*, ed. Merkowitz S M and Livas J C p 619
- [19] Arnaud K A *et al.* (Mock LISA Data Challenge Task Force) 2006. In *Laser Interferometer Space Antenna, Sixth International LISA Symposium AIP Conf. Proc. 873*, ed. Merkowitz S M and Livas J C p 625
- [20] Arnaud K A *et al.* (Mock LISA Data Challenge Task Force) 2007. In this volume, gr-qc/0701139
- [21] Will C M and Wiseman A G 1996. *Phys. Rev. D***54** 4813
- [22] Owen B J and Sathyaprakash B S 1999. *Phys. Rev. D***60** 022002
- [23] LSC Algorithm Library software packages LAL (CVS tag version `iulgroup_s1_20030420`), LALWRAPPER (version `iulgroup_s1_20030416`), and LALAPPS (version `iulgroup-030526`) were used in this analysis. URL [HTTP://WWW.LSC-GROUP.PHYS.UWM.EDU/LAL](http://www.lsc-group.phys.uwm.edu/lal)
- [24] Droz S, Knapp D J, Poisson E and Owen B J 1999. *Phys. Rev. D***59** 124016
- [25] Jaranowski P, Królak A and Schutz B F 1998. *Phys. Rev. D***58** 063001
- [26] Królak A, Tinto M and Vallisneri M 2004. *Phys. Rev. D***70** 022003

- [27] Cornish N J and Crowder J 2005. Phys. Rev. D**72** 043005
- [28] Cornish N J and Porter E K 2006. *Class. Quant. Grav.***23** S761
- [29] Wickham E D L, Stroeer A and Vecchio A 2006. *Class. Quant. Grav.***23** S819
- [30] Cornish N J and Porter E K 2007. Phys. Rev. D**75** 021301
- [31] Stroeer A, Gair J R and Vecchio A 2006. In *Laser Interferometer Space Antenna, Sixth International LISA Symposium* AIP Conf. Proc. 873, ed. Merkowitz S M and Livas J C p 444
- [32] Crowder J and Cornish N 2007. Phys. Rev. D**75** 043008
- [33] Vallisneri M 2005. Phys. Rev. D**71** 022001
- [34] Cornish N J and Porter E K 2007. gr-qc/0701167
- [35] Arnaud K A *et al.* (Mock LISA Data Challenge Task Force) 2007. In this volume, gr-qc/0701170
- [36] Buonanno A, Chen Y and Vallisneri M 2003. Phys. Rev. D**67** 104025